Quantum hyperpolarisation of nuclear spins and multi-modal microscopic imaging with diamond defect spins

David Broadway


orcid.org/0000-0002-7375-8766

Submitted in total fulfillment of the
requirements for the degree of
Doctor of Philosophy

School of Physics,
The University of Melbourne
Australia

October 9, 2019

Declaration of originality

This is to certify that:

1. The thesis comprises only their original work towards the degree of doctor of philosophy except where indicated in the statement of contributions,
2. due acknowledgment has been made in the text to all other material used,
3. the thesis is fewer than 100,000 words in length, exclusive of tables, maps, bibliographies and appendices.

I authorize the Head of the School of Physics to make or have made a copy of this thesis to any person judged to have an acceptable reason for access to the information, i.e., for research, study or instruction.

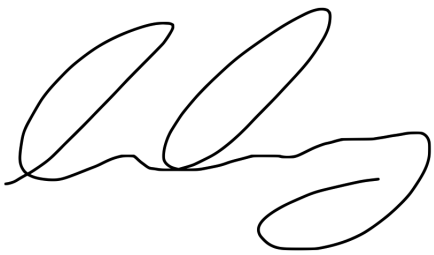

David Broadway

October 9, 2019

Abstract

Quantum technologies promise to impact on several aspects of society. Examples include quantum computing to perform certain calculations significantly faster than current classical computers, quantum cryptography for more secure communications, quantum sensing to make measurements with unprecedented sensitivity and resolution, and specialised quantum devices such as quantum hyperpolarisers for enhanced medical imaging. However, the field is still in its infancy and most quantum technologies have been realised only in delicate laboratory settings with little prospect for real-world applications (e.g. quantum sensors), or are many years away from being mature enough to make an impact (quantum computing). This thesis develops two applications of quantum technologies, in the direction of quantum hyperpolarisation on the one hand and quantum sensing on the other hand, which utilise a quantum system particularly suited for practical applications, the nitrogen-vacancy (NV) centre in diamond. This diamond spin defect can be operated in ambient conditions and the resulting quantum devices can be easily miniaturised for large scale deployment.

Specifically, in the first part of this thesis (chapters 2 to 4), two new techniques to realise hyperpolarisation (HP) of nuclear spins are developed. Through effective HP, ensembles of nuclear spin can be polarised far beyond the normal Boltzmann level, which can be used to enhance the spin signal for nuclear magnetic resonance (NMR) and imaging (MRI). Chapter 2 and 3 focus on exploiting direct cross-relaxation (CR) between the NV spin and the nuclear spin. Chapter 2 investigates a CR-based protocol for sensing, and determines, through a study of the NV physics, under what regimes this protocol can be applied to nuclear spin detection. This study constructs a framework under which HP via CR can be realised. Chapter 3 continues in this direction and demonstrate that CR

can be used to hyperpolarise external nuclear spins. A detailed understanding of the spin bath mechanics is explored and the impact of rogue uncontrolled NV spins on this spin bath is determined. Additionally, this protocol is compared with other HP techniques and shows a remarkable improvement in polarisation rate, however, it is particularly sensitive to magnetic field detuning. To overcome this issue, in chapter 4 a different technique is developed that relies on a dynamical decoupling protocol purposefully modified to achieve HP. This new technique has a slower polarisation rate than CR-based HP but is robust to the experimental errors that exist in scaling these hyperpolarisation techniques.

The second part of this thesis (chapters 5 and 6) exploits the quantum sensing properties of ensembles of NV centres in diamond to develop multi-modal microscopic imaging, which is a promising tool for device diagnosis and the study of mesoscopic phenomena. Specifically, chapter 5 develops and implements a technique for imaging the electric field simultaneously with the magnetic field. The technique is applied to the study of electric fields that are intrinsic to interfaces and junctions. The functionality of electronic devices (such as transistors) are fundamentally dictated by these fields which have traditionally been opaque to probing except at the very surface. While the surface potential is crucial, a wealth of information is contained in the bulk structure which is the focus of this study. In chapter 6 the same sensing protocol is extended to image stress embedded in the diamond rather than electric fields. A series of different deformation sources is used to test and verify that the technique can determine the entire stress tensor with high sensitivity and micrometer spatial resolution. With these new imaging capabilities, extending the traditional magnetic field sensing to electric field and stress, multi-modal NV imaging is a promising example of quantum technology that may have an immediate impact in other fields of science.

Acknowledgement

During my PhD I have had the pleasure to work with many people within my own institution and abroad. This collaboration has greatly assisted me in producing the body of work that is contained in this thesis. I have had a great deal of support from my two supervisors: Prof. Lloyd Hollenberg and Dr. Jean-Philippe Tetienne. Lloyd has put in a tremendous amount of effort and time do build a strong group which has experience in both experiment and theory. Joining such a well establish group allowed me to focus on the science and greatly helped me achieve the work that I conducted. He has an extremely broad knowledge base and has been instrumental in elevating our work to a higher level. Jean-Philippe dealt with helping me on a day to day basis, whether he was coming up with great ideas for experiments or we were arguing about figures for hours in his office, he helped me immensely. His contribution to the working and willingness to help can not be overstated, my thesis would be dramatically different and substantively less complete without his guidance. He is extremely passionate about science and is driven to excel in everything he does and was happy to drag me along in the same direction, much to my betterment.

Throughout my candidature I worked very closely with a few people on various projects. When I started my masters and continued into my PhD I was working with James Wood who was also a PhD candidate at the time. Together we obtained a great deal of experimental results and he was a key contributor in some of my early research. He was always willing to help me understand something even if I was not listening very well, which was a great deal of help throughout my masters and started my PhD on the right foot. Liam Hall has also made significant contributions to my research through developing theory to explain many results that I personally did not understand. He has a

strong analytical mind and has a lot of drive to solve problems that others would give up on. While it took me a long time to start understanding the language of the theorist it has certainly been worthwhile, as my understanding of the underlying physics has greatly improved through working with him.

I have also had the great pleasure of working with Scott Lillie as we both go through our PhDs together. We have worked on many projects together and I have enjoyed his bubbly attitude, his joy at getting new results, and his wacky behaviour in the office (often with myself being just as wacky). We have sat adjacent to each other for many years now and yet he is still enjoyable to be around and have a laugh with, it has truly been a pleasure. On a similar vein, working with Nikolai Dontschuk has been a great experience. While we do love to get into heated debates about basically anything it has been a lot of fun. Whether we were out having whiskey tastings or we were just getting some amazing results in the lab we were enjoying ourselves. He is an extremely passionate man and his passion is infectious to those around him.

I have also received a significant amount of assistance from Dr. David Simpson and Dr. Alastair Stacey, both of which helped me through both masters and my PhD candidature. David was crucial to me starting in this group to begin with and started me on the research direction that I am still following today. He is amazingly friendly and always a pleasure to be around. Alastair is always willing to have a discussion and to help anyone further their understand of physics and the material science that goes into so much of our work. He is both passionate about science and helping people become the best scientists they can be. It has been great to work with both David and Alastair.

I have also had the pleasure to work with many people outside of our group. Whether they were in our department or at another university altogether they have all contributed in some way to accomplishing the science presented in this thesis. There is so many people that have been involved which I would like to acknowledge: Brett Johnson, Jeffery McCallum, Marcus Doherty, Michael Barson, Alex Tsai, Chris Lew, Jacob Lang, Tania Monteiro, and all my other co-authors.

I would be remiss not to acknowledge all of the support I have received from my friends and family over the course of my PhD candidature. Whether they were actively helping me in my work or just there to help me relax they have all contributed to helping

me through this chapter of my life. I would like to give a special thanks to my partner Alisia Kneale who has been there for me throughout this whole process. Whether she was putting up with me coming home late or dealing with me working at home rather than paying attention to her, she has been very kind and compassionate. Everything would have been harder without her around to help me.

Finally, as this University of Melbourne campus is situated on ancient indigenous lands, I would like to acknowledge the Wurundjeri people who are the Traditional Custodians of the Land. I would also like to pay respect to the Elders both past, present and emerging of the Kulin Nation and extend that respect to other Indigenous Australians.

Statement of contribution

Here I will summarise the contributions to the work presented in this thesis. The papers referenced are directly from the list of publications.

Chapter 2 comprises results from three published papers. In Section 2.1 a brief summary of the results from paper [1] is given as an introduction to cross relaxation based sensing, in which I was a key contributor but was performed prior to the start of my PhD candidature. In Section 2.2 the results from paper [2] are given, in which I built the experimental setup, took the measurements, and developed/performed the analysis, all under the direct guidance and assistance of Dr. Jean-Philippe Tetienne and Dr. James Wood. Additional guidance was also given by Dr. David Simpson, Dr. Liam Hall and Dr. Alistair Stacey, all of which were fundamental in the initialisation of the project and responsible for the initial idea. Finally, in Section 2.3 a summary of results from paper [4] is given, where the experiment was mainly conducted by Dr. James Wood. The measurements for the depth dependence were taken by Dr. Jean-Philippe Tetienne and me.

Chapter 3 includes work from two papers [6, 7] that were both experimentally performed by me and Dr. Jean-Philippe Tetienne with guidance from Prof. Lloyd Hollenberg. The theoretical development of the hyperpolarisation technique was conducted by Dr. Liam Hall with input from Dr. Jean-Philippe Tetienne, Prof. Lloyd Hollenberg, and me.

Chapter 4 is based on paper [18], where the experimental measurements, protocols and analysis was developed and performed by myself with input from Dr. Jean-Philippe Tetienne. The Floquet theory and polarisation protocol was developed by Dr. Jacob Lang and Prof. Tania Monteiro. Additional analytic and numerical simulations were also

performed by Mr. Gregory White and Dr. Liam Hall.

Chapter 5 is based on paper [8] where the NV measurements, analysis protocols, theoretical sensitivities, and NV optimisation to electric fields was conducted by myself with input from Dr. Jean-Philippe Tetienne and guidance from Prof. Lloyd Hollenberg. Dr. Marcus Doherty helped with the interpretation of the electrometry measurements as well as contributing an analysis for the disentanglement of electric and stress fields. The device fabrication was performed by Dr. Nikolai Dontschuk, Mr. Alex Tsai, and myself. The theoretical framework for describing the band bending was developed by Dr. Nikolai Dontschuk.

Chapter 6 is based on paper [15], where the NV measurements, analysis protocols, and NV optimisation to stress fields was conducted by myself with input from Dr. Jean-Philippe Tetienne. The device fabrication and characterisation were performed by Dr. Nikolai Dontschuk, Prof. Jodie Bradby, Mr. Daniel McCloskey, Dr. Brett Johnson, Mr. Alex Tsai, Mr. Scott Lillie, Dr. Michael Barson, and myself. The theoretical description of the NV ensembles response to stress was developed by Dr. Marcus Doherty and Dr. Michael Barson. Additionally, Dr. Marcus Doherty developed the framework for processing the stress fields into body forces and both Dr. Marcus Doherty and Dr. Michael Barson performed numerical modelling to calculate the expected body forces from different sources.

List of Publications

2016

1. J. D. A. Wood, D. A. Broadway, L. T. Hall, A. Stacey, D. A. Simpson, J.-P. Tetienne, and L. C. L. Hollenberg. Wide-band, nanoscale magnetic resonance spectroscopy using quantum relaxation of a single spin in diamond. Phys. Rev. B. 94, 1-16 (2016).

2. D. A. Broadway, J. D. A. Wood, L. T. Hall, A. Stacey, M. Markham, D. A. Simpson, J.-P. Tetienne, and L. C. L. Hollenberg. Anticrossing Spin Dynamics of Diamond Nitrogen-Vacancy Centers and All-Optical Low-Frequency Magnetometry. Phys. Rev. Appl. 6, 064001 (2016).

2017

3. J.-P. Tetienne, N. Dontschuk, D. A. Broadway, A. Stacey, D. A. Simpson, and L. C. L. Hollenberg. Quantum imaging of current flow in graphene. Sci. Adv. 3, e1602429 (2017).

4. J. D. A. Wood, J.-P. Tetienne, D. A. Broadway, L. T. Hall, D. A. Simpson, A. Stacey, and L. C. L. Hollenberg. Microwave-free nuclear magnetic resonance at molecular scales. Nat. Commun. 8, 15950 (2017).

5. S. E. Lillie, D. A. Broadway, J. D. A. Wood, D. A. Simpson, A. Stacey, J.-P. Tetienne, and L. C. L. Hollenberg. Environmentally Mediated Coherent Control of a Spin Qubit in Diamond. Phys. Rev. Lett. 118, 167204 (2017).

2018

6. D. A. Broadway, J.-P. Tetienne, A. Stacey, J. D. A. Wood, D. A. Simpson, L. T. Hall, and L. C. L. Hollenberg. Quantum probe hyperpolarisation of molecular nuclear spins. Nat. Commun. 9, 1246 (2018).

7. D. A. Broadway, S. E. Lillie, N. Dontschuk, A. Stacey, L. T. Hall, J.-P. Tetienne, and L. C. L. Hollenberg. High precision single qubit tuning via thermo-magnetic field control. Appl. Phys. Lett. 112, 103103 (2018).

8. D. A. Broadway, N. Dontschuk, A. Tsai, S. E. Lillie, C. T.-K. Lew, J. C. McCallum, B. C. Johnson, M. W. Doherty, A. Stacey, L. C. L. Hollenberg, and J.-P. Tetienne. Spatial mapping of band bending in semiconductor devices using in situ quantum sensors. Nat. Electron. 1, 502-507 (2018).

9. S. E Lillie, D. A Broadway, N. Dontschuk, A. Zavabeti, D. A Simpson, T. Teraji, T. Daeneke, L. C L Hollenberg, and J.-P. Tetienne. Magnetic noise from ultrathin abrasively deposited materials on diamond. Phys. Rev. Mater. 2, 116002 (2018).

10. A. Stacey, N. Dontschuk, J.-P. Chou, D. A. Broadway, M. J. Sear, A. Schenk, J.-P. Tetienne, A. Hoffman, S. Prawer, C. Pakes A. Tadich, N. P. de Leon, A. Gali, and L. C. L. Hollenberg, Evidence for primal sp^2 defects at the diamond surface: candidates for electron trapping and noise sources. Adv. Mater. interfaces 1801449, (2018).

11. J.-P. Tetienne, D. A. Broadway, S. E. Lillie, N. Dontschuk, T. Teraji, L. T. Hall, A. Stacey, D. A. Simpson, and L. C. L. Hollenberg. Proximity-Induced Artefacts in Magnetic Imaging with Nitrogen-Vacancy Ensembles in Diamond. Sensors 18, 1290 (2018).

12. J.-P. Tetienne, R. W. De Gille, D. A. Broadway, T. Teraji, S. E. Lillie, J. M. McCoey, N. Dontschuk, L. T. Hall, A. Stacey, D. A. Simpson, and L. C.L. L Hollenberg. Spin properties of dense near-surface ensembles of nitrogen-vacancy centers in diamond. Phys. Rev. B 97, 85402 (2018).

2019

13. J.-P. Tetienne, N. Dontschuk, D. A. Broadway, S. E. Lillie, T. Teraji, D. A. Simpson, A. Stacey, and L. C. L. Hollenberg. Apparent delocalization of the current density in metallic wires observed with diamond nitrogen-vacancy magnetometry. Phys. Rev. B 99, 014436 (2019).

14. J. E. Lang, T. Madhavan, J.-P. Tetienne, D. A. Broadway, L. T. Hall, T. Teraji, T. S. Monteiro, A. Stacey, and L. C. L. Hollenberg. Nonvanishing effect of detuning errors in dynamical-decoupling-based quantum sensing experiments. Phys. Rev. A 99, 12110 (2019).

15. D. A. Broadway, B. C. Johnson, M. S. J. Barson, S. E. Lillie, N. Dontschuk, D. J. McCloskey, A. Tsai, T. Teraji, D. A. Simpson, A. Stacey, J. C. McCallum, J. E. Bradby, M. W. Doherty, L. C. L. Hollenberg, and J.-P. Tetienne. Microscopic Imaging of the Stress Tensor in Diamond Using in Situ Quantum Sensors. Nano Lett. 1812.01152, acs.nanolett.9b01402 (2019).

16. S. E. Lillie, N. Dontschuk, D. A. Broadway, D. L. Creedon, L. C. L. Hollenberg, and J.-P. Tetienne, Imaging graphene field-effect transistors on diamond using nitrogen-vacancy microscopy. Phys. Rev. Appl. 12, 024018 (2019).

Submitted

17. D. J. McCloskey, N. Dontschuk, D. A. Broadway, A. Nadarajah, A. Stacey, J.-P. Tetienne, L. C. L. Hollenberg, S. Prawer, and D. A. Simpson. Enhanced widefield quantum sensing with nitrogen-vacancy ensembles using diamond nanopillar arrays. Submitted, Preprint arXiv 1902.02464, (2019).

18. J. E. Lang, D. A. Broadway, G. A. L. White, L. T. Hall, A. Stacey, L. C. L. Hollenberg, T. S.Monteiro, and J. -P. Tetienne. Quantum bath control with nuclear spin state selectivity via pulse-adjusted dynamical decoupling. Submitted, Preprint arXiv 1904.00893, 1-15 (2019).

Contents

1

Introduction

The quantum system at the heart of this thesis is the nitrogen-vacancy (NV) centre [1], which is an extremely useful spin defect in diamond. Applications of the NV spin can be broadly separated into four categories: quantum information [2–13], sensing [1, 14–20], imaging [21–27], and hyperpolarisation [28–42]. As a sensor the NV spin sub-levels and quantum properties are strongly dependent on environmental fields near the NV spin. This dependence makes the NV spin capable of measuring static magnetic fields [15, 43–45], electric fields [46, 47], strain and pressure [48, 49], sinusoidal and fluctuating magnetic fields [50–54], and temperature [55–59]. Due to these effects, the NV spin has been used to probe many different systems: 2D materials [21, 60], spectroscopy with resolutions capable of measuring chemical shifts of nuclear spins [61–65], magnetic phenomena like domain walls and skyrmions [22–25], and has even been used for measurements on biological samples [26, 27, 56, 66–70]. The first part of this thesis (chapters 2-4) will investigate new techniques for sensing and hyperpolarisation of nuclear spins, whereas the second part (chapters 5 and 6) will develop new imaging methods. The goal of the present chapter is to give some background information that will help understand the details and context of these new developments. Specifically, in section 1.1 the basics of NV spin measurements are reviewed, as these will be used throughout the thesis. In section 1.2, the various types of experimental implementations of NV experiments are discussed along with the state of the art in their applications, to give context to both parts of the thesis.

1.1 Basics of NV spin measurements

1.1.1 The nitrogen-vacancy (NV) centre

The nitrogen-vacancy (NV) colour centre is an atom-like defect in diamond that consists of a substitutional nitrogen atom adjacent to a lattice vacancy [1], shown in Fig. 1.1a. These defects can be formed during the diamond growth using chemical vapour deposition (CVD) diamond synthesis or can be artificiality created after diamond growth via irradiation or ion-implantation. The NV centre has three possible charge states - the negative charge state NV^- [71] and neutral charge state NV^0, which either could be stable under normal conditions, and the more recently studied positive charge state NV^+ [10, 72, 73] – that is accessed through changes in the band structure or applied potentials. As both the NV^- and NV^0 are colour centres (that is, they absorb and emit light) it is important to filter out any unwanted emissions from the other centres. The zero photon line (ZPL) of both charges states is separated well enough (ZPL(NV^-) = 637 nm versus ZPL(NV^0) = 575 nm [1, 74]) that this is achievable to standard colour filter optics. In this work the charge state that is investigated it the NV^- centre (hereafter refereed to as just NV) due to its useful spin properties.

The electronic ground state of the NV centre is a spin triplet ($S = 1$) with 3 spin sub-levels $|0\rangle$, $|\pm1\rangle$. Optical detection of the spin energy structure of the NV centre is possible due to a variation in the photo-luminescence (PL) emitted from the $|0\rangle$ and $|\pm1\rangle$ spin states [77], shown in Fig. 1.1b. This difference is caused from a stronger coupling of the $|\pm1\rangle$ states to a metastable dark state than the $|0\rangle$ state [78–83]. These different coupling strengths result in the $|0\rangle$ being brighter than the $|\pm1\rangle$ states, facilitating the optical readout of the spin state. An example of the difference in PL from the $|0\rangle$ to $|\pm1\rangle$ states during a laser pulse is shown in Fig. 1.1c. Optically pumping the system also results in an optical spin polarisation [71] of the NV spin into the $|0\rangle$ state due to a stronger coupling from the metastable state into the $|0\rangle$ spin state [84–87]. As a result the laser pulse not only reads out the NV spin state but also initialises it into the $|0\rangle$ state.

The NV spin consists of two electrons that are coupled through the fine interaction to produce a spin $S = 1$ system, giving three spins states, $|0\rangle$ and the degenerate (in

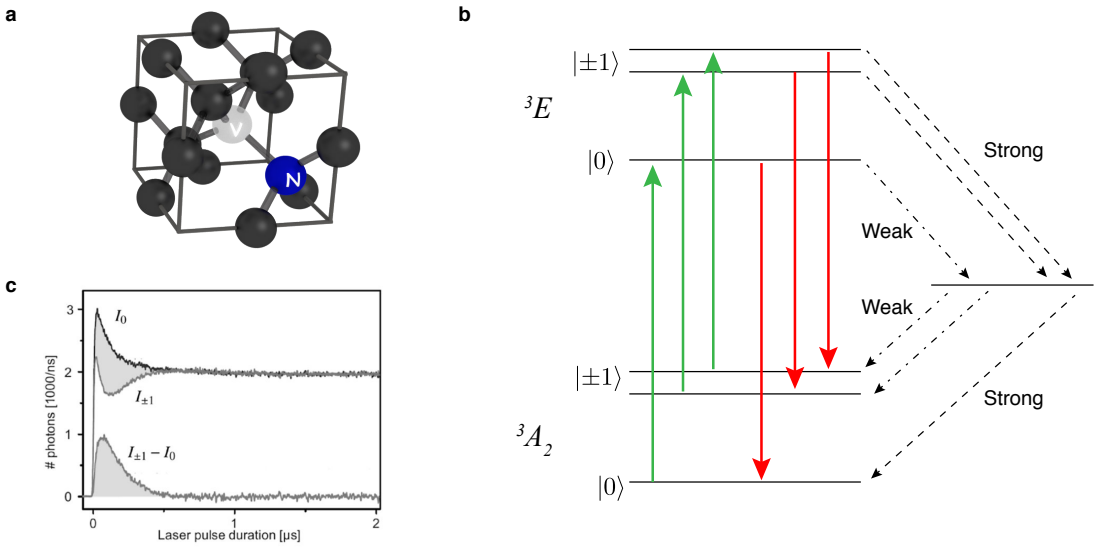

Figure 1.1: The NV- centre in diamond, structure and photo-dynamics a Depiction of NV centre consisting of an adjacent nitrogen and vacancy in the diamond lattice. **b** NV^- electronic structure including the ground state ($^3A_2$) and first excited state (^3E) [75]. The optical transitions are shown as green (laser induced) and red (Photo luminescences, PL) solid lines and the non-radiative transitions to and from the metastable state are shown as dashed lines. **c** Example of the PL trace from a single NV centre during a laser pulse when the NV spin is initialised in the $|0\rangle$ compared with $|\pm1\rangle$ states, taken from Ref. [76].

the absence of magnetic and electric fields) $|\pm1\rangle$ states. On top of this, the nitrogen has a nuclear spin which introduces a hyperfine interaction which splits these states further (Fig. 1.2a). In the presence of a magnetic field, the spin structure is described by the Hamiltonian

$$\mathcal{H} = D_{gs}S_z^2 + \gamma_e \mathbf{B}\cdot\mathbf{S} - \gamma_n \mathbf{B}\cdot\mathbf{I} + Q_{gs}I_z^2 + \mathbf{S}\cdot\mathbf{A}_{gs}\cdot\mathbf{I} \tag{1.1}$$

where $D_{gs} \approx 2.87$ GHz is the zero field splitting [1], γ_e and γ_n are the gyromagnetic ratios of the electron on nuclear spin respectively [71,88], $\mathbf{B}$ is the applied magnetic field vector, $\mathbf{S}$ and $\mathbf{I}$ are the relevant spin operators for the electron and nuclear spin respectively. The hyperfine coupling matrix $\mathbf{A}_{gs}$ defines the coupling strength between the NV electron and nuclear spin in both the parallel and transverse plane [71,76,87–94] and finally Q_{gs} is the quadrupole moment (which is non-zero for the ^{14}N-V only) [76,87,89,94]. In chapters 5 and 6, we will add extra terms to this basic Hamiltonian to include the effect of electric field and strain.

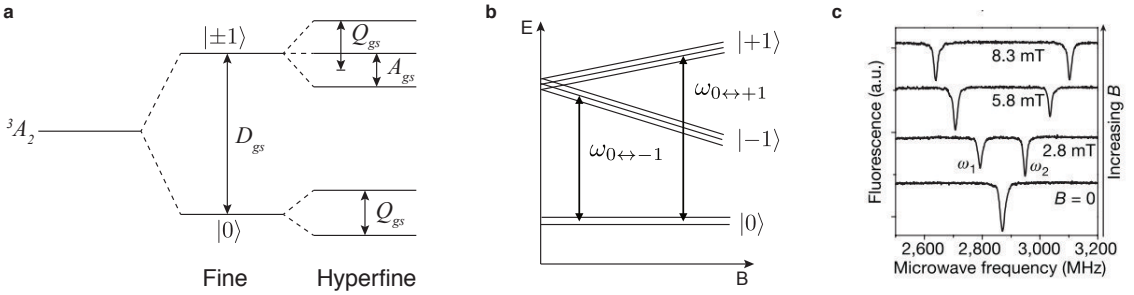

Figure 1.2: Optically detected magnetic resonance (ODMR). a The intrinsic structure of the ground states of the NV centre, comprising of fine and hyperfine splitting [1]. **b** Change in the energy structure under the application of an external magnetic field. **c** ODMR spectra at different magnetic field strengths, taken from Ref. [44]. In these spectra the hyperfine structure is not resolved.

1.1.2 Optically detected magnetic resonance (ODMR)

Magnetic fields applied to the NV spin (either deliberately or stray environmental fields) induce a Zeeman splitting of the $|\pm1\rangle$ spin states, as given in Eq. 1.1 and shown in Fig. 1.2b. Due to this splitting, precision measurements of the NV spin sub-levels is a method for determining the magnetic field strength and direction at the NV centre [44]. These measurements are typically performed using the technique of optically detected magnetic resonance (ODMR) and takes advantage of the difference in PL from the $|0\rangle$ and $|\pm1\rangle$ states. In order to identify the spin energy levels a transition is induced between the $|0\rangle$ and $|\pm1\rangle$ states via a pulsed microwave (MW) or radio frequency (RF) signal. When the pulse is on resonance (i.e. the frequency matches the transitional energy between the states $\omega_{\mathrm{MW}} = \omega_{0\rightarrow\pm1}$) a transition is induced and a decrease in PL is observed. Through mapping of the PL versus the applied frequency it is possible to determine the transition frequency $\omega_{0\rightarrow\pm1}$, see Fig. 1.2c. In principle, there should be hyperfine transitions that split the observed ODMR peaks, however, the coupling strengths only result in splitting on the order of several MHz. As such, broadening, either from power broadening [95] or from spin bath interactions [96], can result in a width of the ODMR peaks that is larger than the hyperfine splitting and thus appear as a single peak.

ODMR is used to identify the energy levels of the NV spin, which is crucial for more complex spin manipulation measurement protocols that require on resonance driving of these transitions [97–99]. As such it is fundamental to performing most measurement

protocols with the NV spin. However, it is not limited to just identifying the transition energies for other protocols. ODMR can also be used as a complete protocol itself to measure static magnetic fields in the environment. For example, ODMR has been used to measure magnetic fields from magnetic bits in a hard drive [45], mapping of fields produced from current in devices [21,100,101], and measurements of magnetic nano-particles in living cells [26]. This style of measurement is used in chapters 5 and 6, where standard ODMR-based magnetometry will be extended to allow simultaneous measurements of electric field or strain.

1.1.3 Rabi

Initialising the NV spin into a given quantum state or superposition is the keystone to multiple pulse quantum control and measurement. However, in order to achieve this the quantum operations or rotations must be defined. In order to define the two most ubiquitous rotation operations, π and $\pi/2$, a Rabi sequence is required [68,102,103]. This involves resonantly driving a transition and mapping the population of a given spin against the driving duration. The control sequence for the NV spin is as follows: an initial laser pulse is used to initialise the NV spin into the $|0\rangle$ state, then a MW pulse is used to drive the NV spin between either of the $|\pm1\rangle$ states and the $|0\rangle$, finally a second laser pulse is applied to readout the spin state and reinitialise the NV spin into the $|0\rangle$ state, the sequence is shown in Fig. 1.3a. An example of a Rabi oscillation measured for a single NV spin is shown in Fig. 1.3b. The π-pulse is then defined as the maximal transfer fo population from the bright $|0\rangle$ state to the $|\pm1\rangle$ states, i.e. the minimal PL, shown in Fig. 1.3c.

A variant of Rabi driving is spin locking, where a $\pi/2$ pulse is first applied before the pulse of variable duration. This puts the NV in a dressed state [18, 104, 105] where this new state has a new set of eigenstates $|\omega_{\pm}\rangle$ whose separation is defined by the driving strength of the applied MWs. This can be an extremely useful technique as is facilitates NV coupling to low frequencies ($\sim$ 1 - 10 MHz). The application of this technique to resonantly couple the NV to nuclear spins, called Hartmann-Hahn or NOVEL, will be used in chapter 3 to hyperpolarise ^{13}C spins internal to the diamond and has been used

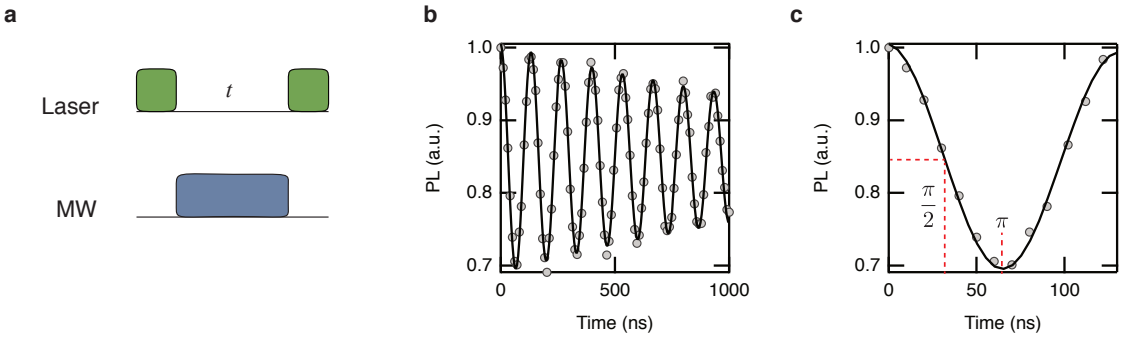

Figure 1.3: Rabi oscillation.a Pulse sequence for NV Rabi measurements, the first laser pulse (green) initialises the NV spin, while the second records the NV spin state. The microwave pulse (blue) is tuned to a transition between $|0\rangle$ and $|\pm1\rangle$ states. **b** Measurement of Rabi oscilations on a single NV spin. **c** Zoom-in of first period of the oscillation shown in **b**. The π time is defined at the minimum value of PL, $t_\pi \approx 66$ ns, while the $\pi/2$ time is given by halfway point, $t_{\pi/2} \approx 33$ ns.

extensively in the literature [28, 29, 34, 36, 41, 99, 104, 106–108].

1.1.4 Relaxation and decoherence

A useful tool for understanding phase accumulation and decoherence is to project states onto the Bloch sphere, which is a visual representation of the superposition of two states and how the populations, phase, and coherences of these states evolves with time or control sequences. The representation takes a state $|\psi\rangle$ that is some combination of two base eigenstates (e.g. $|0\rangle$, $|+1\rangle$) such that,

$$|\psi\rangle = \alpha \exp(i\varphi)\,|0\rangle + \beta \exp(-i\varphi)\,|+1\rangle\,, \tag{1.2}$$

and maps all possible states onto a sphere. The pure states (α or β equal to zero) are the north and south poles of the sphere, which define the z axis. The populations ($|\alpha|^2$ and $|\beta|^2$) are given by the angle, θ, between pure states and the phase, φ, is given by the azimuthal angle. The total coherence of this state vector, $|\psi\rangle$, is represented by the arrow length, r, from the centre, where $r = 1$ (i.e. touching the surface of the sphere) is perfectly coherent and $r = 0$ (i.e. arrow has zero length) represents a system that has zero coherence.

Longitudinal or spin-lattice relaxation or decoherence

Longitudinal relaxation is the reduction of the length of the state vector along the z axis and has a characteristic time, T_1. In the simplest case this is the relaxation of a single pure state into a mixed state, which has an arrow length or state vector length of zero. The Bloch sphere representation of this is shown in Fig. 1.4a. With the NV spin this quantity is measured with the pulse sequence shown in Fig. 1.4b, which consists of an initialisation laser pulse placing the NV into the $|0\rangle$ state followed by a readout laser pulse after a time, τ. An example of a T_1 measurement is shown in Fig. 1.4c showing a typical phonon dominated T_1 of bulk NV spins in the order of milliseconds [109]. T_1 is often referred to as spin-lattice relaxation during to the relaxation mechanism being caused from interactions with lattice phonons. However, this is not strictly the only mechanism as magnetic noise that is at the frequency of the transition between two states can induce a relaxation as well. This magnetically induced relaxation is in fact the basis for the methods developed in chapters 2 and 3 to measure noise spectra and detect proximal spins.

Transverse or spin-spin relaxation

Transverse relaxation is the decoherence of a superposition state, that is the reduction in the length of the state vector in the transverse plane in the Bloch sphere. There are two types of transverse relaxation with characteristic times, $T_2^\star$ and T_2, where $T_2 \geq T_2^\star$. The first is the raw coherence of a superposition state, that is, without any additional control sequences to mitigate some decoherence processes. The Bloch sphere representation of this is shown in Fig. 1.4d, where the spin is projected into a superposition state by applying a $\pi/2$ pulse. Once the spin is in the transverse plane the spin precesses and accumulates phase which can be converted into a population by applying another $\pi/2$ pulse. The NV laser sequence is shown in Fig. 1.4e where the evolution time is now defined between the two microwave pulses rather than the laser pulses. As the time evolves in this sequence an oscillation will occur due to the accumulation of phase in the presence of a detuning between NV and MW frequencies. In the absence of decoherence and a perfectly static environment this oscillation will persist forever. However, due to changing in the local spin states, the applied magnetic field, etc, there is an envelope of decoherence that dampens

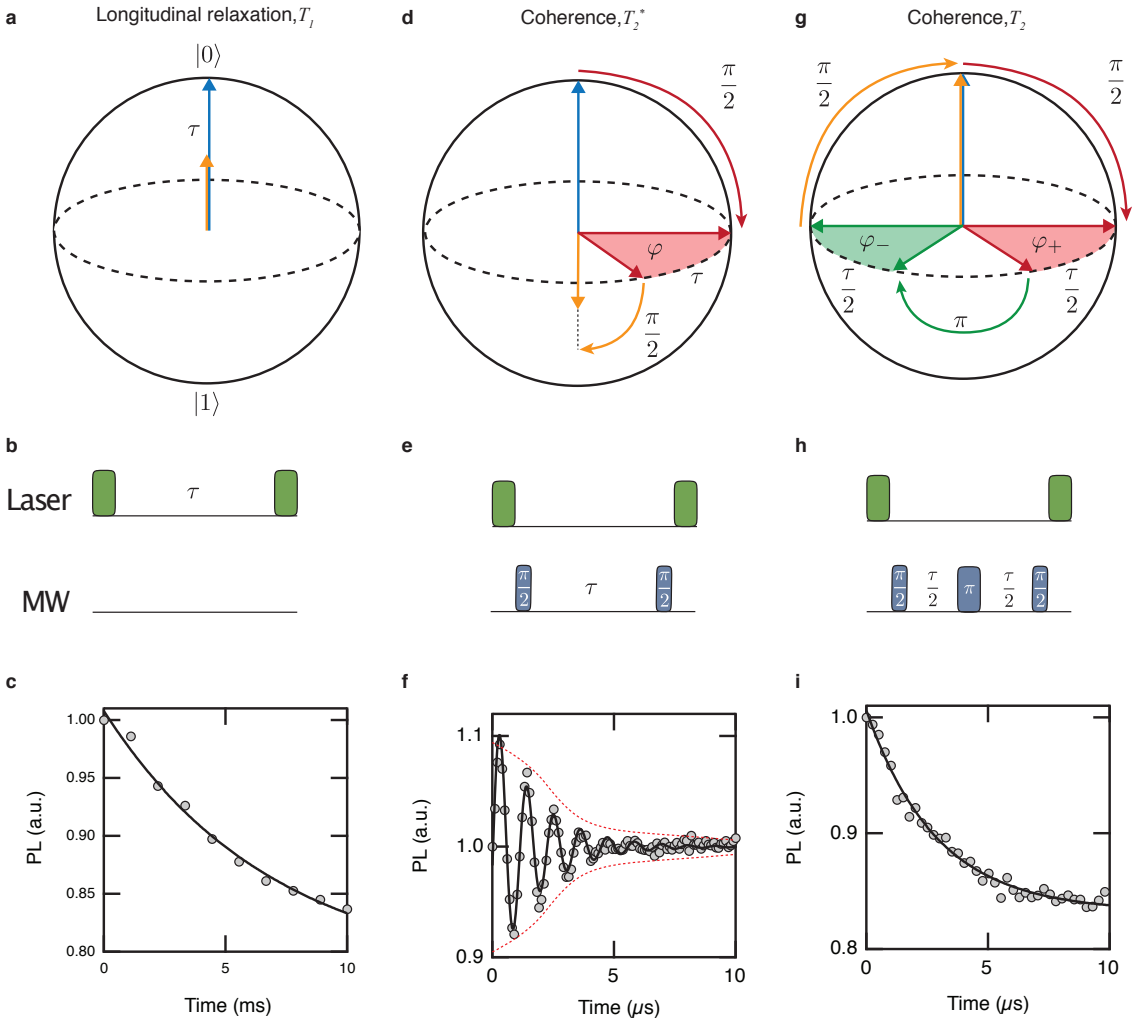

Figure 1.4: Types of decoherence. **a** Bloch sphere representation of longitudinal relaxation. **b** Longitudinal relaxation pulse sequence for NV spins. **c** Experimental data of the longitudinal relaxation of a NV spin where the exponential fit gives the decay time, T_1. **d** Bloch sphere representation of Ramsey sequence with a background DC magnetic field that produces dephasing when in a superposition state. **e** Laser and microwave Ramsey pulse sequence for NV spins. **f** Experimental data of a Ramsey measurement where the coherence time $T_2^\star$ is given by the envelope (red dashed lines). **g** Bloch sphere representation of the Hahn-Echo or Spin-echo sequence. **h** Hahn-echo pulse sequence for NV spins. **i** Experimental data of the Hahn-echo sequence where the fit (exponential whose argument power varies from 1 to 4 depending on bath dynamics [96]) defines the coherence time, T_2.

the oscillation with a characteristic time T_2^*, an example is shown in Fig. 1.4f. This can be interpreted as different static field conditions over the measurements[1] that cause the spin to experience different oscillation frequencies which sum to zero after some time. This can be observed through the broadening of the NV transition line in ODMR that gives the distinct possibility that the NV spin is in fact driven off resonance during some of the control pulses, contributing to a changes in phase.

The quasistatic changes in field that reduces the coherence of the spin can be removed by applying a π-pulse at equal distance between the $\pi/2$-pulses. This Hahn-echo sequence effectively removes a static phase accumulation over the measurement sequence and decouples the spins from this noise source. The Bloch sphere representation of this is shown in Fig. 1.4g. This sequence gives the coherence time as T_2 which is measured by NV spins with the pulse sequence shown in Fig. 1.4h. An example of a T_2 measurement is shown in Fig. 1.4i. Note that for NV spins the T_2 is often significantly shorter than the T_1 time, however, by applying more complicated decoupling pulse sequences this gap can be bridged to the point that T_2 is T_1-limited.

1.1.5 Detection of remote spins with the NV spin

The NV spin is used to measure environmental spins either through a coherent interaction of the NV with the environment or though measuring the magnetic fields produced by the spins' precession. Here we give a brief overview of how these techniques work and the regimes in which they are applicable.

Direct coupling to target spin

One way to measure spins in the local environment is to resonantly couple the NV-target spins. As the NV spin has a zero-field splitting it is possible to Zeeman split the NV energy level into a resonance condition where one of the NV transition frequencies, $\omega_\pm$, are equal to the transition frequency of the target spin, ω_{target}, i.e. $\omega_\pm = \omega_{\text{target}}$. This works for both electron and nuclear spins and will be discussed at length in chapters 2 and 3. When the NV spin and target spin meet the resonance condition there is an increase

[1] For both case of a Gibbs ensemble, i.e., an ensemble of measurements on a single spin or a single measurement on an ensemble of spins.

in the dipole coupling between the spins which leads to flip-flop interactions, shown in Fig. 1.5a. That is the NV spin will flip state (e.g. $|0\rangle \rightarrow |+1\rangle$) and the target spin will flop, which is a flip in the opposite direction (e.g. $|1/2\rangle \rightarrow |-1/2\rangle$). An interaction with a single spin over time would cause an oscillation of the NV spin and the target spin where the period is defined by the coupling strength of the spins. However, if there is an ensemble of target spins, and the target spins are in random states for each measurement, the net interaction will result in an increased relaxation rate of the NV spin. As such the target spin can be detected by monitoring the NV spin longitudinal relaxation rate as the resonance condition is met. This technique is often called cross-relaxation as both NV and target relax faster [33, 109–113]. The NV pulse sequence is shown in Fig. 1.5b.

The filter function (the region in frequency where the technique is sensitive) of this approach is defined by uncertainty in the NV transition frequency, that is, the width of the transition measured in ODMR, i.e. $T_2^\star$, see Fig. 1.5c. The signal to noise ratio (SNR) of this type of coupling can be simplified to [111]

$$\mathrm{SNR}_{T_1} \propto T_2^\star \sqrt{T_1} \tag{1.3}$$

meaning that while this technique does take advantage of the long T_1 time to increase sensitivity it is also limited by the relatively short $T_2^\star$ time.

Coupling to target spins in the rotating frame

Coupling the NV spin to an environmental spin is feasible without directly bringing the NV spin into resonance via Zeeman splitting. Provided the NV or target spin can be placed in a situation where they form dressed states that have identical energy separation to the other spin, an increase in the coupling can occur, resulting in an increase in the relaxation rate. This can be achieved by performing spin locking on the NV spin such that in the rotating frame (i.e. in the frame rotating with the driving microwave) forms eigenstates that have the same energy separation as the target spin. An illustration of this process is shown in Fig. 1.5d. The dressed states are formed by driving the NV spin at a constant frequency, $\Omega^{\mathrm{driving}}$, where the Rabi frequency becomes the splitting ($\omega_{\rho,\pm}$, where ρ denotes rotating frame) of the two dressed eigenstates $|\Omega_\pm\rangle$ in the rotating frame.

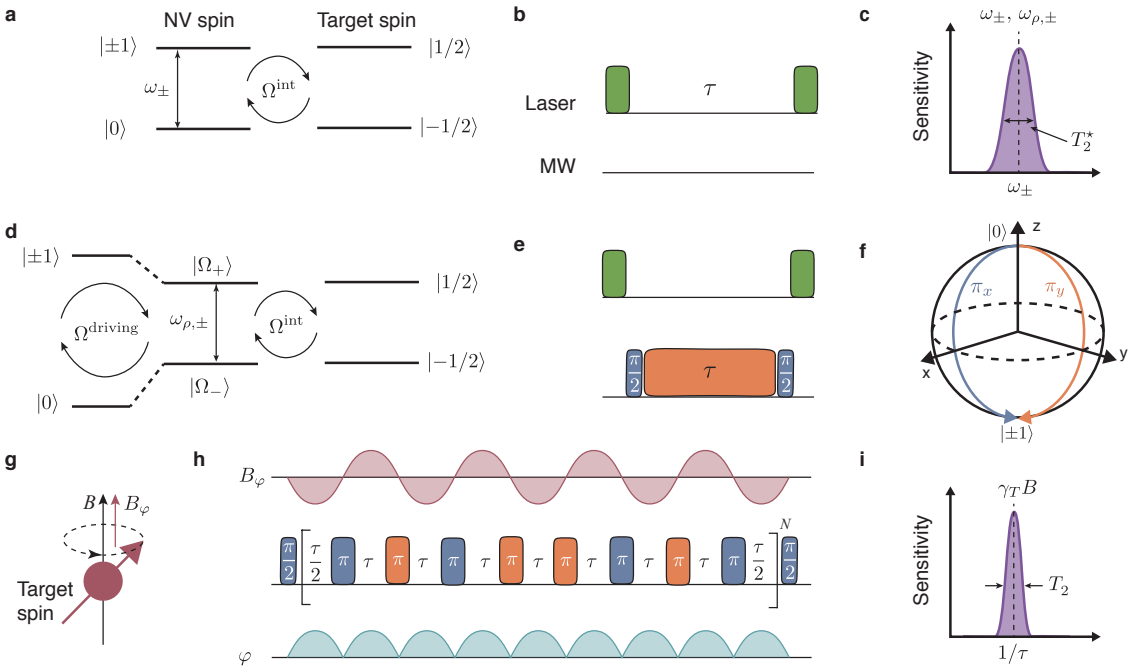

Figure 1.5: Types of remote spin detection with NVs. **a** Illustration of NV spin coupling directly to a target environmental spin via Zeeman splitting the NV into resonance. The effective interaction, Ω^{int} causes the NV spin to relax faster when on resonance (T_1 cross-relaxation) which is the measurement mechanism. **b** Pulse sequence for T_1 based detection of remote spins, including only an initialisation laser pulse and a readout laser pulse. **c** Illustration of the sensitivity of the technique as a function of the detuning from the resonance condition, where the width is given by the NV spin $T_2^\star$. **d** Illustration of Hartmann-Hahn resonant coupling of the NV spin to the target spin, where the NV is brought into resonance by driving the NV spin constantly with Rabi oscillations to produce a dressed states ($|\Omega_+\rangle$, $|\Omega_-\rangle$) that is resonantly coupled to the target. The width of this technique, in the limit of weak driving, is the same as **c**. **e** The pulse sequence for the Hartmann-Hahn sequence that includes a $\pi/2$-pulse around the x-axis, followed by constant driving around the y-axis, and another $\pi/2$-pulse around the x-axis in between the two laser pulses. **f** Bloch sphere where the π-rotations around the x and y axes are defined. **g** Target spin precessing around a background magnetic field, B, that generates a oscillating magnetic field, B_φ. **h** Pulse sequence for XY8 sequence that converts the oscillating magnetic field from target spins into a phase accumulation, φ. **i** The sensitivity of the XY8 sequence as a function of the detuning from the $1/\tau$ resonance, where the width is now given by T_2 which is a function of the number of XY8 iterations, N.

Matching the driving frequency of the NV spin to the transition frequency of the target spin will match the resonance condition [29, 99, 104, 107] (also called the Hartmann-Hahn condition).

The control sequence to perform this Hatmann-Hahn sequence is shown in Fig. 1.5e. This involves including a $\pi/2$-pulse around the x-axis of the Bloch sphere directly after the initialisation laser pulse. After this, continuous driving is applied around the y-axis of the Bloch sphere for time τ, which is followed by another $\pi/2$ pulse around the x-axis, and finally the state is readout with a laser pulse. The axis of the microwave pulses is shown in Fig. 1.5f and is experimentally implemented by a 90° phase shift in the driving field. The filter function of this technique has a width given by dephasing in the rotating frame, which approaches the lab-frame T_2^* in the limit of weak driving. Likewise, T_1 is replaced by its rotating-frame counterpart, $T_{1,\rho} < T_1$. As a result, the T_1 technique has a greater SNR than Hartmann-Hahn in general, however, this technique is easier to implement as the precision alignment of the magnetic field is not as stringent as it is in T_1. As such, both techniques have their advantages and disadvantages. The two approaches will be further compared in chapter 3 in the context of hyperpolarisation.

Matching resonance conditions with a dressed state is not exclusive to just driving the NV spin. It is also possible to rotate the target spin to match the NV spin splitting [103] and to rotate both spins to match their dressed states [104, 114].

Transverse plane measurement techniques

Rather than directly coupling to the target spin, the magnetic field generated from the Larmor precession of the spins can be detected [115, 116]. By applying a magnetic field environmental spins that are not aligned with the magnet field will precess about this axis such that $\omega_{\text{precess}} = \gamma_T B$, which will generate an oscillating magnetic field, B_φ, shown in Fig. 1.5g. In order to measure this oscillating magnetic signal the NV is placed in the transverse plane and a decoupling sequence is used. While a Hahn echo sequence could be used as it is sensitive to AC magnetic fields it is in general not sensitive enough to measure the signal from remote spins, due to the limited coherence of this measurement. In order to increase the coherence and thus the sensitivity of the measurement more effective decoupling sequences need to be implemented. An example of which is the XY8

sequence, shown in Fig. 1.5h. This sequence involves initialisation of the NV spin in the transverse plane, followed by a series of π-pulses equally spaced that rotate the spin around both the x and y axes. The increased number of π-pulses decrease the width of the filter function, i.e. it reduces the range of frequencies that partially match the flipping frequency of the NV spin. As the filter function decreases in width, the overall coherence increase. This is because the coherence is related to the width of the filter function due to the noise that the sequence is correcting for. The inclusion of π rotations around different axes reduces the accumulation of pulses error when compared with single axes techniques like Carr-Purcell-Meiboom-Gill (CPMG) [50, 52, 98, 115, 117]. While CPMG may accumulate more pulse errors it also does not introduce spurious harmonics like XY8 [118].

While both XY8 and CPMG are useful for measuring signals from nuclear spin species they have trouble when measuring electron spin signals due to a significantly faster oscillation. To overcome this restriction sequences like double electron electron resonance (DEER) can be used [119, 120]. This is where π rotations on the target spin are applied along side the NV π rotations. This artificially creates a AC magnetic field signal that matches the NV filter function frequency [115, 116, 120–122].

1.2 Experimental implementations and recent applications

The combination of high sensitivity and small size facilitates the NV spin in measuring objects or fields that are either spatially too localised, or have a small signal strength that cannot be measured with standard techniques. The goal of current efforts in the field is to apply the NV as a sensor to probe interesting samples or processes, from single molecules to entire electronic devices. To physically couple the NV sensor to the target sample and perform the sensing, three major experimental implementations have been developed: single-point, scanning probe, and wide-field imaging. In this section, these different experimental implementations and their recent applications are discussed to give context to the work presented in this thesis, as each technique developed is generally optimised for a specific type of implementation.

1.2.1 Single-point detection

The simplest way to implement NV sensing is to use a static configuration where the sample is fixed relative to a localised single NV sensor. In practice, this can be achieved by placing the sample on the surface of a bulk diamond, or placing nanodiamonds on or within the sample. This single-point detection limits the spatial information that can be ascertained as the measurement is performed in a single location, however, it has the advantage of being relatively simple to implement and is often used to test sensing protocols. This approach will be used in chapters 2 and 3 to develop new techniques for detection and hyperpolarisation of nuclear spins.

These single point detections generally involve illuminating and measuring a single defect in bulk, which is often realised with a confocal microscope. An example experimental set up for NV measurements is shown in Fig. 1.6a. This type of experiment involves a green 532 nm laser that is focused with a diffraction limited spot size, $d = \lambda/2\text{NA}$, where NA is the numerical aperture of the objective, typically $\text{NA} = 1 - 1.6$, which gives $d \approx 160 - 260$ nm. The red photoluminescence (PL) emitted by the NV spin is then captured by this objective and passed through a dichoric mirror to filter the green and red light. The PL is then focused onto an avalanche photodiode that detects the individual photons from the single NV spin (Fig. 1.6b). The laser illumination position can be changed via a piezo stage for the objective or sample, or alternatively by a scanning mirror. Through scanning the system and monitoring the red PL emitted from the diamond, single NV centres are easily located. An example of a confocal scan that detects single NVs centres is shown in Fig. 1.6c. This is also the standard scheme for quantum information applications, where the a single NV spin is located that is coupled to nearby nuclear spins (e.g. ^{13}C) at fixed locations inside the diamond. From here the NV can be used to test quantum protocols, for example quantum error correction codes [2, 3, 13].

While experiments with NVs contained within bulk diamonds are useful it is sometimes more instructive to introduce the diamond into a target material, in which case nanodiamonds are used, see Fig. 1.6f. Nanodiamonds can be introduced into cells and as such are capable of performing measurements inside cells that would have too large of a stand off for bulk diamond measurements. An example of nanodiamonds being taken

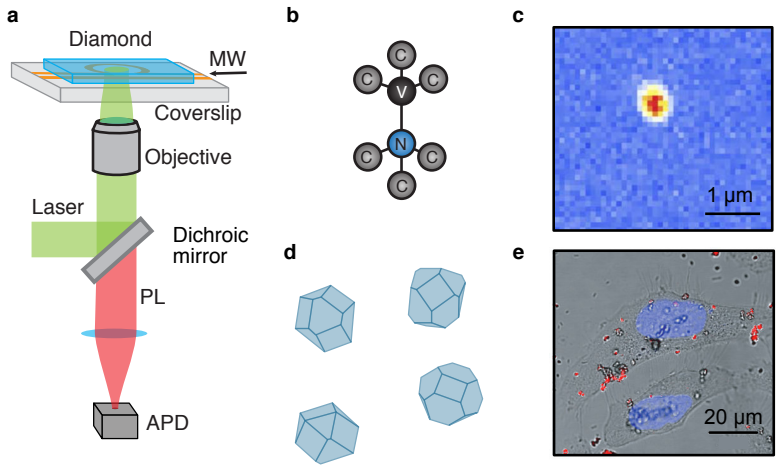

Figure 1.6: Experimental methods of single NV measurements. **a** Diagram of experimental set-up of single NV measurement system, depicting a diamond chip mounted on a glass slide that has a gold pattened resonator for microwave (MW) control. Illumination of the NV ensemble by a green laser and the red NV photoluminescence (PL) is captured with a avalanche photo diode (APD). **b** Illustration of single NV spin in a diamond lattice where a single nitrogen atom is located adjacent to a lattice vacancy. **c** Confocal scan of a single NV that is located through its increased PL over the background. **d** Illustration of nano-diamonds that contain NV spins. **e** Bright-field and confocal fluorescence images of nanodiamond in HeLa cells, where the nucleus is stained (blue) and the NV fluorescence is shown in red, taken from Ref. [68].

into cells for tracking [68] is shown in Fig. 1.6g. Due to the robust and biocompatible nature of nanodiamonds these types of measurements offer a pathway to biophysics application [66, 123]. In chapters 5 and 6 imaging of structures and devices that are constructed on the bulk diamond surface is demonstrated. Recently, similar work has been conducted with nanodiamonds, by producing an even layer of nanodiamond over the entire device [124].

Single-point detection schemes have been particularly useful to demonstrate detection of spins external to the diamond, from the detection of single external electron spins [120] and single protein spins [121, 125] to precision 3D mapping of dark spins with sub nanometre resolution [119]. The NV spin is also being used for more exotic sensing, with measurements of Johnson noise from metals [126] and has been used to detect and interact with pseudo-particles like magons [127] (spin excitation in magnetic materials) and spin waves [24]. Single NV spins in bulk diamond has even been proposed as a way

to detect weakly interacting massive particles (dark matter) that cause lattice damage to the diamond crystal [49].

Application to nuclear magnetic resonance

Nuclear magnetic resonance (NMR) measurements with NVs has seen a significant growth in the last few years from the initial external nuclear spin detections in 2013 [115, 116] to the measurement of chemical shifts in 2017 [61, 63, 64], see timeline in Fig. 1.7a. The first detections of external nuclear spins [115, 116] had very modest sensitivities and spectral resolution, see Fig. 1.7b. However, significant work has been performed since then [111, 128–130] which has lead to the detection of multiple NMR species [131], see Fig. 1.7c. A greater understanding of the techniques and the signals from the nuclear spins has allowed these measurements to be utilised for depth measurements of the NV spins [111, 132] and has found ways to avoid the spurious harmonics [118] that plagued early results. In chapter 2, a microwave-free NMR technique developed by our group [111] will be discussed. While not yet realised, proposals have been made that would allow the NV spin to completely map the nuclear spin positions in a molecule [133–137] which would open the door to structural analysis not yet realised by other techniques.

While the NV spin is extremely sensitive to the fields produced from these spins significant hurdles in improving this sensitivity further were required. These improvements have led to single protein nuclear spin [125] and single nuclear spin [138] detection and has even seen application in measuring the nuclear spins of 2D materials [60]. Recently a new series of measurement protocols were developed that allowed sub kHz measurements of nuclear spins [61–64] enabling chemical shift resolution. The increased frequency resolution (see Fig. 1.7d) has finally bridged the gap between conventional NMR spectrometers that easily measure chemical shifts but require large ensembles of spins and the NV based technology that requires a relatively small number (1 to 10^4) of spins. Measuring chemical shifts on such scale has enormous applications in detection of molecular dynamics for biological, chemical, and medical research.

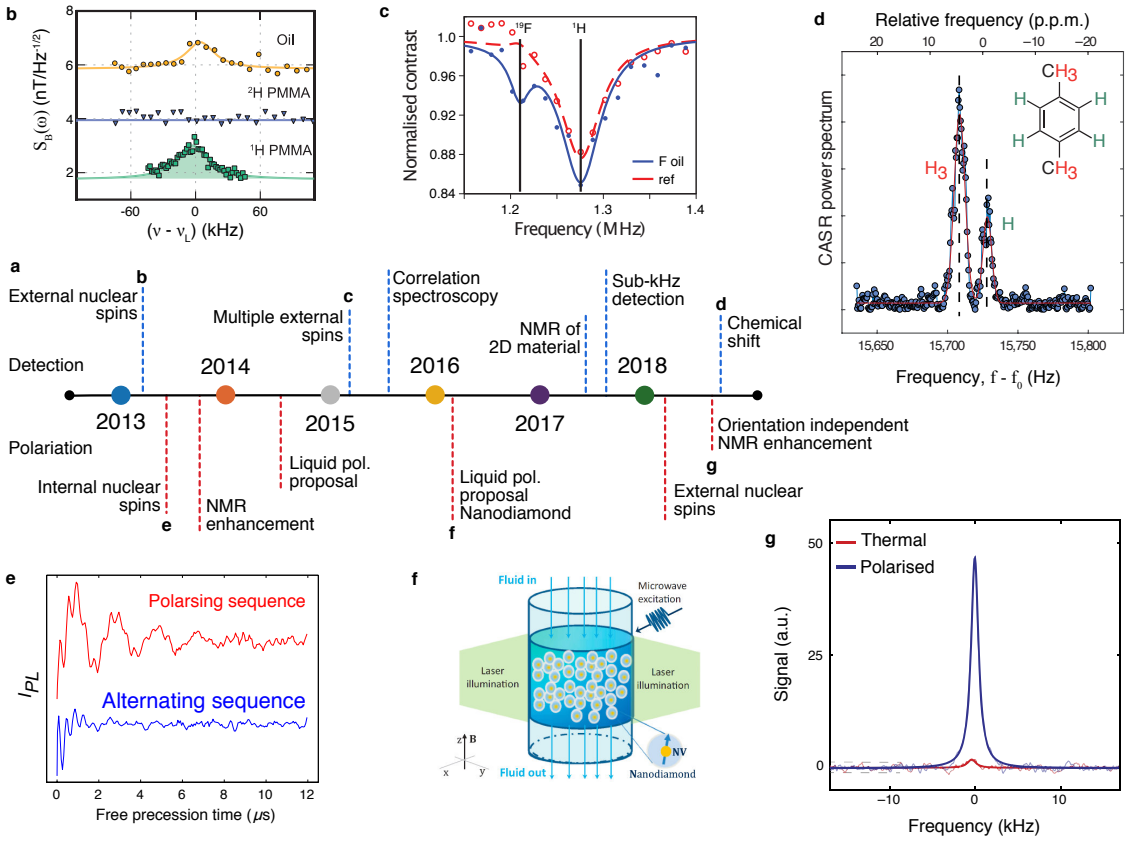

Figure 1.7: Experimental realisation of NMR and hyperpolarisation using NV spins. **a** Timeline of NMR and hyperpolarisation development with NV spins, bold labels indicate the relevant panel from the paper. **b** NMR spectra from XY8-80 detection with the same NV centre under coatings of a liquid sample (immersion oil, yellow), a deuterated solid (^{2}H PMMA, blue), and a protonated solid sample (^{1}H PMMA, green), taken from Ref. [116]. **c** NV NMR spectra using XY8 sequence with ^{19}F oil (blue) and without (red), taken from Ref. [131]. **d** Coherently averaged synchronized readout (CASR) scheme spectrum of xylene. The splitting of 5.3 ± 0.5 p.p.m. (or $\Delta f = 20 \pm 2$ Hz) is the result of chemical shifts associated with the two proton positions (labelled H and H_3), taken from Ref. [61]. **e** Free induction decay ($T_2^\star$) measured on a single NV center while applying the alternating sequence (blue curve, $T_2^\star \sim 0.6$ μs) and while applying the polarization sequence (red curve, $T_2^\star \sim 3$ μs), taken from ref. [29]. **f** Schematic of hyperpolarisation setup containing a hydrogel cell with immobilized nanodiamonds for continuous dynamical nuclear polarisation. [28] **g** Signal gain by DNP under optimized conditions. Blue line shows the ^{13}C NMR signal due to Boltzmann polarization at 7 T, averaged 120 times over 7 hours. Red line is a single-shot DNP signal obtained with 60 s of optical pumping, enhanced 277 times over the 7-T thermal signal (enhanced 149,153 times over polarisation at $B_{\text{pol}} = 13$ mT), taken from Ref. [139].

Application to hyperpolarisation

The principle of using the NV spin to hyperpolarise other spin species relies on the extremely efficient optical polarisation of the NV electron spin (see Fig. 1.1) resulting in an observed population of the $|0\rangle$ state that is typically 80-90% [140]. Several techniques exist to transfer this polarisation to other spins. One common approach is through resonant transfer of polarisation via manipulating the NV spins to meet a Hartmann-Hahn resonance condition, while the NV is constantly receiving more polarisation from the laser. In this fashion, it is possible to generate large polarisation of ensembles of spins in proximity to the NV spin. These techniques were initially demonstrated on internal P1 (nitrogen) electron spins [104] and ^{13}C nuclear spins [29, 30, 34, 38] (see Fig. 1.7a for rough time line of important developments in hyperpolarisation). In chapters 3 and 4, two new techniques to transfer polarisation from NVs to nuclear spins will be presented, one based on direct cross-relaxation in the lab frame (chapter 3), the other on a modified dynamical decoupling protocol (chapter 4). Initialisation of the spin around the NV spin has the benefit of effectively removing the spin bath noise from the NV spin, which results in an increase to the coherence ($T_2^\star$, see Fig. 1.7e) [29, 33, 107] which limits the need to use decoupling sequences, potentially increase the NV spins sensitivity to DC magnetic fields.

Hyperpolarisation of nuclear spins is of particular interest due the reliance of NMR techniques on the polarisation of the nuclear spin targets. As such several proposals for liquid polarisation for these purposes have been put forward [28,32,33,41] (one example is shown in Fig. 1.7f). To enhance the signals in NMR a target nuclear spin needs to be polarised and then measured, either by the NV itself or via another measurement technique. Alternatively, the ^{13}C in nanodiamonds can also be polarised [42] and then used as a localised increased polarisation region for imaging. Recently, NV based hyperpolarisation techniques have been used to polarise spins that are external to the diamond itself [33,36], which if scaled up could facilitate a universal hyperpolarisation mechanism. While these techniques have not been used to demonstrate independent NMR enhancement of external spins, ^{13}C internal polarisation has shown enhancements in both bulk diamond [31,37] and nanodiamond [139], see Fig. 1.7g. Combining the external hyperpolarisation with traditional NMR technique may allow for a significant leap forward in NMR technology,

potentially leading to many important discoveries.

1.2.2 Scanning probe microscopy

It is often advantageous to be able to place the sensor exactly where you want and generate an image of a certain structure by scanning the NV itself. Whether trying to measure a magnetic signal or some more complex noise spectrum, by correlating the position and the coherence or energy levels of the spin images of certain target signals can be acquired [54]. To realise the scanning NV probe two approaches are used, either a nanodiamond is attached to the tip of an atomic force microscope (AFM) [44] (Fig. 1.8a) or a diamond cantilever is micro-machined and a single NV spin is implanted into the tip [141] (Fig. 1.8b). The micro-machined diamond tips have the advantage of better NV qualities and also for precision placement of the NV spins. The grown diamonds also allow for the placing of NV spins away from the tip, which has allowed for interesting measurements involving strong mechanical driving [142] (Fig. 1.8c) and strain response of the NV spins [143].

Precision measurement of the NV energy levels while scanning the NV probe relative to the sample allows for the mapping of magnetic fields across a sample. This has been used to image a single electron spin [122], the current density in nano-wires [101] (Fig. 1.8d), measure static magnetic fields and temperature [144], and imaging of the magnetic field from a hard drive tip [145]. The scanning probe has also been implemented on more exotic materials having measured domain walls [22, 146] (Fig. 1.8e), super-paramagnetic nano-particles [147] and has even measured skyrmions [23], see Fig. 1.8f, and recent work has seen measurements of Johnson noise from different metals to extract their conductivity [148].

While scanning probes offer great advantages in terms of lateral precision and ease of application to sample there are still some drawbacks. As the measurements are performed with a small number of NV spins and the images acquired pixel by pixel, as such the measurement times can be quite long. Furthermore, the stand-off distance between the NV in the scanning probe and the target can be quite large (typically 50 nm at least) compared with the sample being prepared directly on a bulk diamond (down to 2 nm)[2].

[2]This distance will strongly depend on the target, while NV spins have been measured at depths of less than 2 nm fabricating samples onto the sample can introduce stand-off that is similar or larger than the

While scanning systems offer many applications they also introduce additional experimental difficulties. For example, it can be difficult to maintain a constant stand-off distance over long scan times and has issues with lateral drifts. Additionally, there is a real risk of breaking the diamond tip and or the sample. In contrast wide-field imaging is static and thus avoids these issues.

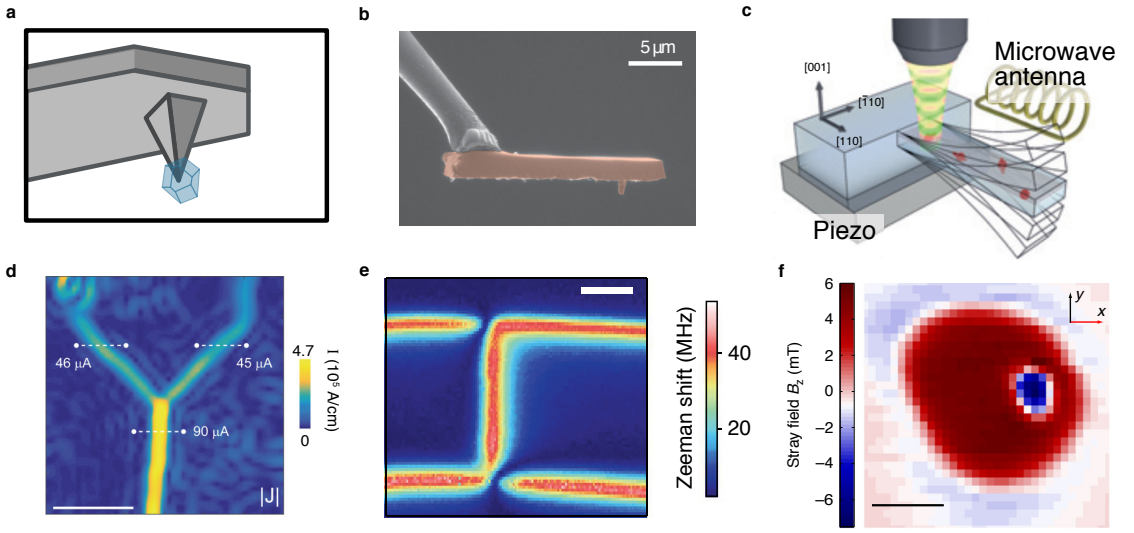

Figure 1.8: Measurements with NV spin with scanning probes. **a** Illustration of atomic force microscope (AFM) tip with a nanodiamond attached to the end which acts as the measurement system. **b** Scanning electron microscope (SEM) image of a single-crystalline diamond nanopillar probe (false colour coded in red) with a single NV centre in its tip, taken from Ref. [141]. **c** Schematic of NV-cantilever coupled system with a resonant driving frequency of ω, which is controller by a piezo-elecment. The NV control is performed using the standard confocal single NV setup, taken from Ref. [142]. **d** Current density image reconstructed from $B_{\parallel}$ from a Pt nanowire, taken from Ref. [101]. **e** Zeeman shift maps above a Bloch-type DW in a Ta/CoFeB/MgO wire, taken from Ref. [146]. **f** Measurement of the stray field in the z-direction generated from a skyrmion, taken from Ref. [23].

1.2.3 Wide-field microscopy

The final method for NV measurements discussed is wide-field imaging. This technique involves simultaneous readout of a large ensemble of NV spins in a bulk diamond. To achieve this, a similar experimental set up is used to the confocal set up, but instead of a tightly focused laser beam, a wide illumination spot is used (typical spot size 200 um on

scanning probe.

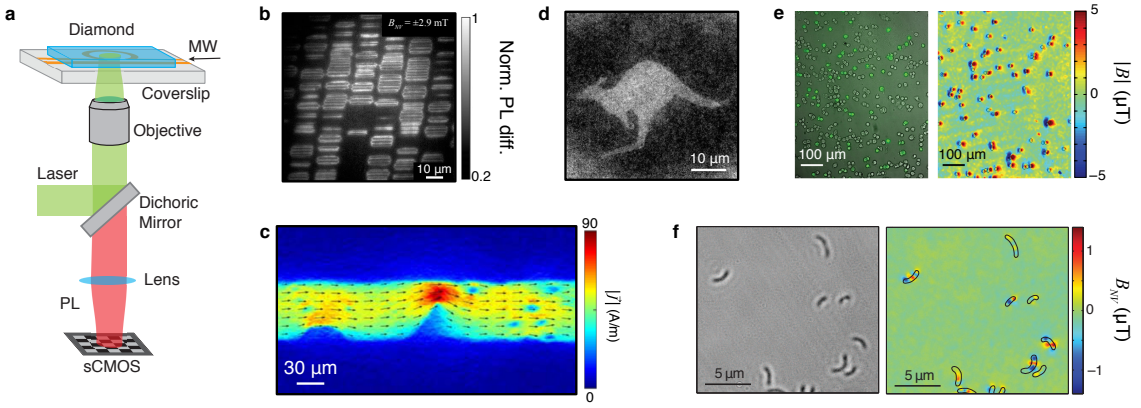

Figure 1.9: Wide-field imaging of condensed matter and biological systems with NV spins. **a** Diagram of experimental set-up of wide-field imaging system, depicting a diamond chip mounted on a glass slide that has a gold pattened resonator for microwave (MW) control. Illumination of the NV ensemble by a green laser and imaging of the red NV photoluminescence (PL) is captured with a sCMOS camera. **b** Single frequency ODMR measurement imaging the magnetic fields produced by bits on a hard drive disk, taken from Ref. [45]. **c** The norm of the current density, $|\mathbf{j}|$, in a graphene ribbon where the black arrows represent vector of the vector $\mathbf{j}$, taken from Ref. [21]. **d** Quantum probe relaxation (T_1) image showing the spatial distribution of Cu^{2+} ions near the $Cu^{2+} \leftrightarrow$ NV resonance at 460 G, where the shape has been made via a PMMA mask, taken from Ref. [149]. **e** Left panel, combined bright-field and fluorescence images of SKBR3 cells that have been stained with a fluorescent dye and labelled with magnetic nanoparticles, where the labelled cells are bright. Right panel, magnetic field image of the same cells producing the expected dipole-like patterns, taken from Ref. [27]. **f** Left panel, Bright-field image of dried Magnetotactic bacteria (MTB) on the diamond chip. Right panel, Image of magnetic field projection along [111] for the same region, with outlines indicating MTB locations, taken from Ref. [26].

the diamond) and the red NV PL is read out by a sCMOS camera, see Fig. 1.9a. Through illuminating and reading out a large ensemble of spins with the camera an image of the PL can be obtained and the desired quantity can be extracted. In order to integrate samples they need to be placed or fabricated directly onto the diamond. For example, magnetic fields from meteorites [150] and hard drive disks [45] (Fig. 1.9b) have been measured by placing the sample onto the diamond substrate. Direct fabrication offers other opportunities for sensing, for example magnetic fields from evaporated wires have been measured [100, 151] and recently the current distribution in a graphene (2D carbon) ribbon was imaged [21], shown in Fig. 1.9c. Similar precision measurements of the NV energy levels have also led to maps of strain fields from polycrystalline diamond [48].

In chapters 5 and 6 of this thesis, a wide-field imaging approach will be employed to demonstrate imaging of the electric field simultaneously with the vector magnetic field (chapter 5), and of the entire stress tensor (chapter 6).

Wide-field NV imaging has been extended to allow detection of external spins. Through mapping the longitudinal relaxation (T_1) of the NV spins against NV energy level different spin species can be identified. This was initially performed on Gd^{3+} electron spins [69] that have a very broadband noise and thus affect the NV spin's T_1 regards of the applied magnetic field. Electron spins with narrow line widths can also be measured [149] and at concentrations that traditional electron spin resonance (ESR) techniques are incapable of measuring, see Fig. 1.9d where Cu^{2+} are measured in a kangaroo-shaped Poly(methyl methacrylate) (PMMA) mould [149]. Wide-field imaging of external spins has also been extended to nuclear spins with multiple spin species [131] and even super-resolution [152] (sub diffraction limited resolution). In chapter 4, a technique to detect and hyperpolarise nuclear spin will be presented and demonstrated on a wide-field imager.

Another application of wide-field imaging is in biology. As diamond is biocompatible it is possible to grow and maintain live cells on the diamond slab. As such diamond had been used to measure magnetic markers in cells [27] (Fig. 1.9e) and has also been used to image live magnetotactic bacteria [26] (Fig. 1.9f). Diamonds have also been used in conjunction to a wide-field set up to map temperature in neurons [123]. While the diamond itself is suitable for biological systems one issue that persists is photo toxicity killing live cells. To avoid this problem the laser incident onto the diamond must be reorientated to minimise the light that escapes through, taking advantage of total internal reflection. This offers the diamond slab a distinct advantage over the nanodiamond approach.

1.3 Thesis layout

Having presented the background physics and state of the art of NV experiments, we can now move to the main results of this thesis, which are divided in two parts. In this first part of this thesis, techniques for hyperpolarisation of nuclear spins are developed. Initially, in chapter 2 a new protocol for detecting remote spins is developed and implemented on nuclear spins that are external to the diamond. This protocol uses cross-relaxation of

the NV spin with the target spin, which when applied multiple times hyperpolarises the target nuclear spins. In chapter 3 the technique is demonstrated to produce a high degree of polarisation on both internal ^{13}C and external ^{1}H nuclear spins. Additionally, it is shown to have a faster polarisation rate than other techniques. However, cross-relaxation is sensitive to magnetic field variations, which can act to restrict the polarisation rate by detuning from resonance. In order to circumvent this issue, in chapter 4 a new protocol is developed that performs adjustments on the pulses of a standard dynamical decoupling sequence, Carr-Purcell-Meiboom-Gill (CPMG). Although this new technique has a slower polarisation rate is has a remarkable resilience to experimental error, making it ideal for scaling of an NV hyperpolarising platform. In the second part of this thesis, ensembles of NV spins are used to demonstrate a multi-modal imaging technique that is capable of detecting magnet, electric and stress fields. Initially, chapter 5 develops a technique for simultaneously imaging both magnetic and electric fields, and is used to study the effects of termination and treatment on surface band bending. Finally, chapter 6 extends this technique to measure stress that is embedded in the diamond. Which is then used to image stress from various source: indentation, scratches, implantation, evaporation of metals, hybrid diamond contacts, and damage from transistor fabrication and operation.

Part I

Detection and hyperpolarisation of nuclear spins with diamond spin defects

Preface to Part 1

The position of nuclei within a molecule, i.e. its tertiary structure, dictates how it interacts with other systems. Most of these nuclei are relatively inert and their position cannot be determined without destroying the molecule, however, some nuclei have a spin whose magnetic field can be measured. Thus, precision measurements of these spins can be a useful tool for identifying the structure and interaction of these systems. Additionally, controlling the nuclear spins directly can be used to store information or enhance standard sensing protocols. As a consequence, it is vitally important to develop techniques that are capable of detecting a very small number of nuclear spins (down to the single spin limit that is required for some molecular detection schemes) and are capable of initialising the nuclear spins in a given state (ideally initialising the entire ensemble of spin into the same state). The first part of this thesis is dedicated to developing techniques towards these goals, i.e. for detecting and hyperpolarising nuclear spins.

In Chapter 2, the framework for understanding cross-relaxation (CR) based spectroscopy [113] is developed for nuclear spins. Single NV spins are used to first demonstrate the applicability of the NV spin in sensing electron spins, given in section 2.1, which is the work presented in the paper Ref [110]. In order to extend this work towards application to nuclear spins a detailed understanding of the NV ground state level anti-crossing (GSLAC) is developed in section 2.2. The spin dynamics around this anti-crossing are explored and found to be commensurate with nuclear spin detection using CR in this region. This knowledge is then implemented in section 2.3, where nuclear magnetic resonance of external hydrogen spins is performed using a single NV spin.

In Chapter 3, the NV centre's influence on the spin bath is investigated. It is demonstrated that through taking repetitive measurements using cross relaxation (CR)

spectroscopy the NV spin imparts its polarisation onto the nuclear spin bath. An in-depth investigation of this technique to hyperpolarise nuclear spin baths is performed on the internal ^{13}C nuclear spin bath. The technique is then extended to polarise external ^{1}H nuclear spins, demonstrating the first external nuclear spin polarisation achieved using an NV centre. In section 3.2, the hyperpolarisation work is extended by looking at a technique to further stabilise the experimental equipment in order to facilitate better polarisation and measurement. In this work it is shown that after polarising a nuclear spin bath it is important to initialise the NV spin into a state that will not destroy the polarisation that it just imparted onto the environment. In section 3.3 a comparison of different hyperpolarisation techniques is conducted, which indicates that lab frame cross-relaxation based hyperpolarisation is faster at polarising than other techniques.

Finally, in chapter 4 a new hyperpolarisation protocol is developed that relies on the deliberate introduction of controlled errors to a standard dynamical decoupling sequence [153]. While this technique is slower than the CR-hyperpolarisation developed in chapter 3, it is more robust to errors and consequently has some advantage when scaled up.

2

From electron to nuclear spin detection using cross-relaxation

Quantum relaxation and decoherence are fundamental aspects of any open quantum system. In many applications using qubits, the aim is to minimise these quantities as much as possible, involving complicated control sequences or rigorous fabrication processes to remove possible spin or charge contamination. However, in sensing applications, decoherence can be utilised rather than feared. Through understanding the mechanisms behind decoherence it is possible to extract information about the qubit environment. Consequentially, qubits characterised in this way can be used as quantum sensors, offering a range of advantages over classical sensors such as increased sensitivity and extremely small sensing volumes. This motivated a vast range of work in understanding and utilising quantum sensors, with the NV spin qubit as a prime example.

In this chapter, a new sensing technique is developed using the NV spin: cross-relaxation (CR) spectroscopy [113]. The technique, extending cross-relaxation based detection [54, 66, 69, 126, 154–156], involves measuring the longitudinal relaxation of the NV spin while varying the sensing frequency. In this fashion the NV spin will sense any noise source that is commensurate with the NV frequency, which in practice can be tuned via application of a static magnetic field. Here it is shown that this technique is broad-band and capable of measuring signals from 10 kHz to 10 GHz. CR-spectroscopy is first developed through applying the sensing protocol to spectroscopy of electron spins in the

diamond, which are in the GHz regime. In order to extend this protocol to sensing nuclear spins in the low frequency regime (< 5 MHz) a detailed understanding of the NV ground state level anti-crossing (GSLAC) is developed with an emphasis on the spin dynamics in this region. Finally, with this understanding CR-spectroscopy is used to detect externally located hydrogen spins that are contained in both solid and liquid samples on the diamond surface.

2.1 Cross relaxation (CR) based spin sensing

Correlating quantum decoherence/relaxation to extract spectral information about fluctuating fields from arbitrary noise sources was initially proposed in a qubit-probe context by Cole & Hollenberg [54]. Fundamentally, this involves monitoring the relaxation time of a qubit in order to determine if there has been a change in the qubit's environment, and can be extended (through knowledge of the qubit-environment interaction) to identify the source of intrinsic relaxation itself. While such techniques have seen a broad range of applications in the transverse plane (i.e. monitoring of the NV T_2 [29, 115, 116, 131–133, 157, 158]), applications employing longitudinal relaxation have been more sparse (i.e. monitoring T_1 [66, 69, 113, 126, 154–156]).

The NV longitudinal relaxation time (T_1) is sensitive to noise sources that are either local or have localised effects in the NV region. When the noise source has a distinct spectral signature that coincides with the NV spin energy level there is an induced decay of the NV spin, which causes a reduction in the NV spin's relaxation time. Due to the NV centre having a relatively small line width ($\Delta\omega \approx 1$ MHz), it is possible to take advantage of this resonant decoherence to identify the frequency of different noise sources. One noise source of interest is the signal generated by other spin species in the local environment. Owing to the NV spin's zero-field splitting ($D \approx 2.87$ GHz), which splits the NV energy levels away from other spin systems, the NV spin can be used to detect other spins, as an NV-target spin resonance condition exists for all common spin species. That is, a resonance condition exist between the NV-target spin system independent on whether the target spin is coupled to other spins or not. Thus, through controlling the applied magnetic field and monitoring the NV spin relaxation time, a spectrum of the environmental noise can be obtained which can be tuned to detect arbitrary frequencies.

As the NV spin is located internal to a diamond there exists several intrinsic sources of noise that can be used as test signals for the technique. The dominant spin signal comes from substitutional nitrogen (P1) centres [6, 71, 159, 160] that are generated during NV centre creation. These atomic defects are useful test spins because they provide sources of both electron and nuclear spin signals that exhibits a strong hyperfine coupling between the two. As such, this defect is utilised to perform CR-spectroscopy and develop the

protocol.

2.1.1 Principle of CR-spectroscopy

Performing CR-spectroscopy involves the standard optical control of the NV and an applied static magnetic fields that is carefully tuned in strength to bring the NV system into resonance with the target spin in question [113]. As an example, we show in Fig. 2.1a a single NV spin is optically addressed with a 532 nm laser, which is used to image, initialise, and readout the NV spin state through a custom built confocal microscope. The excitation source is a solid-state laser emitting at a wavelength $\lambda = 532\,\text{nm}$ (Laser Quantum Gem 532). The objective lens (Olympus UPlanSApo 100×, NA = 1.4 Oil) is mounted on an XYZ scanning stage (PI P-611.3 NanoCube) to allow fast laser scanning. The PL emitted by the diamond sample is separated from the laser light using a dichroic beam splitter and a band-pass filter, and coupled into a multimode fibre connected to a single photon counting module (Excelitas SPCM-AQRH-14-FC). For T_1 measurements, the laser beam is modulated by an acousto-optic modulator (AA Opto-Electronic MQ180-A0,25-VIS) in a double pass configuration, and the PL signal is analysed by a time digitizer (FastComTec P7889). For optically detected magnetic resonance (ODMR) measurements, a 20-μm copper wire is spanned on the surface of the diamond and connected to the output of a microwave generator (Agilent N5181A) modulated by a switch (Mini-Circuits ZASWA-2-50DR+). Laser and microwave modulations are controlled by a programmable pulse generator (SpinCore PulseBlasterESR-PRO 500 MHz). The magnetic field direction and strength were varied by using a permanent magnet affixed to a set of three linear translation stages (PI M-511) allowing XYZ position control. These stages had a resolution of 100 nm which is sufficient to tune the NV into resonance and align the field along the NV axis, thus avoiding any misalignment issues [161].

In isolation, the NV centre's ground state can be modelled with a simplified effective spin Hamiltonian of

$$\frac{\mathcal{H}_{\text{NV}}}{h} = D_{\text{NV}} S_z^2 - \gamma_{\text{NV}} B S_z \tag{2.1}$$

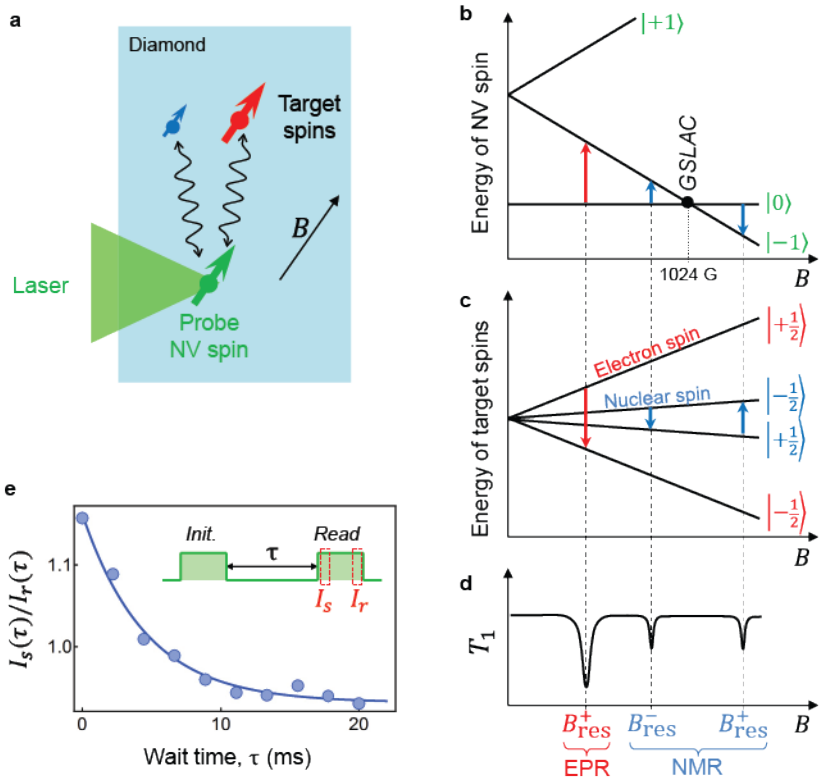

Figure 2.1: Broadband spectroscopy via CR-relaxometry. **a** Schematic of single NV centre (green) interacting with nearby electron (red) and nuclear (blue) spin inside of the diamond lattice. **b** Energy levels of the NV centre as a function of an applied axial magnetic field B. **c** Energy levels of a spin-1/2 electron and nuclear spin under the same magnetic field. **d** Schematic of the NV centre's relaxation time (T_1) across coming into resonance with the electron and nuclear spins. **e** T_1 measurement performed off resonance with any spin species using the pulse sequence shown in the insert.

where h is Planck's constant, $\gamma_{\mathrm{NV}} = -28.035(3)$ GHz/T is the gyromagnetic ratio of the NV electron spin [88], $D_{\mathrm{NV}} \approx 2.87$ GHz is the crystal field splitting, B is the magnetic field projection along the z-axis defined by S_z, the spin-1 operator along the NV centre's symmetry axis.

The NV spin transition of $|0\rangle \rightarrow |-1\rangle$ frequency is approximately given by $\omega_{\mathrm{NV}}(B) = D_{\mathrm{NV}} + \gamma_{\mathrm{NV}} B$ and the target spin frequency can generally be expressed as $\omega_{\mathrm{t}}(B) = \gamma_{\mathrm{t}} B$ where γ_{t} is the gyromagnetic ratio of this particular spin. The resonance condition at $B = B_{\mathrm{res}}$ is thus given by when these two frequencies match,

$$|\omega_{\mathrm{NV}}(B_{\mathrm{res}})| = |\omega_{\mathrm{t}}(B_{\mathrm{res}})| \,. \tag{2.2}$$

When the NV spin transition satisfies this condition at B_{res} the NV and target spins will exchange energy through the dipole-dipole interaction, leading to an increase in the measured spin relaxation rate of both spins. Therefore, through monitoring the NV spin's relaxation rate whilst varying the applied magnetic field strength, a spectrum of the local spins can be obtained (Fig. 2.1d), where features corresponding to spin-spin resonances [113] will become apparent. The resonance condition for electron spins is generally centred about the applied magnetic field of $B = 512$ G, while those for nuclear spins are around $B \approx 1024$ G. In order to apply the technique to nuclear spins an understanding of the level anti-crossing that exists in the 1024 G region will be developed in section 2.2. First, CR-spectroscopy will be demonstrated on electron spins to illustrate the experimental procedure and expected coupling strengths. In this case the technique is denoted CR-EPR in analogy with standard EPR (electron paramagnetic resonance).

2.1.2 CR-EPR spectroscopy of P1 centres

The NV spin's longitudinal relaxation time (T_1) is measured through applying a series of 3-μs laser pulses (see inset in Fig. 2.1e). These laser pulses act to initialise the NV spin into the $|0\rangle$ state while simultaneously measuring the spin state of the NV [82] (see section 1.1 for more detail). Through time resolving the PL intensity throughout the laser pulse and normalising the beginning (first 300 ns, $I_s(\tau)$) to the end (last 300 ns, $I_r(\tau)$), the NV spin state can be determined. The ratio thus $I_s(\tau)/I_r(\tau)$ measures the decay out of $|0\rangle$ after a time τ, where the background decay (no magnetic resonance) is typically $T_1 \sim 5$ ms at room temperature, governed by two-phonon Orbach processes [109]. The magnetic field was finely aligned by exploiting the NV spins PL intensity dependence to transverse magnetic fields [78,162], where the net projected field strength was determined through ODMR at each measurement position.

In order to capture the full electron transitions of the P1 centre (including hyperfine structure) the magnetic field strength was varied over a range of $B \approx 480 - 540$ G, which corresponds to $\omega_{\text{NV}} \approx 1350 - 1530$ MHz. The measurements were performed with single NV spins in a type-1b diamond, which has an ^{14}N concentration of < 200 ppm. A probe time (or interaction time) of $\tau = 40$ μs was used to monitor changes in the relaxation

rate as this single point is enough to detect the spectral signature. In general, the time is determined via the expected coupling strength, i.e. for nuclear spins at the same distance a longer time would be used or in the absence of knowledge about the coupling strength $\tau = 1/2T_1$ is used. The normalised signal from the single time value shows a series of transitions (Fig. 2.2a) where the 5 large amplitude resonances are well known single quantum electron transitions [163–165]. Additionally, the CR-spectrum measures four smaller amplitude resonances (zoom shown in Fig. 2.2b), which are attributed to double quantum transitions (Fig. 2.2c). The spectrum is understood as follows [113,166], first, the hyperfine interaction of the P1 electron and nuclear spin introduces three transition due to the nuclear spin-1. Second, there exist two families of P1 centres, either the electron's orbital is aligned along the crystallographic orientation that the magnetic field is tuned to, i.e. the NV spin axis (on-axis) or it is aligned in one of the three other directions (off-axis and degenerate). This results in 5 observed single and four double quantum resonances.

To elucidate the NV-target interaction effect on the relaxation rate, full T_1 curves were measured both on and off resonance (Fig. 2.2d). The longitudinal relaxation of the NV spin in the absence of magnetic interactions (i.e. off-resonance) is dominated by phonon interactions [109], which results in a single exponential decay of the state, here with a decay rate of $\Gamma_{1,\mathrm{ph}} = 220(20)\ \mathrm{s}^{-1}$. When on-resonance a bi-exponential behaviour is observed, which is generated by the magnetic noise driving only a single transition of the NV spin, introducing an additional decay path and rate $\Gamma_{1,\mathrm{res}}$. Assuming a simple three-level rate equation model in which the interaction creates an additional near-resonance relaxation channel, the relaxation curve takes the form

$$I_s(\tau) = I_\infty \left[1 + \frac{\mathcal{C}}{4}\left(e^{-\Gamma_{1,\mathrm{ph}}\tau} + 3e^{-(\Gamma_{1,\mathrm{ph}}+\Gamma_{1,\mathrm{res}})\tau}\right)\right] \tag{2.3}$$

where I_∞ and $\mathcal{C}$ are constants. Using this equation facilitates the extraction of both the phonon background and interaction induced relaxation rate, which gives the coupling strength of the NV-target system. The spin relaxation rate induced by a single target electron spin (on resonance) at a distance r and forming an angle θ is given by

$$\Gamma_{1,\mathrm{res}} = \frac{1}{\Gamma_2}\left(\frac{\mu_0\gamma_{\mathrm{NV}}\gamma_e h}{2\sqrt{2}}\right)^2\left(\frac{3\sin^2\theta}{r^3}\right)^2 \tag{2.4}$$

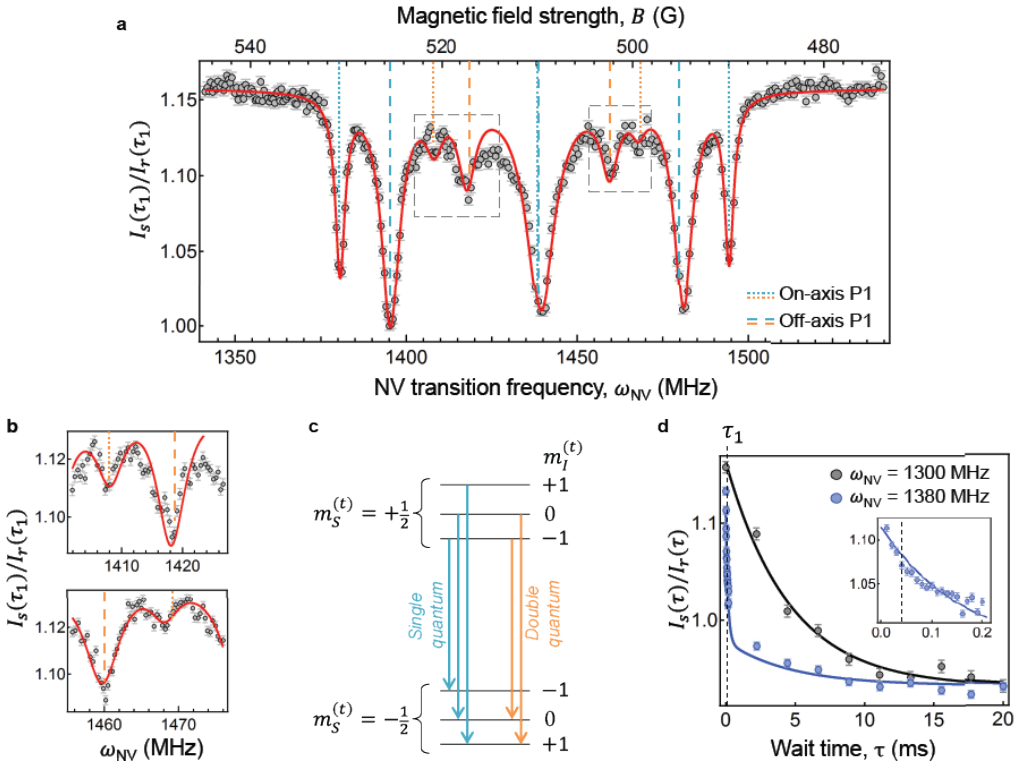

Figure 2.2: CR-EPR of P1 centres in diamond. **a** Single time point CR-spectroscopy performed across the electron resonance with a time $\tau = 40\mu$s. The NV frequency was obtained from ODMR measurements at each magnetic field position. **b** Higher-resolution scan of the region indicated by two dashed boxes in **a** that corresponds with double quantum transitions of the P1 centre. **c** Schematic of the P1 centre energy transition where m_s (m_I) denotes the electron (nuclear) spin projection. The single and double quantum transitions are colour coded to match the spectra in **a** and **b**. **d** Full T_1 measurement of the NV centre both on (blue) and off (black) resonance with the P1 centre. Zoom in for short time in shown as an insert and the τ used for the single point measurements is shown as a dashed line.

where Γ_2 is the total dephasing rate of the NV-target spin system.

In the context on nuclear spin targets, the gyromagnetic ratio of the target spin is orders of magnitude smaller than that of an electron spin, resulting in the spin-spin interaction being similarly weaker. Furthermore, due to the much smaller Larmor frequency of nuclear spins (i.e. ^{1}H or ^{13}C, < 5 MHz) the measurements need to be taken near the ground state level anti-crossing (GSLAC) of the NV. As a consequence, the NV spin states are mixed in this region which may result in limits on the measurements in this regime. In the next section, we look in great detail at the GSLAC, what the spin mixing does to

the detectable transitions frequencies, and under what regime CR-spectroscopy of nuclear spins can be performed.

2.2 Understanding the NV ground state level anti-crossing

As previously described, performing cross-relaxation (CR) spectroscopy involves monitoring the longitudinal relaxation time of the NV spin while varying the probing frequency through modulating the applied magnetic field. Matching the NV transitional energy between the $|0\rangle \rightarrow |\pm 1\rangle$ states to the target spin species energy levels induces a dipole mediated interaction that mutually reduces the lifetime of both spins. Implementing this protocol relies on initialisation of the NV spin into the $|0\rangle$ ground state and quantifying the transition frequency that is being probed. Bringing the NV and target spins into resonance for NV-nuclear spins requires tuning the NV system to the MHz range, which necessitates operation near the ground state level anti-crossing [87] (GSLAC) of the NV spin. The crossing is due to the Zeeman effect, which with the appropriate applied magnetic field splits one of the $|\pm 1\rangle$ states close to being degenerate with the $|0\rangle$ state. In this regime, the hyperfine interaction between NV electron spin and nitrogen nuclear spin, which can be either a spin-1/2 (^{15}N) or spin-1 (^{14}N), introduces a mixing term in the Hamiltonian which results in an anti-crossing feature. As a consequence, it is not apparent that state initialisation is preserved nor a clear probe frequency obtainable. Therefore, in order to perform CR-spectroscopy on nuclear spins a detailed study of the GSLAC in both of these critical aspects is required. Furthermore, the spin dynamics ensuing from the initialised NV state must be understood in order to identify false signals caused by spin mixing. Whilst the NV spin GSLAC structure has been previously studied [12, 30, 39, 87, 162, 167–169], the spin dynamics in this region has yet to be explored.

In this section, GSLAC is investigated in the absence of external nuclear spin signals (i.e. other than within the NV itself). The energy spectrum is obtained through optically detected magnetic resonance (ODMR) and compared with theory, revealing a nuclear polarisation effect caused by state mixing at the GSLAC, introducing a pathway for optical pumping of the NV spin to polarise both the NV electron and nuclear spin, facilitating an extremely good initialisation of the NV probe. The spin dynamics at the GSLAC for both ^{14}N-V and ^{15}N-V are explored; determining that there exist significant spin mixing that is debilitating to CR-spectroscopy at certain magnetic fields strengths. However, these regions can be avoided at the cost of some operational range. In the case of low

noise systems (low nitrogen implantation), CR-spectroscopy can be performed for a full range of nuclear spin signals (from 8 MHz down to 500 kHz), whilst samples with a larger background noise restricts the lower limit.

2.2.1 The ground state level anti-crossing (GSLAC) - theory

A level anti-crossing (LAC) occurs when two or more eigenstates of a system experience state mixing due to higher order interactions when they are about to cross over each other. This results in the states deviating rather than directly crossing. In the case of the NV centre, the ground state level anti-crossing (GSLAC) occurs when an axial magnetic field with a strength of $B_z \approx 1024$ G is applied. This magnetic field Zeeman splits the $|-1\rangle$ state such that it becomes close to being degenerate with the $|0\rangle$ state, shown in Fig. 2.3a. When the $|-1\rangle$ and $|0\rangle$ states energy separation becomes similar to the hyperfine coupling between the NV electron and nitrogen nuclear spin, the GSLAC becomes apparent. The two stable isotopic forms of nitrogen give rise to distinct GSLAC structure [87], as shown in Fig. 2.3b for ^{14}N-V which has a nuclear spin of 1 and shown in Fig. 2.3c for ^{15}N-V which has a nuclear spin of 1/2. The strength of the hyperfine coupling of both NV types is several MHz, which is similar to the transition frequency required to directly couple the NV to free nuclear spins. As such, in order to define and employ CR-spectroscopy for NMR the GSLAC structure and dynamics must be precisely understood.

The relevant Hamiltonians of the two different isotopic NV spin systems are

$$\mathcal{H}\left(^{14}\text{N-V}\right) = DS_z^2 + \gamma_e \mathbf{B}\cdot\mathbf{S} - \gamma_n \mathbf{B}\cdot\mathbf{I} + QI_z^2 + A_\parallel S_z I_z + A_\perp \left(S_x I_x + S_y I_y\right) \tag{2.5}$$

and

$$\mathcal{H}\left(^{15}\text{N-V}\right) = DS_z^2 + \gamma_e \mathbf{B}\cdot\mathbf{S} - \gamma_n' \mathbf{B}\cdot\mathbf{I}' + A_\parallel' S_z I_z' + A_\perp' \left(S_x I_x' + S_y I_y'\right) \tag{2.6}$$

where $D = 2.87$ GHz is the zero field splitting, γ_e (γ_n, and γ_n') is the gyromagnetic ratio of the NV electron (^{14}N and ^{15}N nuclear spin respectively), $\mathbf{B}$ is the applied magnetic field, $\mathbf{S} = (S_x, S_y, S_z)$ is the electron spin operator with $\mathbf{I}$ ($\mathbf{I}'$) being the nuclear spin operator for ^{14}N (^{15}N). The longitudinal and transverse hyperfine couplings are given by $A_\parallel = -2.14$ MHz and $A_\perp = -2.7$ MHz for the ^{14}N-V and $A_\parallel' = 3.03$ MHz and

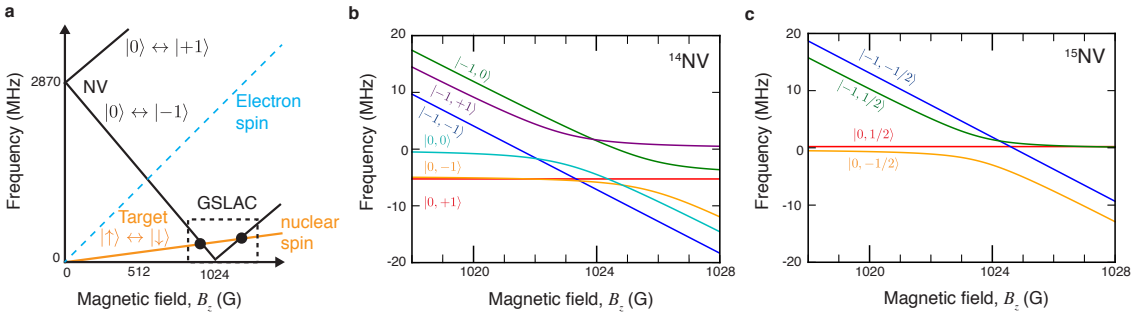

Figure 2.3: Energy levels of the NV near the GSLAC. a Transition energy levels of the NV electron spin (black), a target spin 1/2 electron (blue, dashed), and a target nuclear spin (orange) versus the applied background magnetic field (B_z). **b**,**c** Calculated hyperfine structure for both the ^{14}N-V and ^{15}N-V spins species around the GSLAC, using Eq. 2.5 and Eq. 2.6 respectively. The different states are labelled as $|m_e, m_n\rangle$, where m_e and m_n are the electronic and nuclear spin projection before the GSLAC.

$A'_\perp = 3.65$ MHz for the ^{15}N-V. Finally $Q = -5.01$ MHz is the quadrupole moment of the ^{14}N-V [170].

The energy spectrum is obtained by evaluating the eigenvalues of the Hamiltonian at different axial field strengths B_z and is shown in Fig. 2.3b for ^{14}N-V and Fig. 2.3c for ^{15}N-V. The manifold associated with the spin projection $|+1_e\rangle$ (where e denotes electron spin and n denotes nuclear spin) is not shown as it lies about 6 GHz above the manifold spanned by $|0_e\rangle$ and $|-1_e\rangle$ and does not contribute to the spin mixing effects. We thus consider only the 6 lower-energy states for ^{14}N-V, and the 4 lower states for ^{15}N-V. Away from the GSLAC, the eigenstates have well-defined spin projections along the z-axis. In the electron-nuclear spin space, we denote states as $|m_e, m_n\rangle$ where m_e (m_n) is the electronic (nuclear) spin projection along the z-axis. The hyperfine coupling between the NV nuclear and electron spins results in a splitting of the nuclear spin states for each electronic spin state, due to the longitudinal component $A_\parallel$. Near the GSLAC, the perpendicular component of the hyperfine ($A_\perp$) induces a mixing of some of the z-basis states. This effect is noticeable when the quantization energy between said states becomes of order $A_\perp$. In the case of the ^{14}N-V, the states $|0, +1\rangle$ and $|-1, -1\rangle$ do not mix as they have no hyperfine coupling to any other state, and as such, they remain eigenstates. The rest of the NV states are mixed, that is, the eigenstates are superpositions of z-basis states, creating an avoided crossing. The ^{15}N-V spin also exhibits mixing at the GSLAC. In particular the $|0, -1/2\rangle$

and $|-1,+1/2\rangle$ states become mixed while the $|0,+1/2\rangle$ and $|-1,-1/2\rangle$ states remain eigenstates.

2.2.2 ODMR at the GSLAC

Experimentally, one can probe the NV energy spectrum using optically detected magnetic resonance (ODMR) spectroscopy [43] (see section 1.1.2 for more detail). This is achieved by measuring the photoluminescence (PL) intensity of the NV centre while varying the frequency of an applied RF field, using a purpose-built confocal microscope with green laser excitation. The laser serves both to initialize the NV in the electronic spin state $|0_e\rangle$, and read out the spin state following an RF pulse, exploiting the fact that $|\pm 1_e\rangle$ emit less PL on average than $|0_e\rangle$ [82]. Thus, ODMR allows us to probe the electron spin transitions $|0_e\rangle \rightarrow |\pm 1_e\rangle$. ODMR spectra for magnetic fields varied from 1018 G to 1032 G were recorded, for single ^{14}N-V and ^{15}N-V centres in a high-purity diamond grown by chemical vapour deposition (CVD). The results are shown in Fig. 2.4, where the top (bottom) panels show the $|0_e\rangle \rightarrow |+1_e\rangle$ ($|0_e\rangle \rightarrow |-1_e\rangle$) transitions. The left (right) panels correspond to the ^{14}N-V (^{15}N-V) centre. Comparing with the theoretical expectations for the allowed transitions (shown as black lines), not all expected transitions are observed experimentally. This indicate that the nuclear spin is effectively polarised under optical pumping near the GSLAC, owing to hyperfine-induced spin mixing. This effect has been well documented at the excited state level anti-crossing (ESLAC, [171, 172]), however it has not been previously quantified experimentally across the GSLAC [12]. Using the relative strengths of the $|0_e\rangle \rightarrow |+1_e\rangle$ transitions (Fig. 2.4a,b), we find that the nuclear spin is polarised to $> 90\%$ into $|+1_n\rangle$ for ^{14}N-V across the whole range of fields scanned here. For the ^{15}N-V investigated in Fig. 2.4, the nuclear spin is polarised to $> 90\%$ in $|+1/2_n\rangle$ up to $B_z \approx 1026$ G, however it becomes unpolarised above $B_z \approx 1028$ G.

In the ODMR spectrum for ^{14}N-V (Fig. 2.4c,d), the NV is effectively polarised in the state $|0,+1\rangle$, which remains an eigenstate at all fields. Away from the GSLAC, the only transition allowed is to the state with the same nuclear spin projection, $|-1,+1\rangle$. However, near the GSLAC the state $|-1,+1\rangle$ becomes mixed with $|0,0\rangle$, which creates two eigenstates of the form $|\alpha\rangle = a\,|-1,+1\rangle + b\,|0,0\rangle$. This results in an avoided crossing

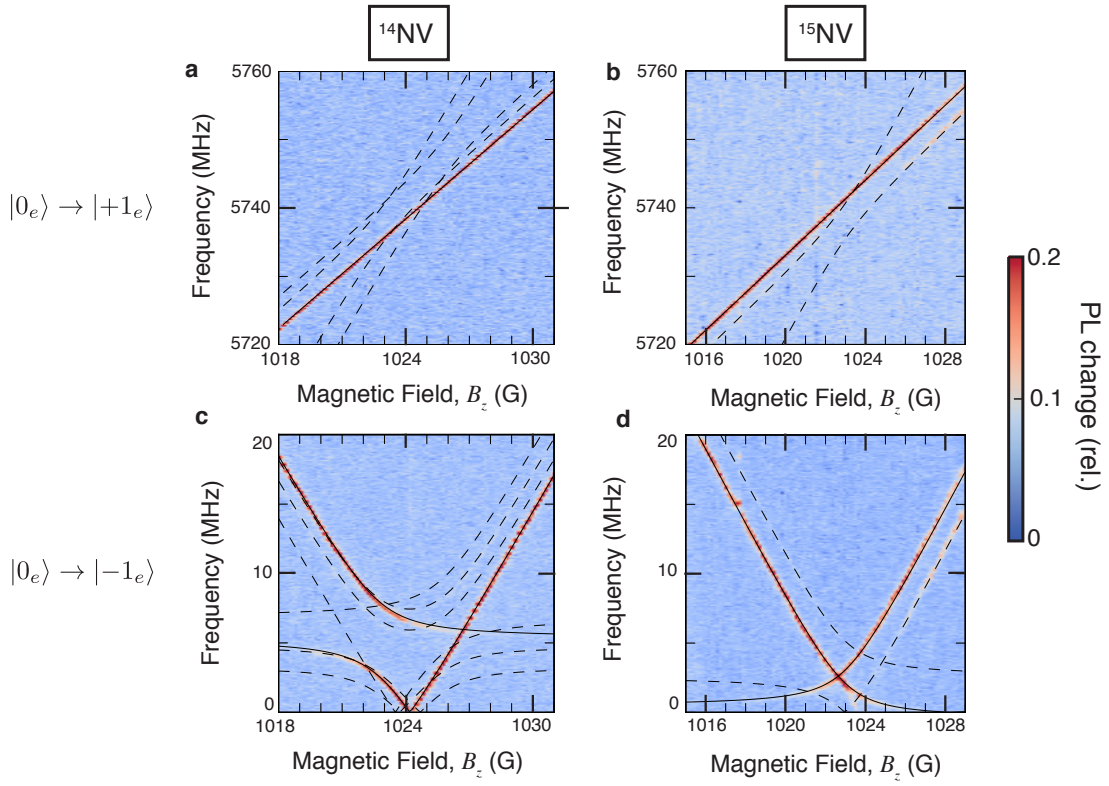

Figure 2.4: Optically detected magnetic resonance (ODMR) performed at the GSLAC. ODMR spectra from ^{14}N-V and ^{15}N-V (left and right respectively) measured for applied axial magnetic fields that are varied around the GSLAC central position of $B_z = 1024\,\mathrm{G}$. **a**,**b** ODMR of the NV transition of $|0_e\rangle \rightarrow |+1_e\rangle$ and **c**,**d** for the $|0_e\rangle \rightarrow |-1_e\rangle$ transition. The theoretical allowed and partly allowed transitions are overlaid. The dynamical nuclear spin polarisation causes some transitions to become dominate (solid black lines), while others have comparatively small to vanishing contrast (dashed lines).

feature centred at $B_z \approx 1022$ G, around the transition frequency $\omega \approx 5$ MHz which corresponds to the quadrupole coupling Q. This leads to little mixing at the allowed crossing at $B_z \approx 1024$ G, which means the dominant transition here is $|0,+1\rangle \rightarrow |-1,+1\rangle$. We observed clear ODMR signatures with resonance frequencies down to 100 kHz in this sample, which is an ultra-high purity chemical vapor deposition (CVD) grown diamond with isotopically purified carbon content ($[^{12}\mathrm{C}] > 99.99\%$). This indicates that the NV spin could in principle be resonantly coupled to most nuclear spin species, which have Larmor frequencies ranging typically from 500 kHz to 5 MHz in this magnetic field regime. However, in reality the minimum observable transition frequency was found to be highly sample dependent.

On the other hand, the ^{15}N-V exhibits a very different spectrum near the GSLAC (Fig. 2.4b,d). Under optical pumping, the spin is effectively polarised in the state $|0,+1/2\rangle$, which remains an z-basis eigenstate at all fields. The allowed transitions from RF driving is a superposition, $|\beta\rangle = a\,|0,-1/2\rangle + b\,|-1,+1/2\rangle$, where the avoided crossing is centred approximately around the initial state $|0,+1/2\rangle$ (see Fig. 2.3c). As a result, the ODMR plot shows two transitions that bend upon approaching vanishing frequencies. They cross at a field $B_z \approx 1024$ G and a transition frequency $\omega'_\times/2\pi \approx 2.65(2)$ MHz determined by

$$\omega'_\times = \sqrt{\frac{A'^2_\perp}{2} + \left(\frac{\gamma'_n}{\gamma_e - \gamma'_n}\right)^2 \left(D - \frac{A'_\parallel}{2}\right)^2}. \tag{2.7}$$

Incidentally, this allows the perpendicular component of the hyperfine interaction ($A'_\perp$) to be measured directly on a single ^{15}N-V centre, which gives here $A'_\perp/2\pi = 3.69(3)$ MHz, in excellent agreement with the ensemble-averaged value of 3.65(3) MHz reported in Ref. [88]. The peculiar GSLAC structure of the ^{15}N-V centre has important consequences for sensing. In particular, the contrast of the transitions decreases rapidly for frequencies below $\omega'_\times$ as they become forbidden. As a result, the ^{15}N-V is unsuited to detecting resonances below about 2 MHz under typical conditions. Most nuclear spin species have transitions within this range, with an exception being hydrogen (^{1}H), which has a Larmor frequency of about 4.4 MHz at this field and could be in principle detected via cross-relaxation with an ^{15}N-V.

2.2.3 A theoretical study of NV nuclear spin polarisation

In this section a theory of NV nuclear spin polarisation through anti-crossing spin mixing is developed, following the treatment given in Ref. [171] which looks at the polarisation of ^{15}N-V at the ESLAC. This treatment is first summarised below before extending to the GSLAC and including the ^{14}N-V.

The excited state Hamiltonian for the ^{15}N-V spin is,

$$H_{\mathrm{ES},15} = D_{\mathrm{ES},15} S_z^2 + \mathbf{B}\cdot\mathbf{S} + \mathbf{S}\cdot\mathbf{A}'_{ES}\cdot\mathbf{I} \tag{2.8}$$

with $\mathrm{D}_{\mathrm{ES},15} = 1435$ MHz and $A'_{\mathrm{ES},\parallel} = A'_{ES,\perp} = 60$ MHz [173]. At the ESLAC the states $|-1,1/2\rangle$ and $|0,-1/2\rangle$ mix, this allows for the transfer of electron and nuclear spin population to occur. However, as the decay path from the excited state favours the electron $|0\rangle$ state and preserves nuclear spin state this mixing will cause a gradual build up of polarisation in a single ground state. The mixing and energy level diagram is shown in Fig. 2.5a ^{14}N-V and Fig. 2.5b ^{15}N-V. The mixing and decay paths indicate the the final state will be the $|0,1/2\rangle$ for ^{15}N-V and $|0,+1\rangle$ for the ^{14}N-V spin, when this mixing is maximal.

Starting with an initial eigenstate of $|\psi\rangle = a\,|0,+1/2\rangle + b\,|0,-1/2\rangle$ the polarisation is defined as $\mathcal{P} = a^2 - b^2$, where $a^2 + b^2 = 1$. The probability of mixing to occur in the excited state and thus nuclear spin polarisation, is given by the probability of the eigenstates $|\gamma\rangle = a\,|-1,+1/2\rangle + b\,|0,-1/2\rangle$ and $|\delta\rangle = b\,|-1,+1/2\rangle - a\,|0,-1/2\rangle$ being the same as the $|-1,+1/2\rangle$ state, such that

$$p_+(^{15}\mathrm{N}) = 2\,|\langle -1,+1/2 \mid \gamma\rangle|^2\,|\langle -1,+1/2 \mid \delta\rangle|^2 \tag{2.9}$$

where the factor of two comes from normalisation and p_+ is given in Fig. 2.5b. The probability of the inverse polarisation occurring is given by $\mathrm{p}_-(B) = \mathrm{p}_+(-B)$. Combining these equations allows for the formulation of master equations that define the rate of population transfer, for example

$$k_{|0,+1/2\rangle} = \frac{(1-\mathcal{P})p_+\Gamma}{2} - \frac{(1+\mathcal{P})p_-\Gamma}{2} - k^0_{\mathrm{eq}}\mathcal{P}, \tag{2.10}$$

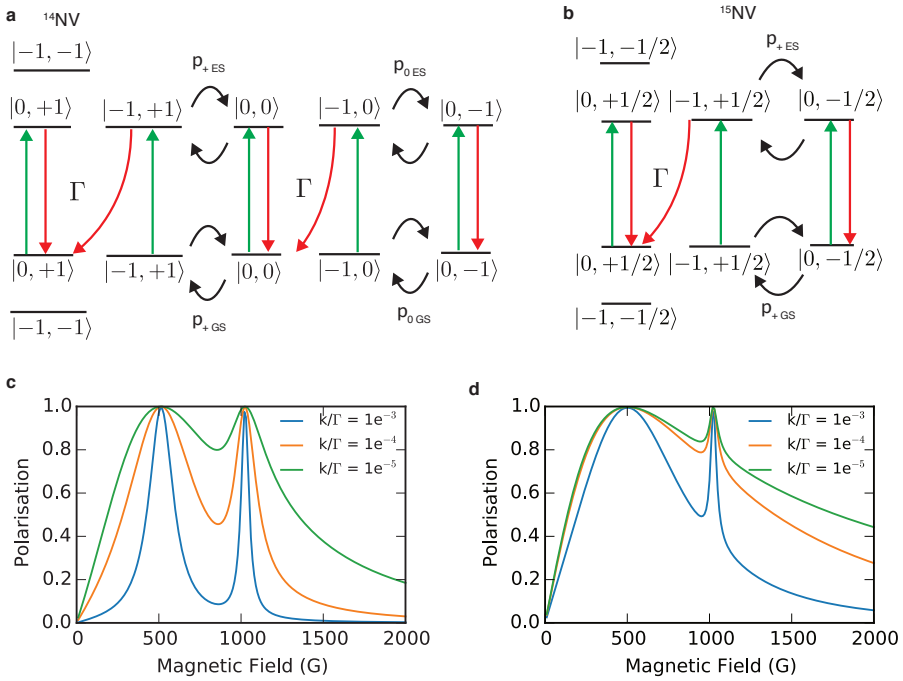

Figure 2.5: Depiction of the mixing of both the ground and excited states at their respective anti-crossing for both the ^{14}N-V **a** and ^{15}N-V **b** spin systems. The probability of mixing is defined as p with a relevant subscript. The spin conserving inter-system crossing is given by Γ. Note that the two anti-crossings do not occur at the same magnetic field strength, the ESLAC is at $\sim$ 512 G which the GSLAC is at $\sim$ 1024 G. Theoretical plots of the polarisation of the NV nuclear spin are show for ^{14}N-V **c** and ^{15}N-V **d** with various values for k/Γ.

is the rate of population transfer into and out of the $|0, 1/2\rangle$ state, where k^0_{eq} constitutes the nuclear T_1 relaxation rate and Γ is the spin conserving inter-system crossing decay. Solving the master equation for $\mathcal{P}$ in the steady state results in

$$\mathcal{P}(^{15}\text{N}) = \frac{p_+ - p_-}{\frac{\Gamma}{k^0_{\text{eq}}} + p_+ + p_-}. \tag{2.11}$$

To model the polarisation at the GSLAC, we follow the same treatment as above where the only difference comes from the mixing terms. Where the probabilities of mixing are just replaced with the ground state equivalent, i.e. $p_{\text{ES}} \rightarrow p_{\text{GS}}$. These two different equations for both the ESLAC and GSLAC are separate and can simply be combined through addition to obtain the total polarisation.

The ^{14}N-V system has six levels rather than four and has two possible mixing terms in the polarisation. These polarisation terms are made up from the four states that mix: $|\gamma\rangle = \alpha\,|0,-1\rangle + \beta\,|-1,0\rangle$, $|\delta\rangle = \beta\,|0,-1\rangle - \alpha\,|-1,0\rangle$, $|\epsilon\rangle = \alpha'\,|0,0\rangle + \beta'\,|-1,+1\rangle$, and $|\zeta\rangle = \beta'\,|0,0\rangle - \alpha'\,|-1,+1\rangle$, resulting in

$$p_+ = 2\,|\langle -1,+1 \mid \epsilon\rangle|^2\,|\langle -1,+1 \mid \zeta\rangle|^2\,, \tag{2.12}$$

$$p_0 = 2\,|\langle -1,0 \mid \gamma\rangle|^2\,|\langle -1,0 \mid \delta\rangle|^2\,, \tag{2.13}$$

where $p_- = p_+(-B)$. The two mixing probabilities are defined in Fig. 2.5a. The mixing and energy level diagram is shown in Fig. 2.5a. Starting with a state $|\psi\rangle = a\,|0,+1\rangle + b\,|0,0\rangle + c\,|0,-1\rangle$ the polarisation of the $|0,+1\rangle$ state is defined as $\mathcal{P} = a^2 - (b^2 + c^2)/2$. The set of master equations for the ^{14}N-V is

$$k_{+1} = b^2 p_+ \Gamma - k^0_{\text{eq}}\mathcal{P} - a^2 p_- \Gamma, \tag{2.14}$$

$$k_0 = -b^2 p_+ \Gamma + \frac{k^0_{\text{eq}}\mathcal{P}}{2} + c^2 p_0 \Gamma, \tag{2.15}$$

$$k_- = a^2 p_- \Gamma - c^2 p_0 \Gamma + \frac{k^0_{\text{eq}}\mathcal{P}}{2}. \tag{2.16}$$

Setting these rates to zero (solving for the steady state) and using the identity ($\sum_i k_i = 0$), the polarisation of ^{14}N-V for both the excited and ground state level anti-crossing is given

by

$$\mathcal{P}(^{14}N) = -\frac{2\left(p_0\left(p_- - 2p_+\right) + p_- p_+\right)}{\frac{3k_{\mathrm{eq}}^0}{\Gamma}\left(2p_0 + p_+\right) + 4\left(p_- p_+ + p_0\left(p_- + p_+\right)\right)}. \tag{2.17}$$

Having modelled the polarisation effect at either the ESLAC or GSLAC, the two effects can now be combined via the substitution $p \rightarrow p_{\mathrm{ES}} + p_{\mathrm{GS}}$. The theoretically expected polarisation is shown in Fig. 2.5c ^{14}N-V and Fig. 2.5d ^{15}N-V for different values of the ratio k_{eq}^0/Γ. This shows a broad peak at 512 G from the ESLAC and a narrow peak at 1024 G from the GSLAC for both systems. The ^{15}N-V spin system has broader polarisation peak due to its larger parallel hyperfine, however this effect is minimized as k_{eq}^0/Γ becomes smaller. As Γ is a decay rate from the excited state to the ground state we can assume that this is constant and thus the change in k_{eq}^0/Γ represents a change in the NV's nuclear decay rate given by k_{eq}^0. Thus, when the NV nuclear spin has a shorter longitudinal relaxation rate the polarisation will exist over a larger range.

2.2.4 Photoinduced spin dynamics as the GSLAC

We now investigate the spin population dynamics near the GSLAC. Our aim is to assess the possibility of measuring the longitudinal spin relaxation time (T_1), as required in order to perform cross-relaxation spectroscopy on nearby nuclear spins [110]. The T_1 time is typically measured by using laser pulses to initialise the NV into $|0_e\rangle$, and read out the probability of being in the $|0_e\rangle$ after a variable delay t (Fig. 2.6a). In practice, the PL signal is integrated at the start of the readout pulse (I_s) and normalised by the PL from the back of the pulse (I_r), as defined previously in section 2.1.2. The normalised signal I_s/I_r can be expressed as [82]

$$\frac{I_s}{I_r}(t) = a + bP_0(t), \tag{2.18}$$

where $P_0(t) = |\langle 0_e|\psi(t)\rangle|^2$ is the population in $|0_e\rangle$ of the current spin state $|\psi(t)\rangle$, $a \approx 1$ is a normalisation constant, and $b \approx 0.3$ relates the NV spin state dependent contrast. The resulting time trace $\frac{I_s}{I_r}(t)$ therefore allows us to estimate the initial population $P_0(0)$, which approaches unity under normal conditions [82], as well as the evolution of the spin

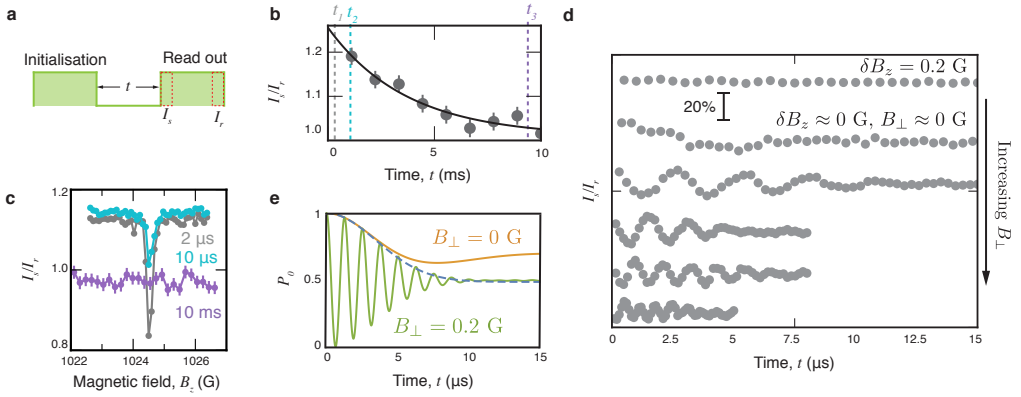

Figure 2.6: PL resonances from spin mixing at the GSLAC. a Laser pulse sequence used to measure the NV state, containing only an initialisation and a readout laser pulse. **b** NV T_1 measurements away from GSLAC indicating $T_1 \approx 5\,\text{ms}$. **c** Single point T_1 measurements taken across the GSLAC for evolution times, $t = 2$ μs (grey), $t = 10$ μs (light blue), and $t = 10\,\text{ms}$ (purple). **d** Time trace measurements at the GSLAC. The top curve is detuned from the GSLAC by $\delta B_z = 0.2\,\text{G}$ and indicates no fluctuation in the NV population. The other measurements have zero detuning, instead a transverse magnetic field has been applied to the NV centre that increases from $B_\perp = 0\,\text{G}$ to $B_\perp \approx 0.5$ (Top to bottom). **e** Average expected time trace from the proposed model.

state under no illumination. In general (away from the GSLAC or ESLAC), the spin population exhibits a simple exponential decay towards a thermal mixture,

$$P_0(t) = \frac{1}{3} + \frac{2}{3}e^{-t/T_1}, \tag{2.19}$$

assuming perfect initialisation (see an example in Fig. 2.6b). In the follow, the axial magnetic field B_z is varied with measuring $\frac{I_s}{I_r}(t)$ for different wait times, t.

^{14}N-V centres

To investigate the spin dynamics at the GSLAcC we start with measurements of ^{14}N-V centres, using the same diamond as before (i.e. CVD diamond with [^{12}C]> 99.99%). In this sample, the main source of magnetic noise comes from the bath of remaining ^{13}C impurities [53]. A scan across the GSLAC for a representative ^{14}N-V centre is shown in Fig. 2.6c, where we probed three time points $t = 2$ μs, 10 μs, and 10 ms. When the NV is far from the GSLAC crossing, an exponential decay is observed as shown in the full time trace in Fig. 2.6b. This decay corresponds to phonon-induced relaxation, with

a characteristic time $T_1 \approx 5$ ms [109]. At the crossing at $B_z \approx 1024$ G, however, a sharp variation in signal is observed (Fig. 2.6c), which is referred to as the "GSLAC feature" or "1024 G feature". Here, the NV spin undergoes population oscillations, as indicated by the 2 μs time point dropping below the 10 ms point.

To understand the origin of this oscillation a reduced effective Hamiltonian, $\mathcal{H}_R$, that only contains the states $|0,+1\rangle$ and $|-1,+1\rangle$ can be used, giving

$$\mathcal{H}_R = \begin{pmatrix} 0 & \gamma_e B_\perp \frac{e^{-i\theta}}{\sqrt{2}} \\ \gamma_e B_\perp \frac{e^{+i\theta}}{\sqrt{2}} & \gamma_e \delta B_z \end{pmatrix}, \tag{2.20}$$

where we introduced the longitudinal detuning from the crossing, $\gamma_e \delta B_z = D - \gamma_e B_z - A_\parallel$, the transverse magnetic field, $B_\perp = \sqrt{B_x^2 + B_y^2}$, and the angle θ defined by $\tan\theta = B_y/B_x$. The transverse field causes a mixing between $|0,+1\rangle$ and $|-1,+1\rangle$ and opens an energy gap associated with a level avoided crossing. Assuming that optical pumping always initialises the NV in the $|0,+1\rangle$ state, and reads out the population in that same state, we then expect oscillations between $|0,+1\rangle$ and $|-1,+1\rangle$ that are mirrored in the PL when in the presence of a transverse magnetic field. Under these conditions, the probability of occupying the state $|0,+1\rangle$ after a wait time t following initialisation is given by

$$P_0(t) = \frac{\delta B_z^2 + B_\perp^2 \left[1 + \cos\left(\gamma_e t \sqrt{\delta B_z^2 + 2B_\perp^2}\right)\right]}{\delta B_z^2 + 2B_\perp^2}. \tag{2.21}$$

The amplitude of the oscillation vanishes when the detuning is much larger than the transverse field ($\delta B_z \gg B_\perp$), far from the avoided crossing region. This is illustrated in Fig. 2.6d (top curve), which was recorded with a detuning $\delta B_z \approx 0.2$ G $\gg B_\perp$. On the other hand, near the avoided crossing where the amplitude is maximal, the frequency of the oscillation is expected to increase as $B_\perp$ is increased. This effect was tested through a series of measurements with varying transverse fields. Experimentally this involved using a permanent magnet to align the field at the 1024 G crossing so that no oscillations are detected. The permanent magnet is then moved in the transverse direction (x or y) to add a transverse field. The results are shown in Fig. 2.6d where reading from top to bottom $B_\perp$ increases, resulting in faster oscillations. Although it is not possible in our

experiments to precisely calibrate the values of $B_\perp$, a rough estimate can be obtained by comparing the measured PL drop as a function of $B_\perp$ to the data from Ref. [162], whose work mapped the NV PL as a function of the magnetic field alignment. One finds that the largest $B_\perp$ applied in Fig. 2.6d (the bottom curve) corresponds to $B_\perp \approx 0.5$ G, and hence an oscillation frequency of approximately 2.8 MHz, according to Eq. (6). This result is in qualitative agreement with the measured frequency of approximately 1.6 MHz.

Damping of the oscillations is attributed to noise in the local magnetic field. In this sample, the noise comes predominantly from the bath of ^{13}C impurities. Examination of this interaction via the rotating wave approximation shows that only the x-z, y-z and z-z components of the dipole-dipole coupling to the NV spin need be considered [96]. The effective magnetic noise from the environment may be regarded as static over the short wait times, t, considered here. We assume that the field components δB_z and $B_\perp$ are normally distributed with means $\langle \delta B_z \rangle$ and $\langle B_\perp \rangle$ and variances $\sigma^2_{B_z}$ and $\sigma^2_{B_\perp}$, respectively. Averaging Eq. (2.21) over these distributions, we find numerically that the decay envelope of $\langle P_0(t) \rangle$ is well approximated by a Gaussian function $e^{-(t/T_\times)^2}$, where the characteristic time $T_\times$ (where $\times$ denotes the decay is from the GSLAC) is given by $T_\times^{-1} = \gamma_e \sigma_{B_\perp}$, regardless of the mean value $\langle \delta B_z \rangle$ and $\langle B_\perp \rangle$ (see Fig. 2.6e). In other words, the damping of oscillations is mainly caused by the fluctuations in the transverse magnetic field. It is interesting to link this damping time $T_\times$ to the dephasing time T_2^* measured in a free induction decay (FID) experiment [174]. Under the same assumptions, the FID envelope takes the form $e^{-(t/T_2^*)^2}$ where $(T_2^*)^{-1} = \gamma_e \sigma_{B_z}/\sqrt{2}$. Moreover, a bath of randomly placed ^{13}C spins around the NV centre leads to $\sigma^2_{B_\perp} \approx \frac{3}{4}\sigma^2_{B_z}$ on average [96], which gives the relation

$$T_\times \approx T_2^* \sqrt{\frac{2}{3}}. \tag{2.22}$$

For the NV centre studied in Fig. 2.6, the damping time of the 1024 G oscillations is $T_\times \approx 5 - 10$ μs, estimated from the curves shown in Fig. 2.6d, hence $\sqrt{\frac{3}{2}} T_\times \approx 6 - 12$ μs. This is significantly shorter than the dephasing time $T_2^* > 50$ μs. We attribute the discrepancy mainly to drifts in the magnetic field applied during the measurements, which leads to overestimating the damping rate $1/T_\times$.

We now consider the case where the magnetic field is aligned along the NV axis, i.e. $\langle B_\perp \rangle = 0$. At the crossing when $\delta B_z = 0$, the averaged population $\langle P_0(t) \rangle$ does not oscillate and still decays with a characteristic time $T_\times$ (see Fig. 2.6e). However, the amplitude of the decay decreases as δB_z is increased. We define the width of the 1024 G feature, denoted $\Delta B_z^\times$, as twice the detuning δB_z applied to obtain a maximum population drop of 30%. We find numerically that $\Delta B_z^\times \approx 4\sigma_{B_\perp}$, which can also be expressed as a function of T_2^* according to

$$\gamma_e \Delta B_z^\times \approx \frac{4}{T_\times} \approx \frac{5}{T_2^*}. \tag{2.23}$$

For the NV studied here, we predict a width $\Delta B_z^\times < 1\ \mu$T for a perfectly aligned magnetic field. We note however that in the measurements of Fig. 2.6c, the width is instead given by the residual transverse field ($B_\perp \approx 0.3$ G in Fig. 2.6c, which could not be maintained to significantly smaller values for extended periods of time due to drifts in the applied magnetic field.

The observation of coherent oscillations at the GSLAC suggests a direct application to DC magnetometry. Indeed, the frequency of the oscillation is directly proportional to the strength of the transverse field according to Eq. (2.21), assuming $\delta B_z \ll B_\perp$. For photon shot noise limited measurements, the magnetic sensitivity is similar to that obtained by FID measurements [53], with the advantage of being an all-optical technique (no microwave or RF field is required).

We now compare the spin dynamics of ^{14}N-V centres at the GSLAC in different diamond samples. Of particular relevance to sensing applications are NV centres implanted close to the diamond surface. We performed measurements of shallow NV centres in a CVD-grown diamond with natural isotopic concentration ([^{13}C]= 1.1%). The NV centres were created by implantation of N^+ ions with an energy of 3.5 keV followed by annealing, resulting in NV centres at a mean depth of 10 nm [175]. Fig. 2.7a shows a scan across the GSLAC for a particular ^{14}N-V centre. A reduction in the PL is observed at a field $B_z \approx 1024$ G, corresponding to the crossing discussed before. However, full time traces (shown in Fig. 2.7b) now reveal a simple offset of the PL at the crossing, with no obvious oscillatory behaviour. This can be understood by the large magnetic noise originating

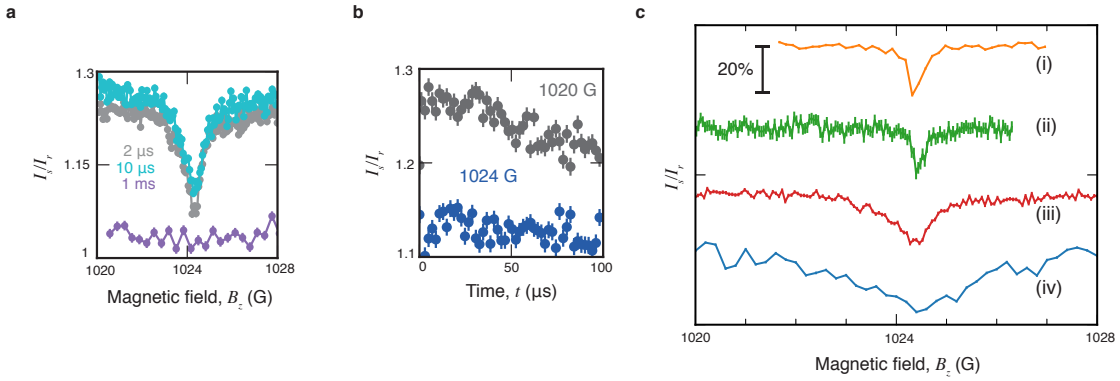

Figure 2.7: GSLAC feature comparison for different samples. a PL scan across the GSLAC for shallow implanted single NVs in electronic grade CVD diamond, using a single point T_1 technique for time points $t = 2, 10, 1000$ μs. **b** Time trace at the GSLAC (blue) and away (grey). **c** Comparison of the GSLAC feature for different samples, where the curves have been offset for clarity. (i) A deep NV centre in an isotopically pure CVD diamond. (ii) Deep NV centre in a diamond with natural isotopic content. (iii) Shallow NV centre in the same diamond as (i). (iv) Deep NV centre in a type-1b diamond. This figure is a modified version of a figure from Ref. [161].

from the surface, which results in a decay time $T_\times$ shorter than the minimum probe time of $t = 1$ μs (limited by the lifetime of the singlet state [82]). The width of the feature in Fig. 2.7a is $\Delta B_z^\times \approx 1$ G (or $\Delta\omega^\times \approx 3$ MHz). By measuring various shallow NV centres in the same sample, we found a range of widths of the 1024 G feature from $\Delta B_z^\times = 1$ to 3 G (or $\Delta\omega^\times = 3$ to 9 MHz). This variability is attributed to different local environments, especially because each NV centre sits at a different distance from the surface. For applications to T_1-based NMR spectroscopy as discussed earlier (section 2.1.2, this implies that nuclear spin species with large gyromagnetic ratios such as ^{1}H (Larmor frequency $\omega \approx 4.4$ MHz at 1024 G) can be resonantly coupled to a shallow ^{14}N-V such as that measured in Fig. 2.7a. However, species with smaller gyromagnetic ratios such as ^{13}C (Larmor frequency $\omega \approx 1.1$ MHz) are generally within the width of the crossing feature in the present sample, and could therefore cannot be detected via cross-relaxation. This motivates further progress in optimising the coherence properties of shallow NV spins, or devising ways to mitigate the effect of dephasing in T_1 measurements.

Finally, we measured the properties of ^{14}N-V centres at the GSLAC in two other settings: (1) deep ^{14}N-V centres in a CVD diamond with [^{13}C]= 1.1%, where decoherence is dominated by the ^{13}C bath rather than surface effects; (ii) deep ^{14}N-V centres in type-Ib

diamond grown by HPHT, where the main source of decoherence is the bath of electronic spins associated with nitrogen impurities. Example scans across the GSLAC are shown in Fig. 2.7c. Deep NVs in CVD diamond showed line widths of the 1024 G feature smaller than $\Delta B_z^{\times} \approx 0.3$ G for most NVs ($\Delta\omega^{\times} \approx 1$ MHz). By contrast, line widths in the type-Ib diamond are of the order of 10-20 MHz, which makes such diamonds unsuited to T_1-based NMR spectroscopy.

^{15}N-V centres

As previously discussed, the energy structure of the ^{15}N-V centre at the GSLAC precludes it from accessing transition frequencies below about 2 MHz. Although this limits the range of nuclear spin species that could be resonantly coupled to the ^{15}N-V, the highly relevant ^{1}H remains accessible. It is therefore important to test the ability to measure the T_1 of ^{15}N-V centres near the GSLAC.

As in the ^{14}N-V case, we recorded PL scans across the GSLAC with different wait times, t. For this study the measurements were performed on shallow ^{15}N-V centres in a CVD diamond only, as this is the most relevant sample for sensing applications. The implantation energy was 3.5 keV and the concentration of ^{13}C is 1.1%, similar to the diamond used in Fig. 2.7a. Fig. 2.8a shows a scan obtained for a particular ^{15}N-V centre. The spin population remains essentially constant across the GSLAC, except at a magnetic field $B_z \approx 1024$ G where a sharp change is observed. Time traces at and away from the feature are shown in Fig. 2.8b and Fig. 2.8c. While the long time scale reveals an exponential decay with a characteristic time $T_1 \approx 2$ ms independent from the magnetic field (Fig. 2.8b), the contrast of the decay is significantly smaller at $B_z \approx 1024$ G. This is due to the initial population being lower, as can be seen from the drop of signal at short time scales (Fig. 2.8c). This 1024 G feature was consistently seen in most NVs investigated, displaying a variety of amplitudes and widths. At this field, the dominant NV transition has a frequency of ≈ 4.3 MHz. This is 1 G beyond the 1023 G crossing observed in the ODMR (see Fig. 2.4), when the NV transition frequency is $\omega'_{\times} \approx 2.65$ MHz.

To understand this 1024 G feature, we consider the energy level structure shown in Fig. 2.3d. As mentioned before, under optical pumping near the GSLAC the ^{15}N-V

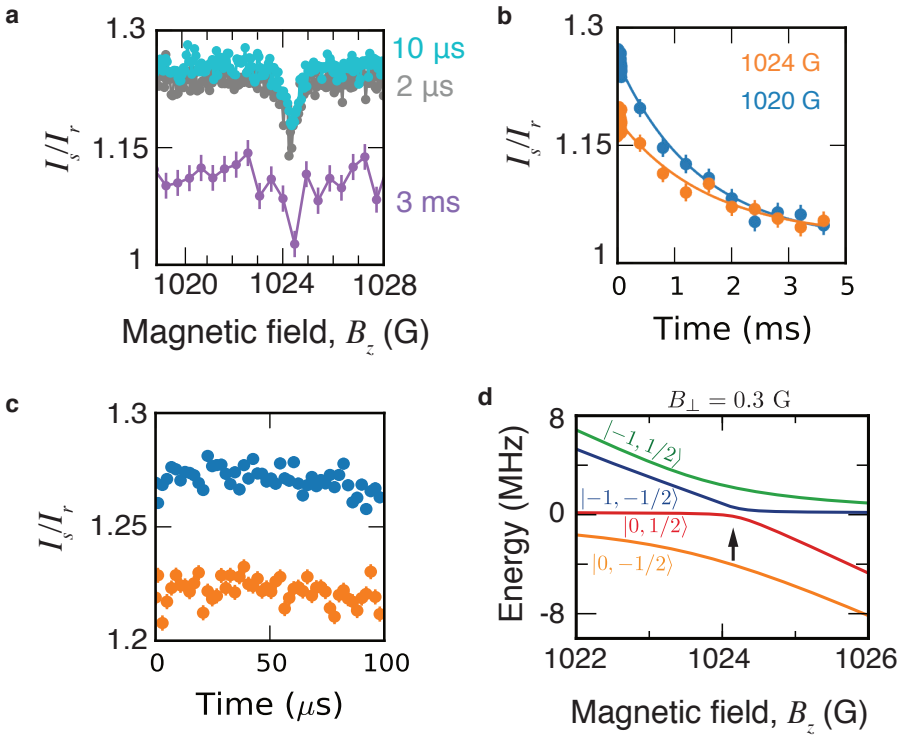

Figure 2.8: GSLAC feature for ^{15}N-V a PL scan across the GSLAC for ^{15}N-V using the single time points of $t = 2, 10, 3000\mu$s. **b**,**c** Time traces on (orange) and off (blue) the GSLAC feature for long (**b**) and short **c** time scales. **d** Energy levels of the ^{15}N-V in the presence of a small perpendicular magnetic field ($B_\perp = 0.3$ G) that induces anti-crossing.

centre is efficiently polarised in the state $|0,+1/2\rangle$. This state crosses the state $|-1,-1/2\rangle$ precisely at 1024 G. These two states cannot be coupled directly by a transverse magnetic field because they have distinct nuclear spin projections. However, they are indirectly coupled to each other via transverse-field-enabled coupling to the other two hyperfine-mixed states, which are superpositions of $|0,-1/2\rangle$ and $|-1,+1/2\rangle$. This is illustrated in Fig. 2.8d, which shows the computed energy levels as a function of B_z in the presence of a finite transverse field, here $B_\perp = 0.3$ G. The transverse field opens a gap between $|0,+1/2\rangle$ and $|-1,-1/2\rangle$ at 1024 G. As a consequence, they become mixed states which can give rise to coherent spin oscillations since optical pumping initialises the NV in the $|0,+1/2\rangle$ state. This situation is reminiscent of the ^{14}N-V case, where the 1024 G feature was due to an avoided crossing between two states coupled via a transverse magnetic field. The main difference here is that the coupling is indirect, mediated by two intermediate states. In the presence of magnetic noise, the coherent oscillations between the two coupled states are expected to be averaged out and appear as a decrease of the initial spin population, as we observed experimentally in this sample (Fig. 2.8c). We note that a transverse-field-induced coupling also occurs at $B_z \approx 1027$ G, between $|0,+1/2\rangle$ and $|\beta_+\rangle \approx |0,-1/2\rangle$ (see Fig. 2.3d). This coupling explains why the dynamic nuclear spin polarisation becomes ineffective around this field, as seen in the ODMR previously (Fig. 2.4).

An unfortunate consequence of the 1024 G feature in the ^{15}N-V centre case is that resonant coupling with a ^{1}H spin would normally occur very close to 1024 G, since the Larmor frequency of ^{1}H is ≈ 4.36 MHz at this field. Therefore, any signature of ^{15}N-V-^{1}H coupling would be overwhelmed by this strong intrinsic feature. It should be noted however that cross-relaxation resonances with nuclear spins should occur on both sides of the GSLAC [110], so that ^{1}H can still be detected before the GSLAC, at a magnetic field $B_z \approx 1022$ G. Moreover, improving the coherence properties (i.e., reducing the noise) of shallow NV centres should significantly reduce the width and amplitude of the 1024 G feature.

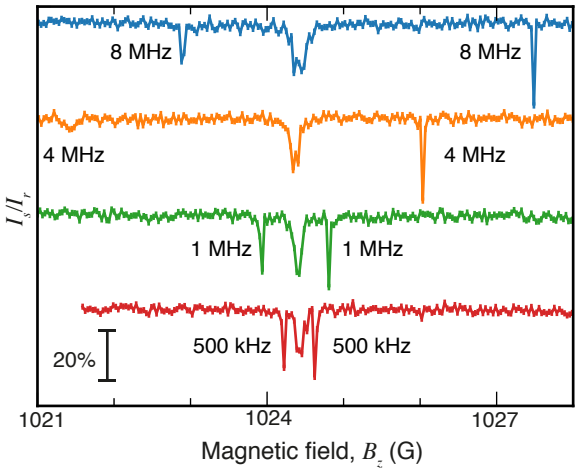

Figure 2.9: Low frequency fluctuating noise detection. PL scan across the GSLAC using a single time $T = 10\mu$s with a ^{14}N-V centre. Each scan has a different applied magnetic noise with a central frequency of 8, 4, 1, and 0.5 MHz, top to bottom. The root-mean-square amplitude of each of the signals is $B_{\mathrm{RMS}} = 1\mu$T. The curves are offset for clarity. This figure is a modified version of a figure from Ref. [161].

2.2.5 All-Optical magnetic-noise spectroscopy

By scanning the magnetic field across the GSLAC, we have shown that the transition frequency of the ^{14}N-V centre can be tuned down to frequencies as low as 100 kHz in diamond samples with low intrinsic magnetic noise. This is approximately an order of magnitude below the transition frequencies exhibited by nuclear species (e.g. ^{13}C) at 1024 G, thus opening the possibility to perform all-optical NMR spectroscopy by detecting cross-relaxation events between a probe NV spin and target nuclear spins [110]. When the NV transition frequency is matched to the nuclear Larmor frequency, the fluctuating nuclear field would cause the NV spin to relax faster, translating into a decreased longitudinal relaxation time, T_1.

In order to test the possibility of detecting fluctuating magnetic fields near the GSLAC, we generated a local magnetic field by running an oscillating current through a wire placed in proximity to the diamond. To mimic nuclear spin detection, we applied signals at various frequencies: 8 MHz, 4 MHz ($\sim$ ^{1}H or ^{19}F), 1 MHz ($\sim$ ^{13}C), and 500 kHz ($\sim$ ^{2}H or ^{17}O). The alternating current was modulated in amplitude and phase to ensure that the NV is not coherently driven and instead experiences noise from a randomly

fluctuating current around a given frequency, similar to the signal from a possible target nuclear spin. The amplitude of the current was adjusted to obtain a root-mean-square field strength of 1 μT, which corresponds approximately to the field generated by a dense organic sample of nuclear spins located at a 5 nm stand-off distance [116]. The probe time was set to $t = 10$ μs to maximise the PL contrast. The resulting spectra (PL as a function of B_z), measured on a deep ^{14}N-V centre in an isotopically-purified CVD diamond, are shown in Fig. 2.9. While the 8 MHz, 1 MHz and 500 kHz detections are clear on both sides of the 1024 G crossing, the 4 MHz detection is weaker before the GSLAC. This is due to the NV transition being very weak in this region because of spin mixing (associated with an avoided crossing), as discussed previously (see Fig. 2.4). Past the GSLAC, however, there is no issue measuring any of the signals and thus NMR spectroscopy would be possible in this region for most commonly found nuclear spin species. We note that the width of the resonances is governed here by the amplitude of the applied field (1 μT) through power broadening. Weaker signals will produce narrower lines, down to the limit of spectral resolution imposed by spin dephasing, characterised by T_2^* [113]. Reaching this limit was not possible in our experiment due to limited precision and stability of the applied magnetic field. This could be improved by using, e.g., an electromagnet [169] or controlling the temperature of a permanent magnet, which will be investigated in section 3.2.

2.3 Nuclear magnetic resonance (NMR) detection via CR-relaxometry

The GSLAC study in the previous section proved that it is possible to use the NV spin for CR-relaxometry of nuclear spin frequencies. However, detection of introduced pseudo-nuclear spin signals and actual remote nuclear spins is quite different. One important consideration is that near surface NV spins have a broader GSLAC feature than the deep NV used as a detection example shown in the last section. This is due to surface noise reducing the coherence and charge stability of near-surface NV spins. In this section, the NV spin is used to detect ^{1}H spins that are located on the surface of the diamond, proving that this technique can indeed be using to resonantly couple with nuclear spin species at diamond interfaces.

To demonstrate CR-relaxometry of external nuclear spins a diamond with shallow NV spins (implanted at 3.5 keV) was used to ensure a depth in the range of $5 - 15$ nm [175]). Hydrogen spins were introduced to the sample surface via both immersion oil and Poly(methyl methacrylate) (PMMA), both of which have been used in previous studies as a proton source [115, 116]. In the published paper (Ref. [111]), NMR detection with ^{14}N-V was demonstrated, which has the most favourable GSLAC structure as discussed in section 2.2.4, however, the ^{15}N-V can also be used through the introduction of a strongly coupled ^{13}C. Below, we focus on the ^{14}N-V case only to illustrate the concept.

The resonance frequency for each CR measurement was obtained through ODMR at each point (Fig. 2.10a) which shows a distinct resonance around $B \approx 1026$ G (green dashed line crossing the ODMR signal) corresponding to NV frequency of $\omega = 4.4$ MHz. To ensure the GSLAC feature or any other spin mixing was not misidentified as a nuclear spin signal, an additional background interaction time was used ($t = 1$ μs, indicates spin mixing) on top of the standard interaction time ($t = 200$ μs, indicates spin-spin interactions). The CR-spectrum shows a clear a signature of ^{1}H spins and the background measurement show no indication of spin mixing (Fig. 2.10b). Comparing the full relaxation curves shows a clear change in the T_1 on resonance (blue) versus the background measurement (grey), shown in Fig. 2.10c. The proton signal was confirmed to be associated primarily with

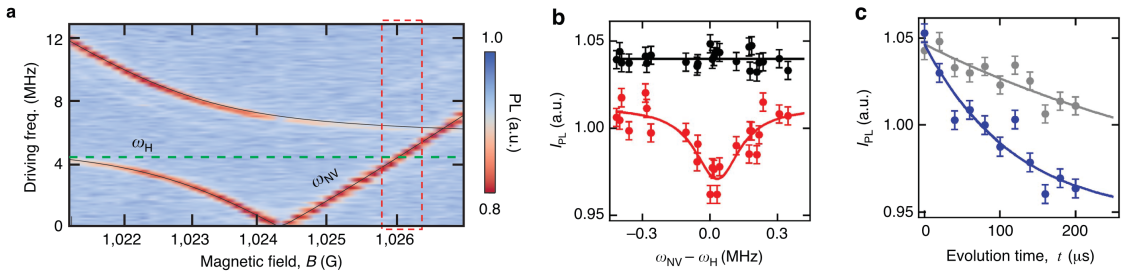

Figure 2.10: NMR detection of external ^{1}H spins using a single ^{14}N-V centre. **a** ODMR spectra of the ^{14}N-V GSLAC with the expected ^{1}H spin resonance shown as a green dashed line. **b** CR-NMR spectrum obtained using a single point T_1 method for $t = 1$ μs (black) and $t = 200$ μs (red), plotted against the NV centres detuning from the expected resonance position. The scan region is shown as a red dashed square on **a**. **c** T_1 curves measured on resonance (blue, 4.4 MHz) and off resonance (grey, 2.7 MHz).

the immersion oil, as the signal significantly reduced upon removal of the immersion oil. Similar to other work that has found the intrinsic layer of ^{1}H spin thickness of 1 nm [131]. Additional measurements on PMMA show that the sensitivity of the CR technique for NMR compares well with the XY8 method (see Ref [111] for more details), however, the spectral resolution is inferior because it is limited by T_2^* rather than T_2.

2.4 Conclusion

In this chapter, the protocol of CR-spectroscopy was developed with the target of measuring both electron and nuclear spins. Initially, the technique was demonstrated on electron spins, which are strongly coupled and are sensed in a regime that is void of any complex ground state spin mixing. Extending this technique towards sensing of nuclear spin motivated the detailed study of the GSLAC. While this study indicated that in some regimes CR-NMR spectroscopy is not functional due to spin mixing (i.e. for noisy samples, or for sensing nuclear spins with low gyromagnetic ratios) it also demonstrated that NV spins are capable of measuring down to 500 kHz, which encapsulates most nuclear spin species. Additionally, the difference in ^{14}N-V and ^{15}N-V was delineated, indicating that the former exhibits a more favourable energy structure for CR spectroscopy. The understanding of the GSLAC of near surface NV spins was used to experimentally realise external nuclear spin detection. While this technique was demonstrated on a strong nuclear spin signal

(^{1}H spins) it in principle can be used to detect any arbitrary nuclear spin provided the bath noise is below the required level.

Compared to existing techniques for NV-based NMR detection, the CR method has the advantage of being all optical (no RF required), but has a lower spectral resolution. In the next chapter, we will explore another distinctive feature of CR, which is that it offers a way to transfer spin polarisation from the NV to target nuclear spins with unprecedented efficiency.

3

Hyperpolarisation of nuclear spins using cross relaxation

Hyperpolarisation – polarisation beyond thermal background – affords opportunities for enhanced magnetic resonance imaging (MRI) [176] and nuclear magnetic resonance (NMR) spectroscopy [177] by generating massive gains in the nuclear spin signal, which is crucial for the development of MRI and NMR on the molecular scale [178]. Identification of nuclear spins and their respective interactions on this scale promises to have enormous benefits in our understanding of biological systems and their interactions, and may be critical to the development of next generation drugs. Consequently, a plethora of different techniques have been developed to perform this task. Hyperpolarisation generally relies on the larger degree of polarisation of electron spins, which is transferred to the nuclear spins of interest through an appropriate protocol. In most cases, high magnetic fields and low temperatures are employed to maximise the natural spin polarisation [179], but this approach imposes a number of technical constraints and its efficacy remains limited. An alternative approach is to use optically initialised electron spins that can obtain a large degree of polarisation at room temperature through optical pumping [180]. Due to the recent advances in quantum technologies for both quantum computing [181, 182] and quantum sensing [1, 50, 54, 115] greater control over individual spins can be realised; facilitating the adaptation and development of hyperpolarisation protocols to individual quantum spins [29, 29, 31, 37–39, 41, 42, 104, 107, 183]. Now that these techniques have

been implemented on the miniaturised scale of a single spin qubit, the quest turns to scaling these techniques so they can be used for macroscopic sample volumes. Despite progress in this direction [28, 32] there are still many hurdles to overcome in order for a quantum-based room temperature hyperpolarisation device to be realised. Some of the most pressing concerns are: what hyperpolarisation protocol can transferring the most polarisation in the shortest time and how robust is this technique to experimental errors?

In this chapter, a new technique for hyperpolarisation is developed that relies on direct cross relaxation of the electron-nuclear spin pair [33, 113], where the electron spin used is the NV spin and the nuclear spin will be a hyperpolarisation target. It is shown that implementing a cross-relaxation measurement scheme induces a polarisation of various target spin baths, mediated via the mutual dipole coupling of the spins that introduces a flip-flop interaction. This hyperpolarisation is first performed on internal ^{13}C spins and is used to confirm the detailed theoretical framework that was developed to describe the method. Then the target is switched to external nuclear spins, where ^{1}H spins on the diamond surface are hyperpolarised. Prior to this work, the NV centre had only been shown to be capable of polarisation nuclear spins are were contained inside of the diamond. While this is significant work and has many application in the production of hyperpolarised nanodiamonds, producing polarised agents that do not contain diamond is vital to many more applications. In the second section of this chapter a technique for further stabilising the experimental apparatus is developed and implemented to explore the dynamics of the spin bath's polarisation after the NV pump is turned off. Finally, cross-relaxation induced polarisation is compared experimentally with other existing polarisation techniques, showing a remarkable speed up.

3.1 Cross relaxation induced polarisation (CRIP)

Measuring spins using T_1-relaxometry has already been developed (previous chapter) as a technique for detection of both electron and nuclear spin species. One benefit of this technique compared with T_2 sensing is that the measurement itself imparts a specific state onto the measured spin. Repeated implementation of the detection sequence results in a polarisation of the target spin bath, which can be used to enhance the signal strength or study the dynamics of a polarised spin bath system.

In this section, a cross relaxation induced polarisation (CRIP) technique is developed. This technique involves using the NV centre in diamond as an effective entropy pump, that acts to remove spin disorder in the local environment about the NV spin. Initially, the confined spin bath of ^{13}C nuclear spins internal to the diamond crystal are utilised to demonstrate the functionality of CRIP and a detailed theoretical framework is developed that agrees with the observed level of ^{13}C spin hyperpolarisation. The technique is then applied to the hyperpolarisation of externally located spins that are placed on the diamond surface. It is demonstrated that the CRIP protocol is capable of imparting a relatively large (on the order of 50%) polarisation to external located ^{1}H spins. This proof of principle experiment illustrates the capability of the protocol, which in principle is tunable to any nuclear spin species and operates at room temperature and represents the first demonstration of hyperpolarisation of nuclear spins external to the diamond lattice.

3.1.1 Principle of the technique

A standard protocol for hyperpolarisation using NV spins relies on applying microwave fields to drive the NV spin into a dressed state, whose energy splitting (frequency of driving) matches that of the target's Larmor frequency [99] (Hartmann-Hahn resonance). This approach (known as NOVEL) enables a cross-relaxation of the spins to occur in the rotating frame, which is mediated by the $A_{z,x}$ and $A_{z,y}$ hyperfine interaction components. In contrast, in the lab frame the polarisation transfer from cross-relaxation induced polarisation (CRIP) is mediated by the greater ($A_{x,y;x,y}$) NV-target hyperfine interaction, increasing the polarisation rate by an order of magnitude over MW-driven techniques, as we will show in section 3.3.

The CRIP protocol is developed using a single NV spin (Fig. 3.1a) that is tuned to resonance and repeatedly initialised after a given interaction time, in order to impart the desired state onto the spin bath (Fig. 3.1b). Just as in CR-spectroscopy of nuclear spins, the resonance condition is met at the ground state level anti-crossing using an ^{14}N-V spin that allows linear tuning of the frequency to match any nuclear spin (Fig. 3.1c). Entropy can be pumped out of the nuclear spin bath through the repeated application of the CRIP protocol (Fig. 3.1d) which selectively only interacts with one of the spin states. For control purposes, the bath can be placed in a deliberately unpolarised state by alternating the polarisation direction. This is achieved through interleaving the CRIP protocol with the inverse protocol, referred to as CRIP^{-1} (Fig. 3.1e), where the inversion comes from initialising the NV spin in the $|-1\rangle$ state rather than the $|0\rangle$ state.

The ensemble response of the nuclear spins from the stimulus of CRIP can be modelled using a master equation that describes the evolution of the polarisation $P(\mathbf{R}, t)$ of an infinitesimal volume of nuclear spins located at position $\mathbf{R}$ from a central NV spin, at time t:

$$\frac{\partial}{\partial t} P\left(\mathbf{R}, t\right) = \left(\beta \nabla^2 - u(\mathbf{R}) - \Gamma_{\mathrm{SL}}\right) P(\mathbf{R}, t) + u(\mathbf{R}), \tag{3.1}$$

which will be derived in the next section. In this equation, $u(\mathbf{R})$ is the rate of polarisation imparted by the interaction with the central NV spin, β is the diffusion coefficient deriving from the dipole interactions between nuclear spins, and Γ_{SL} is the intrinsic relaxation rate. We note that $\mathbf{R}$ is treated as a continuous variable despite the discrete locations of the nuclear spins. The regime of validity of this model and its derivation will be detailed in section 3.1.2.

To probe the polarisation effect experimentally, we monitor the spin-dependent photoluminescence (PL) from the NV [110, 111, 113] during the laser pulses, which decays as a function of the CRIP sequence time as $e^{-\Gamma_{\mathrm{tot}}\tau}$, i.e. we monitor the T_1 of the NV spin. Here Γ_{tot} is the NV longitudinal relaxation rate, which can be expressed as the sum $\Gamma_{\mathrm{tot}} = \Gamma_{\mathrm{bg}} + \Gamma_{\mathrm{CR}}$, where Γ_{bg} is the background rate caused by lattice phonons or surface effects, and Γ_{CR} is due to cross-relaxation. The latter follows a Lorentzian dependence on

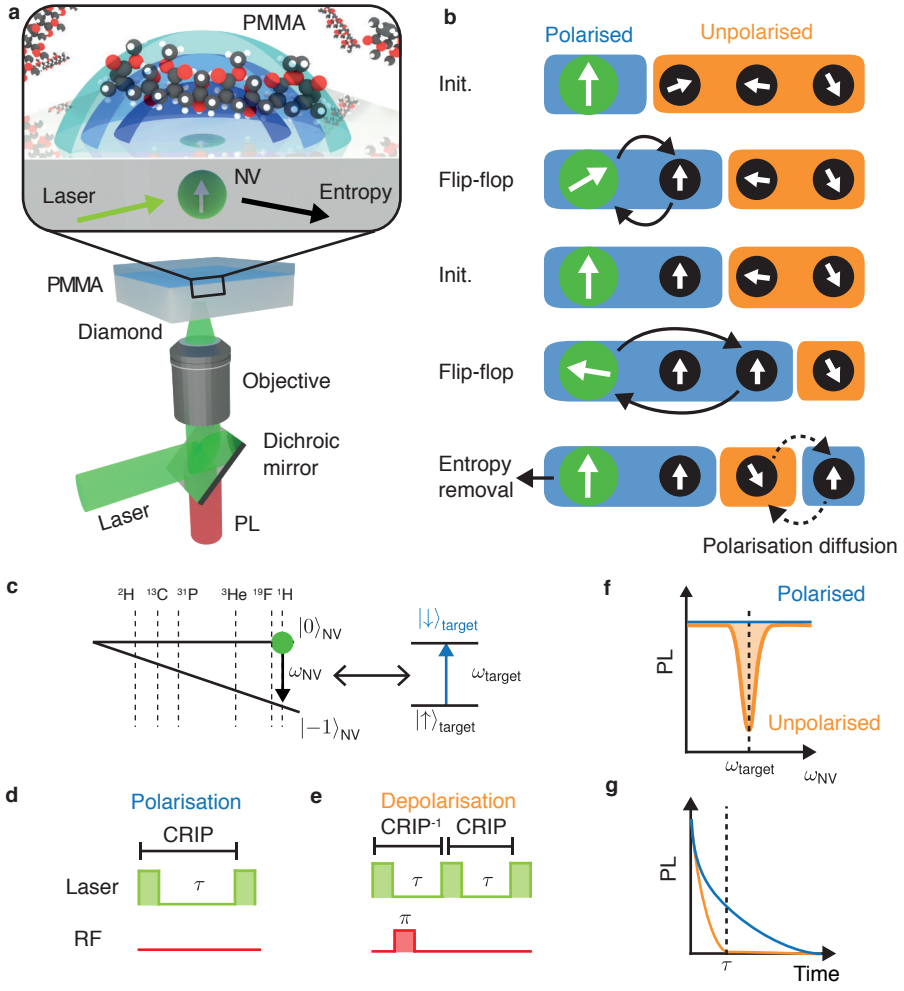

Figure 3.1: CR-based quantum probe hyperpolarisation of nuclear spin ensembles. **a** Schematic of the system showing a near-surface nitrogen-vacancy (NV) spin probe in diamond and a hydrogen nuclear spin target ensemble in molecular Poly(methyl methacrylate) (PMMA) on the surface. The NV probe is initialised by a green laser (532 nm), and read out via its photoluminescence (PL) signal. The shaded blue surfaces denote different regimes of polarisation capabilities arising from the spatial dependence of the nuclear spin coupling to the NV spin. **b** Schematic of cross relaxation induced polarisation (CRIP) implemented on a spin system illustrating the build up of polarisation from repeated application of the CRIP sequence. Diffusion effects act in competition with the CRIP entropy pumping mechanism, but also allow for polarisation at distances beyond that reachable via the hyperfine interaction. **c** Energy-level diagram of the NV (left) showing the relative positions of various target nuclear spins (right) resonance conditions. **d**,**e** The control sequences laser pulses in green, RF pulses in red) used for polarising a target spin ensemble using CRIP (**d**) and for controlled depolarisation using the combined CRIP$^{-1}\times$ CRIP protocol (**e**). **f** Schematic showing the cross-relaxation spectrum obtained by measuring the PL during the CRIP (blue) or depolarisation (orange) sequence with a constant interaction time τ, while scanning the NV frequency ω_{NV}. **g** Similarly, the cross-relaxation curve is obtained by scanning τ with ω_{NV} set at the resonance.

the detuning between the probe and target transition frequencies [113],

$$\Gamma_{\mathrm{CR}} = \frac{A_P^2 \Gamma_2}{2\Gamma_2^2 + 2\left(\omega_{\mathrm{NV}} - \omega_{\mathrm{n}}\right)^2}, \tag{3.2}$$

where A_P^2 is the total effective hyperfine field seen by the NV due to the target spin ensemble, which is related to the polarisation distribution via

$$A_P^2 = \frac{n_{\mathrm{t}}}{2} \int \left[1 - P(\mathbf{R}, t)\right] A^2(\mathbf{R})\, \mathrm{d}^3\mathbf{R}, \tag{3.3}$$

where n_{t} is the density of the target spin ensemble. The key indicator of significant polarisation is therefore a reduction in Γ_{CR}, which manifests as the disappearance of the target ensemble's spectral feature from the cross-relaxation spectrum (Fig. 3.1f), and can be quantified by measuring the cross-relaxation curve at resonance (Fig. 3.1g).

3.1.2 Theoretical description of CRIP protocol

In this section, the general theoretical description of the CRIP protocol from full quantum to a continuum model (Eq. 3.1), which was developed by Liam Hall, has been outlined. This is useful in understanding the procedure and how the theoretical results were calculated.

Hamiltonian of NV-target nuclear spin system

The Hamiltonian of the NV-target nuclear spin system, under the assumption that the external applied magnet field is aligned along the NV axis, is given by

$$\mathcal{H} = 2\pi D \mathcal{S}_z^2 + \gamma_{\mathrm{NV}} B_0 \mathbf{S}_z + \sum_j \left[\mathbf{S} \cdot \mathbf{A}_j \cdot \mathbf{I}_j - \gamma_{\mathrm{n}} B_0 \mathbf{I}_z^{(j)}\right] + \sum_{k>j} \mathbf{I}_j \cdot \mathbf{B}_{jk} \cdot \mathbf{I}_k, \tag{3.4}$$

where $\mathbf{S}_{x,y,z}$ are the Pauli spin matrices of the spin-1 system of the NV, $D = 2.87\,\mathrm{GHz}$ is the corresponding zero-field splitting, B_0 is the external field strength, γ_{NV} and γ_{n} are the gyromagnetic ratios of the NV and target spins, $\mathbf{I}_{x,y,z}^{(j)}$ are the Pauli spin matrices of target spin j, $\mathbf{A}_j$ is the hyperfine tensor describing the spin-spin interaction between the NV and spin-j, $\mathbf{B}_{jk}$ is the tensor describing the magnetic dipole interaction between spins

j and k; and summation over j, k refer to all spins in the spin bath.

Mapping onto a continuum model

To solve Eq. 3.4 for an arbitrary number of target spins, N_{S}, each with a separate hyperfine coupling to the central NV spin, A_j, and with mutual dipole couplings, B_{jk}, we assume a starting density matrix of

$$\rho(0) \quad = \quad (|0\rangle\langle 0|)_{\mathrm{NV}} \bigotimes_j \Big(p_j |\uparrow\rangle\langle\uparrow| + (1-p_j)|\downarrow\rangle\langle\downarrow| \Big)_{\mathrm{t_j}}. \tag{3.5}$$

The population of the NV $|0\rangle$ state is at a minimum when $t = \tau = \frac{\sqrt{2}\pi}{A_0}$, i.e. at the trough of the oscillation given by the coupling strength between the two spins. The affect of hyperfine coupling onto the NV spin population is given by,

$$p_{\mathrm{NV}}(\tau) \quad = \quad 1 - \sum_j \frac{A_j^2}{A_0^2} p_j(0), \tag{3.6}$$

where $A_0^2 \equiv \sum_j A_j^2$ is the total hyperfine coupling field.

Inversely, the change in population of spin j is given by

$$\Delta p_j \quad = \quad -p_j \frac{A_j^2}{A_0^2} - \sum_k (p_j - p_k) \left(\frac{\tau}{2} |B_{jk}| + \frac{C_{jk}^2}{A_0^2} \right), \tag{3.7}$$

where B_{jk} is the magnetic dipole coupling between spins j and k, and $C_{jk}^2 \equiv A_j^2 A_k^2 / A^2$ is the effective hyperfine-mediated diffusion strength.

To correctly model the extent of the influence that central NV spin has on the nuclear spin bath, it is important to extend the spatial region to at least 200 nm in size. Corresponding to $N_{\mathrm{S}} \sim 10^{10}$ number of spins and some $\sim 10^{20}$ different couplings. As a consequence, using the discrete model is computations expensive. To circumvent this dilemma, the discrete model (Eq. 3.7) is mapped onto a temporally and spatially continuous description. These mappings are described in the following text.

Time-dependent probability field. As the regions of polarisation considered in this work are larger than the hyperfine core of the environment, which itself is comprised of

the order of 10^4 spins, instead of considering the time-dependent populations of discrete spins, we instead consider the time-dependent probability field of the environmental spins having an average density, n_{t},

$$p_j \quad \mapsto \quad p\left(\mathbf{R}, t\right). \tag{3.8}$$

In essence, $p\left(\mathbf{R}, t\right)$ is the average probability of spins in an infinitesimal volume at position $\mathbf{R}$ (relative to the NV) being in state $|\uparrow\rangle$ at time t, which can be converted into a polarisation via $P(\mathbf{R}, t) = 1 - 2p(\mathbf{R}, t)$.

Probability field dynamics. In the discrete description, the probability of finding spin j in its $|\uparrow\rangle$ state is monitored at discrete multiples of the optimal interaction time, τ. Ignoring probability diffusion, this would behave as a geometric series. As we are interested in times $t \gg \tau$, we map changes in p_j over time to

$$\Delta p_j \quad \mapsto \quad \tau \frac{\partial}{\partial t} p\left(\mathbf{R}, t\right) \tag{3.9}$$

Hyperfine coupling field. As with the population field, we also map the discrete hyperfine couplings to a continuous field whose strength is determined by its position relative to the NV, $\mathbf{R}$.

$$A_j \quad \mapsto \quad A\left(\mathbf{R}\right). \tag{3.10}$$

Total hyperfine coupling strength. The summation over all hyperfine couplings is mapped to an integral,

$$A_0^2 \quad \mapsto \quad n_{\mathrm{t}} \int A^2\left(\mathbf{R}\right) \, \mathrm{d}^3\mathbf{R}. \tag{3.11}$$

Probability diffusion. We put $p_j \mapsto p\left(\mathbf{R}, t\right)$ and $p_k \mapsto p\left(\mathbf{R} + \mathbf{r}, t\right)$, and discretise the Laplacian operator to get

$$\sum_k \left(p_j - p_k\right) B_{jk} \quad \mapsto \quad \langle r \rangle^2 \sqrt{\langle B^2 \rangle} \nabla^2 p\left(\mathbf{R}, t\right). \tag{3.12}$$

Additional sources of relaxation. To account for additional sources of environmental spin-lattice relaxation, where applicable, we add an additional probability sink in which any probability outside equilibrium decays at a rate $\Gamma_{\mathrm{SL}} = \frac{1}{T_{\mathrm{SL}}}$, whose rate is given by

$$R_{\mathrm{SL}} = -\Gamma_{\mathrm{SL}} \left(p\left(\mathbf{R}, t\right) - \frac{1}{2} \right). \tag{3.13}$$

The differential equation describing the evolution of this system is thus given by

$$\begin{aligned} \frac{\partial}{\partial t} p\left(\mathbf{R}, t\right) = & -u(\mathbf{R}) p\left(\mathbf{R}, t\right) + \beta \nabla^2 p(\mathbf{R}, t) \\ & - \Gamma_{\mathrm{SL}} \left(p\left(\mathbf{R}, t\right) - \frac{1}{2} \right), \end{aligned} \tag{3.14}$$

where

$$u(\mathbf{R}) = \frac{A^2(\mathbf{R})}{\tau A_0^2} \tag{3.15}$$

is the effective source, or cooling, coefficient at position $\mathbf{R}$ relative to the NV, and

$$\beta = \frac{1}{2} \langle r \rangle^2 \sqrt{\langle B^2 \rangle} \tag{3.16}$$

is the effective probability diffusion coefficient related to the intra-bath interactions B_{jk}. Recasting Eq. 3.14 in terms of the polarisation $P(\mathbf{R}, t) = 1 - 2p(\mathbf{R}, t)$, we gives Eq. 3.1.

For cases in which the dephasing rate of the NV spin, Γ_2, is greater than the hyperfine coupling to the desired target, i.e. $\Gamma_2 \gg A_0$, the population of $|0\rangle$ state of the NV spin will exhibit an exponential time dependence. As such, for this regime we instead make the replacement

$$u\left(\mathbf{R}\right) = \frac{A^2(\mathbf{R})}{2\Gamma_2}. \tag{3.17}$$

Experimentally, Γ_2 is obtained via the T_1-relaxometry spectrum (with the interleaved sequence), since Γ_2 defines the width of the cross-relaxation resonances [113]. We note that Γ_2 is expected to decrease upon polarisation of the ^{13}C bath, see section 3.1.4 for details. However, the effect is relatively small, and as such in the calculations kept Γ_2 constant and equal to the unpolarised case. For the ^{1}H case, the dephasing is dominated by surface effects, and is therefore unaffected by the ^{1}H polarisation.

Upon solution of Eq. 3.14 for the probability field $p(\mathbf{R}, t)$ at some time, t, or equivalently the polarisation $P(\mathbf{R}, t)$, we may determine the total number of spins polarised at time t:

$$N_{\mathrm{pol}}(t) \equiv n_{\mathrm{t}} \int P(\mathbf{R}, t)\, \mathrm{d}^3\mathbf{R}. \tag{3.18}$$

3.1.3 Polarisation of internal ^{13}C spins

With the theoretical description developed we next turn to the experimental demonstration of the technique. The experimental apparatus consists of a custom-built confocal microscope and a permanent magnet mounted on a scanning stage, the same setup used, and described, in chapter 2. Experimentally, we first demonstrate our technique on the inherent 1.1% ^{13}C spin ensemble surrounding a NV probe in the diamond substrate by tuning to the ^{13}C resonant condition at $B_*(^{13}\mathrm{C}) = 1024.9$ G. Comparison of the cross-relaxation spectra for CRIP and depolarisation sequences (Fig. 3.2a) shows the complete removal of the ^{13}C resonance peak for interaction times of $\tau = 4$ μs, indicating efficient polarisation of the nearest spins, as compared with the target prepared using the depolarising sequence. This is confirmed in the cross-relaxation curves as a function τ (Fig. 3.2b, inset), where the polarised case shows no evolution of the NV spin state, while the unpolarised case shows coherent flip-flops between the NV and the ^{13}C spins.

To investigate the extent of the polarisation effect, we increase the interaction time τ so as to be sensitive to more remote ^{13}C spins, up to the limit set by the NV centre's intrinsic spin-phonon relaxation rate, $\Gamma_{\mathrm{bg}} \approx 200$ ms^{-1}. The resulting cross-relaxation curves obtained at the ^{13}C resonance using the CRIP and depolarisation sequences are shown in Fig. 3.2b, from which we extract the total relaxation rate, Γ_{tot}. By subtracting Γ_{bg} obtained from the off-resonance relaxation curve (Fig. 3.2b, green data), we deduce the ^{13}C-induced relaxation rate $\Gamma_{\mathrm{CR}} = \Gamma_{\mathrm{tot}} - \Gamma_{\mathrm{bg}}$, which decreases from $\Gamma_{\mathrm{CR}}^{\mathrm{unpol}} \approx 250$ ms^{-1} with the depolarisation sequence, to below the noise floor of the measurement after 5 hours of CRIP, $\Gamma_{\mathrm{CR}}^{\mathrm{pol}} \lesssim 19$ s^{-1}. We use Eq. (3.1) (with $\beta = 0.0335$ nm^{2}s^{-1} corresponding to the given ^{13}C density) to calculate the time-dependence of the radial polarisation profile for total polarisation times of 1-10^6 s, as depicted in Fig. 3.2c. By relating the spatial

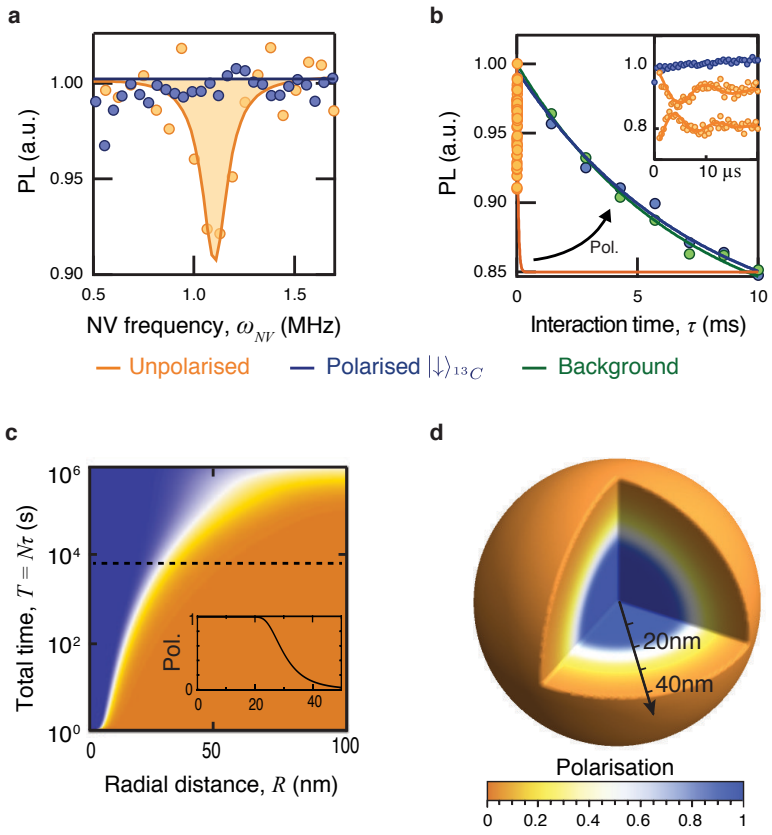

Figure 3.2: Cross-relaxation induced polarisation of ^{13}C spins in diamond. a Cross-relaxation spectra of a single NV spin near the ^{13}C resonance ($\omega_{\mathrm{NV}} = 1.1$ MHz), obtained with an interaction time $\tau = 4$ μs using the CRIP sequence (blue) and the depolarisation sequence (orange, only the readout following the NV initialisation in $|0\rangle$ is shown). Sequences were repeated $N = 10^5$ times at each point. **b** Cross-relaxation curves obtained by increasing τ at the ^{13}C resonance with the CRIP sequence (blue) and depolarisation sequence (orange), and off-resonance to obtain the background relaxation curve (green). Zoom-in at short times for the polarised (blue) and unpolarised case (orange, top and bottom curves correspond to the NV initialised in $|0\rangle$ and $|-1\rangle$, respectively). **c** Calculated radial polarisation profiles relative to the NV spin (averaged over all angles), calculated from Eq. (1) for a random 1.1% ^{13}C spin ensemble for varying total polarisation times, $T = N\tau$. Inset: profile along dashed line, corresponding to $T = 2$ h. **d** Three-dimensional representation of the polarisation distribution at $T = 2$ h.

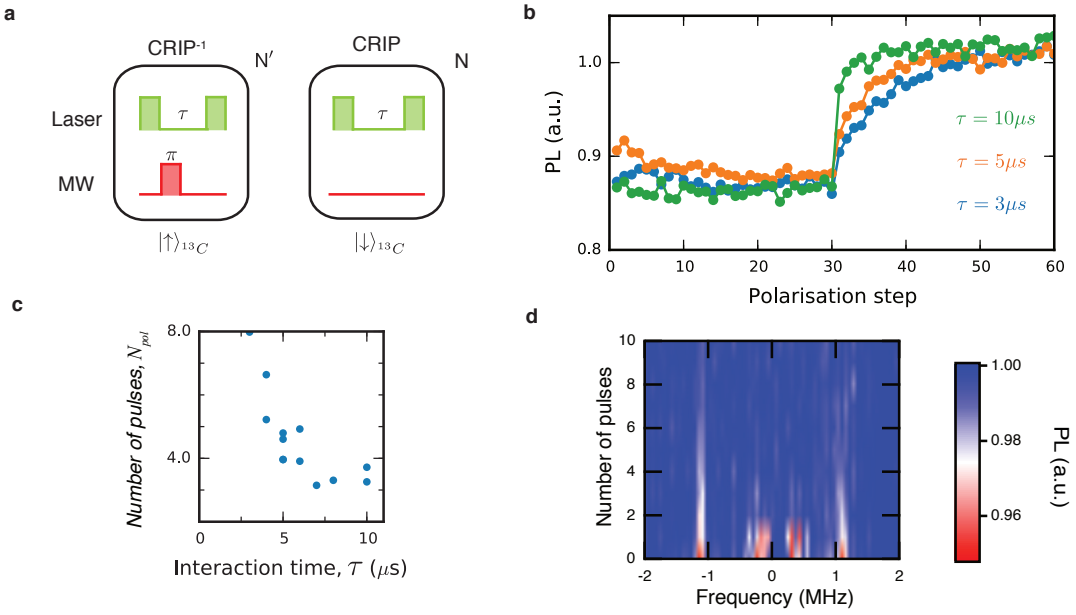

Figure 3.3: ^{13}C polarisation dynamics. **a** Pulse sequence used to investigate the polarisation dynamics. **b** Full sequence of 30 CRIP^{-1} pulses followed by 30 CRIP as shown in **a**, for different interaction times τ. **c** Characteristic time for polarisation as a function of interaction time. **d** T_1-relaxometry spectrum across the GSLAC, as a function of CRIP pulse number, obtained using the sequence shown in **a** with a fixed total number of CRIP and CRIP^{-1} pulses ($N' = N = 30$). The interaction time was 3 μs. Negative frequency denotes past the GSLAC.

polarisation distribution, $P(\mathbf{R}, t)$, to the cross-relaxation rate, Γ_{CR}, via Eq. (3.2), we find the theoretical results are consistent with the experiment for polarisation times in excess of two hours (Fig. 3.2c, dashed line). Examination of the spatial polarisation distribution (Fig. 3.2c, inset, and Fig. 3.2d) implies a polarisation level of more than 99% within 21 nm of the NV, equating to a 6×10^6-fold increase on thermal polarisation for some 3×10^5 spins.

^{13}C polarisation dynamics

It is also important to characterise the rate of polarisation. In order to do this, we initially polarise the bath in one direction then measure the rate of polarisation in the other direction. Precisely, a series of $N = 30$ laser pulses were applied with a π-pulse (i.e. CRIP^{-1}), which produces a spin bath in the $|\uparrow\rangle$ state. This is followed by N pulses without the π-pulse (i.e. CRIP) producing a polarisation in the opposing direction, i.e.

$|\downarrow\rangle$ state (Fig. 3.3a). The PL readout for each laser pulse as a function of pulse number for three interaction times $\tau = 3, 5, 10\,\mu$s is shown in Fig. 3.3b. The resulting polarisation curves were fitted with exponentials ($\mathrm{PL} = a\exp(N/N_{\mathrm{pol}}) + b$) in order to determine the characteristic polarisation time, $T_{\mathrm{pol}} = N_{\mathrm{pol}}\tau$ (Fig. 3.3c). It is important to note that due to the relatively short interaction time used in these measurements, the contrast obtained is dominated by the few nearest spins and is therefore an indication of the rate of polarisation for nearby ^{13}C spins, which results in an efficiently polarised bath after a few tens of μs.

Finally, in order to test the sequence robustness to frequency variation (change in resonance position) we performed a magnetic sweep across both resonances and the GSLAC, shown in Fig. 3.3d. This presents four features, two related to ^{13}C (outside peaks) and two to the GSLAC (inside peaks). The polarisation region width is roughly 0.1 - 0.2 MHz, which is governed by the T_2^* of the NV spin. Additionally, the number of pulses required to polarise the nearest ^{13}C spins is different for the different sides of the GSLAC. This is due to the different hyperfine coupling strengths of the two resonance conditions, see section 3.3 for details.

3.1.4 Effect of ^{13}C polarisation on NV spin coherence

As the limiting factor of the dephasing time of the NV spin (T_2^*) is noise from the ^{13}C bath (for the deep NVs considered here), it is expected that polarisation of the ^{13}C spins will result in an increase in the T_2^* of the NV. This effect was observed in previous works that employed a Hartmann-Hahn resonance to transfer polarisation [29, 107]. To measure T_2^*, one usually performs a free induction decay (FID, or Ramsey) experiment. However, such a measurement cannot be done at the cross-relaxation resonance because it would interfere with the flip-flop dynamics of the NV-^{13}C interaction. A solution is to polarise the bath at the resonant field then quickly shift the field to off the resonance and perform the T_2^* measurement, following the sequence shown in Fig. 3.4a. To implement this, a coil was attached to the board holding the diamond (schematic shown in Fig. 3.4b). A TTL pulse was used to generate a DC field from the coil to act as a quick field switching mechanism, allowing the polarisation to occur at the resonance frequency and the

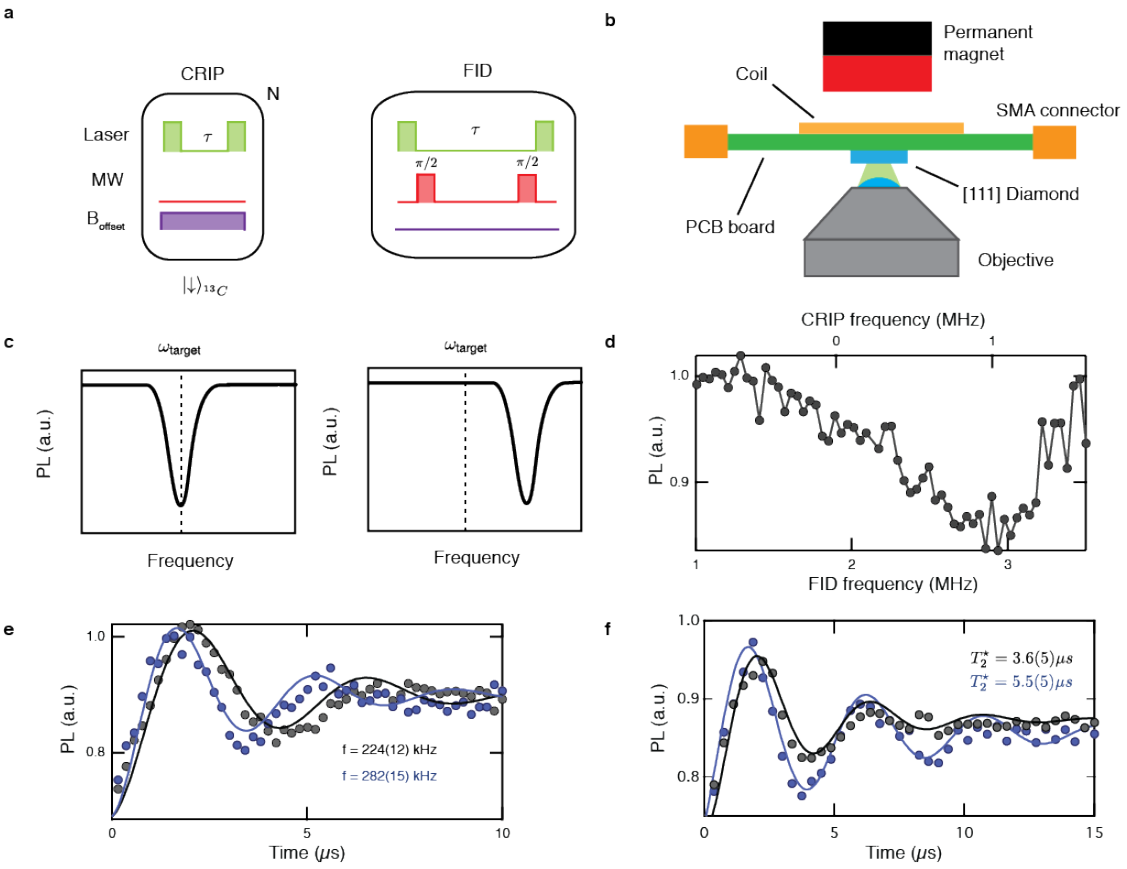

Figure 3.4: Effect of ^{13}C polarisation on the free induction decay. **a** Pulse sequence for CRIP polarisation at the resonant frequency followed by an FID measurement at a different frequency, using a magnetic field offset pulse. **b** Schematic of the experimental set up with the coil for the field offset. **c** Example ODMR of the NV during the CRIP phase (left) and during FID measurements (right). **d** FID signal as a function of NV frequency as measured during the CRIP phase (top axis) and during the FID phase (bottom axis). The FID wait time is $\tau = 4$ μs. A detuning of 0.2 MHz was applied when driving the NV in the FID measurement. **e** FID curves obtained from a similar sweep as in **d**. The two curves show the case where the CRIP phase is on resonance (blue, polarisation) and off resonance (black, no polarisation). **f** Long FID measurement taken at a fixed frequency with the CRIP phase on resonance (blue, polarisation) and off resonance (black, no polarisation). The applied driving detuning was different in the two case in order to obtain the same oscillation frequency.

measurement to be performed at another frequency, as illustrated by the ODMR spectra shown in Fig. 3.4c. The field offset thus applied was $B_{\mathbf{offset}} \approx 0.7$ G, turned on while a series of polarisation pulses was implemented. The offset was then turned off and the FID measurement performed.

We first performed a single-τ FID measurement as a function of the magnetic field, across the ^{13}C resonance (after GSLAC). The resulting spectrum is shown in Fig. 3.4d, where ω_{NV} (measured by an ODMR spectrum at each magnet position) was scanned from -1.0 MHz to 1.5 MHz during the CRIP polarisation phase (with the field offset on), corresponding to 1 MHz to 3.5 MHz during the FID measurement (field offset off). For the polarisation phase, we used $N = 10$ CRIP pulses, and for the FID we used $\tau = 4$ μs, and a driving frequency detuned by 0.2 MHz from the NV frequency so as to induce an oscillation in the FID response. The CRIP+FID sequence is repeated many times at each magnet position, so that the ^{13}C bath should be efficiently polarised when on resonance. The data reveals a feature centred on the NV-^{13}C resonance, i.e. when $\omega_{\mathrm{NV}} = 1.1$ MHz during the polarisation phase. To interpret this feature, we measured full-length FID curves while scanning the magnetic field. Fig. 3.4e shows the resulting curves with the CRIP at the resonance or off the resonance. The main difference between the two FID curves is in the frequency of the oscillation, which differ from each other by 58(27) kHz. This difference is attributed to a change in the DC magnetic field seen by the NV, induced by polarisation of the nearest ^{13}C spins. However, the envelope of the oscillation shows a similar decay time (T_2^*) in both cases, which means the ^{13}C polarisation was not sufficient to significantly reduce the magnetic noise seen by the NV. To increase the extent of the ^{13}C polarisation, we performed a longer measurement at just two fixed frequencies, on and off resonance. In addition, we adjusted the driving frequency detuning such that the FID oscillation showed the same frequency with and without polarisation, for ease of comparison. The results are shown in Fig. 3.4d, and reveal a $\sim$50% increase of T_2^* from 3.6(5) μs to 5.5(5) μs upon polarisation, similar to previous results with Hartmann-Hahn based polarisation [29, 107]. The improvement is limited by the magnetic field stability during CRIP, as the switching introduces a time dynamic in the NV probing frequency, limiting the time on resonance.

An alternative way to probe a change in T_2^* is by examining the resonance feature

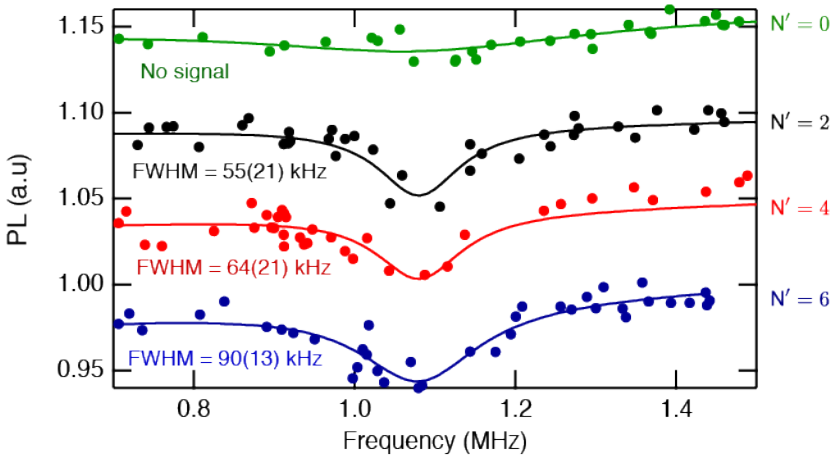

Figure 3.5: Effect of ^{13}C polarisation on the resonance linewidth. The graph shows the ^{13}C spectrum under the sequence shown in Fig. 3.3a, with $N = 10$ and $N' = 0, 2, 4, 6$, from top to bottom, with an interaction time is $\tau = 5$ μs. A trend is found from fitting the signal with a Lorentzian (solid line): indicating an increase in the feature width for less polarised spin baths, i.e. larger N'.

width in the T_1-relaxometry spectrum, since it is directly given by the dephasing rate $1/T_2^*$ [113]. To test this, we implemented the sequence of Fig. 3.3a, with $N = 10$ and a varying number of CRIP^{-1} pulses, N'. The results are shown in Fig. 3.5. When $N' = 0$, there is no signal as the ^{13}C bath is polarised. As N' is increased, the feature width increase from 55(12) kHz for $N' = 2$ to 90(13) kHz for $N' = 6$, where no difference was observed for larger values of N'. The FWHM was extracted from a Lorentzian fit with a slight linear background to account for the tail of the GSLAC feature. This result agrees with the direct FID measurement, that is, polarisation of the ^{13}C spin bath results in a slight increase in the T_2^* of the NV spin.

3.1.5 Polarisation of external ^{1}H spins

With the basic protocol established, we now move to the polarisation of molecular ^{1}H nuclear spins external to the diamond crystal. A solution of poly(methyl methacrylate), PMMA, was applied directly to a diamond surface [115] with single NV spin probes located 8-12 nm below the surface. The initial criteria for finding suitable NVs involved finding a trade-off between maximising the NV-H coupling (shallow), and minimising the coupling to sparse electronic surface defects (deep) which limit the NV linewidth and the background

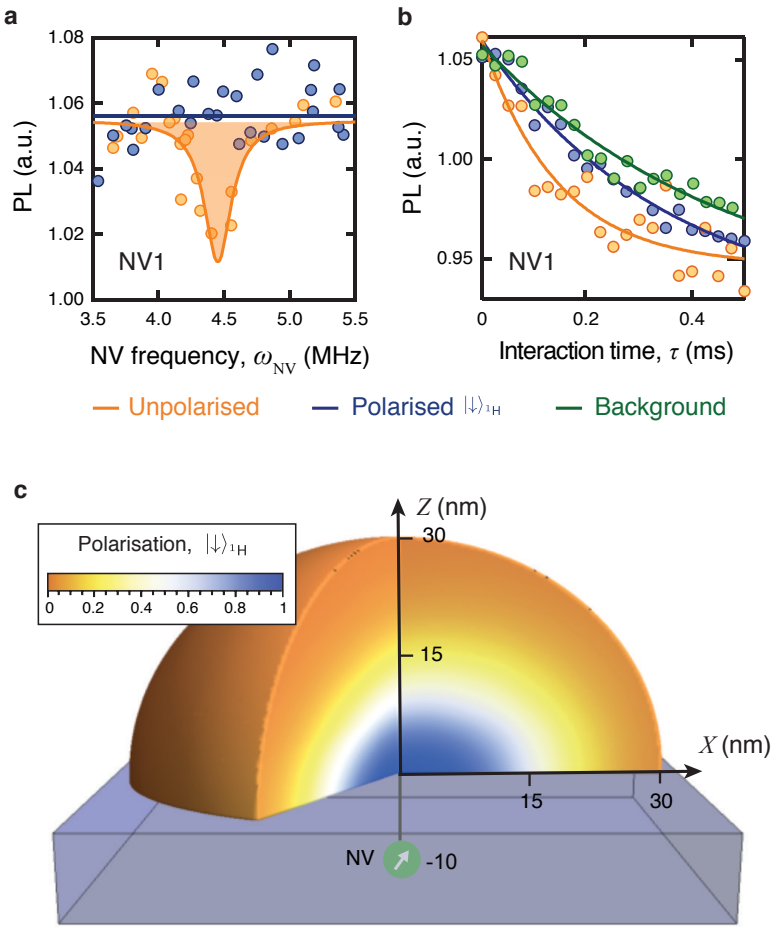

Figure 3.6: Polarisation of external molecular ^{1}H spins. **a** Cross-relaxation spectra near the ^{1}H resonance ($\omega_{NV} = 4.4$ MHz), for a single NV spin located 10 nm below a PMMA layer, obtained using $\tau = 20$ μs and $N = 10^5$ with the CRIP sequence (blue) and the depolarisation sequence (orange). **b** Cross-relaxation curves obtained by increasing τ at the ^{1}H resonance with the CRIP sequence (blue) and depolarisation sequence (orange), and off-resonance to obtain the background relaxation rate (green). **c** Three-dimensional representation of the ^{1}H spin polarisation distribution in PMMA on the surface of a diamond (blue block), calculated from Eq. (3.1) in the steady state. This figure is adapted from Ref. [184].

T_1 time. The surface is also known to retain a 1-2 nm thick layer of protons of density commensurate with that of PMMA [131], which we therefore regard as being part of the target proton system to be polarised.

The CRIP sequence was applied with the external magnetic field tuned to resonance at $B_*(^1\mathrm{H}) = 1026.2$ G. Application of the CRIP sequence to NV1 for $\tau = 20\,\mu$s (Fig. 3.6a) shows the removal of the hydrogen spectral feature (blue), as compared with the depolarising sequence (orange). From the cross-relaxation curves after 1 hour of CRIP (Fig. 3.6b), we extract ^{1}H-induced rates for the unpolarised ($\Gamma_{\mathrm{CR}}^{\mathrm{unpol}}$) and polarised ($\Gamma_{\mathrm{CR}}^{\mathrm{pol}}$) PMMA ^{1}H spin ensembles to be 2.71 ms^{-1} and 0.96 ms^{-1}, respectively. With a much higher diffusion constant and spin-lattice relaxation rate ($\beta = 781$ nm$^2 s^{-1}$, $\Gamma_{\mathrm{SL}} = 1\mathrm{s}^{-1}$ [185]) relative to the intrinsic ^{13}C case, the ^{1}H system is expected to effectively reaches steady-state within a few seconds, which is compatible with the measurement time. The ratio $\Gamma_{\mathrm{CR}}^{\mathrm{unpol}}/\Gamma_{\mathrm{CR}}^{\mathrm{pol}} = 2.8(3)$ (consistent with the value of 2.4(3) obtained using another NV), is in good agreement with the solution to Eq. 3.1 for the PMMA ensemble, which gives a ratio of 2.2 in the steady state. The corresponding spatial polarisation distribution is shown in Fig. 3.6c, indicating that the system reaches 50% average polarisation over a volume of approximately (26 nm)^3. Thus, we conclude that the single NV has increased the average polarisation of roughly a million hydrogen spins by six orders of magnitude over the room temperature Boltzmann thermal background.

Similar results were observed on two different NV spins, NV2 and NV3, with PMMA (Fig. 3.7a,b). However, current limitations in near surface NV charge state stability leads to single NV spins being lost before a full measurement suite could be performed. In order to eliminate false positives in these measures due to changes in the local magnetic environment we utilised the following suite of measures in order: background - depolarisation - polarisation - background. Unless the two background relaxation rates matched, we excluded that NV from the data pool. This lead to many NV spins that exhibited a faster relaxation time when depolarised compared to the polarised case but were not consistent in the background rate. However, we never observed the opposite, that is, we did not observe a condition where the polarised signal had a faster relaxation rate than the depolarised signal. While this is a promising condition we conclude that additional work is required in order to create stable near surface NV spin, allowing consistent hyperpolarisation and

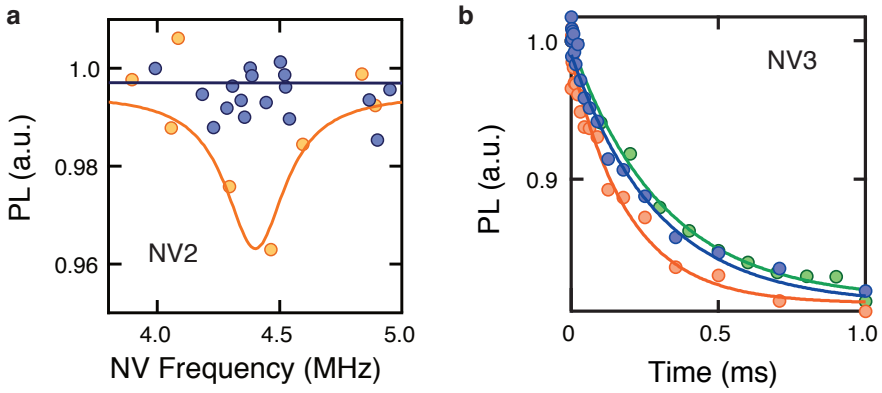

Figure 3.7: Polarisation of external molecular ^{1}H spins for additional NV spin a Cross-relaxation spectra near the ^{1}H resonance ($\omega_{NV} = 4.4$ MHz), for a single NV spin (NV2), obtained using $\tau = 20$ μs and $N = 10^5$ with the CRIP (blue) and the depolarisation sequence (orange). **b** Cross-relaxation curves for a single NV spin (NV3) obtained by increasing τ at the ^{1}H resonance with the CRIP sequence (blue) and depolarisation sequence (orange), and off-resonance to obtain the background relaxation rate (green).

readout.

3.1.6 Improvements and scale-up

There is scope for improvement on these proof-of-concept results: for example, engineering NV depths to 5 nm would increase the rate of target spin polarisation by an order of magnitude, and improvements in the inherent NV dephasing rate Γ_2 (e.g. via improved surface properties) will allow for more precise tuning to different nuclear spin species. As the protocol is all optical, scaling up for high-volume production could be achieved by stacking multiple NV arrays (Fig. 3.8a) and/or increasing the effective interaction area via surface patterning [130], however, issues such as the creation and control of homogeneous DC magnetic fields over the spatial extent of the ensemble are ongoing endeavours that are beyond the scope of the work presented here.

The results presented here indicate that the CRIP protocol could produce macroscopic quantities of MRI contrast agents with high polarisation levels. For example, we consider ^{13}C isotopically enriched HEP (hydroxyethyl propionate, $^{13}C_5H_{10}O_3$), a well-known MRI contrast agent [35]. Using a single hyperpolarisation cell comprised of two

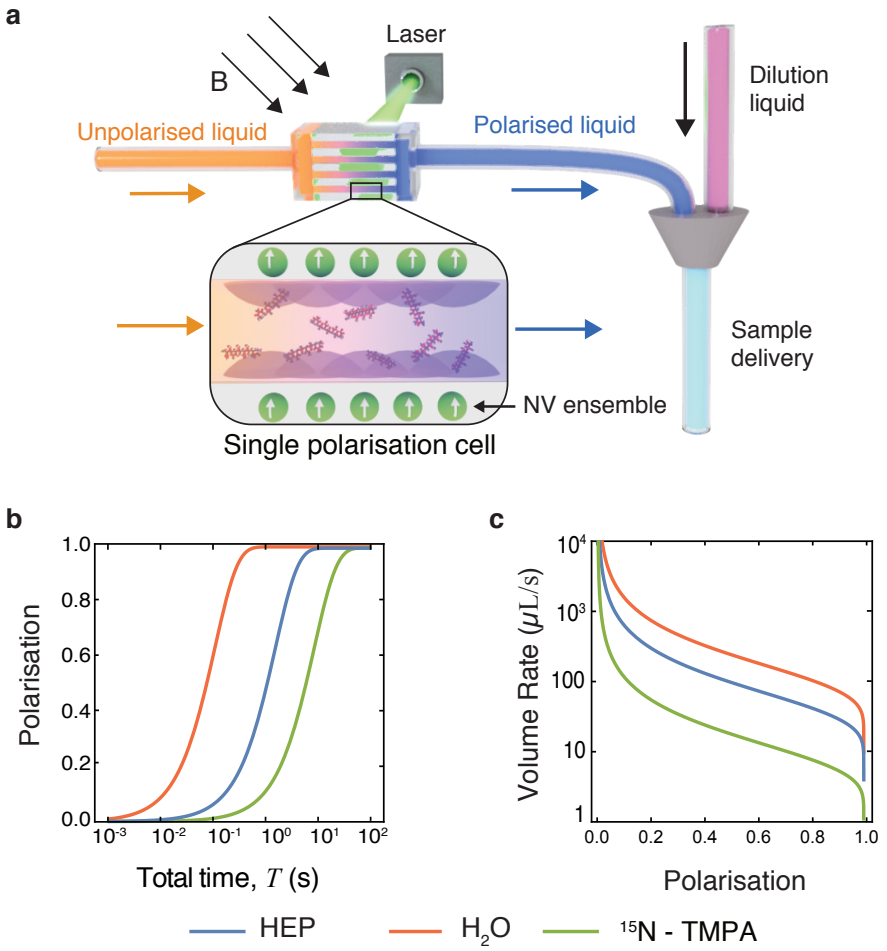

Figure 3.8: Proposal for an universal MRI contrast agent hyperpolarisation platform. **a** Schematic of a quantum polarisation stack comprising multiple diamond membranes, each containing NV array layers on both sides, in a homogeneous magnetic field tuned to the nuclear gyromagnetic ratio of the target agent spin species. The unpolarised agent in concentrated solution (orange) flows into the stack channels, where the liquid is polarised through the application of CRIP (via a pulsed laser). The out-flowing polarised liquid (blue) is then diluted for use. Zoomed schematic shows a single polarisation cell comprising a channel formed by dual diamond membranes each with a near-surface NV layer. **b** Average polarisation level from a single polarisation cell, for various targets (HEP, H_2O, and ^{15}N-TMPA), calculated for varying polarisation times assuming perfect mixing of a 1 M target agent solution with a cell height of 1 μm. There is a correction in the x-axis title from the original published paper [33], where the unit was incorrectly labelled as milliseconds instead of seconds. **c** Outflow rate (after dilution to 1mM for application delivery) from 10 polarisation cells at different levels of polarisation.

NV arrays in diamond membranes separated by 1 μm (see zoomed schematic in Fig. 3.8a; we assume an NV density of $4{\times}10^{11}$ cm^{-2} over a 4 mm $\times$ 4 mm diamond surface [149]), the rate of polarisation transfer to a concentrated 1M precursor HEP solution is 4 μL s^{-1} at a polarisation level of 80%. The polarisation levels for different contrast agents in 1M precursor solutions are plotted against polarisation time (assuming perfect mixing occurs over these timescales) in Fig. 3.8b. In Fig. 3.8c, we plot the final delivery rate after dilution to 1 mM for a stack of 10 cells, showing that delivery rates of order 100 μL s^{-1} for clinical applications [186] are achievable.

The degree of polarisation is determined by both the coupling strength to the NV spin (high gyromagnetic ratio means a higher polarisation rate) and the diffusion rate (defined by the interaction strength between the target nuclear spins). In contrast agents the diffusion rate is often slow to increase the polarisation lifetime, so ideally to get better rate the coupling strength between the NV spin and target needs to be enhanced. If the target spins experience a hyperfine coupling then this strength can be increase through hyperfine mediated transitions. As a consequence, new types of MRI contrast agents could be developed that involve an encapsulated central electron spin that is surrounded by nuclear spins. This type of molecular electron-nuclear spin contrast agent could dramatically enhance the uses of hyperpolarisation platforms that take advantage of electron to nuclear spin-transfer but would come at the cost of polarisation lifetime.

3.2 Thermo-magnetic field control

One of the great advantages of the NV spin is its capability to operate at room temperature. Whilst this avails many applications of the NV spin to systems that require room temperature, it also plagues the NV with concerns about variations in the ambient room conditions. One issue is how the magnetic field from permanent magnetics depends on temperature. In the previous section on hyperpolarisation, the measurements were post processed in order to remove magnet drift. While this processing can be implemented in order to minimise false signal, there are many instances where it is far more advantageous to have a stable qubit of which producing hyperpolarised spin is a prime example.

In this section, we use the temperature dependence of the field strength in a permanent magnet as a way to control and stabilise the magnetic field in our single-NV experiments. We first demonstrate that active control of the magnet temperature allows the B field to be scanned in a range sufficient for CR spectroscopy, as we illustrate by recording CR spectra of both electron and nuclear spins. Next we consider the long term stability of the NV frequency from room temperature variations and show that the resulting fluctuations can be mitigated via this active temperature control. Finally, we take advantage of this newly obtained long term stability to investigate the polarisation and depolarisation dynamics of the ^{13}C nuclear spin bath via cross relaxation induced polarisation (CRIP), which garners valuable information about the evolution of polarised spin baths during NV dark periods.

3.2.1 Temperature controlled permanent magnet

Most applications of the NV spin, either for quantum information or sensing, require control over the spin sub-levels such that the frequency can be modulated to the desired value and that it will remain stable at this frequency during the experiment. Typically, this control is achieved by a permanent magnet that varies the applied magnetic fields over a range of $B = 0 - 0.4$ T [64]. While electromagnets may offer a similar range, they introduce additional complexities in the experimental apparatus that detracts from the generally simple setup. Additionally, the majority of such magnets are bulky and therefore incompatible with most standard confocal microscopes. While permanent magnets can

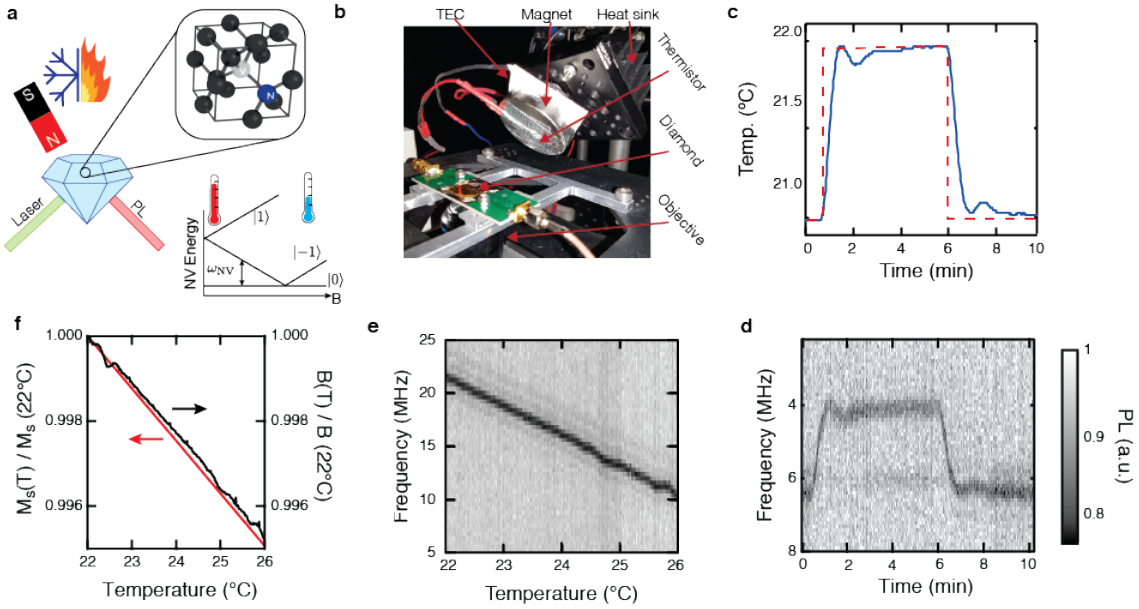

Figure 3.9: Temperature controlled permanent magnet scheme. **a** Depiction of a nitrogen-vacancy (NV) centre in diamond excited with a green laser and subject to the field produced by a temperature controlled magnet. The NV state is read out via the red photoluminescence (PL). The NV $|\pm 1\rangle$ states are split by the magnetic field applied along the quantization axis, where the magnet produces less field at hotter temperatures. **b** Picture of the magnet attached to a TEC module. **c** Step function in the set temperature (red dashed line) and the corresponding thermistor temperature reading (blue). **d** Corresponding optically detected magnetic resonance (ODMR) map from a single NV centre during the temperature pulse showing the $|0\rangle \rightarrow |-1\rangle$ spin transition with a background field $B \sim 1020$ G. **e** ODMR mapped as a function of the set temperature. **f** Black curve: relative change in magnetic field B vs temperature, as extracted from **e** using the relationship $\omega_N V = D - \gamma_e B$, giving a temperature coefficient of $\alpha_0 = -0.094\%/°\text{C}$. Red curve: relative change in magnetisation M_s vs temperature, as calculated from the specified temperature coefficient of our magnet ($\alpha_0 = -0.12 \pm 0.1\%/°\text{C}$). Both plots are normalised by their respective values at $T = 22°\text{C}$.

be easily implemented they also introduce two problems. First, adjusting the magnetic filed strength requires physical movement [110, 111, 113, 149, 184, 187], which can be introduced through motorised or piezoelectric translational stages but can significantly limit the magnetic field strength precision. Second, while the NV spin is relatively insensitive to small environmental temperature variations the magnet is not. The magnetisation of a permanent magnet is temperature dependent and quite often experiences a sharp gradient around room temperature. As a consequence, without adequate temperature control over long measurements the main source of experimental error in tuned cross relaxation experiments can become the magnetisation stability [103]. The instability of the magnet can then limit the resolution and efficiency of many techniques.

The applied magnetic field strength introduces a Zeeman effect in the NV spin, splitting the degenerate states allowing tuning to arbitrary frequencies (as previously discussed in chapter 2.1). Here the magnetic strength is controlled through varying the temperature of a magnet, which results in a change in the magnetisation (Fig. 3.9a). The temperature control is conducted by attaching a thermoelectric cooler (TEC) with a temperature feedback sensor (thermistor) attached to the opposite side (Fig. 3.9b). This feedback was passed to a controller (TE technology TC-720) for proportional integral derivative (PID) control with Ziegler-Nichols method tuning. The magnet is a 50 mm $\times$ 12.5 mm grade N38 neodymium (NdFeB) disc with a NiCuNi coating (AMF Magnetics). The specified temperature coefficient of the magnetisation M_s around room temperature is $\alpha_0 = \partial M_s/\partial T = -0.12 \pm 0.1\%/^{\circ}\text{C}$ with a Curie temperature of 310-370°C.

To test the ability to control the magnet temperature, a 1°C step function was applied about ambient conditions (Fig. 3.9c, red dashed line) using the PID controller, to measure the thermal settling time of the magnet. Given the physical dimensions of the magnet, the thermal settling time for this modest temperature change (blue) is considerable (several minutes). For smaller temperature changes, in the regime $< 0.2^{\circ}$C, the settling time reduces to $<$ 1 minute. Performing an ODMR sweep every 10 s during the temperature change shows a direct correlation between the NV frequency ω_{NV} and the measured temperature of the permanent magnet, see Fig. 3.9d. Here, the 1°C change in temperature translates into a change of 2.5 MHz in ω_{NV} at a field of $B \sim 1020$ G (i.e. $\gamma_e B \sim 2860$ MHz). Mapping the NV frequency response to a ramp in temperature

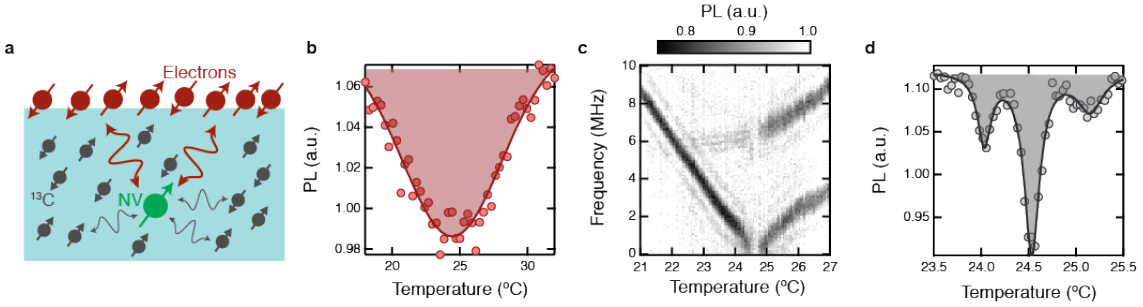

Figure 3.10: CR-spectroscopy via temperature scanning. **a** Depiction of the NV sensing external electrons (red) and internal ^{13}C spins (dark grey). **b** CR spectrum ($\tau = 100$ μs) across the frequency range $\omega_{\mathrm{NV}} = 1426-1445$ MHz (via temperature scanning between 18 and 32°C), showing a peak corresponding to unpaired electrons ($g = 2$). (c) ^{14}NV hyperfine structure across the GSLAC as mapped by temperature scanned ODMR. **d** CR spectrum ($\tau = 2$ μs) across the GSLAC (ω_{NV} varied from -2 to 2 MHz), where the two outer peaks correspond to ^{13}C spins. In (d), the measurement sequence alternates initialisation of the NV in $|0\rangle$ and $|-1\rangle$ before the free evolution time (see Fig. 4a(i)), to prevent net polarisation transfer to the ^{13}C bath [184]. The data shown is the readout following initialisation in $|0\rangle$ only.

(Fig. 3.9e), showed a linear response that is quantitatively consistent with the magnet specifications (Fig. 3.9f). This response demonstrates a magnetic field scanning range of 0.5% via varying the magnet temperature by only 4°C (i.e. from 22 to 26°C), which corresponds to a 10 MHz range at $B \sim 1020$ G (Fig. 3.9e). With temperature variations up to 100°C achievable with standard TECs, magnetic variation up to 12.5% (i.e. ~ 120 G in the magnetic range used in Fig. 3.9e) may be achieved, which is sufficient to detect the spectra of electron-nuclear coupled systems with a large hyperfine splitting [110]. On the other hand, the smallest temperature step size achievable with our current setup is 0.01°C, corresponding to a change of 26 kHz. This is a two-fold improvement over the resolution achieved in previous works using motorised translation stages [103,110], which are capable of a 400-nm axial step size or 65 kHz around the ground state level anti-crossing (GSLAC) [161].

3.2.2 CR-spectroscopy via temperature scanning

The use of temperature enabled magnetic field scanning can be used to perform CR spectroscopy, which is demonstrated here on a single NV spin and has been previously demonstrated by Mamin et al [188]. First the technique is demonstrated on a target of

electronic spins located on the diamond surface (Fig. 3.10a, red). To this end, we use a near-surface NV centre ($\sim 5-10$ nm deep [111]), and a permanent magnet fixed such that $B \sim 512$ G. The magnet temperature is then controlled to finely scan B across the free electron resonance $\omega_{\mathrm{NV}} = \gamma_e B = 1435$ MHz. Fig. 3.10b shows the spectrum obtained by measuring the PL intensity I_{NV} following a free evolution time $\tau = 100$ μs, which maps changes in the T_1 time as $I_{\mathrm{NV}} \propto \exp(-\tau/T_1)$. The dip centred at a temperature $T = 24°\mathrm{C}$ (corresponding to $\omega_{\mathrm{NV}} = 1435$ MHz as measured by ODMR) is the signature of unpaired electron spins assumed to be associated with surface termination states or dangling bonds. By tuning the magnetic field close to the GSLAC (where $\omega_{\mathrm{NV}} < 5$ MHz), it is also possible to detect nuclear spin species (Fig. 3.10a, black). Fig. 3.10c shows an ODMR map obtained from a deep NV centre (~ 1 μm from the surface) by scanning the temperature from 21 to 27°C near $B = 1024$ G. The avoided crossing in the higher temperature range (i.e. lower magnetic field) is characteristic of the GSLAC structure for the ^{14}NV centre, as studied in section 2.2. The CR spectrum, measured using $\tau = 2$ μs, reveals three features (Fig. 3.10d), just like in section 3.1.3 with the physical scanning. Namely, the central feature is caused by state mixing at the GSLAC and the two outer peaks are the signature of ^{13}C nuclear spins in the diamond lattice, which come into resonance with the NV before and after the GSLAC [161, 184].

3.2.3 Magnetic stabilisation through maintaining temperature

A number of applications, such as high precision measurements [63], long decoupling sequences and hyperpolarisation of external spins [36,184] require that the NV spin remains on resonance (with a driving field or a given spin species) for hours to days. While it is possible to post-process to remove off-resonance data, this is an undesirable solution for hyperpolarisation where off-resonant conditions limit the degree of polarisation transferred to the spin bath. By carefully controlling the temperature of the magnet, it is possible to significantly improve the long term stability of the NV frequency. In the absence of active temperature control, we observe variations in the room temperature (Fig. 3.11a) that result in changes in the NV frequency on the order of 2 MHz over the course of 20 hours (Fig. 3.11b, orange line). Including the PID loop to maintain a constant temperature of

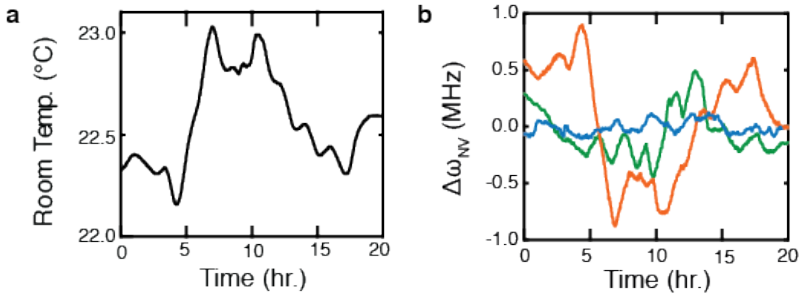

Figure 3.11: Stabilisation of permanent magnet. **a** Typical recording of the room temperature vs time, measured with the thermistor attached to the magnet, in the absence of active temperature control. **b** Variations in the NV frequency near the GSLAC, without temperature control (orange) showing a strong anti-correlation with **a**, with first order stabilisation (green) and with second order stabilisation (blue). In the measurements leading to the green and blue curves, the room temperature fluctuations were similar to **a**.

the magnet (as measured by the thermistor) reduces the change in frequency to 800 kHz peak to peak (Fig. 3.11b, green line), however, there is still an effect on the magnetisation from changes in the temperature of the room itself. This effect can be reduced by setting up a second order correction loop based on the measured ambient temperature, such that the changes to the magnet temperature set point are defined as

$$\Delta T_{\mathrm{M}} = -\frac{\alpha_{\mathrm{R}}}{\alpha_{\mathrm{M}}}\Delta T_{\mathrm{R}} + \frac{\alpha_{\partial}}{\alpha_{\mathrm{M}}}\frac{\partial T_{\mathrm{R}}}{\partial t} \tag{3.19}$$

where $\alpha_{\mathrm{M}} = 2.7$ MHz/°C is the direct change in magnetisation from temperature, T_{M} and T_{R} are the thermistor reading of the magnet and room temperature, respectively, and Δ denotes difference from original value. α_{R} and α_{∂} gives the change in magnetisation from the difference and derivative of the room temperature respectively, as measured empirically. This is simply a proportional derivative (PD) feedback loop acting on the set point, which is combined with the PID loop acting on the TEC. Using this second order feedback reduces the changes to 200 kHz (Fig. 3.11b, blue line), offering an improvement in stability by an order of magnitude compared to a non-controlled temperature. This is a similar improvement to previous results using a temperature controlled stage with extensive insulation [189]. Importantly, the remaining fluctuations in the NV frequency are within the intrinsic ODMR linewidth for typical near-surface NV centres ($\sim$ 500 kHz), reducing

the noise limit for long measurements to the intrinsic level. These fluctuations could be further reduced by simply changing to a common samarium-cobalt (SmCo) magnet which has a lower temperature coefficient $\alpha_0 = 0.04$. This would return a stability of ~ 60 kHz and a resolution of ~ 8 kHz, which is close to the smallest linewidths achievable with NV spins [9].

3.2.4 Lifetime measurements of spin bath polarisation

As a final experiment, we consider the polarisation of a small ensemble of ^{13}C spins using cross relaxation induced polarisation (CRIP) [184]. By repeatedly initialising the NV in the same spin state and tuning its frequency to the ^{13}C resonance, it is possible to gradually polarise the ^{13}C bath, as demonstrated in section 3.1.3 (also in Ref. [39]). Since the polarisation build up occurs over long time scales (typically hours), instabilities in the NV frequency often limit the maximum level of polarisation achievable and the ability to monitor its evolution under a variety of conditions. Here, we use the improved stability to investigate the lifetime of the ^{13}C polarisation. We first characterise the NV-bath interaction by using a sequence in which the NV spin is alternated between being initialised in $|0\rangle$ and $|-1\rangle$ before the free evolution time τ (Fig. 3.12a(i)). By tuning the NV frequency on resonance with ^{13}C (after the GSLAC, see Fig. 3.10d) and varying τ, we observe a coherent oscillation (Fig. 3.12b) whose frequency denotes the total coupling strength to the ^{13}C bath [184]. Using an optimal evolution time $\tau_{\text{opt}} = 1.9$ μs (half the period of the flip-flop oscillation), we then apply N polarisation steps to polarise the bath in the $|\uparrow\rangle$ state (by initialising the NV in $|0\rangle$) followed by N steps to polarise the bath in $|\downarrow\rangle$ (by initialising the NV in $|-1\rangle$), see sequence in Fig. 3.12a(ii). The resulting polarisation curve is plotted as a function of step number in Fig. 3.12c, and shows saturation of the polarisation after about 10 steps. Here only the spins within the coupling strength of $\Gamma = 1/\tau_{\text{opt}}$ are probed, corresponding to a distance from the NV of < 1 nm. We also note that each polarisation step results in a maximum possible transfer of one quantum of polarisation and thus with $N = 10$ there is a maximum possible transfer of 10 nuclear spins.

The contrast between the polarised and unpolarised spin bath states allows mea-

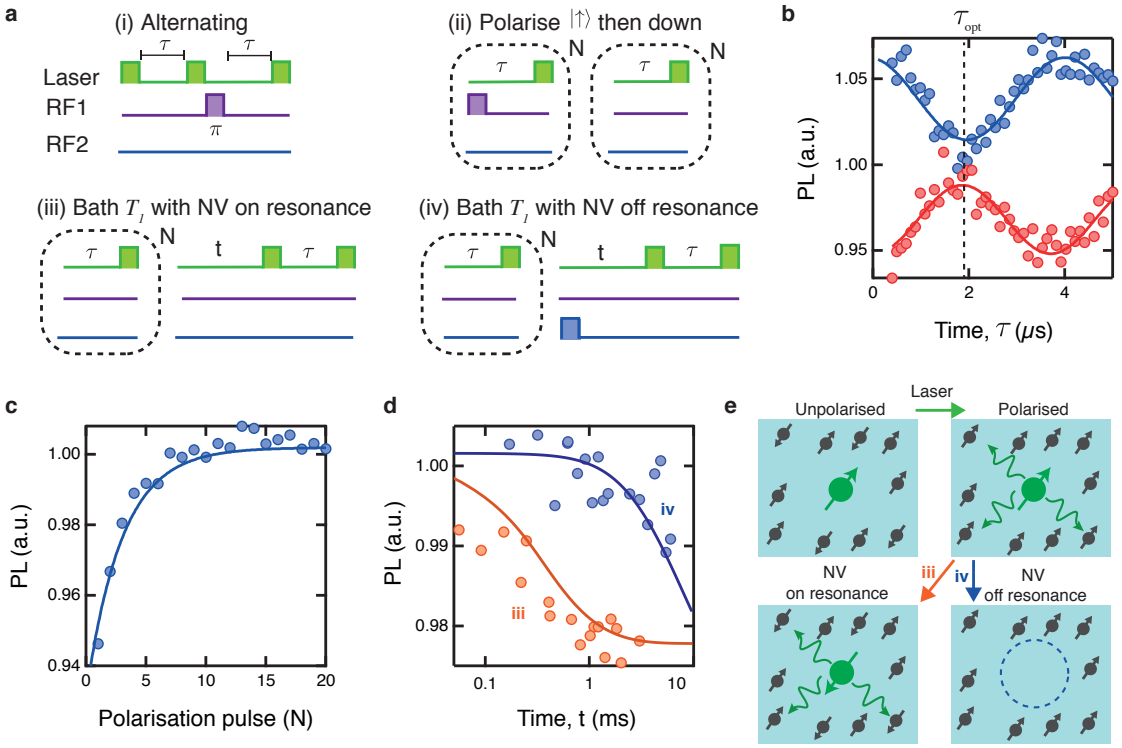

Figure 3.12: Application of improved magnet control to hyperpolarisation measurements. **a** Pulse sequences used for the study of the ^{13}C polarisation where radio frequency RF1 is on resonance with $|0\rangle \rightarrow |-1\rangle$ transition (frequency $\approx$ 1.1 MHz) and RF2 is on resonance with $|0\rangle \rightarrow |+1\rangle$ (frequency $\approx$ 5.74 GHz). The pulse sequences have the effect of: (i) preventing polarisation of the bath, (ii) measuring the polarisation rate, (iii) measuring the lifetime of the spin bath polarisation with the NV on resonance and (iv) off resonance. **b** Interaction with ^{13}C bath on resonance using the alternating sequence (i). **c** Dynamics of the ^{13}C bath polarisation obtained using pulse sequence (ii) with $\tau = 1.9$ μs. **d** Lifetime measurements of the polarisation of the ^{13}C, showing a short lifetime $1/\Gamma_{pol} = 250(50)$ μs when the NV spin was allowed to interact with the bath after polarisation (orange) and a significantly extended lifetime $1/\Gamma_{pol} \sim 10$ ms when the NV was flipped to an off-resonance state (blue). Solid lines are numerical simulations of the spin bath under the pulse sequence. **e** Schematics of the effect of the NV spin on the bath polarisation.

surements of the lifetime of the polarisation. To achieve this, the bath is initially polarised by applying $N = 50$ polarisation steps, then after a time period t the polarisation of the bath is measured again (Fig. 3.12a(iii)). By performing the measurement while still at the NV-^{13}C resonance, we obtain a decay of $T_1^{\text{pol}} = 250 \pm 50$ μs (Fig. 3.12d, orange data). The decay time of this polarisation is limited by the NV spin T_1 (50 ± 5 μs on resonance). While the inner core is polarised and no longer interacting with the NV spin, the outer shell which is unpolarised can interact with the NV during the probe time t, causing a drastically shortened NV T_1. Once the NV has decayed it acts as an additional noise source interacting with the polarisation of the spin bath (Fig. 3.12e, bottom left). This effect can be suppressed by initialising the NV into the $|+1\rangle$ state before the evolution time t (Fig. 3.12a(iv)), effectively turning off the NV-^{13}C interaction (Fig. 3.12e, bottom right). Including this NV spin flip extends the T_1 of the bath to the order of ten milliseconds (Fig. 3.12d, blue), which is limited by the phonon limited T_1 of the NV, on the order of milliseconds [109]. These results agree well with theory (Fig. 3.12d, solid lines). We note that the acquisition time for each curve in Fig. 3.12d was $\sim$ 20 hours, during which the resonance condition was maintained; this would not have been possible to achieve without active temperature control with our apparatus.

We now compare our temperature-controlled permanent magnet to alternative approaches. Reaching the required magnetic field strength (e.g., $\sim$ 0.1 T in this work) is very challenging using a standard electromagnet or solenoid, due to the restricted access to the diamond sample in typical confocal microscopes which employ bulky high numerical aperture objective lenses in quasi-contact with the sample, and to heating induced by the large currents required. Ignoring heating-related drifts and instabilities, the stability of the magnetic field generated by an electromagnet is ultimately limited by the stability of the current source. Commercially available current sources generally feature a long term relative stability of the order of $10^{-3} - 10^{-4}$ for currents in the Ampere range, and a setting resolution and noise level of the same order. For an NV centre near the GSLAC, this translates into 300 kHz to 3 MHz fluctuations (long term and noise) and setting resolution. In contrast, in this work we obtained fluctuations as low as 100 kHz (200 kHz peak to peak), with a resolution of 26 kHz and a noise negligible compared to the environmental noise [190]. Thus, our approach already outperforms the electromagnet-based solution,

for a fraction of the cost. Moreover, it could be further improved – by more than an order of magnitude – by using a permanent magnet material with a lower α_0.

3.3 Comparison of different hyperpolarisation techniques

Hyperpolarisation promises to have a myriad of application, some involving internal ^{13}C spin polarisation [139, 191–193] and others focused on external spin polarisation [33, 194]. As a consequence, several different hyperpolarisation technique have arisen, including: Hartmann-Hahn (NOVEL), cross relaxation induced polarisation (CRIP), Landau-Zener [139,192,193,195], and dynamical decoupling (PulsePol [196] and PolCPMG, developed in chapter 4). Both ^{13}C and external spin applications desire a polarisation transfer rate that is as fast as possible, while maintaining usability for application, i.e. is robust enough to experimental errors. In this section we look at the polarisation rate of two techniques, NOVEL and CRIP. The aim is to benchmark the CRIP method developed in section 3.1.3 to alternative methods. We restrict our comparison to NOVEL because other techniques (Landau-Zener, dynamical-decoupling) rely on the same coupling mechanism but are expected to exhibit a slower polarisation rate than NOVEL. Thus, NOVEL constitutes a good reference point, in addition to being relatively simple to analyse analytically.

All of the NV hyperpolarisation techniques utilise the dipole-dipole interaction (also known as hyperfine coupling) of the NV-nuclear spin pair in order to transfer the polarisation. In this fashion, a NV-nuclear spin system is coupled with some hyperfine tensor $\mathbf{A}$, which depends on the distance R and angle Θ between the two spins (Fig. 3.13a). In order to resonantly couple the two spins – maximising the polarisation transfer – the energy levels of the NV spin is made to match that of the nuclear spin (Fig. 3.13b). This can be achieved through direct coupling (cross-relaxation, CR) or in the rotating frame (i.e. driven dressed states, Hartmann-Hahn). These different resonance regimes involve different hyperfine coupling terms, leading to a change in the angular dependence (Fig. 3.13c) and the overall strength of the interaction (Fig. 3.13d). As a consequence it is predicted that CR coupling past the ground state level anti-crossing (GSLAC) will exhibit a stronger interaction and thus a faster polarisation rate than other techniques for most angular positions of the nuclear spins. Thus, when these techniques are implemented on

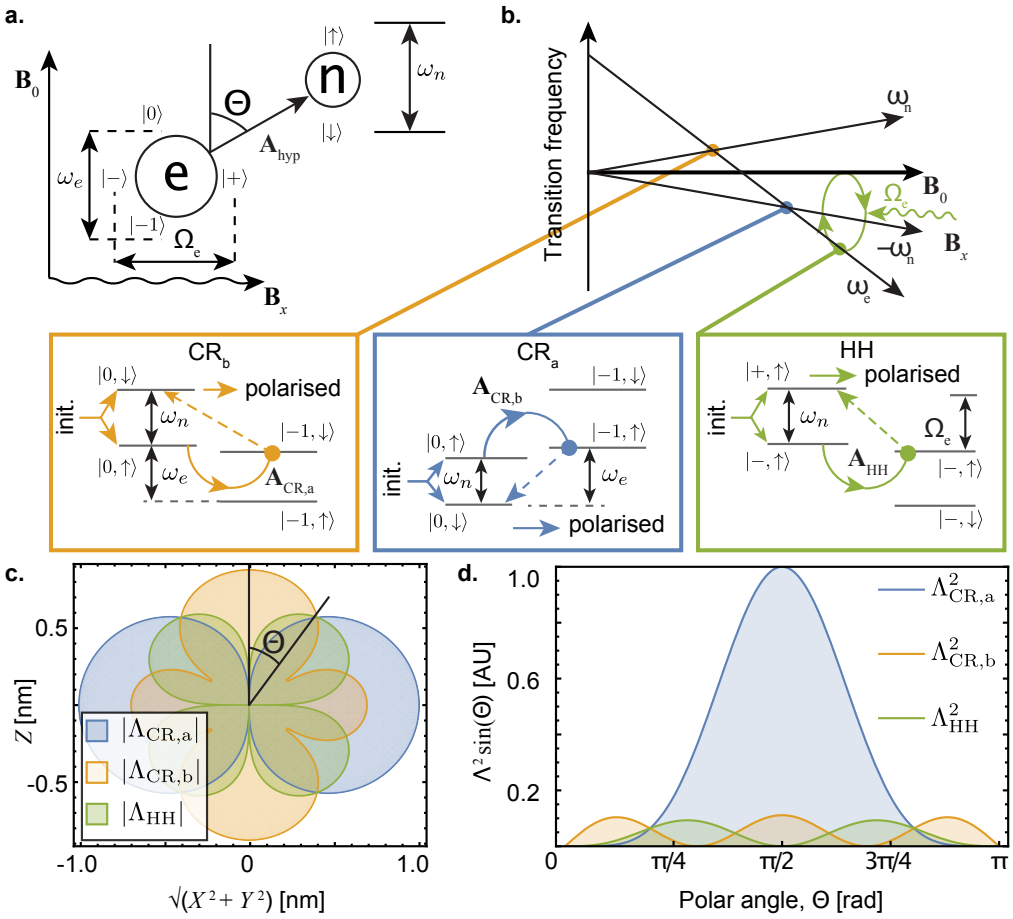

Figure 3.13: Overview of NV DNP mechanisms. **a** Schematic of electron-nuclear hyperfine geometry employed in DNP schemes. Hartmann-Hahn schemes employ an RF field (B_x) to drive the electron spin's Rabi frequency (Ω_e) into resonance with the nuclear Larmor frequency (ω_n); whereas the lab-frame cross-relaxation approach uses the external static field to tune the electron spin's Larmor frequency (ω_e) to that of the nuclear spin. **b** Transition frequency structure of the NV and nuclear spin, and corresponding polarisation protocols associated with the schemes studied in this work. **c** Hyperfine lobe structure of the 1 MHz contours of an NV coupled to a ^{1}H nuclear spin showing the angular dependence of the hyperfine couplings associated with these schemes. **d** Relative solid-angle contributions to the total NV-ensemble coupling vs polar angle, Θ.

an ensemble of spins, CR based hyperpolarisation should reign supreme in polarisation rate. In this section, we experimentally investigate the difference in the coupling strengths of CR and Hartmann-Hahn (HH) hyperpolarisation with the internal ^{13}C spin bath.

3.3.1 Experimental verification of coupling strength variation

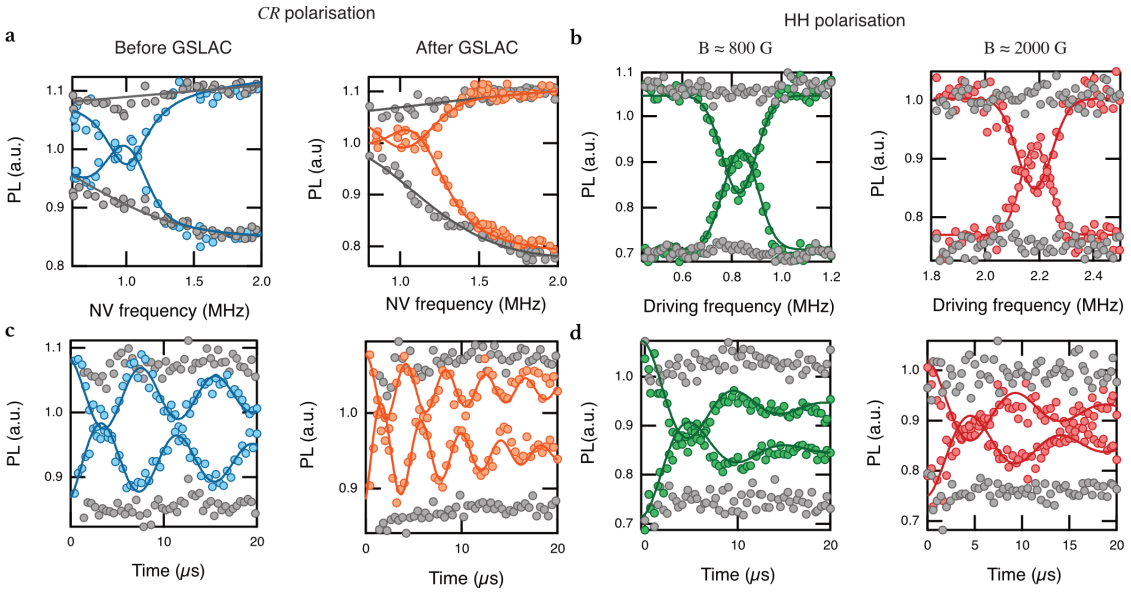

Figure 3.14: Spectral and time comparison. **a** Comparison of the spectral signature of ^{13}C for the different hyperpolarisation conditions (both before and after the GSLAC) with a depolarised bath (coloured) and a polarised bath (grey). The change in the low frequency spectra in T_1 is caused by the GSLAC feature (see Sec. 2.2). **b** Same as in **a** but for HH at two different magnetic field strengths. **c** Comparison of the time dynamics of the interaction, where the probe frequency is given by the maximum in **a**, i.e. approximately 1 MHz. **d** time dynamics for the HH interaction.

To investigate the hyperpolarisation technique differences, we first look at the spectral signature of detection and hyperpolarisation. For CR, the magnetic field strength is scanned across around the GSLAC region, both before and after. Spectra were taken with both the depolarisation sequence (alternating initialisation between $|0\rangle$ and $|-1\rangle$, see section 3.1.1 for details) which produces the detection of the nuclear spin signal (Fig. 3.14a, colour) and with a polarisation sequence (always initialising in $|0\rangle$), which produces no signal when the bath is polarised (Fig. 3.14a, grey). An additional feature is observed at low frequency due to the intrinsic GSLAC feature. The spectrum can also be obtained

for the HH polarisation technique, in which the driving strength (and thus the driven frequency of the Rabi oscillations) is modified in order to ascertain the resonance condition (Fig. 3.14b). This was conducted at both $B \approx 800$ G and $B \approx 2000$ G, in which no change in the spectrum was observed, indicating that the spectral broadening of the HH resonance condition may be independent on the driving strength.

In order to determine the coupling strength with the spin bath, the time dynamics of the interaction needs to be observed. In the case of CR, the magnetic field is tuned to match the spectral maximum and the NV is allowed to interact with the bath for a varied time, τ. When the bath is polarised (Fig. 3.14c, grey) no interaction is observed, as the bath has been initialised in the non-interacting state. However, when the depolarised sequence is used (Fig. 3.14c, colour) an oscillation is observed. This oscillation is defined by the coupling strength of the NV-nuclear spin system. It is observed that the resonance after the GSLAC (CR_a) has a stronger coupling than before (CR_b). Similar experiments for the HH condition also demonstrates a slower oscillation (Fig. 3.14d), indicating a smaller coupling strength. A direct comparison for a single NV for both CR_a and HH is shown in Fig. 3.15a.

The coupling strength of the three different techniques is given by

$$\begin{aligned}
\Lambda_{\mathrm{CR,a}} &= \frac{1}{\sqrt{2}}\sqrt{(A_{xx}^2 - A_{yy}^2) + (A_{xy} + A_{yx})^2} \\
&= \frac{3a}{\sqrt{2}R^3}\sin^2(\Theta) \qquad (3.20) \\
\Lambda_{\mathrm{CR,b}} &= \frac{1}{\sqrt{2}}\sqrt{(A_{xx}^2 + A_{yy}^2)} \\
&= \frac{a}{\sqrt{2}R^3}\left|3\cos^2(\Theta) - 1\right| \qquad (3.21) \\
\Lambda_{\mathrm{HH}} &= \frac{1}{\sqrt{2}}\sqrt{A_{zx}^2 - A_{zy}^2} \\
&= \frac{3a}{2R^3}\left|\sin(\Theta)\cos(\Theta)\right| \qquad (3.22)
\end{aligned}$$

where R is the distance between the NV and target, Θ is the polar angle of this separation (Fig. 3.13a), and $a = \frac{\mu\hbar}{4\pi}\gamma_{NV}\gamma_T$. As the coupling strength is given by the angular position of the spins, the average coupling for both HH and CR_a can be computed for all possible bath conditions (Fig. 3.15b, colour map). These results indicate a stronger coupling for

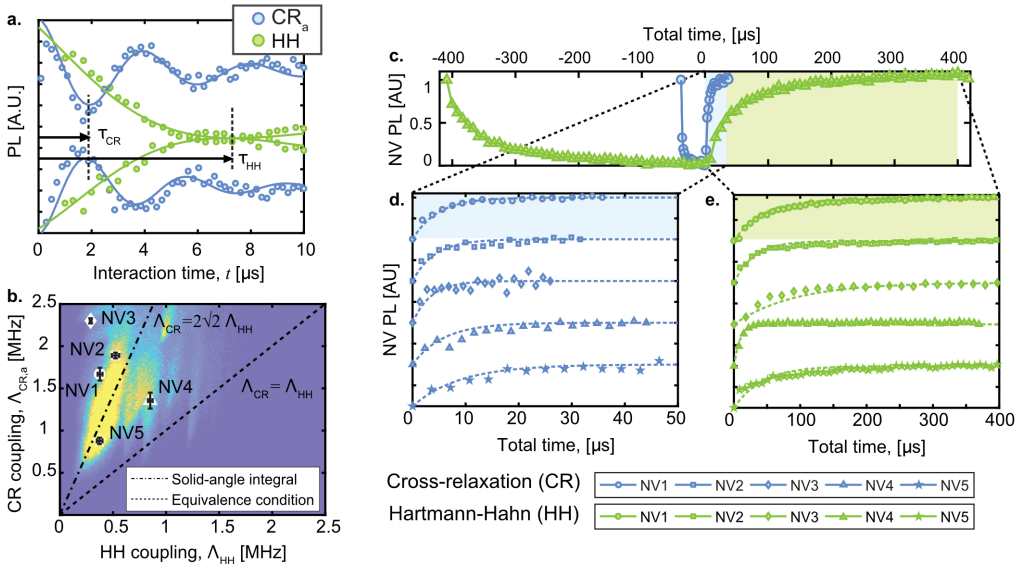

Figure 3.15: Study of native ^{13}C polarisation. **a** Resonant longitudinal spin dynamics of NV1 under depolarisation (alternating CR/iCR (blue), where iCR = CRIP^{-1} from section 3.1.3 and HH/iHH (green)) sequences. Fits are used to extract CR and HH hyperfine components. **b** Scatter plot of hyperfine couplings, $\Lambda_{\mathrm{CR,a}}$ vs. Λ_{HH}, extracted for NVs 1-5 laid over their probability distribution. Equivalence line ($\Lambda_{\mathrm{CR,a}} = \Lambda_{\mathrm{HH}}$, dashed) and average solid integrals ($\Lambda_{\mathrm{CR,a}} = 2\sqrt{2}\Lambda_{\mathrm{HH}}$, dot-dashed) also shown. Here yellow denotes a higher probability than blue. **c** Polarisation and anti-polarisation buildup of NV1 under CR$_a$ (circles) and HH (triangles) sequences. **d**. Zoomed plot of NV1-5 polarisations showing how polarisation timescales are related to CR hyperfine couplings. Theoretical curves (dashed) are constructed from extracted couplings in **b**. **e** As in **d**, but for HH polarisation sequence.

the CR$_a$ condition, with an average improvement of $\Lambda_{\mathrm{CR,a}} = 2\sqrt{2}\Lambda_{\mathrm{HH}}$, which is consistent with the experimentally measured values for several NVs (Fig. 3.15b, overlaid data points).

To confirm that polarisation rate and coupling strength are related we directly measured the polarisation rate. This was achieved by first polarising the bath in one direction (e.g. $|\downarrow\rangle$) followed by a polarisation into the opposite direction (e.g. $|\uparrow\rangle$). The same procedure was implemented in section 3.1.3 and 3.2.4, where the polarisation rate is measured by how quickly the signal goes from maximum contrast to minimum (Fig. 3.15c after time $t = 0$). Comparing the same NV spin for both CR$_a$ (Fig. 3.15d) and HH (Fig. 3.15e) shows a significant speed up in polarisation rate (note the x-axis time scale difference), which is consistent with the difference in coupling strength. This confirms that CR based hyperpolarisation does indeed transfer polarisation from the NV spin to the nuclear spin

bath faster than other techniques, at least in the case of the internal ^{13}C bath, allowing a greater polarisation to be achieved. In the case of spins external to the diamond where the coupling is much weaker, dephasing must be taken into account. For CRIP, the polarisation rate is then given by Eq. 3.17, inversely proportional to the dephasing rate Γ_2. On the other hand, for HH the effect of dephasing may be mitigated through strong microwave driving (which requires a large magnetic field to maintain the HH resonance condition). Further work is thus needed to compare CRIP to HH and other techniques in the various scenarios relevant to applications.

3.4 Conclusion

In summary, we have experimentally demonstrated hyperpolarisation of molecular nuclear spins under ambient conditions by employing a direct cross relaxation scheme with a single NV spin. The technique works at low field, room temperature, requires no RF fields, and operates directly on the target molecules without the need for catalysts or free radicals. With high polarisation rates and tunability, there are excellent prospects for scale-up of the system to produce macroscopic quantities of a range of contrast agents at polarisation levels required for molecular MRI/NMR. The technique can be extended to other nuclear spin species and may also provide pathways in quantum information for initialisation of quantum simulators, or increasing the fidelity of operations through spin-bath neutralisation.

A temperature control scheme was implemented on a permanent magnet and was shown to be capable of performing magnetic field sweeps to produce CR spectra of electron and nuclear spins. Controlling the magnet temperature improved the long term stability of the NV spin frequency from ± 1 MHz to ± 100 kHz and could be further improved on with different magnet materials. With the increased stability, dynamics of the ^{13}C polarised bath were explored. These results indicated that for small polarised regions the NV spin can significantly limit the lifetime of the polarisation imparted onto the bath. However, this effect can be mitigated by initialising the NV into a non-interacting state.

Finally, the performance of cross relaxation induced polarisation was compared with that of Hartmann-Hahn. In this study it was found, both experimentally and theoreti-

cally, that CRIP benefits from a stronger coupling strength than HH because it relies on a different (stronger) component of the hyperfine interaction, which can lead to faster/larger polarisation in ideal scenarios. However, further work is needed to determine if this intrinsic advantage of CRIP survives in the presence of strong dephasing, to which HH and other techniques are expected to be more robust. In the next chapter, we develop and investigate one such alternative technique, based on dynamical decoupling.

4

Hyperpolarisation of nuclear spins via dynamical decoupling protocols

Applications of diamond based hyperpolarisation include the production of highly polarised contrast agents for enhanced sensitivity in NMR [197, 198], as proposed in Section 3.1.6, and as a method of initializing nuclear spin-based quantum simulators [199]. Experimental realisation of these goals requires the NV hyperpolarisation platform be scaled to operate on ensembles of NVs that are spatially expansive (spanning > 10 μm in x and y) and shallow ($z < 10$ nm from the surface). However, samples of this nature introduce significant NV spin dephasing due to the NV-NV and NV-N interactions [200], which restricts the viability of hyperpolarisation techniques. In the case of cross relaxation induced polarisation (CRIP, detailed in Section 3.1.3), while the technique possesses the fastest raw polarisation rate, it is particularly sensitive to dephasing (and by extension, to static field inhomogeneities) which inhibits the resonant polarisation transfer condition from being met. In addition, the proximity to the GSLAC induces random spin mixing in noisy samples, significantly deteriorating the NV electron spin polarisation (detailed in Section 2.2). Techniques such as Hartmann-Hahn (HH) do not suffer from the GSLAC issue but are still sensitive to dephasing and introduce another scaling issue: the sensitivity to inhomogeneities in the microwave driving power. One solution is to rely on dynamical decoupling (DD) to refocus the NV spin, making the technique more robust to experimental inhomogeneities (or errors) while minimising any further loss in polarisation

rate from natural dephasing.

In this chapter, a dynamical decoupling based technique is developed that has a similar polarisation rate to Hartmann-Hahn yet is significantly more robust to experimental errors common to scaling [153]. This technique (termed PolCPMG) is a modified version of the common dynamical decoupling (DD) sequence Carr-Purcell-Meiboom-Gill (CPMG) with rotational adjustment that deviate the NV spin from the Bloch sphere transverse plane, leading to a separation of the nuclear spin state's resonant coupling times. As a consequence, the sequence produces spectrally distinct features that can be tuned to through varying the evolution time between rotations. The protocol is developed both experimentally and theoretically on the NV-^{13}C coupled spin system, which shows commensurate polarisation rates to similar techniques under ideal conditions (e.g. HH and PulsePol [196]). Finally, the robustness to both frequency and power detuning is directly imaged with a wide-field NV imaging platform. Through the deliberate introduction of significant detunings, the technique is demonstrated to be applicable to large regions (> 10 μm) and is a useful calibration tool for other hyperpolarisation techniques.

4.1 Principle of the technique

Dynamical decoupling (DD) sequences are ubiquitously used in NV experiments to decouple the NV spin from undesirable noise sources while increasing the sensitivity to a target frequency, through performing a series of π-rotations on the NV spin. Due to the symmetry of these sequences the NV spin couples similarly to both nuclear spin states, which prohibits any build up of polarisation from the NV-nuclear spin interaction. Recently, a new DD technique which concatenates two asymmetric sequences together was developed, PulsePol [196]. This asymmetry separates the nuclear spin states which allows the sequence to directly couple to one spin state only; generating an effective flip-flop Hamiltonian of the coupled electron-nucleus spin system, facilitating the transfer of polarisation from the NV spin. Protocols based on DD are by construction more robust to frequency detuning and π-rotations errors, both of which are present in scaling of the NV hyperpolarisation platform.

Here, a different approach to PulsePol is proposed where the asymmetry that enables

the polarisation transfer is encoded in the spin rotations by deliberately introducing an adjustment on the rotation angle $\delta\theta \neq 0$. Instead of π-flips, the protocol uses a static adjustment on the rotations, such that $\theta = \pi + \delta\theta$. The modified rotations are performed on the commonly-used Carr-Purcell-Meiboom-Gill (CPMG) sequence, consisting of a simple train of equally spaced rotations around a fixed axis which is experimentally simple to perform, resulting in a polarising form of CPMG (PolCPMG). The asymmetry introduced here behaves differently to the PulsePol version, as it separates the spin states in evolution time rather than in NV initialisation state. However, the PolCPMG protocol still results in an effective flip-flop Hamiltonian that has a polarisation transfer rate similar to that of HH and PulsePol, while offering an increased robustness to frequency detunings and phase errors respectively. In this section, the theoretical framework for understanding PolCPMG is developed and the protocol is implemented on the internal ^{13}C spin bath.

4.1.1 Theoretical framework

Consider a system composed of a single NV spin **S** coupled with a single nuclear spin **I** under a magnetic field aligned along the z-axis (Fig. 4.1a). The electron spin is subject to a train of microwave pulses with a period τ, with each pulse inducing a rotation of angle $\theta = \pi + \delta\theta$ around the x-axis (Fig. 4.1b). In practice, the rotations may be generated by rectangular pulses and the angle tuned via an appropriate frequency detuning and/or pulse duration. In the frame rotating with the driving microwave field, and neglecting counter-rotating terms, the Hamiltonian reads

$$\hat{H}(t) = \omega_L \hat{I}_z + \hat{S}_z \mathcal{A} \cdot \mathbf{I} + \hat{H}_p(t) \tag{4.1}$$

where ω_L is the nuclear Larmor frequency, $\mathcal{A}$ is the hyperfine field felt by the nuclear spin (with a perpendicular projection $A_\perp$ relative to the z-axis), and $\hat{H}_p(t)$ is the pulse control Hamiltonian. As the Hamiltonian is periodic, $\hat{H}(t+\tau) = \hat{H}(t)$, Floquet theory provides the natural framework for analysing the dynamics [201].

Resonant interactions between the coupled NV-^{13}C spin system can be found by locating level anti-crossings (LAC) in the Floquet phases, where the LAC arises from the presence of a non-zero hyperfine coupling, indicating the periods τ for which the driven

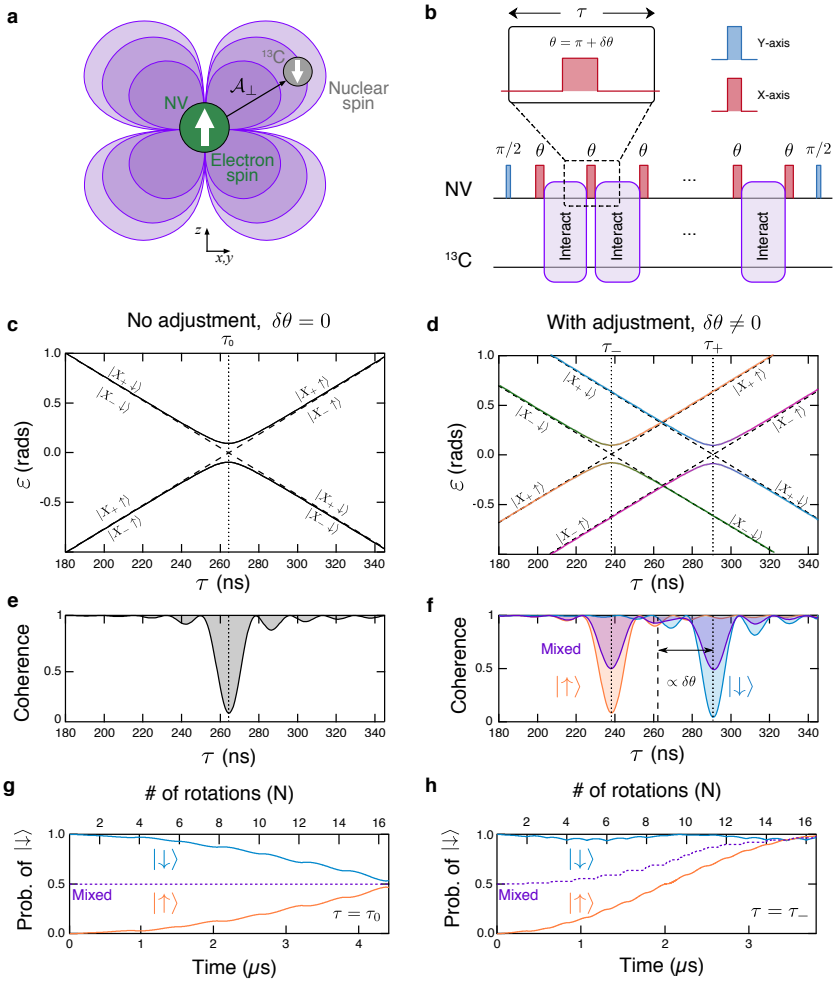

Figure 4.1: Concept of rotational adjusted dynamical decoupling for HP. a Depiction of a central spin qubit (e.g., the NV centre in diamond) surrounded by a bath of nuclear spins (^{13}C). The contour lines represent the transverse hyperfine field, $\mathcal{A}_\perp$, felt by the nuclear spins. **b** Schematic of the PolCPMG dynamical decoupling sequence, which comprises N pulses separated by a period τ. Each pulse rotates the spin qubit around the x-axis by an angle $\theta = \pi + \delta\theta$, except for the initial and final pulses that rotate the qubit by $\pi/2$ around the y-axis. **c, d** Floquet phases of the NV-^{13}C coupled system periodically driven by the unit sequence shown in (b), as a function of τ, with $\delta\theta = 0$ (c) and $\delta\theta = \pi/10$ (d). Parameters are $\omega_L = 1.9$ MHz and $\mathcal{A}_\perp = 180$ kHz. Dashed lines indicate the uncoupled case ($\mathcal{A}_\perp = 0$). **e, f** Coherence of the spin qubit as a function of τ after a CPMG (f) and PolCPMG (g) sequence comprising $N = 32$ pulses, with the qubit initialised in $|X_+\rangle$ and the nuclear spin initialised in $|\uparrow\rangle$ (magenta), $|\downarrow\rangle$ (blue) or in a completely mixed state (purple). In (e) all the different cases are overlapped and shown in black. **g, h** Time evolution of the nuclear spin state during the CPMG sequence with $\tau = \tau_0$ (g) and during the PolCPMG sequence with $\tau = \tau_-$ (h), with the system initialised as in (f). Here $\mathcal{A}_\perp/2\pi = 380$ kHz.

electron spin has, on average, a non-zero interaction with the nuclear spin [201]. In the normal CPMG sequence ($\delta\theta = 0$, Fig. 4.1c) the nuclear spin states ($|\uparrow\rangle$ and $|\downarrow\rangle$) are degenerate at the LAC at $\tau_0 = \frac{\pi}{\omega_L}$, which is used as a nuclear spin detection protocol [116, 125]. While useful as a detection scheme (through monitoring the coherence while varying the interaction time τ, Fig. 4.1e), the degeneracy prohibits any build up of polarisation from this sequence. The static rotation adjustment lifts this degeneracy to produce four distinct Floquet modes (Fig. 4.1d) corresponding to $|X_\pm\rangle|\uparrow\downarrow\rangle$ with $|X_\pm\rangle = (|0\rangle \pm |1\rangle)/\sqrt{2}$, where the NV $m = 0$ ($|0\rangle$) and $m = 1$ ($|1\rangle$) are the $\hat{S}_z$ eigenstates of the NV spin. The degeneracy is removed by introducing an offset in the Floquet phase betwixt these states, which manifests as a separation of the resonance condition in the interaction time. These two avoided crossings occur at two different periods approximately given by

$$\tau_\pm \approx \tau_0 \left(1 \pm \frac{\delta\theta}{\pi}\right), \tag{4.2}$$

leading to two resonances in the coherence spectrum (Fig. 4.1f) [153]. Importantly, these avoided crossings involve pairs of fully orthogonal states for both electron and nuclear spins, for instance the τ_- crossing mixes the states $|X_+\rangle|\uparrow\rangle$ and $|X_-\rangle|\downarrow\rangle$. This means that a system initialised in $|X_+\rangle|\uparrow\rangle$ and periodically driven at $\tau = \tau_-$ will undergo oscillations between these two states, as if they were governed by a flip-flop Hamiltonian. Initialisation in $|X_+\rangle$ is naturally done in the CPMG sequence through the initial $\pi/2$ pulse around the y-axis (Fig. 4.1b), which means that the polarisation effect is obtained simply by introducing an adjustment to the rotation angle of the control pulses, and by choosing τ accordingly.

The dynamics of the coupled spin system were explored under the standard CPMG sequence at $\tau = \tau_0$ (Fig. 4.1g) and under the PolCPMG sequence at $\tau = \tau_-$ (Fig. 4.1h). During CPMG the nuclear spin $|\uparrow\rangle$ and $|\downarrow\rangle$ states evolve symmetrically, resulting in no change of net polarisation for a mixed state. While with PolCPMG, the $|\downarrow\rangle$ state does not evolve (i.e. it remains polarised) whereas the $|\uparrow\rangle$ state monotonically evolves to become $|\downarrow\rangle$ state, resulting in a net polarisation into the nuclear spin $|\downarrow\rangle$ state. The total time required

to achieve full nuclear spin polarisation can be obtained in the limit of instantaneous pulses,

$$t_{\mathrm{PolCPMG}} = \frac{\pi(\pi \pm \delta\theta)}{A_\perp \cos\left(\frac{\delta\theta}{2}\right)} \approx \frac{\pi^2}{A_\perp} \tag{4.3}$$

where the $\pm$ sign corresponds to the $\tau_\pm$ resonances. This is just a factor $\pi/2$ longer than with the HH protocol and similar to that of PulsePol [196], under ideal conditions.

To highlight the differences in CPMG, PolCPMG, and PulsePol, numerical simulations of the Floquet phase (Fig. 4.2a-c) and the coherence spectrum (Fig. 4.2d-f) for all three protocols were calculated with a given hyperfine coupling, $\mathcal{A}_\perp/2\pi = 180$ kHz, and finite pulse duration, $t_p^0 = 40$ ns . The finite pulse duration introduces a difference in the Floquet phases for CPMG and PolCPMG in terms of the LAC width but does not change the overall behaviour of the systems. While the rotational asymmetry in PolCPMG produces two distinct LACs that can be used to tune to different spin states, with PulsePol, there is one avoided crossing and one true crossing at a single resonance condition, $\tau = 3\pi/\omega_L$. Therefore, in order to control the polarisation transfer direction PulsePol requires the NV to be initialised in a given state (starting the sequence with a $-\pi/2$ rather than a $\pi/2$). While PolCPMG has the option to change evolution time while maintaining the initial rotation or change the initial rotation while maintaining the same evolution time. In either case both protocols result in similar polarisation rate but have different robustness to certain sources of error, discussed in more detail in section 4.3.

4.1.2 Experimental apparatus

The experiments were conducted at room temperature with a custom-built wide-field fluorescence microscope of the type discussed in section 1.2.3. The NV-diamond sample used in these experiments was a 2 mm $\times$ 2 mm $\times$ 50 μm electronic grade single-crystal diamond with {110} edges and a (001) top facet with a 1 μm-thick layer of ensemble NV spins with a natural isotopic abundance, $[^{13}\mathrm{C}] = 1.1\%$. The diamond was glued to a glass cover slip with patterned microwave waveguide. Optical excitation was performed with a 532 nm Verdi laser that was gated using an acousto-optic modulator (AA Opto-Electronic MQ180-A0,25-VIS) and focused to the back aperture of an oil immersion objective lens (Nikon CFI S Fluor 40x, NA = 1.3). The photoluminescence (PL) from the NV centres

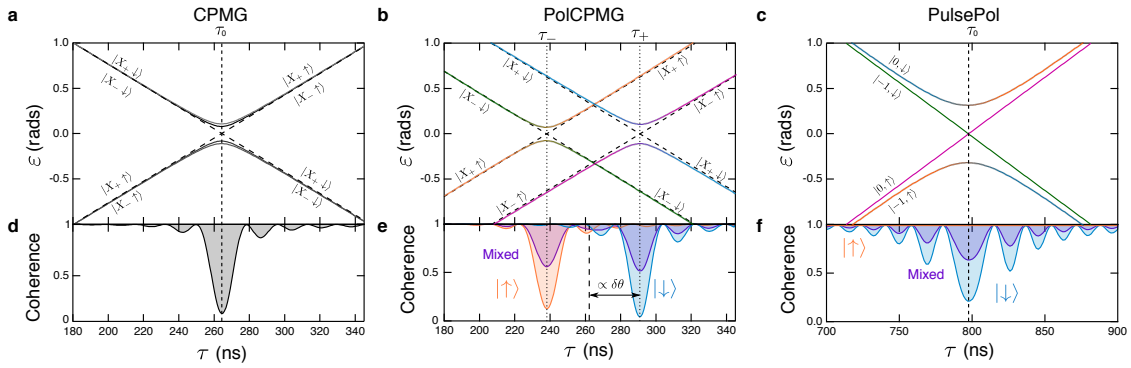

Figure 4.2: Floquet spectra with finite pulse duration. a-c Floquet spectra of the NV-^{13}C coupled system driven by **a** CPMG without error, **b** PolCPMG with $\delta\theta = \pi/10$ and **c** PulsePol. Parameters are $\omega_L/2\pi = 1.9$ MHz, $\mathcal{A}_\perp/2\pi = 180$ kHz, $t_p^0 = 40$ ns. The error $\delta\theta$ in **b** is achieved by setting the pulse duration to $t_p = 44$ ns. Dashed lines indicate the uncoupled case ($\mathcal{A}_\perp = 0$). **d-f** Coherence of the electron spin after a CPMG **d** or PolCPMG **e** sequence comprising $N = 32$ pulses, or after a PulsePol sequence comprising 12 repetitions of the unit sequence. The electron spin is initialised in $|X_+\rangle$ in (d,e) and in $|0\rangle$ in **f**, and the plotted signal is $\langle 2\hat{S}_x\rangle$ in (d,e) whilst it is $\langle 2\hat{S}_z\rangle$ in (f). The nuclear spin is initialised in $|\uparrow\rangle$ (orange), $|\downarrow\rangle$ (blue) or in a completely mixed state (purple). In (d) all the different cases are overlapped and shown in black.

is separated from the excitation light with a dichroic mirror and filtered using a bandpass filter before being imaged using a tube lens (f = 300 mm) onto a sCMOS camera (Andor Zyla 5.5-W USB3). Microwave excitation was provided by a signal generator (Rohde & Schwarz SMBV100A) gated using the built-in IQ modulation and amplified (Mini-circuits HPA-50W-63+). A pulse pattern generator (Spincore PulseBlasterESR-PRO 500 MHz) was used to gate the excitation laser, microwaves, and to synchronise the image acquisition. A static magnetic field of strength $B = 1765$ G was applied along the NV axis using a permanent magnet.

In all experiments, the laser spot diameter was about 100 μm at the NV layer and the total CW laser power at the sample was 300 mW. The laser pulse duration for each NV spin initialisation/readout was 20 μs, chosen as a trade-off between readout contrast and initialisation fidelity. In sections 4.1.4 & 4.2 , the PL signal was averaged over a small region (1.6 μm $\times$1.6 μm) to avoid issues arising from spatial inhomogeneities (especially in microwave frequency and power). Such an area corresponds to an estimated total of 10^5 NV centres. The exposure time of the camera was 1 ms and the total acquisition time several minutes for each measurement. In section 4.3, a 30 μm $\times$30 μm area was

imaged and analysed. Each 0.8 μm $\times$0.8 μm pixel in the image contained about 5×10^4 NV centres. The exposure time of the camera was 10 ms and the total acquisition time several hours.

4.1.3 Implementation of polarisation measurements

In order to spatially map the polarisation across a region of inhomogeneous magnetic field and driving power in section 4.3 a camera was required. As a consequence,, the overall sequence was adapted to accommodate the time scale mismatch between the duration of a single polarisation cycle (initialise-PolCPMG-readout) and the exposure time of the camera (Fig. 4.3a). The building blocks of any sequence involve a combination of two sequences that can be repeated R times. The first involves initialising the NV spin, performing PolCPMG, and finally reading out the NV spin state, where the initial rotation is a $\pi/2$, producing a $|X_+\rangle$ state (Fig. 4.3b). The second is a copy of the first with the initial rotation replaced with a $3\pi/2$, producing a $|X_-\rangle$ state (Fig. 4.3c). In order to measure the NV coherence in the absence of any ^{13}C polarisation these two states need to be alternated (i.e $|X_+\rangle$, $|X_-\rangle$, $|X_+\rangle$, ..., $|X_-\rangle$) and the signal from both combined (Fig. 4.3d). For all other experiments, the ^{13}C bath is first reset by applying $R = 500$ cycles with $|X_-\rangle$ before switching polarisation direction. That is, R cycles of a sequence with $|X_+\rangle$ and variable parameters (t_p, τ, N etc.), then perform a single $|X_+\rangle$ sequence during camera exposure to readout the ^{13}C polarisation state (Fig. 4.3e). This procedure acts to allow varied N values to be probed while limiting the readout pulse to $R = 1$, removing additional averaging effects.

4.1.4 Identification of the spectral response of PolCPMG

As mentioned above, the PolCPMG protocol is experimentally tested using an ensemble of NV centres in diamond interacting with the bath of ^{13}C nuclear spins naturally present in the diamond (1.1% abundance). A magnetic field $B_z = 1765$ G is applied along the NV axis, giving a ^{13}C Larmor frequency $\omega_L = 1.9$ MHz. The pulse rotation adjustment, $\delta\theta$, is controlled via the pulse duration, t_p, of a rectangular pulse (Fig. 4.4a). Given a π-rotation pulse duration of $t_p^0 = \frac{\pi}{\Omega}$ (e.g. $t_p^0 = 40$ ns) where Ω is the electronic Rabi frequency, the

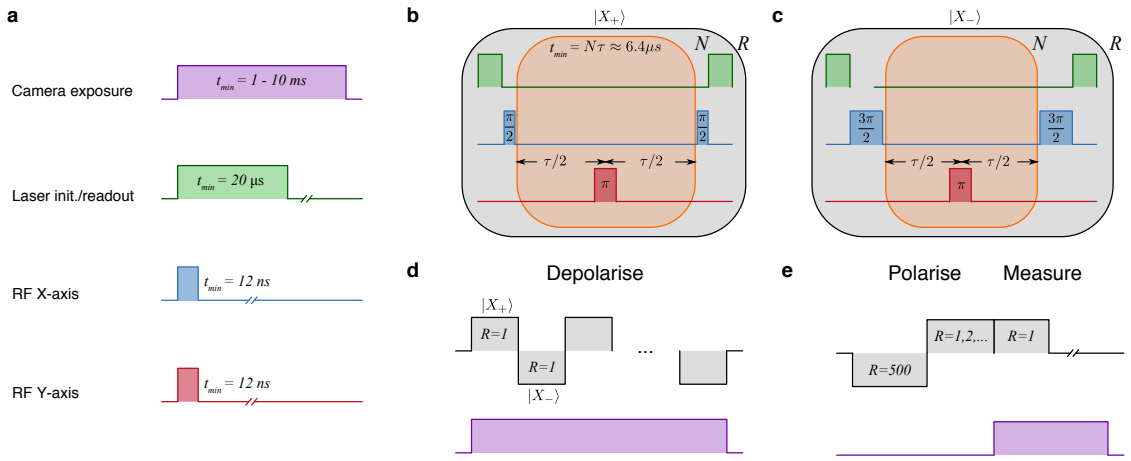

Figure 4.3: Hyperpolarisation sequences using a sCMOS. (a) Legend of pulse sequence including with minimum time for each action. (b) PolCPMG sequence, which comprises a laser initialisation, a $\pi/2$ rotation to initialise in $|X_+\rangle$, a series of π-rotations (where the rotations errors are introduced), a second $\pi/2$ rotation to project into the z-basis and a final readout laser pulse. (c) As in (b) except with an initial $3\pi/2$ rotation to initialise in $|X_-\rangle$, producing the opposite polarisation. (d) Depolarisation sequence, in which initialisation is alternated between $|X_+\rangle$ and $|X_-\rangle$ to prevent polarisation build-up. (e) Polarisation sequence, in which the bath is initially polarised in one direction (no camera exposure) then the polarisation build-up with the opposite initialisation is measured. The individual components have independent parameters (N, τ, R), facilitating the parameter exploration in the main text.

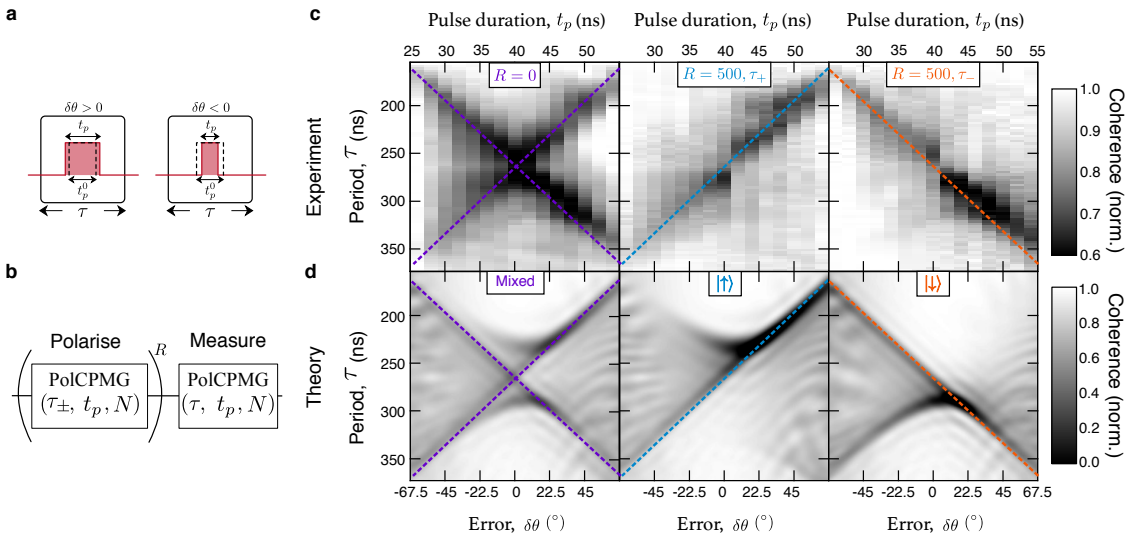

Figure 4.4: Observation of ^{13}C hyperpolarisation. **a** The flip-angle error $\delta\theta$ is controlled by the pulse duration t_p relative to the nominal duration t_p^0 corresponding to a π rotation. **b** Sequence used to probe the nuclear polarisation. **c** NV spin coherence measured with the sequence shown in **b** as a function of τ and t_p, with $R = 0$ (top plot) and with $R = 500$ at $\tau = \tau_+$ (middle) or $\tau = \tau_-$ (bottom). Parameters are $\omega_L = 1.9$ MHz, $t_p^0 = 40$ ns and $N = 32$. **d** Calculated NV spin coherence after a single application of PolCPMG, taking into account the ^{14}N hyperfine structure and inhomogeneous broadening (see details in SI). The NV is coupled to a single ^{13}C spin ($\mathcal{A}_\perp = 180$ kHz) initialised in a mixed state (top plot), in $|\uparrow\rangle$ (middle) and in $|\downarrow\rangle$ (bottom). In **c**,**d**, the dashed lines correspond to the resonance positions from Eq. (4.2).

rotational angular adjustment is defined as

$$\delta\theta = \pi \frac{t_p - t_p^0}{t_p^0}. \tag{4.4}$$

To test the spectral response of the protocol under different polarisation regimes a sequence is used that first performs R applications of PolCPMG with a fixed period $\tau = \tau_\pm$ to polarise the ^{13}C bath, followed by a single application of PolCPMG with a variable τ to probe the state of the bath (Fig. 4.4b). The coherence spectra were obtained for different values of the pulse duration t_p from 24 ns to 54 ns (in steps of 2 ns) corresponding to an error $\delta\theta$ from $-63°$ to $+63°$, under three different polarisation regimes (Fig. 4.4c). With no polarisation ($R = 0$), the bath is in a mixed state and so two resonances are visible at positions well matched by Eq. (4.2) (dashed lines in Fig. 4.4c, left). For the polarised cases (i.e. $R = 500$ at $\tau = \tau_+$ or $\tau = \tau_-$) only one of the two resonances is resolved,

indicating that the ^{13}C bath has been efficiently polarised in the $|\uparrow\rangle$ and $|\downarrow\rangle$ states for the τ_+ and τ_- cases respectively (Fig. 4.4c, middle and right).

The variations in amplitude and additional features seen in Fig. 4.4c originate from the intrinsic hyperfine splitting due to the nitrogen nucleus of the NV (here ^{14}N, which is a spin-1), which means that the NV spin may be driven slightly off-resonance depending on the ^{14}N state. Numerical simulations of the NV-^{13}C system including the ^{14}N hyperfine structure are shown in Fig. 4.4d. With the ^{13}C in a mixed state (left plot), three resonances are resolved near $t_p = t_p^0$, which translates into a single broad line in the experiment. This effect of frequency detunings is largely suppressed in some regimes, which is particularly obvious in the polarised coherence maps (Fig. 4.4d, middle and right) where for $\delta\theta > 0$ the change in coherence is larger and is mirrored in the experiment. This indicates a convergence of the spectral features of the three hyperfine states, suggesting in this regime the sequence is more robust to frequency detunings, which will be discussed more in Section 4.2.

4.2 Polarisation dynamics: rate and optimum working conditions

The relative amplitudes of the NMR spectral features act as a detection for the degree of polarisation within the sensing volume of the NV probe (corresponding to 5-10 spins typically). That is, when one of the spectral features has an amplitude of zero then the nuclear spins are completely polarised, likewise if both amplitudes are equal then the nuclear spins are perfectly mixed. As such, through measuring these amplitudes the total polarisation can be determined. To study the dynamics of the polarisation transfer, the full spectrum was taken with a the number of repetitions, R, for a given pulse duration, $t_p = 44$ ns corresponding to $\delta\theta = +18°$, and with the period set to $\tau = \tau_+ = 288$ ns polarising the ^{13}C bath in the $|\uparrow\rangle$ state. Increasing the number of repetitions. R, causes a gradual change in both amplitudes. As the nuclear spin population is polarised, the signal from the resonance that is repeated (τ_+, $|\uparrow\rangle$) decreasing to zero, while the signal from the other resonance (τ_-, $|\downarrow\rangle$) increases. Measuring the full spectrum is a good way to determine the total polarisation in situations were changes in contrast are expected (i.e.

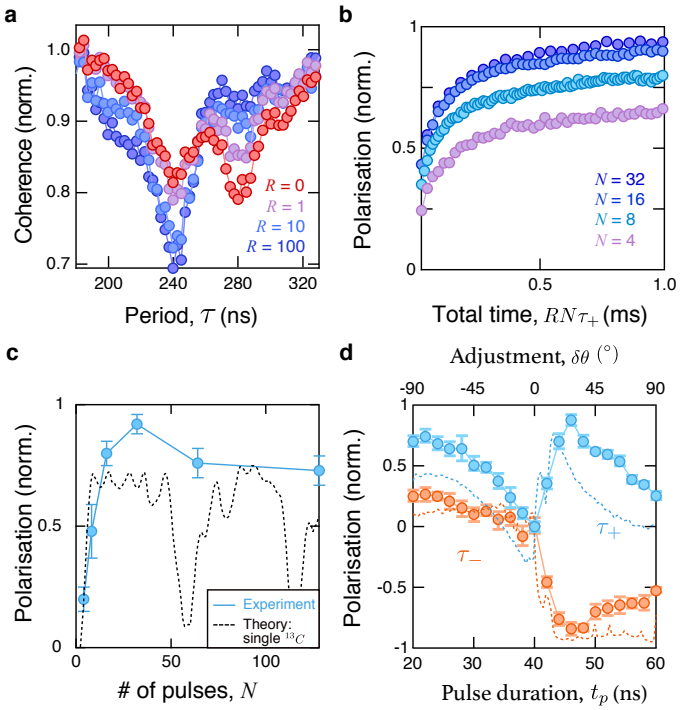

Figure 4.5: Polarisation dynamics. **a** PolCPMG spectra taken immediately after R repetitions of the PolCPMG sequence at $\tau = \tau_+ = 288$ ns, for different values of R, with $N = 32$. **b** Polarisation of the ^{13}C spin bath as a function of R plotted in terms of the total sequence time, $T = RN\tau_+$, for different values of N. A polarisation value of 1 (-1) means that all the spins within the NV sensing volume are in the $|\uparrow\rangle$ ($|\downarrow\rangle$) state. **c** Polarisation after $T = 1$ ms as a function of N. The dashed line is the theory for a single ^{13}C ($A_\perp/2\pi = 180$ kHz), including the ^{14}N hyperfine structure and inhomogeneous broadening. **d** Polarisation after $R = 500$ cycles as a function of t_p, with $N = 32$. For each value of t_p, τ was adjusted to the resulting τ_+ (blue) or τ_- (orange) resonance. Dashed lines are numerical simulations.

in the robustness tests done in Section 4.3), however, in the static detuning condition it is sufficient to measure the relative changes in the peak of a single resonance, as will be done from now on in this section.

Initially, the effect of the number of π-pulses on the polarisation rate and saturation is explored. This involves first polarising the bath with the $|X_-\rangle$ sequence for $R = 500$ (using an initial rotation of $3\pi/2$, see Section 4.1.3), followed by the $|X_+\rangle$ sequence with a varied R. The polarisation rate starts with a shape change, which is attributed to interactions with the more strongly coupled ^{13}C spin that contribute to a significant portion of the spin signal, and are more readily polarised (Fig. 4.5b). The rate of polarisation then

slows down significantly as the more remote spins are now addressed, until the polarisation reaches relative saturation after a few milliseconds. The polarisation after $T = 1$ ms increases until $N = 32$ before decreasing at larger N (Fig. 4.5c). This change in polarisation can be understood to originate from the oscillation produced by the flip-flop Hamiltonian. The optimal number of pulses (corresponds to the maximal polarisation transfer) for a single ^{13}C is expressed by Eq. (4.3), which in this case ($A_\perp = 180$ kHz) is met when $N = 32$. Including the NV hyperfine takes this simple oscillation and produces a complex polarisation efficiency spectrum (Fig. 4.5c, black dashed line), where the position of dips in efficiency is dependent on the hyperfine coupling strength. Where averaging over multiple different ^{13}C spin acts to smooth the prediction further.

Finally, the saturation polarisation after $R = 500$ cycles of the PolCPMG sequence is explored with different rotation adjustments $\delta\theta$ (via the choice of t_p), varied between $-90°$ and $+90°$. The measurement procedure involved first polarising the spin bath with a varied rotation adjustment, followed by a measurement of the polarisation. Where to remain consistent the same rotation adjustment, $\delta\theta = +18°$, was used for all of the polarisation measurements. The results shown in Fig. 4.5d indicate ineffective polarisation around $\delta\theta = 0$ due to overlap of the two resonances. After the resonances become distinct, a maximum is observed in the positive $\delta\theta$ regime for both τ_+ and τ_-, corresponding to the larger dips in contrast that were observed in the spectrum (Fig. 4.4). At the same time it is observed that negative $\delta\theta$ values produce less polarisation up until extremely large adjustments, $\delta\theta = -90°$. These results are in reasonable agreement with theory (dashed lines in Fig. 4.5d) and outline an optimal working condition for the PolCPMG sequence.

4.3 Robustness to frequency, power, and phase errors

With the optimum working conditions for PolCPMG determined ($\delta\theta \approx +30°$, $N = 32$) we now change focus to the robustness of the protocol to additionally detunings. For comparison with existing techniques the polarisation after one cycle ($R = 1$) was calculated for PolCPMG, PulsePol, and HH, under the presence of three different detunings: microwave driving frequency, $\Delta\omega$, microwave driving strength, $\Delta\Omega$, and microwave phase variation between the x- and y-axis, $\Delta\varphi$ (Fig. 4.6a). The calculation maintained a fixed evolution

time, τ, of the nominal value of τ_+ (i.e. determined with $\Delta\omega = 0$). Both PolCPMG and PulsePol show remarkable robustness to frequency detunings and importantly the polarisation remains larger than 80% for frequency detunings $|\Delta\omega| \lesssim 2.8$ MHz, which covers the experimentally relevant situation of a 1 MHz inhomogeneous broadening on top of the ^{14}N hyperfine structure of the NV (shown as black dashed lines). Unlike HH that has a particularly poor robustness to any detunings, making it incompatible for applications without a polarised NV nuclear spin and extremely precise frequency and power uniformity. Additionally, PolCPMG is much more robust than PulsePol with respect to phase errors $\Delta\varphi$ while the reverse is true for power detuning, $\Delta\Omega$, indicating that either technique could be useful depending on the uncontrolled errors that are confronted in a specific equipment.

Finally, the robustness of PolCPMG was experimentally tested by real-space mapping of the nuclear polarisation. Here, a wide-field imaging setup was used that illuminates a ~ 100 μm region of the same diamond sample as before, i.e. a 1-μm-thick layer of NV centres near the diamond surface (Fig. 4.6b). Where the polarisation of the ^{13}C nuclear spin bath was measured after the application of PolCPMG for $T = 1$ ms. Gradients in the driving frequency, $\Delta\omega$ (via the applied static magnetic field) and in the driving power, $\Delta\Omega$ (via the applied microwave field) were deliberately introduced along the x and y spatial directions respectively. Due to the magnetic field being applied by a permanent magnet and the driving field being emitted from a single wire these gradients are quite strong over a small 30×30 μm^2 region. In principle experiments can be constructed such that this magnitude of gradients exist on the millimetre to centimetre scale. Despite these strong detunings the measurement reveals a polarisation in excess of 80% over this region despite a variation of $\Delta\omega = -3.5$ to 6 MHz and of $\Delta\Omega = \pm 25\%$. Where the degree of polarisation was determined by measuring the full spectrum and comparing the two amplitudes for each pixel (Fig. 4.6d).

4.4 Conclusion

In summary, a new dynamical decoupling based hyperpolarisation protocol, PolCPMG, was developed. This protocol introduces an asymmetry in the common CPMG sequence

that removes the nuclear spin state degeneracy, allowing the technique to be used for hyperpolarisation. The polarisation rate is comparable to other driven techniques, which while slower than CR based hyperpolarisation, has significant robustness to errors that limit the use of CR hyperpolarisation. In particular, this protocol is robust to frequency, driving power, and phase detuning, which can act to restrict the use of CR and HH based hyperpolarisation. While PulsePol has a similar robustness, it involves implementing extra microwave phases, which can be experimentally difficult to realise with standard hardware. On the other hand, PolCPMG is experimentally straight forward to implement, which is a distinct advantage for scaling up and hyperpolarisation applications. As such, it is a promising route towards the goal of NV-based hyperpolarisation of macroscopic volumes of external samples, which could enable ultra-sensitive NMR spectroscopy for in-line chemical analysis or cell biology studies [202,203] or form the basis of a quantum simulator [199]. In these endeavours, the ability to directly image the nuclear polarisation over 10's of μm via near-surface NVs as demonstrated here may become an ubiquitous tool. More generally, our work paves the way to systematic engineering of error-enhanced protocols for quantum information processing and quantum sensing.

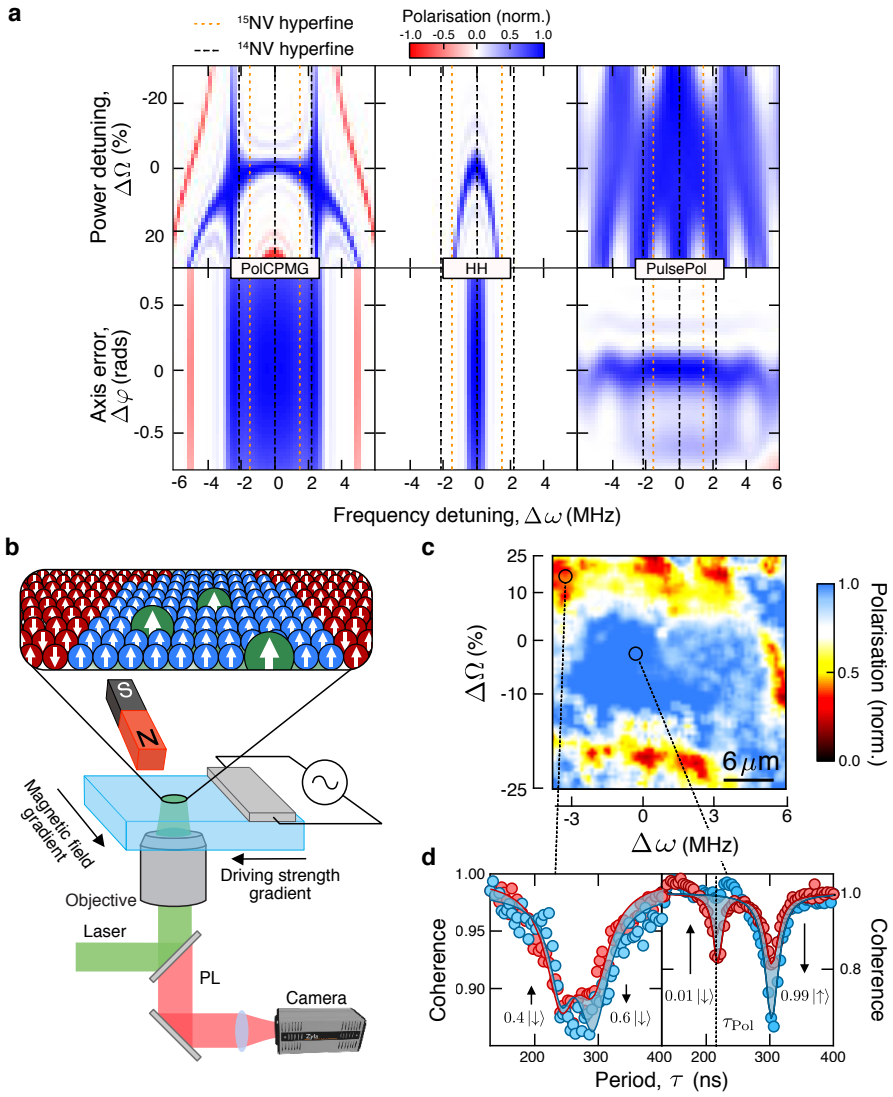

Figure 4.6: Robustness of the protocol. **a** Calculated polarisation of a single ^{13}C ($\mathcal{A}_\perp = 180$ kHz) after applying a single cycle of the PolCPMG (left column), PulsePol (middle) and HH (right) protocols, as a function of $\Delta\omega$ and $\Delta\Omega$ (top plots) and $\Delta\varphi$ (bottom). All other parameters are kept constant, set to their nominal values. For PolCPMG, we used $\delta\theta = +30°$, $N = 32$ and $\tau = \tau_+ = \tau_0(1 + \delta\theta/\pi)$. The graph shows a typical NV spin resonance spectrum, with the vertical dashed lines indicating the three ^{14}N hyperfine transitions. **b** Experimental setup to image the nuclear polarisation. **c** Polarisation map of a 30×30 μm region under deliberate gradients of $\Delta\omega$ along y and of $\Delta\Omega$ along x. **d** PolCPMG spectra from two selected regions with low polarisation (left panel) and high polarisation (right panel). The dashed vertical line indicates the value of $\tau = \tau_{\mathrm{Pol}}$ used for the polarisation step.

Conclusion to Part I

In Part I, the focus was on developing techniques that enable hyperpolarisation of nuclear spins through the NV spin. In chapter 2, cross relaxation of NV spins with electron and nuclear spins was explored to develop the experimental procedure and understanding for performing hyperpolarisation with this method. Then in chapter 3 cross relaxation induced polarisation was developed and demonstrated on both internal ^{13}C spin as well as external ^{1}H spins. This was the first time that NV spins were shown to be capable of polarising external nuclear spin species and may lead to many applications of hyperpolarisation as it is completely tunable to any spin species. As this technique is sensitive to magnetic field alignment a study was conducted to further enhance the stability of permanent magnetics that are used. With this increased sensitivity we were able to show that while the NV spin is capable of imparting polarisation onto the spin bath, if left unchecked it can also remove it. This is vitally important for hyperpolarisation application but can be controlled through placing the NV in a non-interacting state. The CRIP protocol was also compared with other NV based hyperpolarisation techniques and was found to have a increased polarisation rate, potentially making it more viable to scaling. Finally in chapter 4, a different hyperpolarisation technique was developed that utilises dynamical decoupling to transfer polarisation while maintaining significant robustness to scaling induced detunings. It remains to be seen which issue is more important for scaling hyperpolarisation, increased polarisation rate or greater resilience to error. In either case, this part has detailed avenues for both situations and laid the ground work for a universal hyperpolarisation platform to be developed in diamond.

Part II

Multi-modal microscopic imaging with diamond spin defects

Preface to Part 2

Single NV spins have been shown to be good quantum sensors for magnetic fields (B), electric fields (E), temperature (T), and stress/strain (σ). Imaging such fields at the nano/micro-scale is useful for learning about the source of these fields, e.g. electronic processes in a material or device of interest. Single NV measurements, either in bulk or through a scanning tip, have accessed a great wealth of information about these fields and the interplay of different materials. However, due to only using a single NV orientation the amount of obtainable vectorial information is restricted. While imaging using a 2D ensemble of NV spins can overcome this restriction, experiments so far have been focused mainly on magnetic fields, as measuring the much smaller effects of $E/T/\sigma$ is challenging. In the second part of the thesis, we develop a methodology based on ensembles of NV spins in a single crystal to allow multi-modal imaging of full vector fields and illustrate it through a number of example applications. Utilising a more complete version of the ground state Hamiltonian than is typically used, we show that the full E-vector or the full σ-tensor can be imaged simultaneously with the B-vector. This amounts to a full ground state Hamiltonian fitting with all four NV orientations to obtain global information about the fields impinging onto or embedded inside of the diamond.

In chapter 5, magnetic and electric fields are imaged with ensembles of NVs. This multi-modal measurement technique is developed from the simple single NV case to the ensemble case, in order to extract the full vector information. Using this technique electric fields intrinsic to the diamond through surface related band-bending are investigated. The electric field is determined for a series of different NV probe depths, for two surface terminations (hydrogen and oxygen), and for a series of different surface treatments. These measurements constitute a new characterisation method to enable greater control of dia-

mond device fabrication by new information for feedback. Finally, both the magnetic and electric fields are mapped from a current carrying electronic device that has a non-trivial bulk charge injection.

In chapter 6, stress that is embedded into the diamond is imaged. The technique for extracting the full stress tensor is developed and experimentally verified through the engineering of stress patterns. Various forms of stress generation are measured: scratches, indents, implantation, and fabrication. Imaging reveals the degree of stress induced by these modifications, and as a consequence we show that stress needs to be considered when taking precision measurements lest the stress contribution be mistaken as a magnetic field.

5

Imaging electric fields from band-bending in diamond

Imaging and detection of phenomena in condensed matter systems often involves measuring the magnetic field that is produced by the sample of interest. Many sensing systems are sensitive to magnetic fields – SQUID, atomic vapour cells, nitrogen vacancies, etc. – which are often used to scan across the sample on an atomic force microscope (AFM) to image the magnetic landscape. A great wealth of knowledge is contained in the location, strength, and direction of the magnetic field – the current distribution, ferromagnetic edge states, spin hall effect, etc. – which are related to the movement and location of charges and spins. This charge migration and accumulation is also accompanied by potentials and their related electric fields. Hence, in order to obtain a full picture of these phenomena it is important to measure both the magnetic and electric fields.

In this chapter a methodology to simultaneously image magnetic (B) and electric (E) fields is developed. This new technique is used to perform measurements of electric fields that are intrinsic to, and embedded inside of, the diamond from surface induced band-bending. While electric fields have been measured with NV spins before [1, 47, 173], this is the first time they have been imaged, indicating a clear step towards utilising the technique on intricate and interesting devices that are sensitive to the exact electrical conditions of the diamond either as a conductor or an insulting substrate. The multimodal technique developed in this thesis opens up a new imaging technique for the NV

system. Here this technique is used to investigate the effect of 3D band banding near interfaces for diamond surface studies and potential optimisation of surface chemistry. Additionally, the technique is also used to study embedded electronic devices and their effect on the substrate electronic physics.

5.1 Simultaneous magnetic and electric field imaging

In this section we develop our approach to imaging both magnetic and electric fields. To begin with the principles of electrometry with a single NV is investigated, including optimising the sensitivity of the NV spin to electric fields. Then this is extended to measurements with NV ensemble, showing that it is possible to extract the full E and B vectors simultaneously by using information from all four orientations.

5.1.1 Electrometry with a single NV

We first develop an understanding of how the NV spin responds to electric fields and how this can be extracted in the ensemble case. To this aim, the Hamiltonian of a single NV centre and its dependence on electric fields is discussed before extending to ensemble measurements.

The spin Hamiltonian of the NV electron spin ($S = 1$) in the presence of a magnetic field $\mathbf{B} = (B_X, B_Y, B_Z)$ and electric field $\boldsymbol{\mathcal{E}} = (\mathcal{E}_x, \mathcal{E}_y, \mathcal{E}_z)$ is given by [1, 173]

$$\mathcal{H} = (D + k_{\parallel}\mathcal{E}_z)(S_Z^2 - 2/3) + \gamma_{\mathrm{NV}}\mathbf{S}\cdot\mathbf{B} - k_{\perp}\mathcal{E}_x(S_X^2 - S_Y^2) + k_{\perp}\mathcal{E}_y(S_X S_Y + S_Y S_X), \tag{5.1}$$

where $\mathbf{S} = (S_X, S_Y, S_Z)$ are the spin-1 operators, $D \approx 2870$ MHz is the temperature-dependent zero-field splitting, $\gamma_{\mathrm{NV}} = 28.035(3)$ GHz/T is the isotropic gyromagnetic ratio, and $k_{\parallel} = 0.35(2)$ Hz cm/V and $k_{\perp} = 17(3)$ Hz cm/V are the electric susceptibility parameters [1, 173]. Here XYZ is the reference frame of the NV defect structure as defined in Fig. 5.1a, where Z is the major symmetry axis defined by the direction joining the nitrogen and the vacancy, and X is a minor symmetry axis defined as being orthogonal to Z and also contained within one of the three reflection planes.

The frequencies of the $|0\rangle \rightarrow |\pm 1\rangle$ spin transitions, $f_{\pm}$, can be computed by numer-

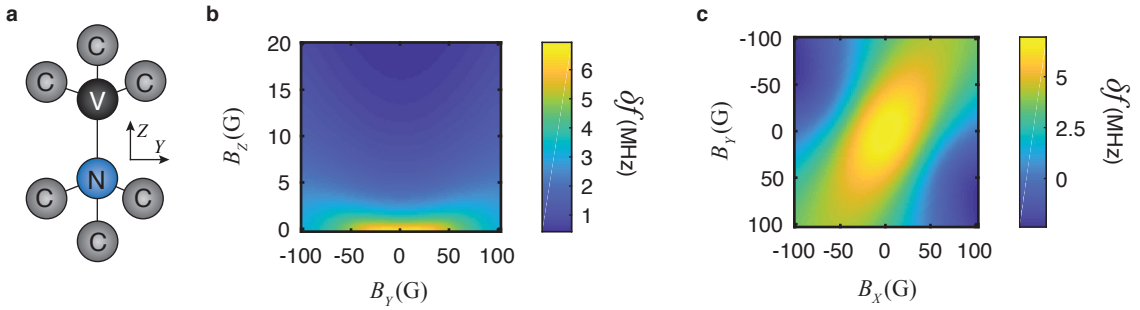

Figure 5.1: Electric field sensitivity for a single axis. **a** Single NV spin where XYZ is the reference frame associated with the NV defect structure, with Z being along a $\langle 111 \rangle$ direction and X the minor axis [46]. **b**,**c** Shift of the NV spin transition, $\delta f = f_+(\boldsymbol{\mathcal{E}}) - f_+(0)$, due to an electric field of strength $|\boldsymbol{\mathcal{E}}| = 5 \times 10^5$ V/cm, plotted as a function of (B_Y, B_Z) with $B_X = 0$ in **b** and as a function of (B_X, B_Y) with $B_Z = 0$ in **c**.

ically diagonalising the above Hamiltonian. For ease of description, in what follows we will make use of the approximation

$$f_\pm(\boldsymbol{\mathcal{E}}, \mathbf{B}) \approx D + k_\parallel \mathcal{E}_z + 3\Lambda \pm \sqrt{\mathcal{R}^2 - \Lambda \mathcal{R} \sin\alpha \cos\beta + \Lambda^2} \tag{5.2}$$

where the various quantities are are defined as

$$\Lambda = \frac{\gamma_e^2 B_\perp^2}{2D}, \qquad \mathcal{R} = \sqrt{\gamma_{\mathrm{NV}}^2 B_Z^2 + k_\perp^2 \mathcal{E}_\perp^2}, \qquad B_\perp = \sqrt{B_X^2 + B_Y^2}, \qquad \mathcal{E}_\perp = \sqrt{\mathcal{E}_x^2 + \mathcal{E}_y^2},$$
$$\tan\alpha = \frac{k_\perp \mathcal{E}_\perp}{\gamma_{\mathrm{NV}} B_Z}, \qquad \beta = 2\phi_B + \phi_F, \qquad \tan\phi_B = \frac{B_Y}{B_X}, \qquad \tan\phi_F = \frac{\mathcal{E}_y}{\mathcal{E}_x}. \tag{5.3}$$

This approximation is valid under the situation where $\Lambda, \mathcal{R} \ll D$ [46], which is a good approximation for the cases explored in this section. The numerical simulation use the full Hamiltonian to avoid any issues with the approximation.

The expression of $\mathcal{R}$ describes the interplay between the magnetic and electric fields. Which results in the sensitivity to the transverse electric field ($\mathcal{E}_\perp$) becoming maximised when the longitudinal component of the magnetic field (B_Z) is minimised and to a lesser extent, when the transverse magnetic field ($B_\perp$) is minimised, due to the Λ^2 term in Eq. (5.2). To illustrate this, a simulation of the shift $\delta f = f_+(\boldsymbol{\mathcal{E}}) - f_+(0)$ caused by an electric field of $|\boldsymbol{\mathcal{E}}| = 5 \times 10^5$ V/cm perpendicular to the NV axis is plotted as a function of (B_Y, B_Z) in Fig. 5.1b. We see that there is indeed a dramatic decrease in the expected

NV frequency shift with B_Z, e.g. from $\delta f \approx 7$ MHz at zero magnetic field to $\delta f \approx 1$ MHz with just $B_Z = 10$ G, and a milder effect of the transverse magnetic field, for instance the shift is still $\delta f \approx 5$ MHz under $B_Y = 50$ G (with $B_Z = 0$). There is also a dependence on the orientation of $\mathbf{B}$ in the transverse (XY) plane as shown in Fig. 5.1c, which is related to the direction of both $\mathbf{B}$ and $\boldsymbol{\mathcal{E}}$ relative to the defect minor axis X, as captured by the $\cos\beta$ term in Eq. (5.2). For transverse magnetic field strengths of the order of 50 G, the loss of sensitivity due to a non-optimal angle β is relatively mild (a factor 2 at most), and as such careful alignment of $\mathbf{B}$ in the transverse plane to match a given direction of $\boldsymbol{\mathcal{E}}$ is not critical. Note that the shift induced by the longitudinal electric field ($\mathcal{E}_Z$) is usually much smaller than that from $\mathcal{E}_\perp$ because $k_\parallel \ll k_\perp$, even though it does not decrease with the application of a magnetic field.

5.1.2 Multi-modal sensing with NV ensembles

In general, measuring the two spin transition frequencies $f_\pm$ from a single NV centre gives access to only a single scalar quantity, for instance B_Z knowing $B_\perp$ and $\mathcal{E}_\perp$, or $\mathcal{E}_\perp$ knowing B_Z and $B_\perp$. However, we will show that it is possible to extract much more information using an ensemble of NV centres in a single crystal diamond, namely the full vector components of both $\boldsymbol{\mathcal{E}}$ and $\mathbf{B}$ (six parameters in total) can be inferred simultaneously. In essence, this is because an NV ensemble provides four independent measurements since Z can be along one of the four <111> crystal directions, denoted $Z_{K=A..D}$. As a result, there are eight spin transition frequencies to be measured, which will be shown to be sufficient to extract the six unknown field components, in addition to the zero-field splitting D.

In practice, however, measuring the eight spin transition frequencies is non trivial as they typically overlap in a small magnetic field. To circumvent this problem, we apply a bias magnetic field $\mathbf{B_0}$ carefully oriented so that all eight resonances can be resolved in an ODMR spectrum [45] (Fig. 5.2a). This strategy and other similar strategies have been used to measure the vector components of a small magnetic field δB generated by current flow in graphene [21,204,205] and many other condensed matter systems [45,100,151,206–213]. Here we extend this strategy to allow measurement of electric field at the same time. For electrometry, $\mathbf{B_0}$ must satisfy several criteria:

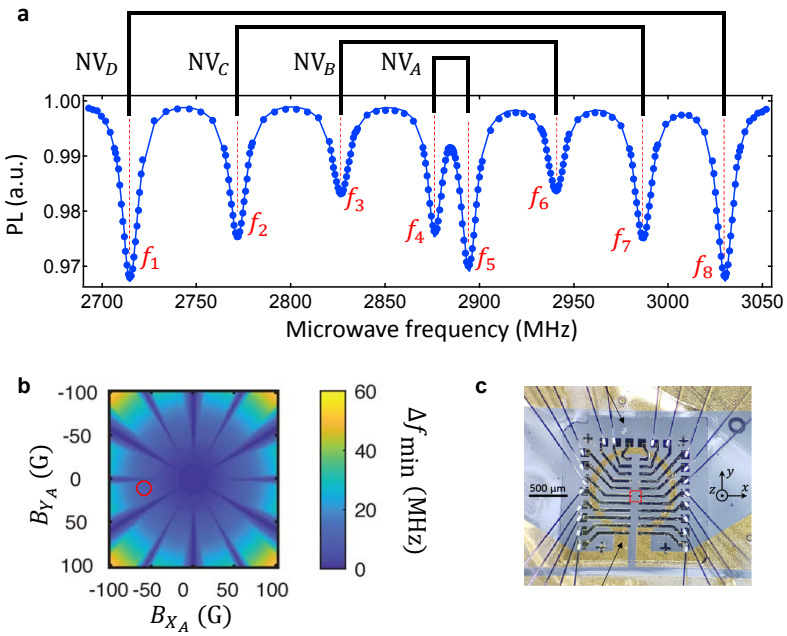

Figure 5.2: Optimisation for electric field ensemble measurements a Typical ODMR spectrum measured under this magnetic field $\mathbf{B}_0$, and conventions for the NV transition frequencies $\{f_i\}_{i=1..8}$ and for the NV families $\{\mathrm{NV}_K\}_{K=A..D}$. The solid line is a fit with eight Lorentzian lines with free amplitudes and widths. **b** Minimum separation between the eight ODMR lines as calculated from Eq. (5.4), as a function of the transverse magnetic field (B_{X_A}, B_{Y_A}) relative to Z_A, which is the symmetry axis of the NV family optimised for electric field sensitivity (i.e., $B_{Z_A} = 0$). The red circle indicates the regime used in the experiments, which corresponds to a magnetic field with Cartesian components $\mathbf{B}_0 \approx (35, 13, -50)$ G in the lab frame xyz. **c** Photograph of a diamond used in this study with the lab frame axes. The red box indicates the typical size of the imaging.

1. The direction of $\mathbf{B}_0$ is chosen perpendicular to one of the $\langle 111 \rangle$ directions (e.g., $\mathbf{B}_0 \perp Z_A$) in order to maximise the sensitivity of the corresponding NV centres (family NV_A) to electric fields.

2. The direction of $\mathbf{B}_0$ within the transverse plane is varied so that the projections of $\mathbf{B}_0$ along the four NV axes $Z_{K=A..D}$ are as distinct to each other as possible.

3. The amplitude $|\mathbf{B}_0|$ is chosen as a trade-off between electric field sensitivity which prescribes $|\mathbf{B}_0|$ to be minimised (see Fig. 5.1) and sufficient spacing between adjacent ODMR lines (so they can be resolved given their linewidth).

To illustrate the last two points, we calculated the minimum splitting between any of the

eight ODMR lines, $\{f_i\}_{i=1..8}$, defined by

$$\Delta f_{\min} = \min\left(\sqrt{(f_1 - f_8)^2}, \sqrt{(f_1 - f_7)^2}, \ldots, \sqrt{(f_7 - f_8)^2}\right) , \tag{5.4}$$

as a function of (B_{X_A}, B_{Y_A}) when $B_{Z_A} = 0$ (i.e., $\mathbf{B}_0 \perp Z_A$) and $\boldsymbol{\mathcal{E}} = \mathbf{0}$ (Fig. 5.2b). In experiments, we typically aim for a nominal minimum separation $\Delta f_{\min} \sim 20$ MHz, which allows variations in the ODMR frequencies across the field of view of several MHz to be measured. As can be seen in Fig. 5.2b, this requires a magnetic field strength of the order of $|\mathbf{B}| \sim 60$ G, with a wide range of directions allowed within the X_A, Y_A plane. A typical experimental ODMR spectrum is shown in Fig. 5.2a produced with a magnetic field of $\mathbf{B}_0 = (35, 13, -50)$ G, in the lab frame xyz defined in Fig. 5.2c. With this ODMR spectrum we define our convention to label the eight NV resonance frequencies and the four NV families. With this $\mathbf{B}_0$, the symmetry axes for the four NV families have unit vectors expressed as follows in the xyz lab frame:

$$\mathbf{u}_{\mathrm{NV}_A} = \left(0, \sqrt{\frac{2}{3}}, -\sqrt{\frac{1}{3}}\right) \tag{5.5}$$

$$\mathbf{u}_{\mathrm{NV}_B} = \left(\sqrt{\frac{2}{3}}, 0, \sqrt{\frac{1}{3}}\right) \tag{5.6}$$

$$\mathbf{u}_{\mathrm{NV}_C} = \left(0, -\sqrt{\frac{2}{3}}, -\sqrt{\frac{1}{3}}\right) \tag{5.7}$$

$$\mathbf{u}_{\mathrm{NV}_D} = \left(-\sqrt{\frac{2}{3}}, 0, \sqrt{\frac{1}{3}}\right) . \tag{5.8}$$

To illustrate how the presence of electric fields affects the ODMR spectrum, we show ODMR data from a sample described in Section 5.2.6 (PL image shown in Fig. 5.3a). The ODMR spectra of selected regions are shown in Fig. 5.3b-d when optimised for simultaneous vector electrometry and magnetometry (b-c), and when optimised for just magnetic field sensing (d). The spectra in Fig. 5.3b are taken from two regions of low electric field and show no visible shift in the NV frequencies (relative to each other), illustrating the good uniformity of $\mathbf{B}_0$ over these length scales (20 μm separate the two plotted regions). However, in Fig. 5.3c there is a clear difference between the two spectra, where the blue spectrum corresponds to a large $\mathcal{E}_z$ (as will be explained in Section 5.2.6). The central

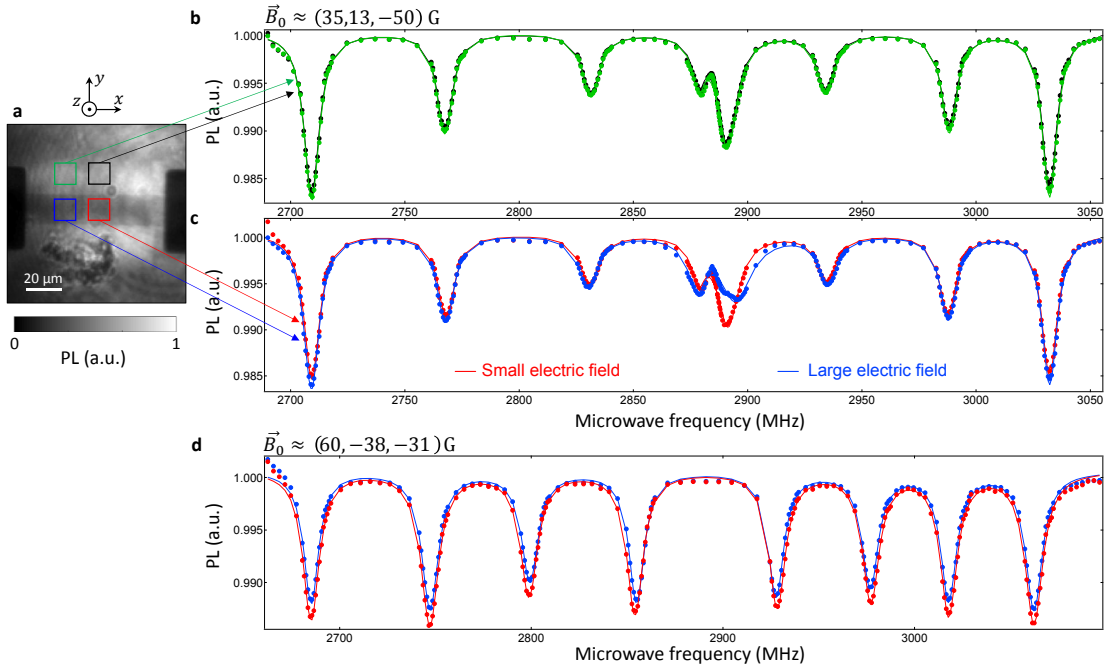

Figure 5.3: Comparision of ODMR for different electric fields a PL image of a sample described in Section 5.2.6. **b**, **c** ODMR spectra averaged over the regions delimited by the square boxes in (a), where the blue box corresponds to a larger $\mathcal{E}_z$ compared to the other 3 boxes (see details in Section 5.2.6), recorded under a bias magnetic field $\mathbf{B}_0 \approx (35, 13, -50)$ G. **d** ODMR spectra of the same regions as in (c) but under a magnetic field $\mathbf{B}_0 \approx (60, -38, -31)$ G. In (**b** - **d**), the solid lines are data fits with eight Lorentzian lines with free amplitudes and widths. This figure is adapted from Ref. [187].

lines (f_4 and f_5, family NV_A) exhibit shifts by up to 4 MHz (based on a Lorentzian fit of the whole spectrum) as well as an extra broadening, compared with the reference red spectrum. The other lines are also slightly shifted, which is observable for f_3 and f_6 (family NV_B), and continues to diminish in strength as the NV families experience a larger B_Z (NV_C and NV_D). Under a non-optimised $\mathbf{B}_0$ (Fig. 5.3d) where all the NV families have a significant B_{Z_K} component. These observations are consistent with a change in electric field between the two regions, which shifts the NV frequencies to an extent that depends on the angle formed between $\mathbf{B}_0$ and the NV symmetry axis (see Fig. 5.1a).

The broadening of f_4 and f_5 seen in Fig. 5.3c is attributed to a combination of two effects. First, the electric field associated with this sample is expected to be non-uniform across the thickness of the NV layer, causing an inhomogeneous broadening. The second source of apparent broadening is caused by a splitting of each NV line into two lines cor-

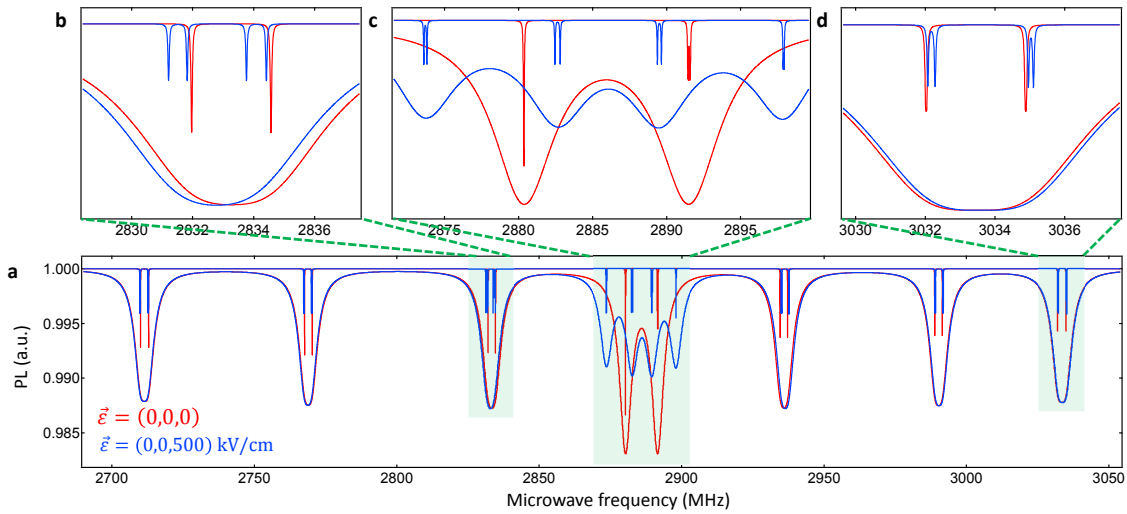

Figure 5.4: Simulation of the effect of electric field on an ensemble ODMR a ODMR spectrum obtained by computing the 32 transition frequencies (see details in text) and applying a Lorentzian lineshape with a fixed arbitrary amplitude and a full width at half maximum (FWHM) of 5 MHz (broad lines, comparable to those in the experiment) or 50 KHz (narrow lines, for ease of visualisation). The magnetic field is taken to be $\mathbf{B}_0 \approx (35, 13, -50)$ G as in the experiment, while the electric field is null for the red spectrum, and $\boldsymbol{\mathcal{E}} = (0, 0, 500)$ kV/cm for the blue spectrum. (**b** - **d**) Close-up views of **a**.

responding to the two sub-groups of NV centres distinguished by their orientation, i.e. N-V (where the vacancy is closer to the diamond surface than the nitrogen atom) or V-N (the vacancy is closer). In the absence of electric field, the NV transition frequencies are invariant under this inversion, but this is no longer the case in the presence of an electric field [46, 214], especially when the axial component of the magnetic field is vanishing ($B_{Z_A} \sim 0$). To illustrate this, we computed the transition frequencies for the eight possible NV orientations (four directions and NV/VN inversion) and generated an ODMR spectrum by applying a Lorentzian lineshape to each resonance.

For completeness we also included the hyperfine interaction of the NV electron spin with the ^{15}N nuclear spin (spin-$\frac{1}{2}$), so that the total Hamiltonian of the system is

$$\begin{aligned} \mathcal{H} \quad &= (D + k_{\parallel}\mathcal{E}_z)(S_Z^2 - 2/3) + \gamma_{\mathrm{NV}}\mathbf{S}\cdot\mathbf{B} + k_{\perp}\mathcal{E}_y(S_X S_Y + S_Y S_X) \\ &\quad -k_{\perp}\mathcal{E}_x(S_X^2 - S_Y^2) - \gamma_n B_Z I_Z + A_{\parallel} S_Z I_Z + A_{\perp}\left(S_X I_X + S_Y I_Y\right), \end{aligned} \tag{5.9}$$

where $\mathbf{I} = (I_X, I_Y, I_Z)$ is the nuclear spin operator, $\gamma_n = -4.316$ MHz/T is the nuclear

gyromagnetic ratio, and $A_{\parallel} = 3.03$ MHz and $A_{\perp} = 3.65$ MHz are the hyperfine parameters [88]. One thus has a total of 32 lines in the ODMR spectrum (2 electron spin transitions for each of the eight possible NV orientations and the 2 possible nuclear spin states), although some of them are nearly degenerate resulting in only eight lines being usually resolvable under our experimental conditions (due to the intrinsic linewidth of 1-2 MHz in our samples [210] and additional power broadening). Illustrative simulated spectra are shown in Fig. 5.4a, obtained using $\mathbf{B}_0 \approx (35, 13, -50)$ G as in the experiment, and an electric field either null (red spectrum) or of $\boldsymbol{\mathcal{E}} = (0, 0, 500)$ kV/cm (blue). As expected, the presence of an electric field affects especially the central lines (called f_4 and f_5 according to our previous definition), which split further apart from each other, and additionally split into two sub-lines corresponding to the two possible orientations within family NV_A (i.e. N-V vs. V-N, see Ref. [46,214]), separated by nearly 9 MHz. A higher resolution spectrum (sharp lines in Fig. 5.4) reveal additional splittings by < 400 kHz caused by the hyperfine interaction, which is highly suppressed for a purely transverse magnetic field. The other lines are also shifted overall by the electric field, where the high-resolution spectrum (Figs. 5.4c,d) reveals a small splitting induced by the orientation inversion (N-V vs. V-N) on top of the usual hyperfine splitting of ≈ 3 MHz.

5.1.3 Fitting procedure

We now describe our procedure to analyse the ODMR data and infer both the magnetic field $\mathbf{B}$ and electric field $\boldsymbol{\mathcal{E}}$ simultaneously. To determine the unknown values $(D, B_x, B_y, B_z, \mathcal{E}_x, \mathcal{E}_y, \mathcal{E}_z)$ from the measured frequencies $\{f_i\}_{i=1..8}$, we seek to minimise the root-mean-square error function

$$\varepsilon(D, \mathbf{B}, \boldsymbol{\mathcal{E}}) = \sqrt{\frac{1}{8}\sum_{i=1}^{8} \left[f_i - f_i^{\mathrm{calc}}(D, \mathbf{B}, \boldsymbol{\mathcal{E}})\right]^2} \tag{5.10}$$

where $\{f_i^{\mathrm{calc}}(D, \mathbf{B}, \boldsymbol{\mathcal{E}})\}_{i=1..8}$ are the calculated frequencies obtained by averaging over both the NV orientation for the corresponding NV family and over the nuclear spin state ($m_I = \pm 1/2$). Each frequency $f_i(D, \mathbf{B}, \boldsymbol{\mathcal{E}}, \mathbf{u}_{\mathrm{NV}_K}, m_I)$ is obtained by projecting $\mathbf{B}$ and $\boldsymbol{\mathcal{E}}$ into the NV reference frame knowing the orientation of the Z axis, numerically computing the

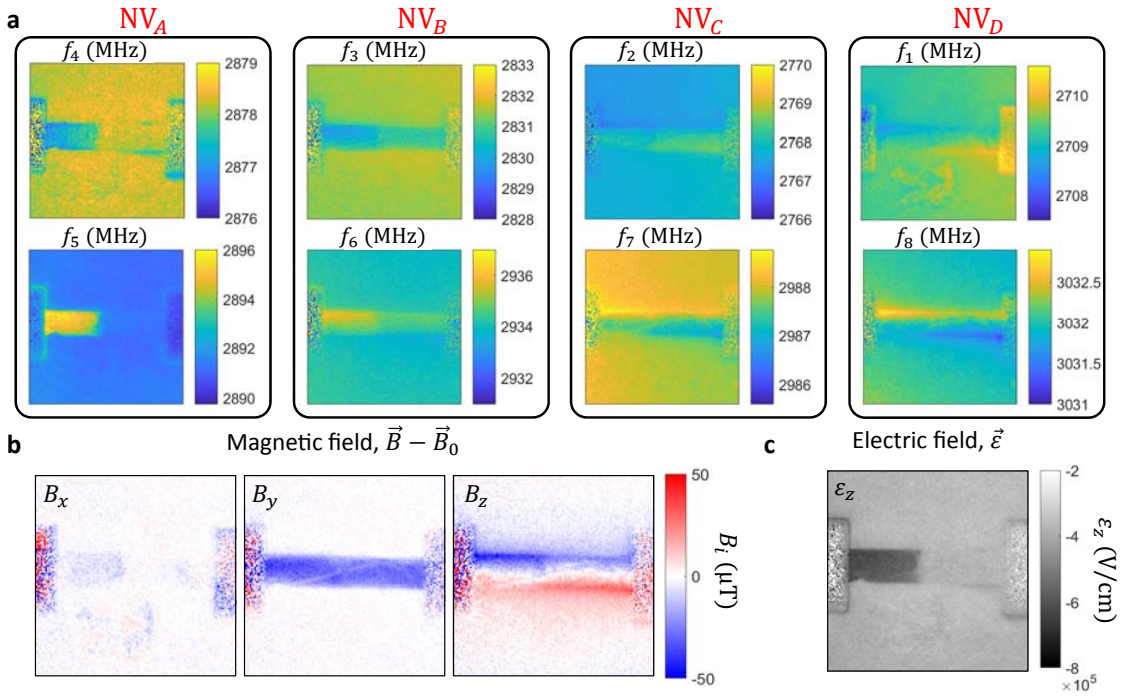

Figure 5.5: Fitting procedure for magnetic and electric fields. **a** Maps of the frequencies $\{f_i\}_{i=1..8}$ obtained by fitting the ODMR spectrum at each pixel. The region shown is the same as that in Fig. 5.3a, and the bias magnetic field is $\mathbf{B}_0 \approx (35, 13, -50)$ G. (b,c) Maps of the magnetic field components **b** and out-of-plane electric field component $\mathcal{E}_z$ **c** obtained after reconstruction. In **b** a plane subtraction was applied to remove the background field $\mathbf{B}_0$.

eigenvalues of the Hamiltonian Eq. (5.9), and deducing the relevant transition frequencies.

While it is possible in principle to fit all seven parameters, we found that the fit would not reliably converge for all the pixels within the field of view, resulting in very noisy electric field images and hence large uncertainties. We conclude that the noise level of our measurements (the uncertainty in the $\{f_i\}_{i=1..8}$ data is 20-60 kHz for a single pixel, see Table B.1) is insufficient to perform a full vector fit for each pixel. On the other hand, we found that fixing $(\mathcal{E}_x = 0, \mathcal{E}_y = 0)$ and letting only $\mathcal{E}_z$ free, which is the expected non-zero component (see section 5.2), solved the convergence issues resulting in much smoother images. In all the data we therefore fit only the five parameters $(D, B_x, B_y, B_z, \mathcal{E}_z)$, while fixing $(\mathcal{E}_x = 0, \mathcal{E}_y = 0)$. We also note that because the measurement and model are averaging over the N-V and V-N sub-families, there is an ambiguity in the overall sign of the determined electric field. In other words, $\boldsymbol{\mathcal{E}}$ and $-\boldsymbol{\mathcal{E}}$ yield the same ODMR spectrum,

hence one measures $|\mathcal{E}_z|$ when $(\mathcal{E}_x = 0, \mathcal{E}_y = 0)$. Solutions to determine the sign of $\boldsymbol{\mathcal{E}}$ include using preferentially-oriented NV centres [214, 215] and applying an external electric field [47].

As an illustration of the reconstruction process, Fig. 5.5a shows the eight frequency maps obtained for the same area as in Fig. 5.3a. In this example, a current $I = 700$ μA is applied to a conductive channel patterned on the diamond surface (this device will be discussed in detail in section 5.2.6). This current produces a magnetic field distribution through the Bio-Savart law, resulting in a complex landscape in the frequency maps. After reconstruction following the procedure outlined above, one obtains the maps of the 3 vector components of $\mathbf{B}$ (Fig. 5.5b) as well as $\mathcal{E}_z$ (Fig. 5.5c). The magnetic field maps are consistent with the magnetic field expected from a uniform current density in a flat wire [21]. On the other hand, the $\mathcal{E}_z$ map shows a very different distribution with minimal cross-talk with the magnetic field, illustrating the effectiveness of the reconstruction method.

5.1.4 Experimental apparatus

The NV imaging set-up is a custom-built wide-field fluorescence microscope similar to that used in chapter 4 and in Refs. [21, 45]. The diamonds were glued on a glass cover slip patterned with a microwave waveguide, connected to a printed circuit board (PCB) with silver epoxy. The diamond devices were electrically connected to the cover slip via wire bonding, and to the PCB board with silver epoxy. The voltage through the device (Section 5.2.6) was applied using a source-meter unit (Keithley SMU 2450) operated in constant voltage mode. All measurements were performed in an ambient environment at room temperature, under a bias magnetic field $\mathbf{B}_0$ generated using a permanent magnet.

Optical excitation from a 532 nm Verdi laser was gated using an acousto-optic modulator (AA Opto-Electronic MQ180-A0,25-VIS), beam expanded (5x) and focused using a wide-field lens ($f = 200$ mm) to the back aperture of an oil immersion objective lens (Nikon CFI S Fluor 40x, NA = 1.3). The photoluminescence (PL) from the NV centres is separated from the excitation light with a dichroic mirror and filtered using a bandpass filter before being imaged using a tube lens ($f = 300$ mm) onto a sCMOS camera (Andor Zyla 5.5-W USB3). Microwave excitation was provided by a signal generator

(Rohde & Schwarz SMBV100A) gated using the built-in IQ modulation and amplified (Mini-Circuits ZHL-16W-43+) before being sent to the sample board. A pulse pattern generator (Spincore PulseBlasterESR-PRO 500 MHz) was used to gate the excitation laser and microwaves and to synchronise the image acquisition. The total CW laser power at the sample was 300 mW. The optically detected magnetic resonance (ODMR) spectra of the NV layer were obtained by sweeping the microwave frequency while repeating the following sequence: 10 μs laser pulse, 1 μs wait time, 300 ns microwave pulse with total acquisition times of several hours typically.

5.2 Applications to measurements of surface band-bending

At the interfaces of a semiconductor with another material the local charge distribution in the semiconductor is modified to account for differences in the two materials' electronic band structure. This amounts to a migration and accumulation of charges at these interfaces, which is known as band-bending. Consequently, the precise determination of the band-bending contains information on how these interfaces interact and is crucial to the development of electronic devices, such as field-effect transistors (FETs) [216–218]. Additionally, it is vital to improving the design of specific semiconductor junctions and solid-state qubit devices [219–221]. While some techniques have been developed in order to measure the band-bending at interfaces, they are surface sensitive, and thus are unable to determine information about the band-bending extent [219–221]. This restriction motivates the development of techniques that can probe locally inside of the material and access information about the depth of the band-bending.

Quantum sensors based on semiconductor defects offer a possible solution to this problem as they can be placed virtually anywhere inside the semiconductor. To probe band-bending, one approach is to measure the associated electric field, related to band-bending via the standard relation

$$\boldsymbol{\mathcal{E}}(\mathbf{r}) = \frac{1}{q}\nabla E_V(\mathbf{r}), \tag{5.11}$$

where $E_V(\mathbf{r})$ is the energy of electrons at the valence band maximum relative to the Fermi

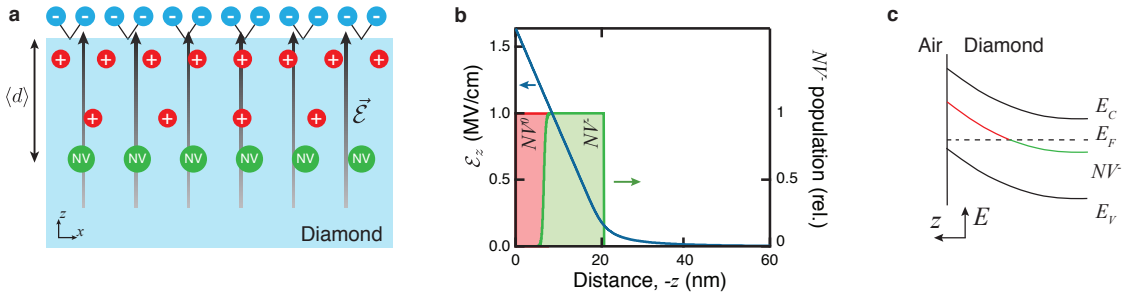

Figure 5.6: Mapping band-bending with in-situ quantum sensors. a, Principle of the experiment, where NV sensors (green dots) probe the electric field associated with surface band-bending, here visualised as a distribution of space charge density. **b**, Calculated electric field profile for a typical (001)-oriented, oxygen-terminated diamond surface, modelled as a layer of surface acceptor defects with a density of states centred at 1.5 eV above the valence band maximum [229] and a surface density $D_{sd} = 0.1$ nm^{-2}. The implanted substitutional nitrogen and NV defects are taken to be uniformly distributed over the range $d = 0-20$ nm (i.e. $\langle d \rangle = 10$ nm), with a total areal density of 0.1 nitrogen/nm^2. The green line is the NV$^-$ population at equilibrium, and the green (red) shading represents the region where the NV$^-$ (NV^0) charge state is dominant. **c**, band diagram near the surface, where E_C is the conduction band minimum, E_V the valence band maximum, E_F the Fermi level, and NV$^-$ represents the charge transition level of the NV centre, i.e. NV$^-$ is the stable charge state when this level is below E_F. This figure is adapted from Ref. [187].

level (q is the electron charge). This is possible with the NV centre in diamond, which has been shown to be sensitive to electric fields [47, 222] and can be positioned with a resolution of less than 1 nm in depth and 20 nm in the x and y direction through precision implantation [223–225]. Making them ideal candidates for a proof of principle experiment of measuring band-bending in semiconductors via quantum sensors. In the following we will focus on diamond, however, the concept is general and could be applied in the future to other semiconductor systems that host a quantum defect exhibiting a Stark effect, with promising candidates recently found in silicon [226] and silicon carbide [227, 228].

5.2.1 Probing band-bending via electrometry

At the diamond surface the bands bend to neutralise any surface charge due to ionised adsorbates or surface defect states, resulting in an electric field perpendicular to the surface with a magnitude $\mathcal{E}_z(z) = \frac{1}{q}\frac{dE_V}{dz}$ (Fig. 5.6a). To probe this electric field, nitrogen ions were implanted to form NV centres [210], following a spatial distribution that can be

approximated as uniform over the depth range $d = 0 - 2\langle d \rangle$, where $\langle d \rangle$ is the (tunable) mean implantation depth [175]. To estimate $\mathcal{E}_z$, we first consider the case of commonly used oxygen-terminated diamond. It was recently found that such samples typically host surface defects that introduce an acceptor level into the band-gap, with densities (D_{sd}) as high as 1 nm^{-2} [229]. An example of a calculated electric field profile for this scenario (with parameters representative of our implanted samples) is plotted in Fig. 5.6b, predicting a maximum value at the surface of $\mathcal{E}_z \approx 1.6$ MV/cm and a characteristic decay length of ~ 15 nm. Where $\mathcal{E}_z$ is positive (i.e., the electric field points towards the surface) which corresponds to the bands bending upward (Fig. 5.6c), as expected from a positive space charge density near the surface (see Fig. 5.6a).

As a consequence of the band-bending, only NVs deeper than a certain threshold (here ≈ 7 nm for $\langle d \rangle = 10$ nm) exist in the negatively charged state (NV$^-$) usable for sensing (Fig. 5.6c). Subsequently, greater control over band-bending can lead to creating stable NV spin (either ensemble or single) that are extremely close (<5 nm) from the diamond surface. This is extremely useful for sensing and hyperpolarisation application as the NV depth limits the interaction strength. The expectation value for an electric field measurement, i.e. $\mathcal{E}_z(z)$ averaged over the NV$^-$ distribution, is $\langle \mathcal{E}_z \rangle \approx 600$ kV/cm, well in the range of sensitivity of the NV centre [47]. However, it is important to note that the presence of the NV centres (and related implantation defects) affects the surface band-bending, for instance a lower NV density would increase the spatial extent of the band-bending. For truly non-invasive measurements of band-bending, the NV density could be reduced to the single site limit [230], although this approach is not compatible with real-space imaging.

5.2.2 Probing band-bending vs depth

To demonstrate the 3D mapping capability of this technique, several diamonds were used that each had a different implantation energy, generating a series of mean NV depths ($\langle d \rangle$) that can be probed (Fig. 5.7a). In principle, this could be achieved on a single diamond chip with multiple masked implantations, or a gradient implant could be performed, allowing a simpler 3D mapping of surface treatments. In a selection of oxygen terminated (O-term)

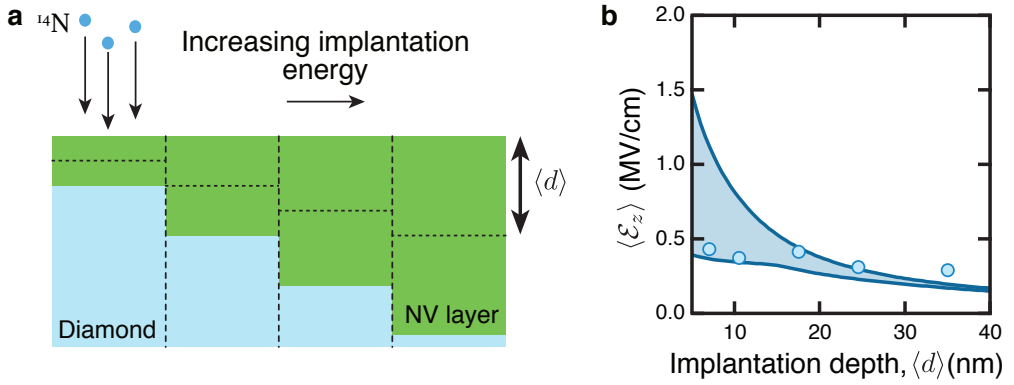

Figure 5.7: Electric field versus implantation depth. **a**, Schematic of procedure for producing samples with different mean implantation depths, $\langle d \rangle$, where the different diamond samples were exposed to different implantation energies, forming NVs at different ranges from the surface. **b**, Electric field, $\langle \mathcal{E}_z \rangle$, as a function the mean implantation depth, $\langle d \rangle$, for O-terminated diamond. Solid lines: result of the band-bending model described in Fig. 5.6b with $D_{sd} = 0.06$ nm^{-2} (lower curve) and $D_{sd} = 1$ nm^{-2} (upper), with the shading representing intermediate values.

samples it was observed that the electric field decreased from 432±10 kV/cm at $\langle d \rangle \approx 7$ nm to 291 ± 5 kV/cm at $\langle d \rangle \approx 35$ nm (Fig. 5.7b). This is consistent with the theoretical prediction for a range of acceptor densities of $D_{sd} = 0.06 - 1$ nm^{-2} (Fig. 5.7b, blue band), where a detailed description of the band-bending model can be found in Appendix C. The acceptor layer, D_{sd}, originates from defects in the formation of the oxygen terminated surface, observed in Ref. [229] and called sp2 defects. While some variations are observed outside of this prediction band there are many sources of additional modification to the prediction, such as, the influence of surface roughness, the presence of other types of surface or bulk defects than those considered in the model, and a depth profile different from that assumed. Additionally, changes in the surface chemistry prior to implantation or the implantation parameters themselves can change the depth distribution of the NV samples, which can add to some uncertainty in the experimental results.

These experiments illustrate the ability of the technique to probe band-bending vs depth. However, it should be noted that in our samples the high density of implanted nitrogen does contribute to the observed band-bending (as explained in Appendix C) and so varying $\langle d \rangle$ also changes the band-bending profile itself rather than just the probe location. Less invasive measurements could be performed by using a lower implant density such that

the band-bending is dominated by intrinsic effects (e.g. surface defects) independent of the measurement.

5.2.3 Effect of the surface termination

Different surface terminations and treatments will change the number and type of acceptors or defects that exist on the diamond surface. Two types of termination are commonly used for diamond surfaces: hydrogen-terminated (H), which is the natural termination produced from diamond growth, and oxygen-terminated (O), which is the termination typically obtained after standard (oxidative) cleaning procedures. In the case of hydrogen-termination, the surface has a lower electron affinity which, combined with an adsorbed acceptor layer (water and relevant compounds), leads to an efficient charge transfer in ambient air [231, 232]. As a consequence, the H-terminated surface generates significant band-bending (thus a large electric field) [233]. In contrast, an ideal O-terminated surface itself should not produce any significant band-bending, however, the presence of surface defects is often observed in processed samples leading to the presence of a non-zero band-bending [229].

To image the effect of both surface terminations, a channel of H-termination was fabricated on a background O-terminated surface (Fig. 5.8a), revealing an increase from 372 ± 5 kV/cm in the O region to 410 ± 5 kV/cm in the H region in this sample. By fitting the band-bending model to the measured increase in $\langle \mathcal{E}_z \rangle$ caused by the H termination (Fig. 5.8b), the density of hydrogen related charged surface adsorbates (acceptors) can be determined[1], $Q_{sa} \approx 0.07$ nm^{-2}, which is in rough agreement with the value derived from surface resistivity measurements is given in Appendix C. Additionally, the density of oxygen related surface defects, D_{sd}, can also be determined by the raw electric field measurement, which will be discussed shortly. It is important to note that the two types of acceptor states introduced in the model (surface defects and adsorbates) are not equivalent because of their different energy levels, in particular only the latter can give rise to a 2D hole gas (2DHG, see Section 5.2.6). Furthermore, the resonance energy transfer from the

[1]Note hat the surface absorbates (whose density is given by Q_{sa}) and the surface defects (whose density is given by D_{sd}) are not the same thing. The defects are part of the diamond, for example dangling bonds. Where the absorbates are additional molecules that are donating charge to the diamond surface defects.

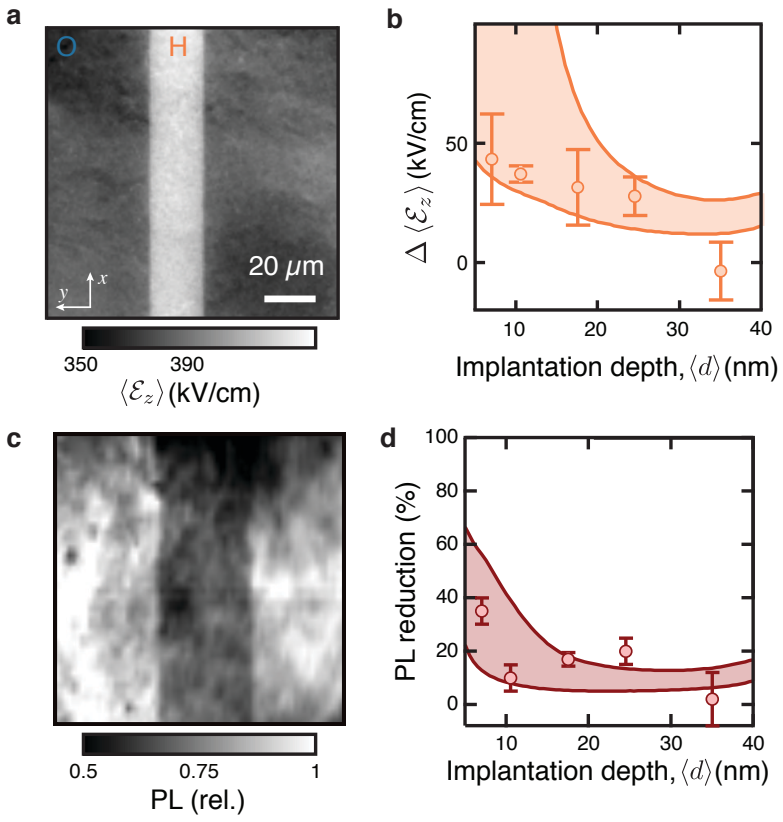

Figure 5.8: Electric field and surface termination. **a**, $\langle \mathcal{E}_z \rangle$ map of an H-terminated channel on an O-terminated background ($\langle d \rangle \approx 10$ nm). **b**, Difference $\Delta\langle \mathcal{E}_z \rangle = \langle \mathcal{E}_z \rangle_{\mathrm{H}} - \langle \mathcal{E}_z \rangle_{\mathrm{O}}$ between the electric field measured for H- and O-terminated diamond. Solid lines: model using a fixed density of charged surface adsorbates, $Q_{sa} = 0.07$ nm^{-2}, and with $D_{sd} = 0.08$ nm^{-2} (upper curve) and $D_{sd} = 1$ nm^{-2} (lower). We note that the calculated $\langle \mathcal{E}_z \rangle$ takes into account the NV$^-$/NV^0 threshold distance, whose dependence on $\langle d \rangle$ and D_{sd} (see Appendix C. **c**, PL image of an H-terminated channel ($\langle d \rangle \approx 7$ nm). **d**, PL reduction of the H region relative to the O region, as a function of $\langle d \rangle$. Solid lines: model using the same parameters as in inset of **a**. Vertical error bars: $\pm\sigma$ where σ is the standard deviation.

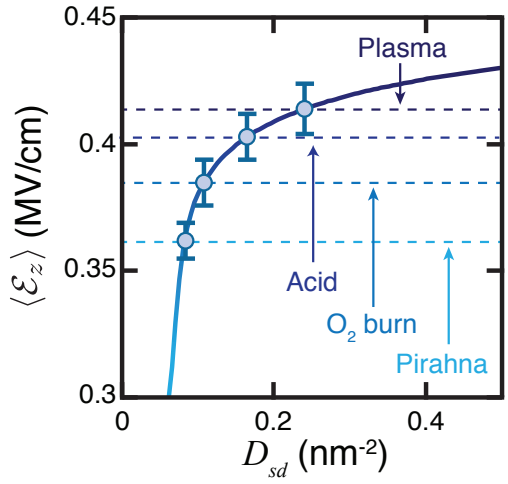

Figure 5.9: Electric field and surface treatment. $\langle \mathcal{E}_z \rangle$ vs D_{sd} calculated for $\langle d \rangle = 17$ nm. The dashed lines and data points indicate the measured $\langle \mathcal{E}_z \rangle$ values for a comparable sample following various surface treatments, performed in order: oxygen plasma (as used to form the O termination), acid cleaning, oxygen burning and piranha treatment. Vertical error bars: $\pm\sigma$ where σ is the standard deviation.

NV centres to the conducting 2DHG may be present for the lowest implantation depths ($\langle d \rangle \lesssim 10$ nm) effectively increasing the mean depth of the NV centres contributing to the signal, and as such it may provide an explanation to the fact that the measured increase in electric field by the H termination is somewhat smaller than expected.

A consequence of the increased band-bending is a decrease in the effective number of NV^- centres, hence a decrease in detected NV PL (Fig. 5.8c), since the NVs closest to the surface become charge neutral [72]. This is illustrated in Fig. 5.8d, which shows the PL reduction as a function of $\langle d \rangle$, which has a similar response to the electric field and is consistent with the theoretical prediction.

As the band-bending can place the NV in the unfavourable charge state it motivates the need to minimise band-bending via surface engineering for quantum sensing applications, where the NV^- to surface distance is critical [15]. As a step towards this goal, various surface treatments were applied in an attempt to reduce the density of surface defects. Initially, the diamond is exposed to a soft oxygen plasma (5 min at 50 W, 14 MHz radiofrequency with a 0.7 torr O2/Ar pressure) optimized to render the surface non-conductive via oxygen termination, while minimizing the amount of diamond etching. Then the diamond was exposed to an acid cleaning (15 minutes in a boiling mixture

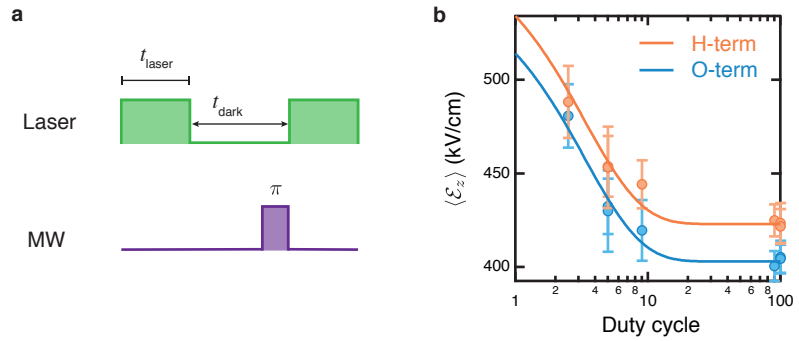

Figure 5.10: Effect of laser on the measured electric field. a Pulse sequence for ODMR defining the laser pulse time and the wait time. **b** Electric field measurements for oxygen (blue) and hydrogen (orange) terminated diamond for different laser duty cycles, solid line is an exponential fit to the data.

of sulphuric acid and sodium nitrate) followed by an O_2-burn (i.e. annealing at 500°C in oxygen-rich atmosphere similar to the process used in Ref. [125]), and finally, cleaned in a piranha solution (mixture of 4 ml of sulphuric acid and 2 ml of hydrogen peroxide heated to 90°C) for 10 minutes. Through measuring the electric field at each step of the procedure a clear trend of decreasing electric fields was observed, where the oxygen plasma produced an electric field of $\langle \mathcal{E}_z \rangle \approx 414 \pm 10$ kV/cm which was reduced to a minimum of $\langle \mathcal{E}_z \rangle \approx 362 \pm 6$ kV/cm after the piranha treatment (Fig. 5.9). The diamond was also exposed to the oxygen plasma a second time, which was consistent with the initial measurement, indicating that the overall observed change was due to surface treatment. Additionally, this trend is broadly consistent with direct measurements of D_{sd} reported recently [229]. The observed electric field reduction corresponds to a reduction of surface defects, D_{sd}, by nearly a factor 3 according to our theory and results in a change in the mean NV^- depth from ≈ 23 nm to ≈ 19 nm. These results illustrate the value of in-situ electric field measurements, which may provide new insights into semiconductor surfaces and the effect of surface processing.

5.2.4 The effect of laser intensity on the electric field

To investigate the effect of the laser, the electric field was measured as a function of the laser intensity. This was achieved through varying an extended dark time in the standard ODMR pulse sequence (Fig. 5.10a), which acts to change the overall intensity of

the laser through changing the duty cycle. In order to remain consistent with the other measurements and to eliminate the complication of under pumping the NV spins (i.e. not initialising the NV spins), the peak power and laser pulse duration remained constant and only the dark time changed. The duty cycle can thus be described as,

$$\text{Duty cycle} = \frac{t_{\text{laser}}}{t_{\text{wait}} + t_{\text{laser}}}. \tag{5.12}$$

where $t_{\text{laser}} = 20$ μs. Since photo-currents have been measured to be long lived (minutes compared to the microsecond time scale of the laser pulsing sequence), we expect varying the average laser power via pulsing to be equivalent to vary the laser power in a CW experiment. A decrease in $\langle \mathcal{E}_z \rangle$ by about 15% was observed when the duty cycle was increased from 2.5% to nearly 100% (Fig. 5.10b), i.e. a factor 40 increase in average laser intensity. Indicating that the laser does indeed introduce a change in the measured electric field, in this case more laser power results in a suppression of the electric field, likely due to ionisation of nitrogen defects on top of converting NV^- to NV^+. All other measurements were performed with a duty cycle close to 100 in order to maximise the signal-to-noise ratio, and as such they include a small but measurable effect of the laser. This electric field laser dependence is consistent with results discussed in Section 5.2.6, where the change in E-field is more dramatic.

5.2.5 Electric field vs diamond etching

A commonly used fabrication technique is etching of the diamond, whether it be globally or in sections through masking. In previous work NV diamond samples have been produced that utilise etching to remove implantation damage near the surface [234, 235]. As such, it motivates a study into how this etching changes the electric field seen by NV spins and consequently the $NV^{-/0}$ ratio. To this end, a diamond implanted at $d \approx 0 - 35$ nm was used with two separate etches (≈ 15 nm per step) that were partly overlapping.

The first etching was done by a process illustrated in Fig. 5.11a, where embedded Tic/Pt/Au contacts were made (see motivation and details in section 5.2.6) and subsequently removed via acid etching. Following the etching, the diamond was optically clear indicating that there was no metal left, and a recess of ≈ 15 nm was measured by AFM in

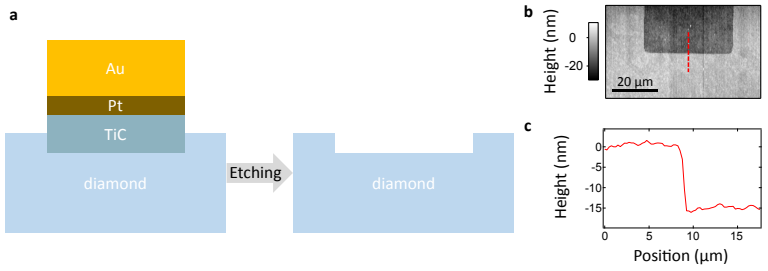

Figure 5.11: Etching the diamond a Illustration of the etching process: the TiC layer formed by annealing is etched away, leaving a recess. **b** Atomic force microscopy (AFM) image of a region thus etched. **c** Line cut extracted from **b** revealing a ≈ 15 nm etching step.

the regions formerly occupied by the TiC/Pt/Au stack (Fig. 5.11b,c). The second etching step was done by reactive ion etching (RIE) through a Au mask, which was subsequently removed via acid etching (15 minutes in a boiling mixture of sulphuric acid and sodium nitrate). An etching step of ≈ 15 nm was measured by AFM and optical profilometry. The etching mask was chosen to partly overlap with the regions etched during the first etching step, so that the diamond eventually had regions that were etched only once (≈ 15 nm, due to either step 1 or step 2) or etched twice (≈ 30 nm, due to both steps) as well as non-etched regions (Fig. 5.12a). Due to the acid cleaning that was applied as the final step of the process, all the surfaces should be nominally identical, i.e. oxygen-terminated.

The topography, electric field, and PL images of a selected area are shown in Figs. 5.12a-c, respectively, with line cuts shown in Fig. 5.12d. The electric field is found to be correlated with the surface height, namely the more the diamond was etched, the smaller the electric field became. On the other hand, the PL shows a less trivial correlation, where it is larger in the regions etched once (≈ 15 nm etching) than in the regions etched twice (30 nm) or not etched at all. To interpret these results, let us first consider the effect of the first etching step, which decreased the electric field by $\approx 25\%$ and increased the PL by a factor ≈ 2, despite etching away 15 nm off the estimated depth range of the NV centres, $d \approx 0 - 35$ nm. This implies a dramatic reduction in band-bending, such that for instance the depletion region for NV^- decreased from 27 nm (i.e. NV^- only at depths $d = 27 - 35$ nm, a 8-nm-thick layer) to just 5 nm (NV^- at $d = 20 - 35$ nm, where $d = 0 - 15$ nm has been etched). A smaller change is observed in the electric field as

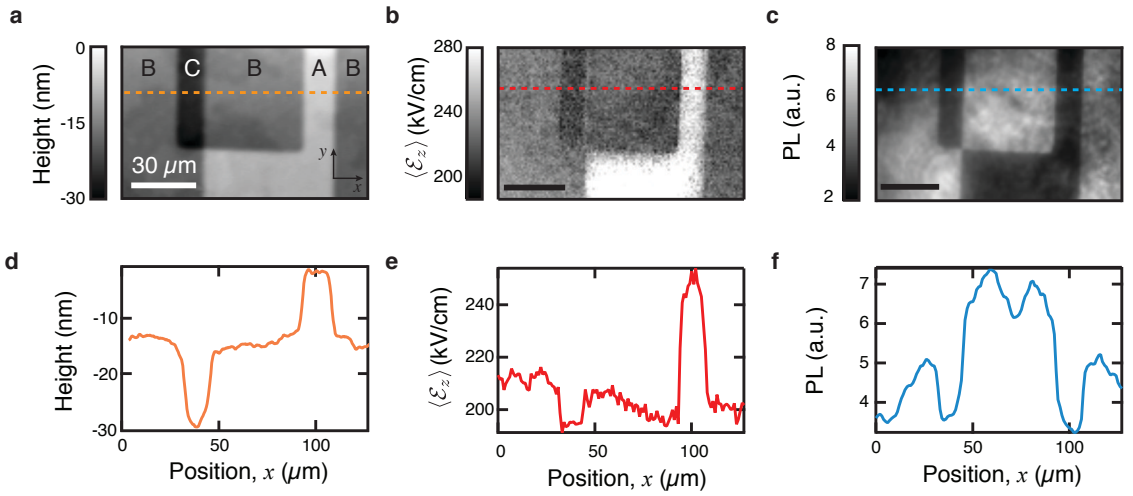

Figure 5.12: Electric field measurements after etching a Topography image of the diamond surface obtained by optical profilometry, highlighting (A) a non-etched region, (B) regions etched once and (C) a region etched twice. **b** Electric field map of the same area as in **a**. The plotted range is capped to 280 kV/cm to highlight spatial variations, with actual values reaching up to 320 kV/cm. **c** Corresponding PL image. (**d** - **f**) Line cuts extracted from (**a** - **c**), taken along the dashed lines shown in the images.

it is averaged over the NV^- depth distribution, which changes non-trivially as both the band-bending and average depth change. This results in only a small decrease in $\langle \mathcal{E}_z \rangle$ (by $\approx 25\%$) upon etching even though the change in PL predicts E_z to be significantly smaller (by a factor of 5) . A possible explanation for the dramatic reduction in band-bending invokes the presence of sub-surface defects present in the non-etched region and induced by the hydrogen plasma initially applied to the sample, which may have resulted in diffusion of hydrogen atoms into the diamond [236]. The etching would then remove these defects to leave only the surface-termination-induced defects as the source of band-bending.

Assuming the second etch results in the same surface as the first etch, with the same density of surface defects, we would expect the PL to decrease relative to the first etch, which it does by a factor ≈ 2. The assumptions made above (5 nm depletion layer and NV depth range $d = 0 - 35$ nm before etching) are clearly over simplistic as they predict no PL at all after a 30 nm etch. Most likely, the implantation profile (at energy 10 keV for this sample) produced a tail that extends deeper than 35 nm. The further decrease in $\langle \mathcal{E}_z \rangle$ upon the second etch can be explained by an increase in the band-bending extent (i.e., the length scale of the bending) while the total bending (i.e. the energy offset at the surface)

remains unchanged. This is to be expected as a significant number of nitrogen defects (donors) have been etched away, leaving a diamond with a lower nitrogen concentration hence a more dilute space charge density. As a consequence, the bands spatially extend further into the diamond to accumulate the same amount of change. This increased spatial extent decreases the gradient across the NV layer and thus decreases the electric field. While further work is needed to fully understand the multiple competing effects, these results illustrate the value of in-situ electric field measurements, which provide new insight into band-bending.

5.2.6 Electric field in an operating device

The hydrogen terminated surface bends the diamond bands past when the valance band crosses the Fermi level, producing a two-dimensional hold gas (2DHG) at the diamond-air interface. Electrical interfacing of H-term diamond is typically difficult with simple evaporated contacts due to high contact resistance or poor adhesion of most metals [237,238]. A more efficient but more complex solution is to form contacts embedded into the diamond, e.g. by diffusing Ti atoms into the diamond forming robust TiC contacts. Specifically, a stack of Ti/Pt/Au (thickness (10/10/70 nm) was evaporated onto the diamond masked by a photoresist pattern. After lift-off of the photoresist leaving Ti/Pt/Au contacts, the sample was annealed at 600°C for 20 mins in hydrogen gas (10 Torr). At this temperature, Ti atoms are able to diffuse into the diamond, and conversely carbon atoms are able to diffuse into the Ti layer, thus forming a TiC layer extending about 15 nm into the diamond (see Section 5.2.5). The thick Au layer serves as the primary contact material for electrical interfacing, while the Pt layer is introduced to act as a barrier preventing diffusion of Au and Ti atoms across the Ti/Au interface. The use of such a process is to form a clean quasi-one-dimensional interface with the H-terminated channels subsequently fabricated. Together with the high expected work function of TiC (≈ 5 eV [239]), this results in more consistent formation of Ohmic contacts than with conventional 2D interfaces of H-terminated diamond with Au [237] or Ti [238]. These contacts then had H-terminated channels 100 μm in length and 20 μm in width (Fig. 5.13a,b) fabricated between them.

We now have a closer look at the electric field maps of the operating device where

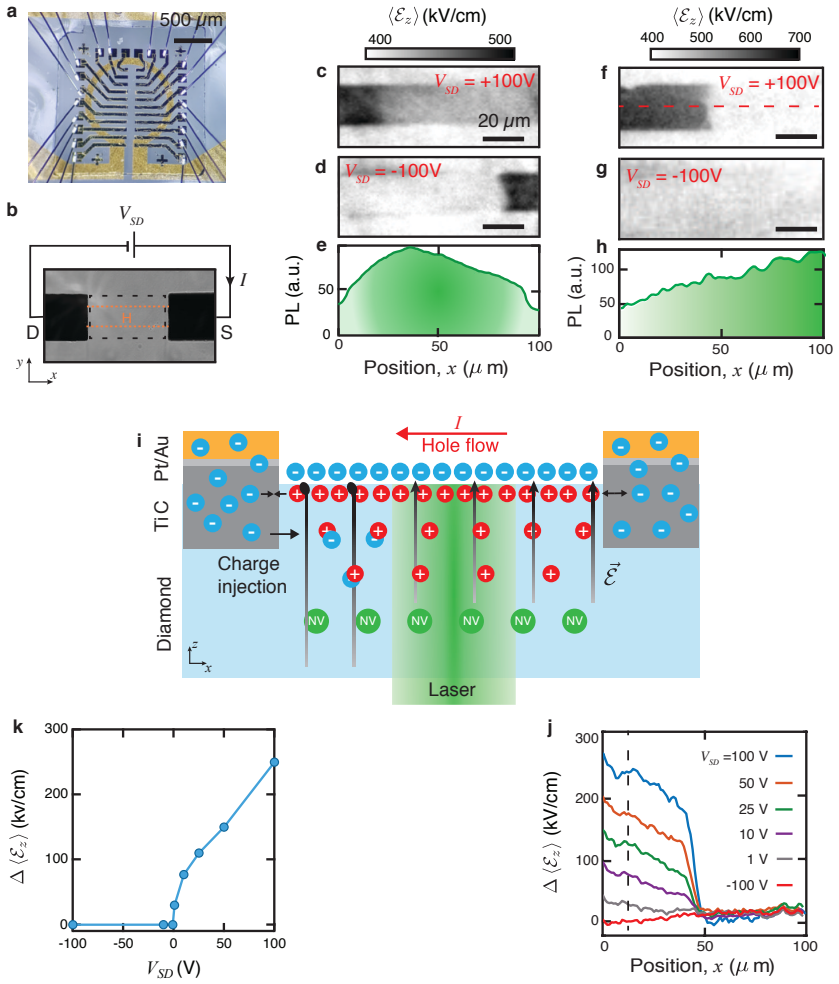

Figure 5.13: Electric field in a two-terminal device. **a**, Photograph of the diamond with the fabricated devices. **b**, Optical bright-field image of a device showing the TiC/Pt/Au contacts in dark, defined as source (S) and drain (D). The optically-transparent 2DHG channel is indicated by orange dotted lines. The black dashed box defines the area imaged in **c-h**. **c,d** $\langle \mathcal{E}_z \rangle$ map under an applied voltage $V_{SD} = +100$ V (**c**) and $V_{SD} = -100$ V (**d**), corresponding to a current through the channel of $I \approx \pm 400$ μA. Note that this current generates a magnetic field that is completely separable from the electric field and can be imaged simultaneously. **e**, Line cut of the PL along the channel, indicative of the laser spot profile (symbolised by the shading under the curve). **f-h**, Same as **c-e** but with the laser spot offset by 50 μm to the right. **i**, Diagram illustrating the different recombination and trapping processes for electrons under laser illumination and bias voltage. The TiC contact extends $\approx$ 15 nm deep into the diamond, with the NV centres implanted at a mean depth $\langle d \rangle \approx 17$ nm. **j**, Line cuts of $\langle \mathcal{E}_z \rangle$ taken along the channel (see dashed line in **f**) for different voltages V_{SD}, with the laser spot centred as in **f-h**. **k**, Electric field measured at the position indicated by the black dashed line in **j**, plotted as a function of V_{SD}. In **j,k**, the zero-voltage value was subtracted to show only the increase caused by the applied voltage, $\Delta\langle \mathcal{E}_z \rangle$.

both magnetic and electric fields are measured simultaneously (see Section 5.1.3). Upon applying a voltage $V_{SD} = +100$ V to the H-term channel, an increase in $\langle \mathcal{E}_z \rangle$ was observed (by up to a factor 2) in a well-defined region of the channel extending over ≈ 20 μm from the drain (Fig. 5.13c). Inversion of the voltage ($V_{SD} = -100$ V) caused the feature to move to the other contact (Fig. 5.13d) i.e. remaining at the hole drain. The lateral extent of this increase in electric field was also observed to depend on the position (and thus intensity) of the laser illumination spot used for the NV measurements, which had a $1/e$ diameter of ~ 120 μm. When the laser was moved from the centre position (Fig. 5.13c-e) to being focused on the right contact (Fig. 5.13f-h) a dramatic change in the feature was observed. In the region with lower illumination (left) the electric field appeared to extend further from the contact (≈ 40 μm, Fig. 5.13f) , where on the other hand, the contact with greater illumination (right) no longer shows any feature under negative voltage (Fig. 5.13g).

These observations are qualitatively interpreted as being due to combination of two competing effects, illustrated in Fig. 5.13i: the injection of electrons from the drain contact into charge traps in the diamond bulk, increasing the electric field seen by the NV centres, and laser-induced ionisation of these charge traps, allowing the electrons to escape via the conduction band and returning the electric field to its zero-voltage value. These charge traps are likely the substitutional nitrogen impurities that are normally ionized by the band-bending and become neutral near the drain contact when the voltage is applied. This interpretation is corroborated by the observed negative capacitance for these devices (see Section 5.2.7). Line cuts taken at different voltages (Fig. 5.13j) reveal that the electric field decreases steadily from the contact (with a maximum value that increases monotonically with voltage, see Fig. 5.13k) before dropping off abruptly at a specific position independent of voltage (but dependent on laser position), even though the laser intensity increases approximately linearly with position (Fig. 5.13h). This suggests the existence of a strong non-linearity in the ionisation process as a function of laser intensity, possibly due to a change in the ionisation energy of the charge traps caused by ionisation of a second species of defects [240]. These experiments illustrate how previously un-observable lateral changes in electric field, resulting from a complex contact/diamond junction, can be directly imaged and correlated with the electrical properties of the device (here a negative capacitance).

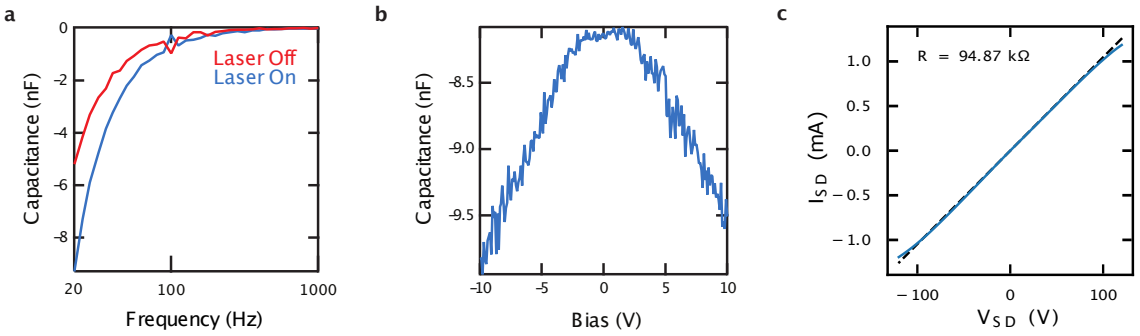

Figure 5.14: Electrical characterisation of hydrogen terminated wires. **a** Capacitance under a bias voltage $V_{SD} = 10$ V, as a function of the frequency of the AC signal. **b** Capacitance at 20 Hz as a function of the bias voltage (laser on). **c** Source-drain current as a function of the applied DC voltage.

5.2.7 Electrical characterisation of the devices

The electrical properties of the hydrogen terminated channels were characterised first by DC measurements to determine the device resistance (Keithley 2400 SMU), and then with a small AC voltage test signal (10 mV peak to peak) applied by a LCR meter (HP 4284A) to determine the complex device impedance (Z). The resistance of the devices was modified by the 532 nm laser illumination required by NV measurements. Upon illumination the resistance of all devices dropped from $R \approx 90\,\mathrm{k\Omega}$ to $R \approx 75\,\mathrm{k\Omega}$ ($V_{SD} = 10$ V). Green laser illumination is known to optically pump charge carriers in nitrogen doped diamond through deep defects and surface defects [241]. The photo-induced carriers in our devices were observed to have a long life-time with photo-currents taking minutes to decay. Prolonged laser exposure resulted in a gradual and permanent increase in the device resistance. After multiple days of continuous laser illumination the devices typically exhibited dark resistances of $R > 100\,\mathrm{M\Omega}$ (illuminated resistances of $R \approx 500\,\mathrm{k\Omega}$), which can be explained by a decrease in dark hole density with no change in the photo-induced carrier density. The reduction of hole density indicates a loss of surface acceptors either by laser induced removal of the hydrogen termination or by the formation of a surface contamination that prohibits transfer doping of the diamond.

The device exhibited an Ohmic response within the applied DC bias range of $V_{SD} = 100$ to $V_{SD} = -100\,\mathrm{V}$ shown in Fig. 5.14c, with a sub linear response seen above $V_{SD} = 100\,\mathrm{V}$, consistent with a drift saturation velocity of $v_{\mathrm{drift}} = 5 \times 10^6\,\mathrm{cm\,s^{-1}}$ [237]. However,

AC measurements revealed a non-zero parallel capacitance in the diamond device. At low frequencies the device exhibits a large negative capacitance (Fig. 5.14a, red line), which becomes positive ($\approx 10\,\mathrm{pF}$) above 1 kHz. We interpret this capacitance as a result of the geometrical differences between the TiC contacts, which extend $\Delta z \approx 15\,\mathrm{nm}$ into the diamond, and the conductive H-terminated channel, which is confined within $z \approx 1\,\mathrm{nm}$ [237] of the surface, resulting in charge build up at subsurface TiC-diamond interface, below the 2D hole gas. The frequency response of the negative capacitance is inconsistent with a parasitic inductance, and is understood to result from the transient relaxation current (δj) after a small voltage step not decreasing monotonically (i.e. $\frac{d\delta j}{dt} > 0$ at some time, t, after the voltage step) [242, 243]. The microscopic cause of this unusual transient response is device specific, for our devices we postulate that the negative capacitance is a result of carrier trapping dynamics across the metal TiC and p-type diamond interface similar to the cause of negative capacitance seen in silicon based p-n junctions [244].

Fig. 5.14b shows the low frequency negative capacitance response to the applied DC bias. The symmetry around $V_{\mathrm{SD}} = 0$ suggests that TiC-diamond interfaces at both contacts behave consistently under a particular bias direction. Electric field images of the biased interfaces suggest that this negative capacitance corresponds with the increased electric field and occurs when the interface is forward biased, i.e. when the p-type H-terminated channel is positively biased with respect to the TiC. This indicates that either holes are injected into the TiC, electrons are injected into the diamond or both. As TiC is typically metallic [245], these holes rapidly recombine, however electrons injected into the conduction band far away from the diamond surface may have a longer lifetime. Trapping of these electrons in ionised donor defects re-distribute charge within the diamond resulting in a change in the electric field at the NV layer and cause a positive transient response in the current due to the hole density increasing to maintain charge neutrality with the adsorbed acceptor layer. Laser illumination pumps any filled trap states reducing the measured electric field, and increase the magnitude of the positive component of the current transient which results in the increase in the negative capacitance at low frequencies shown in Fig. 5.14a (blue line).

5.3 Conclusion

We have used an new technique with ensembles of NV spins to measure both magnetic and electric fields simultaneously. To this end, the NV spin's sensitivity to electric fields was investigated and the conditions for optimising this sensitivity while maintaining access to all four NV orientations was determined. This is an extension of previous work that had looked at a electric fields through a single NV spin rather than using all four orientations. Using our method, the NV sensing platform was used to image electric fields that are intrinsic to diamond surface due to band-bending at this interface. It was shown that through varying the NV location the electric field can be probed at a range of different depth, offering opportunity to develop a fully 3D band-bending sensor. Through detailed measurements of the electric field both the diamond termination type and the quality of surface were investigated, where the latter was used to optimise surface treatments to minimise unwanted defects. Finally, this technique was used to probe undesirable charge injection from a 2DHG device and show that bulk illumination can be effective at minimising these effects.

Our method could be used to address a variety of questions in diamond electronics. It could, for example, be used to examine hole transport behaviour in boron delta-doped diamond [246, 247], which is of interest in the future development of high-power FETs. Probing band-bending in the vicinity of the delta layer could provide insight into why the high hole mobilities predicted for these structures (which also provide high carrier density) have not been achieved so far. Furthermore, our technique could be used to investigate hydrogen-terminated diamond FETs, which are also of potential value in the development of high-power and high-frequency electronics [248, 249]. It could, in particular, help understand the origin of the suppression of weak anti-localisation observed at low temperature [250, 251], which is thought to be related to the spatial modulations of the confining potential (and thus band-bending). More generally, systematic studies of the spatial distribution of band-bending near the diamond surface could provide valuable knowledge on the surface and sub-surface defects present as a result of surface processing and device fabrication, which may in turn guide the optimization of the hole mobility and hole carrier density in diamond-based FETs, which are the two key parameters governing

device performance.

Finally, another exciting prospect is to combine electric field mapping with other quantum sensing modalities such as current flow mapping [21,101] and noise spectroscopy [14, 126]. This would allow charge transport and band-bending to be simultaneously monitored in three-terminal FET devices based on the H-terminated diamond surface or in other 2D electronic systems such as graphene.

6

Mapping the full stress tensor in diamond with sub-micrometer spatial resolution

Stress or strain in crystalline solids cause a deviation from the standard shape of the unit cell. As modifications of the bond lengths of a crystal can change the materials properties, the precision measurement of mechanical stress at the nanoscale is of fundamental importance to the development of new materials and the enhancement of current ones. Stress is characterized by six independent parameters (forming a tensor), which in principle can all be exploited in strain engineering to tune or enhance the properties of materials and devices, and can be used in nanomechanical sensors for chemical or biological analysis. However, existing techniques to probe the local stress are generally incapable of measuring the entire tensor. In this chapter, it is demonstrated that imaging based on an ensemble of NV centres can achieve spatial mapping of the full stress tensor, with a sub-micrometer spatial resolution and a sensitivity noise floor in the order of 1 MPa.

To illustrate the effectiveness and versatility of the technique, the full stress tensor is measured in a broad range of experimental situations, including mapping the stress induced by localized implantation damage, nano-indents and scratches. In addition, surprisingly large stress contributions from functional electronic devices fabricated on the diamond are measured, which demonstrates sensitivity to deformations in materials outside the diamond. This technique could enable in situ measurements of the mechanical response of diamond nanostructures under various stimuli, with potential applications in

strain engineering for diamond-based quantum technologies and in nanomechanical sensing for on-chip mass spectroscopy.

Stress has been measure using NV diamond sensors previous to this work [48,143] but did not reconstruct the full stress tensor. Additionally, several other group have also used ODMR to extract out the stress tensor [209, 213, 252] that were developed simultaneously and independently to this work and focused on different applications.

6.1 A method for imaging the full stress tensor

Pressure is a powerful thermodynamic quantity often used to modify a material's properties [253]. Most notably, pressure induced stress enhances the charge carrier mobility in modern electronics [254–256]. It allows the tuning of the optical properties of materials [257–259], can confer them with a ferroelectric nature [226, 260], or even make them better superconductors [261]. Despite these successes, stress engineering is still a largely unexplored field considering the huge parameter space available; indeed, stress is characterized by six parameters (three axial components and three shear components, defining the stress tensor) which, in principle, can be continuously and independently varied over many orders of magnitude to optimize the functional properties of materials [253].

Key to material innovations is the ability to characterise stress at the nanoscale, and in particular to quantitatively determine the six components of the stress tensor. Existing methods to probe stress in solids typically rely on the interaction between a beam of probe particles (usually electrons or photons) with the stressed material [262–270]. However, these techniques are generally sensitive to only one or a convolution of the stress components. Exceptions include off-axis electron holography [271], but at the cost of sample destruction to produce suitably thin lamellae (under 200 nm thickness, which may cause strain release), and off-axis Raman spectroscopy [272], but at the expense of a spatial resolution limited to millimeter scales.

Here, we describe a radically different approach, which relies on atomic-sized strain sensors embedded into the material to characterise the local strain. In recent years, several materials have been found to host such in-situ strain sensors, in the form of optically addressable point defects that exhibit strain-dependent energy levels. These include dia-

mond [143, 273, 274], silicon carbide [227] and silicon [226]. To date, however, real-space mapping of the full stress tensor using in-situ sensors has remained elusive, in part due to the difficulty of addressing a sufficiently dense ensemble of sensors while retaining the capability to extract all the tensor components. Here we investigate the case of the nitrogen-vacancy (NV) defect in diamond [1], whose previous works have achieved two-dimensional (2D) imaging of a single strain component [48, 275] and outlined a method to extract the entire tensor [273, 276]. Single NV defects have also been proposed for nanomechanical sensing, including vector force sensing and mass spectroscopy [143].

In this section, a method for imaging the full nanoscale stress tensor with NV centre is presented. It relies on ODMR spectroscopy using a similar setup and principle as in chapter 5 except that the analysis is extended to include the effect of stress in addition to electric field. To explain the technique, the spin-mechanical coupling in an NV ensemble is first reviewed (6.1.1) and then an example of ODMR detection is given (6.1.3). In Section 6.2, the technique will be demonstrated experimentally and applied to spatially non-uniform features induced by scratches, implantation damage, nano-indents and devices fabricated on diamond.

6.1.1 Spin-mechanical coupling in NV ensembles

Here we show that the spin resonance frequencies of an NV ensemble, which can be probed via ODMR spectroscopy as shown in Chapter 5, contain sufficient information to infer the full stress tensor, i.e. determine both the axial and shear components (Fig. 6.1a). To see that, we extend the theory of spin-mechanical coupling well established for single NV [143] and extend it to the case of an ensemble of NVs in a single crystal. As we will see, the use of multiple NV orientations enables the full reconstruction of the local stress tensor. By using a thin layer of NV centres, we can then spatially map the stress tensor in two dimensions and study the effect of localized strain-inducing features (Fig. 6.1b).

The NV electronic ground state is governed by the spin Hamiltonian whose terms are often neglected due to their small contribution. In order to full realise the effect of

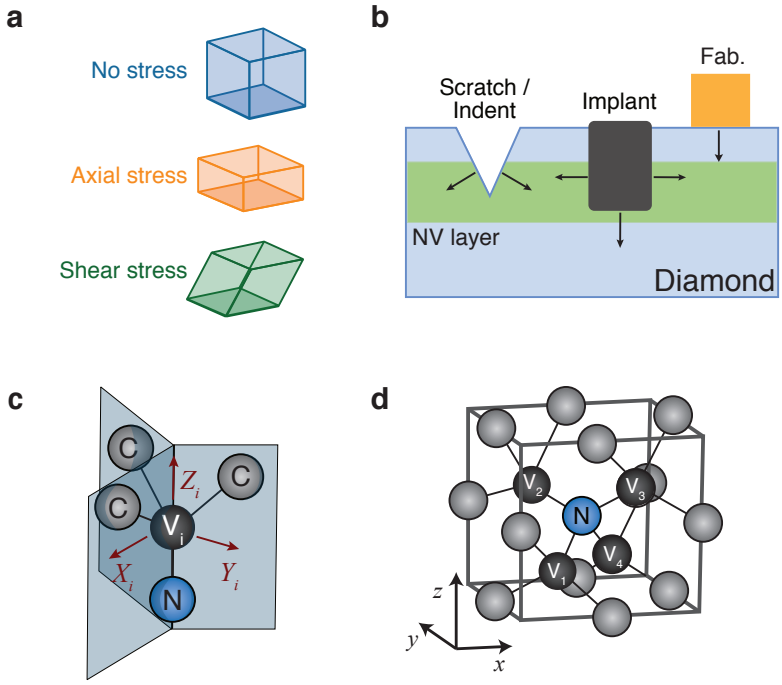

Figure 6.1: Stress-tensor mapping with nitrogen-vacancy centres. **a** Schematic of the unit cell of the diamond crystal under different stress conditions: no stress (blue), axial stress (orange), and shear stress (green) **b** Schematic cross-section of the diamond illustrating how the NV layer (green band) is used to probe the stress produced by local features. **c** Defect structure of the NV and its native coordinate system (X_i, Y_i, Z_i). **d** Unit cell with the four NV orientations depicted as different vacancy locations V_i $(i = 1, 2, 3, 4)$. The stress tensor is expressed in the natural coordinate system of the cubic lattice, (xyz).

stress we include these additional terms given a Hamiltonian of [173],

$$\begin{aligned} H_i = (D + \mathcal{M}_{Z_i})S_{Z_i}^2 + \gamma_{\mathrm{NV}}\mathbf{B}\cdot\mathbf{S} \\ - \mathcal{M}_{X_i}(S_{X_i}^2 - S_{Y_i}^2) + \mathcal{M}_{Y_i}(S_{X_i}S_{Y_i} + S_{Y_i}S_{X_i}), \end{aligned} \tag{6.1}$$

where $D \approx 2.87$ GHz is the temperature-dependent zero-field splitting parameter, $\gamma_{\mathrm{NV}} = 28.035(3)$ GHz/T is the NV gyromagnetic ratio [1], $\mathbf{S}_i = (S_{X_i}, S_{Y_i}, S_{Z_i})$ are the spin-1 operator, $\mathbf{B}$ is the applied magnetic field, and $\boldsymbol{\mathcal{M}}_i = (\mathcal{M}_{X_i}, \mathcal{M}_{Y_i}, \mathcal{M}_{Z_i})$ is the effective electric field which contains the true electric field as well as the effect of stress.. Here (X_i, Y_i, Z_i) is the coordinate system of the NV defect structure (Fig. 5.6c), and the index $i = 1, 2, 3, 4$ denotes the NV orientation with respect to the diamond unit cell (Fig. 6.1d).

The relation between $\boldsymbol{\mathcal{M}}_i$ and the local stress is most conveniently expressed by

defining the stress tensor with respect to the diamond unit cell coordinate system (xyz) defined in Fig. 6.1d [143]. This gives

$$\begin{aligned} \mathcal{M}_{X_i} &= b\sigma_X^{\text{axial}} + c\sigma_{X_i}^{\text{shear}} + k_\perp E_{X_i} \\ \mathcal{M}_{Y_i} &= \sqrt{3}b\sigma_Y^{\text{axial}} + \sqrt{3}c\sigma_{Y_i}^{\text{shear}} + k_\perp E_{Yi} \\ \mathcal{M}_{Z_i} &= a_1\sigma_Z^{\text{axial}} + 2a_2\sigma_{Z_i}^{\text{shear}} + k_\parallel E_{Z_i} \end{aligned} \tag{6.2}$$

where the stress susceptibility parameters are $a_1 = 4.86(2)$, $a_2 = -3.7(2)$, $b = -1.15(3)$, and $c = 3.5(3)$ in units of MHz/GPa [143], $k_\perp$ and $k_\parallel$ are the electric field susceptibility (as defined in Chapter 5), and $\mathbf{E} = (E_X, E_Y, E_Z)$ is the applied electric field. The contributions of the axial stress components which are independent of the NV orientation [276] were separated,

$$\begin{aligned} \sigma_X^{\text{axial}} &= -\sigma_{xx} - \sigma_{yy} + 2\sigma_{zz} \\ \sigma_Y^{\text{axial}} &= \sigma_{xx} - \sigma_{yy} \\ \sigma_Z^{\text{axial}} &= \sigma_{xx} + \sigma_{yy} + \sigma_{zz}, \end{aligned} \tag{6.3}$$

from those of the shear stress components which do depend on the NV orientation,

$$\begin{aligned} \sigma_{X_i}^{\text{shear}} &= 2f_i\sigma_{xy} + g_i\sigma_{xz} + f_i g_i \sigma_{yz} \\ \sigma_{Y_i}^{\text{shear}} &= g_i\sigma_{xz} - f_i g_i \sigma_{yz} \\ \sigma_{Z_i}^{\text{shear}} &= f_i\sigma_{xy} - g_i\sigma_{xz} - f_i g_i \sigma_{yz}. \end{aligned} \tag{6.4}$$

The functions f_i and g_i evaluate to ± 1 depending on the NV orientation. Namely, using the vacancy positions $i = 1, 2, 3, 4$ as defined in Fig. 5.6d, we have $(f_1, f_2, f_3, f_4) = (+1, -1, -1, +1)$ and $(g_1, g_2, g_3, g_4) = (-1, +1, -1, +1)$. Where the spin-mechanical interaction of the NV is invariant under inversion of the nitrogen and the vacancy, therefore there are only four orientations to consider in contrast to true electric fields, as discussed in Chapter 5.

In general, the set of four Hamiltonians $\{H_1, H_2, H_3, H_4\}$ is characterized by a total of 13 parameters: the temperature-dependent zero-field splitting parameter D, the mag-

netic field $\mathbf{B} = (B_x, B_y, B_z)$, the electric field $\mathbf{E} = (E_x, E_y, E_z)$, and the stress tensor $\overleftrightarrow{\sigma} = \{\sigma_{xx}, \sigma_{yy}, \sigma_{zz}, \sigma_{yz}, \sigma_{xz}, \sigma_{xy}\}$ (in Voight notation), all expressed in the crystal frame (xyz coordinate system). To allow inference of these 13 parameters from the 8 ODMR frequencies, we must make assumptions, which may introduce systematic errors in the inferred stress values. First, we assume that the stress is null except near the deliberately introduced features (scratches, implantation damage, indents etc.). In reality, there may exist a residual stress across the sample [275]. This assumption allows us to use the ODMR data far from those features to estimate D and $\mathbf{B}$, by minimising the error function $\varepsilon(D, \mathbf{B})$. Second, we assume that there is no net electric field, i.e. $\mathbf{E} = 0$. In reality, an electric field may be present in the NV layer as a result of charge effects in the diamond bulk and band-bending at the diamond surface as discussed in Chapter 5. The affect of electric fields on fitting the stress parameters is discussed in the next section.

6.1.2 Separation of the stress parameters

As the stress tensor is described by six independent parameters, a measurement relying on a single NV centre is not sufficient to infer the full stress tensor even if the effective field $\mathcal{M}_i$ is completely determined [273]. However, by using a small ensemble of NV centres with multiple orientations, it is possible to determine all six stress components in the corresponding volume, assuming a uniform stress within this volume. To see that, we consider the limit of small magnetic fields $|\mathbf{B}| \ll D$, for which the spin transition frequencies are given by [47, 143]

$$(\omega_\pm)_i = D + \mathcal{M}_{Z_i} \pm \sqrt{(\gamma_{\mathrm{NV}} B_{Z_i})^2 + (\mathcal{M}_{X_i})^2 + (\mathcal{M}_{Y_i})^2}. \tag{6.5}$$

As the effective field, $\mathcal{M}$, contains both electric field and stress, systematic errors in the stress values may be present as a result of the assumptions made in the model converting the frequencies $(\omega_\pm)_i$ into stress, in particular, neglecting the true electric field, $\mathbf{E}$. In Chapter 5 we found that in samples comparable to those used here, an electric field perpendicular to the diamond surface exists owing to surface band bending, with values up to $E_z \sim 500$ kV cm^{-1}. We first examine the effect of a non-zero E_z on the determination of

the shear stress components. By using Equation (6.2-6.4), we find that the sum frequencies

$$S_i \equiv (\omega_+ + \omega_-)_i = D + \mathcal{M}_{Z_i}. \tag{6.6}$$

Through expanding $\mathcal{M}_{Z_i}$ and including E_z this becomes

$$S_i = D + a_1\sigma_Z^{\text{axial}} - \frac{k_\parallel}{\sqrt{3}} f_i E_z + 2a_2(f_i\sigma_{xy} - g_i\sigma_{xz} - f_i g_i\sigma_{yz}). \tag{6.7}$$

Using all four orientations a series of linear equations can be determined, such that

$$\begin{aligned} S_1 - S_2 - S_3 + S_4 &= 8a_2\sigma_{xy} - \frac{4k_\parallel}{\sqrt{3}}E_z \\ S_1 - S_2 + S_3 - S_4 &= 8a_2\sigma_{xz} \\ S_1 + S_2 - S_3 - S_4 &= 8a_2\sigma_{yz} \\ S_1 + S_2 + S_3 + S_4 &= 4D + 4a_1\sigma_Z^{\text{axial}}. \end{aligned} \tag{6.8}$$

Thus, the presence of E_z will affect only the σ_{xy} component. Precisely, the assumption $E_z = 0$ in the stress reconstruction amounts to offsetting σ_{xy} by $-\frac{k_\parallel}{2a_2\sqrt{3}}E_z$ where $a_2 < 0$. For instance, the $\sigma_{xy} \approx 10$ MPa background observed in some of the σ_{xy} maps (see Section 6.2) can be attributed to an electric field of $E_z \approx +350$ kV cm^{-1} uniform across the field of view, in line with the values reported in Chapter 5. Furthermore, since the magnetic field does not enter Equation (6.8), the assumption that there is no background stress away from the local features should not affect the outcome for these four quantities, which then correspond to the net stress including a non-zero background contribution if present. Thus, using four possible orientations can be used to uniquely determine the three shear stress components $(\sigma_{xy}, \sigma_{xz}, \sigma_{yz})$ as well as the sum of the axial components, $(\sigma^{\text{axial}} = \sigma_{xx} + \sigma_{yy} + \sigma_{zz})$.

In order to determine the axial components individually the frequency differences need to be used, such that

$$D_i \equiv (\omega_+ - \omega_-)_i = 2\sqrt{(\gamma_{\text{NV}}B_{Z_i})^2 + (\mathcal{M}_{X_i})^2 + (\mathcal{M}_{Y_i})^2}, \tag{6.9}$$

which gives a set of four equations with only two unknowns. For instance σ_{xx} and σ_{yy},

where σ_{zz} can be expressed as a function of $(\sigma_{xx}, \sigma_{yy})$ and the measured $\{S_i\}$. However, these four equations are not linear and not necessarily independent with respect to the unknown parameters. In particular, in the situation where all the shear components are null, $\sigma_{xy} = \sigma_{xz} = \sigma_{yz} = 0$, Equation (6.9) reduces to

$$\begin{aligned} D_i^2 = \frac{4\gamma_{\mathrm{NV}}^2}{3}(f_i g_i B_x + g_i B_y - f_i B_z)^2 \\ + 4b^2(-\sigma_{xx} - \sigma_{yy} + 2\sigma_{zz})^2 \\ + 12b^2(\sigma_{xx} - \sigma_{yy})^2. \end{aligned} \tag{6.10}$$

In this situation only a single combination of σ_{xx} and σ_{yy} can be inferred from the measured $\{D_i\}$, which means that these axial stress components cannot be resolved individually. However, when the shear components are non-zero the difference forms an overdetermined system that is likely to have a unique solution. To test this, we numerically explored the full parameter space for the six stress components and evaluated the error ε comparing the NV frequencies calculated with a given σ_0 versus those calculated with a trial solution σ_{trial}, while holding the other parameters D and $\mathbf{B}$ constant. We found that there is indeed a unique solution that gives a vanishing error, $\sigma_{\mathrm{trial}} = \sigma_0$, except when two of the three axial shear components are null (in which case there are two solutions, where the incorrect solution simply swaps two of the axial components) and of course when all three shear components are null (as discussed above). This conclusion holds regardless of the value of the magnetic field or of the other stress components. Thus, this method enables the full stress tensor to be determined with no ambiguity, as long as at least two of the shear stress components are not exactly null.

Additionally, the electric field can add further complexity to this problem. To illustrate, let us consider the situation where σ_{xx} is the only non-zero stress component and E_z is the only non-zero electric field component. Then Equation (6.9) becomes

$$D_i^2 \quad = 4(\gamma_{\mathrm{NV}} B_{Z_i})^2 + 4(-b\sigma_{xx} - \tfrac{2f_i}{\sqrt{6}} k_\perp E_z)^2 + 4(\sqrt{3}b\sigma_{xx})^2. \tag{6.11}$$

Here, an error on B_{Z_i} would act as a simple offset on σ_{xx}, while E_z has a more subtle effect as it can add or subtract to the σ_{xx} term depending on the NV orientation. Moreover,

when the other stress components are present, an error on the magnetic field may also act to bias the estimated stress values in a way that depends on the other stress values. In other words, the assumptions made may introduce not just a global offset on the stress maps but also a distortion of the spatial features.

To test these effects, we used a set of experimental data and compared the stress maps produced by different analysis procedures. Namely, instead of assuming no electric field and background stress, we estimated the magnetic field (far from the local stress features) by including an electric field along z, i.e. minimising the residual function (ε) containing just the Hamiltonian components $D, \mathbf{B}, E_z$ ($\varepsilon(D, \mathbf{B}, E_z)$), or by including a background axial stress along z, i.e. minimising $\varepsilon(D, \mathbf{B}, \sigma_{zz})$, or by including both at the same time. The stress tensor was then determining by fitting the whole image again (but including the stressed regions) while holding D, $\mathbf{B}$ and E_z to the previously determined values. As expected, the shear components as well as σ_Z^{axial} are essentially unchanged by the analysis procedure, except for a global offset in σ_{xy} due to the electric field. On the other hand, these various methods affect the axial stress components not only as a global offset, but also by changing the values near local features. For example, the increase in σ_{xx} near the implanted region can vary from 20 MPa to nearly zero depending on the initial assumptions, compensated by an opposite variation in σ_{yy} or σ_{zz} (since the sum is well determined). This means that the uncertainty on these individual axial components can be up to 100%, calling for caution when extracting quantitative information from the corresponding maps. Nevertheless, the fact that the stress maps exhibit the expected symmetry (e.g., σ_{xx} maximum on the x axis and minimum on the y axis, see section 6.2.1) indicates that the different axial components have been sensibly separated.

6.1.3 ODMR detection of stress

Experimentally, similar to the electric field measurements in Chapter 5, we measured the frequencies $(\omega_\pm)_i$ for the four possible NV orientations by recording optically-detected magnetic resonance (ODMR) spectra under a small applied magnetic field $\mathbf{B}$ aligned so that all eight transitions can be resolved simultaneously [21, 184], as shown in Fig. 6.2a. As a preliminary test, we investigated the stress induced from scratching the diamond

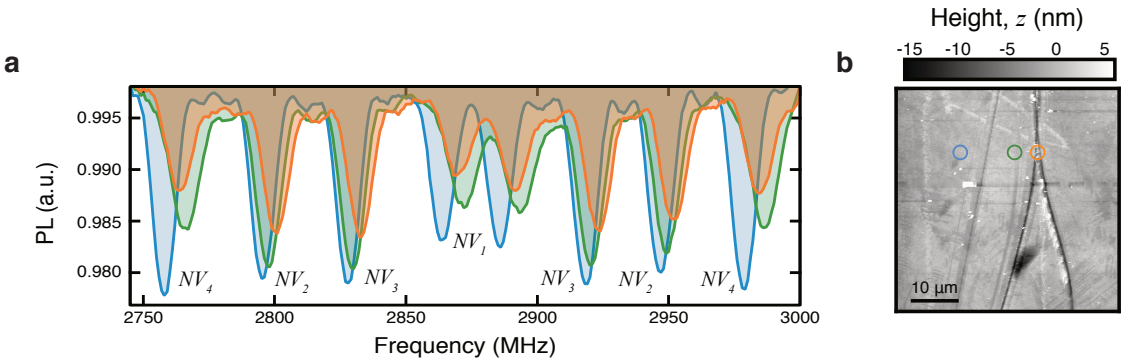

Figure 6.2: ODMR detection of stress. **a** Optically-detected magnetic resonance spectra under an external magnetic field of strength $B \sim 50$ G, recorded from NV centres at three different locations in a scratched diamond indicated by circles in **b**: away from scratch damage (blue), underneath a scratch (orange), and adjacent to a scratch (green). Each resonance is labelled according to its corresponding NV orientation. **b** Atomic force microscopy (AFM) image of the diamond surface showing scratches created with a diamond scribe.

with a diamond tipped scribe [277], generating cuts that are less than a micron wide and range from 5 to 20 nm in depth (Fig. 6.2b), with the NV layer extending from about 5 to 30 nm below the surface [210]. A reference ODMR spectrum (i.e. away from any scratch) is shown in blue in Fig. 6.2a, which is used to infer the magnetic field, here $(B_x, B_y, B_z) \approx (22, -13, -40)$ G. An ODMR spectrum taken from underneath the scratch is shown in orange and exhibits a shift of about 10 MHz that is relatively uniform across all the resonances, suggesting the presence of a predominantly axial stress field with an amplitude in the GPa range. An ODMR spectrum taken from a region adjacent to the scratch is shown in green, and exhibits shifts that are markedly different for different NV orientations. This variation in the shift, S_i, is the signature of a contribution from shear stress. While each NV experiences the same lab frame axial stress contribution ($\mathcal{M}_z$) they all have different shear contributions. Therefore non-uniform shifting of the ODMR frequencies is a strong indication of shear stress in the system.

The effect of electric field was previously discussed and found to have small changes to the fitting of the stress parameters. In this example the effect of the stress is so strong that the relatively small effect of the electric field can be ignored. Additionally, as was discussed in Chapter 5, the electric field mainly affects the inner ODMR spectral features due to a sensitivity drop off with larger axial magnetic fields. While the individual axial

stress component experience this same diminishment of sensitivity, the shear stress and the sum of axial components does not, as they are also contained in $\mathcal{M}_z$ term. As a consequence the ODMR can be tuned away from the E-field sensitive regime when the individual axial components are not required.

The ODMR data is analyzed by first fitting the ODMR spectrum at each pixel with a sum of eight Lorentzian functions with free frequencies, line widths and amplitudes. The resulting frequencies $\{\omega_{\pm,i}\}$ $(i = 1 \dots 4)$ are then used to infer the Hamiltonian parameters (denoted as a vector $\mathbf{p}$) by minimising the root-mean-square error function

$$\varepsilon(\mathbf{p}) = \sqrt{\frac{1}{8}\sum_{i=1}^{4}\sum_{j=\pm}\left[\omega_{j,i} - \omega_{j,i}^{\mathrm{calc}}(\mathbf{p})\right]^2} \tag{6.12}$$

where $\{\omega_{\pm,i}^{\mathrm{calc}}(\mathbf{p})\}$ are the calculated frequencies for a given set of parameters $\mathbf{p}$ obtained by numerically computing the eigenvalues of the spin Hamiltonian for each NV orientation.

6.2 Imaging stress from various sources

With the method of measuring the full stress tensor developed we now investigate implementing this technique on a range of sources of stress. Starting with imaging stress from implantation damage in the shape of a ring, which are particularly important as the symmetry of the system helps to confirm that the stress tensor is indeed extracted correctly.

6.2.1 Stress from implant damage

To test the method for reconstructing the full stress tensor, C_3 molecules were implanted into the diamond to create localized regions of damage extending 5-10 nm below the diamond surface. Implantation is commonly used in diamond to introduce dopants for electrical devices [278] or produce buried graphitic electrical wires [279]. The resulting confined amorphous carbon has a different density to diamond, thus introducing an embedded force that pushes in all directions (Fig. 6.3a). It also causes a reduction in PL from the NV defects by about 25%, as seen in Fig. 6.3a. Here, the implant pattern is a circular ring of 1.5 μm width and 50 μm diameter. The embedded force from the damage

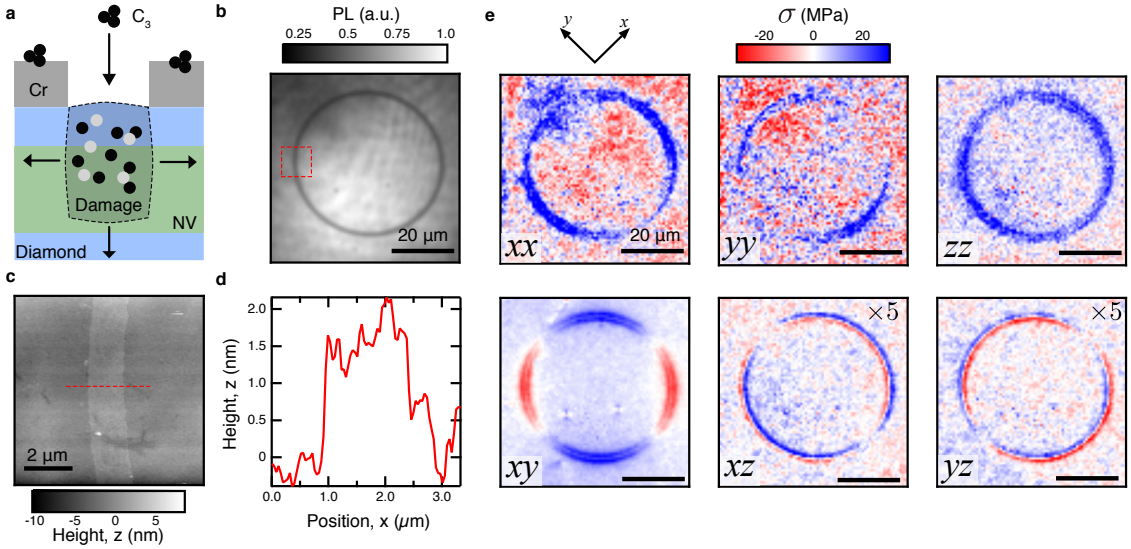

Figure 6.3: Stress induced by implantation damage. **a** Schematic of the stress induced by locally implanting C_3 molecules in the diamond. **b** NV PL image of an annulus-shaped implanted region. **c** AFM image of a segment of the annulus (dashed box in **b**). **d** AFM profile across the implanted region (dashed line in **c**). **e** Spatial maps of the six stress tensor components measured with the NV sensors in the same region as in (b). The amplitude of the σ_{xz} and σ_{yz} components has been multiplied by a factor of 5.

is sufficient to cause a bulging of the diamond surface [280], which was measured by atomic force microscopy (AFM) to be on the order of 2 nm in this case (Fig. 6.3c,d).

The spatial maps of the six stress tensor components near this circular ring are shown in Fig. 6.3e, revealing ring-shaped patterns with stress values of up to tens of MPa (corresponding to ODMR frequency shifts in the 100 kHz range), much smaller than from the scratch discussed briefly in Section 6.1.3 and discussed in more detail in Section 6.2.4. The pixel-to-pixel noise is about 1 MPa (standard deviation) for the three shear stress components, against 10 MPa for the axial stress components, with a total acquisition time of about 10 hours. Where this loss in sensitivity comes from the magnetic field projection B_{Z_i} suppressing the axial contribution to the splitting with larger fields, as discussed in Section 6.2. This loss of sensitivity could be mitigated by performing sequential measurements minimising B_{Z_i} for each NV orientation. Nevertheless, all stress components exhibit resolvable features, and the different symmetries indicate they have been sensibly separated. We note that the axial components have a positive value near the damaged region indicating a compressive stress, consistent with an expansion of the

lattice caused by the implantation [280]. The smallest spatial features in Fig. 6.3e have a size of the order of 1 μm. Moreover, implanted regions separated by less than 1 μm were also resolved in the stress maps, indicating a sub-μm spatial resolution close to the optical diffraction limit (≈ 400 nm [45]).

The values of stress measured here are in agreement with Raman spectroscopy [280] performed on a similar sample, which indicates an axial stress of 20 ± 20 MPa in the damaged region (close to the noise floor of our Raman set-up). This validates the NV technique as a sensitive and quantitative tool to characterise the stress in diamond, with the added benefit of an access to the complete tensor information.

6.2.2 Stress from nano-indents

As a second test, we performed a series of nano-indents in the diamond surface using a Berkovich tip with a tip radius of 200 nm to a load of 1 N, resulting in pyramidal impressions typically with a maximum depth of 30 nm (see AFM image of a representative indent in Fig. 6.4a, and line cut in Fig. 6.4b). Slight swelling around the perimeter of the impression but no major structural fractures are observed. Likewise, no discontinuities indicative of fracture formation were observed in the load-unload curve. This suggests that the diamond has been plastically deformed under these indentation conditions similar to previous reports [281, 282]. It is likely that the indented region contains pressure induced graphitic material as observed recently [283]. Fig. 6.4c reveals the quenching of the NV PL within the impression (by about 10%) due to this reduction in crystal quality. Beyond the perimeter of the indent the impact on the strain can be quantified. The stress maps are presented in Fig. 6.4d and reveal stress values up to 0.2 GPa for the in-plane components ($\sigma_{xx}, \sigma_{yy}, \sigma_{xy}$), the other components being much weaker indicating that the deformed material pushes predominantly in the directions parallel to the surface of the undeformed diamond.

6.2.3 From stress to body force

To facilitate the interpretation of the stress maps, it is convenient to plot the body force instead, where the Cartesian components are derived from the stress tensor giving the

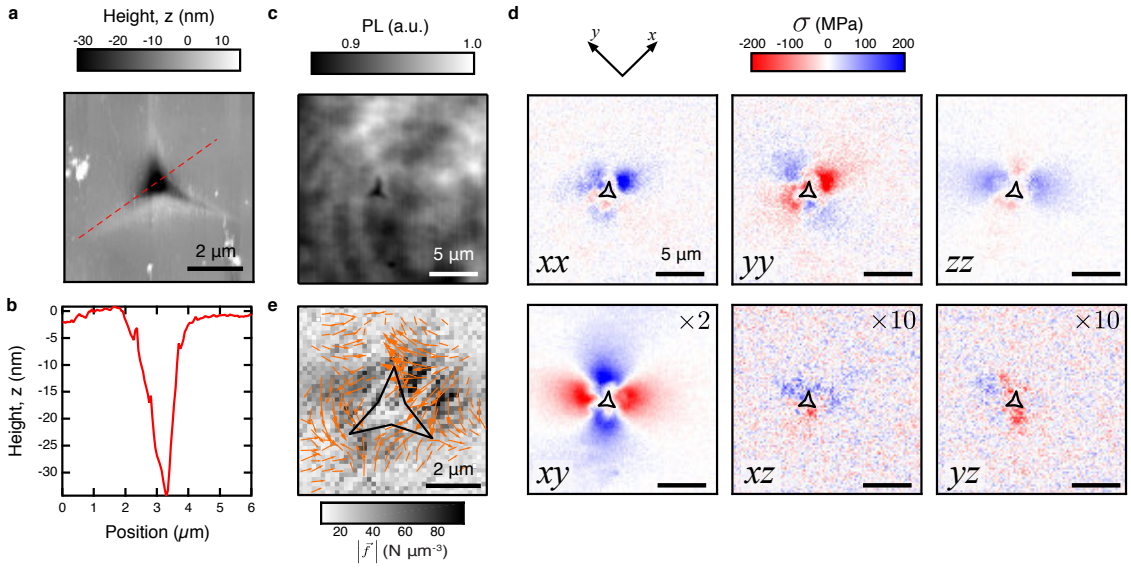

Figure 6.4: Stress induced by a nano-indent. **a** AFM image of a representative nano-indent in the diamond surface. **a** AFM profile across the indent (dashed line in (a)). **c** NV PL image of a region containing a nano-indent. **d** Spatial maps of the six stress tensor components in the same region as in (b). The black shapes represent the contour of the nano-indent as determined from the PL image. **e** Map of the body force deduced from the stress tensor using Equation (6.13). The colour denotes the magnitude $|\mathbf{f}_{\parallel}|$ while the overlaid arrows indicate the projected force in the xy plane.

body force equations of

$$\begin{aligned} -f_x &= \partial_x \sigma_{xx} + \partial_y \sigma_{xy} + \partial_z \sigma_{xz} \\ -f_y &= \partial_x \sigma_{xy} + \partial_y \sigma_{yy} + \partial_z \sigma_{yz} \\ -f_z &= \partial_x \sigma_{xz} + \partial_y \sigma_{yz} + \partial_z \sigma_{zz}. \end{aligned} \tag{6.13}$$

The x and y derivatives can be readily computed from the stress maps while the z derivatives can be estimated through a suitable approximation. The measured stress components are averaged over the thickness of the NV layer

$$\bar{\sigma}_{ij}(x,y) = \frac{1}{\Delta} \int_{z_0-\Delta/2}^{z_0-\Delta/2} \sigma_{ij} dz \tag{6.14}$$

where z_0 and Δ are the mean depth and thickness of the NV layer, assuming that the NV defects are uniformly distributed within the slab. Our aim is to use the stress equations to express the averaged body forces

$$\bar{f}_i(x,y) = \frac{1}{\Delta} \int_{z_0-\Delta/2}^{z_0-\Delta/2} f_i dz \tag{6.15}$$

in terms of the measured averaged stress components $\bar{\sigma}_{ij}$ so that we can use the measurements to obtain the average body forces and interpret their origin.

To do this, we integrate the stress equations

$$\begin{aligned} -\frac{1}{\Delta} \int_{z_0-\Delta/2}^{z_0+\Delta/2} f_x dz &= \frac{1}{\Delta} \int_{z_0-\Delta/2}^{z_0+\Delta/2} \frac{\partial \sigma_{xx}}{\partial x} + \frac{\partial \sigma_{xy}}{\partial y} + \frac{\partial \sigma_{xz}}{\partial z} dz \\ -\frac{1}{\Delta} \int_{z_0-\Delta/2}^{z_0+\Delta/2} f_y dz &= \frac{1}{\Delta} \int_{z_0-\Delta/2}^{z_0+\Delta/2} \frac{\partial \sigma_{xy}}{\partial x} + \frac{\partial \sigma_{yy}}{\partial y} + \frac{\partial \sigma_{yz}}{\partial z} dz \\ -\frac{1}{\Delta} \int_{z_0-\Delta/2}^{z_0+\Delta/2} f_z dz &= \frac{1}{\Delta} \int_{z_0-\Delta/2}^{z_0+\Delta/2} \frac{\partial \sigma_{xz}}{\partial x} + \frac{\partial \sigma_{yz}}{\partial y} + \frac{\partial \sigma_{zz}}{\partial z} dz \end{aligned}$$

which gives

$$\begin{aligned} -\bar{f}_x &= \partial_x \bar{\sigma}_{xx} + \partial_y \bar{\sigma}_{xy} + \frac{1}{\Delta}[\sigma_{xz}(z_0 + \frac{\Delta}{2}) - \sigma_{xz}(z_0 - \frac{\Delta}{2})] \\ -\bar{f}_y &= \partial_x \bar{\sigma}_{xy} + \partial_y \bar{\sigma}_{yy} + \frac{1}{\Delta}[\sigma_{yz}(z_0 + \frac{\Delta}{2}) - \sigma_{yz}(z_0 - \frac{\Delta}{2})] \\ -\bar{f}_z &= \partial_x \bar{\sigma}_{xz} + \partial_y \bar{\sigma}_{yz} + \frac{1}{\Delta}[\sigma_{zz}(z_0 + \frac{\Delta}{2}) - \sigma_{zz}(z_0 - \frac{\Delta}{2})]. \end{aligned}$$

If Δ is sufficiently small (i.e. NV layer sufficiently thin), then we could immediately apply the above by making the approximation that each $1/\Delta$ term is negligible,

$$\begin{aligned} -\bar{f}_x &= \partial_x \bar{\sigma}_{xx} + \partial_y \bar{\sigma}_{xy} \\ -\bar{f}_y &= \partial_x \bar{\sigma}_{xy} + \partial_y \bar{\sigma}_{yy} \\ -\bar{f}_z &= \partial_x \bar{\sigma}_{xz} + \partial_y \bar{\sigma}_{yz}. \end{aligned} \tag{6.16}$$

This is equivalent to stating that the out-of-plane (z) derivatives of the respective stress components are negligible at z_0. Alternatively, we can appeal to Leibniz integral rule to identify

$$\frac{d}{dz_0}\bar{\sigma}_{ij} = \frac{1}{\Delta}\frac{d}{dz_0}\int_{z_0-\Delta/2}^{z_0+\Delta/2} \sigma_{ij} dz = \frac{1}{\Delta}(\sigma_{ij}(z_0+\Delta) - \sigma_{ij} z_0).$$

Thus, the neglect of the third term in the above may instead be interpreted as stating that the average stress components depend little upon the depth of the NV layer z_0 (i.e. Δ is sufficiently large to capture all z dependence). So, in either limit – Δ much smaller than z variations or Δ much larger than z variations – we can adopt the approximate equation, Equation (6.16).

In intermediate situations, one can derive an estimate for the z derivatives as follows. If we assume that the stress decays in the z direction as $\sigma_{ij}(z) = \sigma_{ij}(0)\exp(-z/L)$ where L is the characteristic decay length, then for $L \gg z_0, \Delta$ we can approximate the z derivative term as

$$\frac{1}{\Delta}[\sigma_{ij}(z_0+\frac{\Delta}{2}) - \sigma_{ij}(z_0-\frac{\Delta}{2})] = \frac{\sigma_{ij}(z_0)}{\Delta}[e^{-\frac{\Delta}{2L}} - e^{+\frac{\Delta}{2L}}] \tag{6.17}$$

$$\approx -\frac{\bar{\sigma}_{ij}}{L} \tag{6.18}$$

where the bar denotes the average over the layer of width L. Hence

$$\begin{aligned} -\bar{f}_x &= \partial_x \bar{\sigma}_{xx} + \partial_y \bar{\sigma}_{xy} - \frac{\bar{\sigma}_{xz}}{L} \\ -\bar{f}_y &= \partial_x \bar{\sigma}_{xy} + \partial_y \bar{\sigma}_{yy} - \frac{\bar{\sigma}_{yz}}{L} \\ -\bar{f}_z &= \partial_x \bar{\sigma}_{xz} + \partial_y \bar{\sigma}_{yz} - \frac{\bar{\sigma}_{zz}}{L}. \end{aligned} \tag{6.19}$$

L is expected to be similar to the characteristic decay length observed in the xy

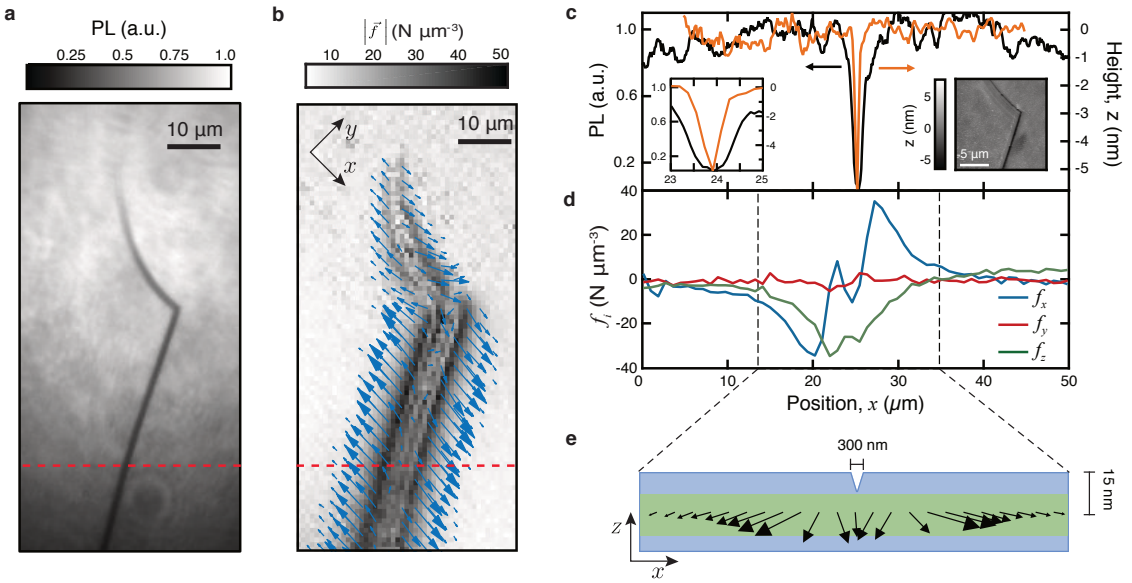

Figure 6.5: Stress induced by a superficial scratch. **a** PL image of a region containing a scratch. **b** Map of the body force magnitude for the region imaged in (a), with the overlaid arrows indicating the force projected in the xy plane. **c** Line cuts of the PL (black) and AFM profile (orange) taken along the red dashed line shown in (a). The left inset is a zoom-in; the right inset is an AFM image of the angled section of the scratch. **d** Corresponding line cuts of the three body force components (in and out of plane). **e** Schematic of the diamond cross-section (not to scale), with the overlaid arrows indicating the body force projected in the xz plane as derived from **d**.

plane, i.e. a few microns. In practice, we find that the third term in the right hand side of Equation (6.19) is negligible in calculating f_x and f_y, but is dominant in calculating f_z, i.e. we have $\bar{f}_z \approx \frac{\bar{\sigma}_{zz}}{L}$. The body force was calculated using Equation (6.19), taking $L = 3$ μm.

The body force near the indent is shown in Fig. 6.4e, revealing a complicated pattern. This pattern indicates that the tips of the impression push mostly outwards while there is an inward force at its flat edges. Additionally, this illustrates that Berkovich indentation results in a significant shear stress component, which is known to aid phase transformation [282] and may have application potential.

6.2.4 Stress from superficial scratches

We now return to scratches made with a diamond scribe to map the full stress tensor. Scratching the diamond surface can result in plastic deformation [282]. Similar to the

indent case, there is so sign of fracture of the diamond. A PL image of a scratched region is shown in Fig. 6.5a, where the scratch appears as a dark streak due to the reduction in crystal quality. The body force derived from the measured stress tensor is plotted in 6.5b. For this shallow scratch (5 nm deep at most, see AFM profile Fig. 6.5c and image in inset), the magnitude of the body force reaches about 40 N μm^{-3} corresponding to a stress of up to 0.2 GPa. Deeper scratches like those depicted in Fig. 6.1g,h can produce in excess of 1 GPa of stress. The body force decays from the center of the cut over distances of several micrometers, much larger than the width of the physical cut ($\approx$ 300 nm FWHM, see AFM profile in Fig. 6.5c, orange line) and the width of the PL quenching feature ($\approx$ 1 μm FWHM, black line in Fig. 6.5c). This illustrates that even a very shallow cut can elastically deform the diamond over distances significantly larger than the size of the cut itself. To gain more insight into the direction of the force, we plot the three force components across the scratch in Fig. 6.5d, represented as arrows overlaid on the diamond cross-section in Fig. 6.5e. Interestingly, the force remains mostly perpendicular to the diamond surface over several micrometers about the cut even though the NV sensors are located at a distance of $\approx$ 15 nm from the surface. This behaviour suggests a highly anisotropic propagation of the stress along the diamond surface.

6.2.5 Stress from device fabrication

As a final illustration of the technique, we mapped the stress resulting from the fabrication of electronic devices on diamond, which is of interest for high-power and high-frequency electronics applications [284] and for studies of charge transport using NV-based magnetometry [21, 285]. First, we fabricated a strip of Ti/Au (thickness 10/100 nm) on the bare diamond surface by thermal evaporation and lift-off (Fig. 6.6a,b), and found that the strip induces a small but measurable compressive stress in the diamond (Fig. 6.6c,d) especially near the edges of the strip ($\sim$ 10 MPa). Here, we plot the sum of the axial stress components, $\sigma_Z^{\text{axial}} = \sigma_{xx} + \sigma_{yy} + \sigma_{zz}$, as this gives a significantly improved signal-to-noise ratio over the individual components (as explained in section 6.2.6), as well as one of the shear stress components, σ_{xy}. We note that the weight of the deposited metal amounts to a pressure of about 0.02 Pa, and as such cannot account for the measured

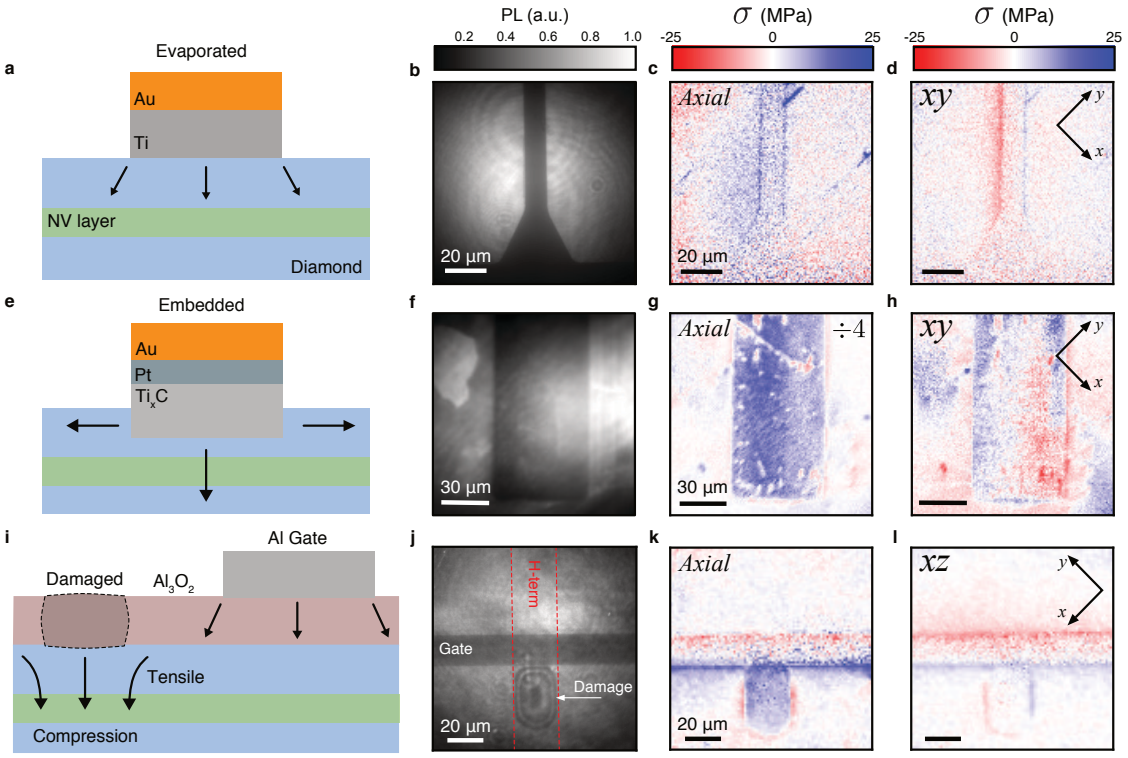

Figure 6.6: Stress induced by device fabrication. **a** Schematic cross-section of a device consisting of an evaporated metallic wire (Ti/Au). **b** PL image of a typical device. **c**, **d** Corresponding maps of the total axial stress $\sigma_Z^{\text{axial}} = \sigma_{xx} + \sigma_{yy} + \sigma_{zz}$ **c** and of the shear stress component σ_{xy}. **e-h** Same as **a-d** but for an embedded TiC/Pt/Au contact. **i-l** Same as **a-d** but for a transistor device where the conductive channel is formed by a hydrogen-terminated ('H-term.') region of the diamond surface (delimited by red dashed lines in **j** but giving no PL contrast), insulated via a Al_2O_3 oxide layer and controlled by a top Al gate (appears dark in the PL). A defect formed in the oxide layer above the conductive channel while operating the device, visible through a fringe pattern in the PL. **l** shows the σ_{xz} map.

stress. Also visible in Fig. 6.6c are some polishing marks, producing an axial stress of up to $\sigma_Z^{\text{axial}} \sim 40$ MPa.

Next, we fabricated TiC/Pt/Au contacts that extend about 15 nm into the diamond, through evaporation of a Ti/Pt/Au stack (thickness 10/10/70 nm) and subsequent annealing [184] (Fig. 6.6e,f). Such embedded contacts have been used in chapter 5 (Section 5.2.6) to form low-resistance ohmic contacts with the two-dimensional hole gas (2DHG) present on a hydrogen-terminated diamond surface [184, 286] as well as in high-power electronics [287]. As seen in the stress maps (Fig. 6.6g,h), there is a large compressive stress in the diamond below the TiC contact ($\sigma_Z^{\text{axial}} \sim 100$ MPa). This is expected because TiC has a lower atomic density than diamond. It is relatively uniform across the contact except for some small spots (a few μm in size) where there is no stress, indicative of imperfections in the formed TiC layer.

We then fabricated a transistor device based on the 2DHG at the diamond surface [286,288], by first patterning the surface termination to form a conductive (hydrogen-terminated) channel on an otherwise insulating (oxygen-terminated) surface, similar to the device made in Section 5.2.6, and then covering the whole surface with a 50-nm insulating layer of Al_2O_3, and evaporating a metallic top gate (Al, 50 nm thick). While operating the device, we observed the formation of a defect in the Al_2O_3 layer above the conductive channel next to the gate, as illustrated in Fig. 6.6i and seen in the PL image (Fig. 6.6j). The stress maps (σ_Z^{axial} in Fig. 6.6k and σ_{xz} in Fig. 6.6l) reveal a compressive stress under the oxide defect ($\sigma_Z^{\text{axial}} \sim 20$ MPa) and a tensile stress just outside the defect. The presence of the metallic gate on top of the oxide induces a stress of similar magnitude in the diamond, although the odd parity of σ_Z^{axial} is in contrast with the fully compressive stress observed in Fig. 6.6c suggesting a non-trivial mediation by the oxide layer, possibly through permanent deformation of the oxide under the gate while operating the device. These experiments illustrate that the technique can be applied to monitor mechanical deformations in materials and devices outside the diamond, through the elastic stress applied to the diamond substrate as a result, which could find applications as a diagnostic tool for device variability or failure analysis.

6.2.6 Sensitivity of the method

The sensitivity of the stress measurements, which dictates the smallest detectable change (in space or time) for a given integration time, is limited by statistical errors arising from the statistical noise in the measured NV frequencies $(\omega_\pm)_i$. The latter originates from photon count noise in the ODMR data, which has contributions from both the photon shot noise and dark counts from the camera. To characterise this noise, we calculate the standard deviation from an ensemble of pixels in a region of the image where the stress is relatively uniform, i.e. the pixel-to-pixel noise. We find this noise (ζ) to be typically of the order of $\zeta \sim 1$ MPa for the shear components and $\zeta \sim 10$ MPa for the axial components for a 1×1 μm^2 pixel and a total integration time of 10 hours, with no significant improvement with longer acquisition indicating that this is close to the technical noise floor. As expected, the error is larger on the axial stress components than on the shear components, because of the difference in sensitivity of the NV frequencies to these different components. Indeed, the shear components are obtained from a linear combination of the sum frequencies $\{S_i\}$ (Eq. 6.8), with a sensitivity

$$\frac{\partial S_i}{\partial \sigma_{xy}} \sim a_2 \approx 4 \text{ MHz GPa}^{-1}. \tag{6.20}$$

In contrast, the individual axial components are derived from the difference frequencies $\{D_i\}$ (Eq. 6.10) which has a sensitivity, in the limit $\gamma_{\mathrm{NV}} B_{Z_i} \gg \mathcal{M}_{\perp,i}$ [275],

$$\frac{\partial D_i}{\partial \sigma_{xx}} \sim b \frac{\mathcal{M}_\perp}{\gamma_{\mathrm{NV}} B_{Z_i}} \approx 2 \text{ MHz GPa}^{-1} \times \frac{\mathcal{M}_\perp}{\gamma_{\mathrm{NV}} B_{Z_i}}, \tag{6.21}$$

where $\mathcal{M}_\perp \doteq \sqrt{\mathcal{M}_{X_i}^2 + \mathcal{M}_{Y_i}^2}$. The suppression factor $\frac{\mathcal{M}_\perp}{\gamma_{\mathrm{NV}} B_{Z_i}}$ depends on the exact conditions but is typically below 0.1, which results in a statistical noise on the axial components (as obtained by solving the overdetermined problem) typically an order of magnitude larger than that on the shear components. We note that the sum of the axial components, $\sigma_Z^{\mathrm{axial}} = \sigma_{xx} + \sigma_{yy} + \sigma_{zz}$, is fixed by the sum frequencies $\{S_i\}$ and therefore is not affected by this suppression factor, yielding a statistical noise down to 1 MPa. For applications where measuring the individual axial stress components with maximum sensitivity is desirable, we could perform four consecutive ODMR measurements with an external magnetic field

optimized to minimise B_{Z_i} for each NV orientation sequentially. Such a sequential measurement strategy would also allow much larger stress values to be measured (up to 100 GPa), currently limited to a few GPa by the minimum spacing between adjacent ODMR lines (20-30 MHz) [210].

6.3 Conclusion

In summary, we presented a method to quantitatively image the full stress tensor below the surface of a diamond, at room temperature, using a layer of NV strain sensors. We illustrated the versatility of the technique by experimentally mapping the stress under a number of scenarios, from localized implantation damage to nano-indents to devices fabricated on the diamond surface. With our current experimental set-up, the spatial resolution is limited by the diffraction limit ($\approx$ 400 nm) but could be improved by implementing super-resolution techniques [289, 290]. The measurement sensitivity is of the order of 1 MPa per 1×1 μm^2 pixel for typical acquisition times ($\sim$ 10 hours), and could be improved by an order of magnitude through futher optimisation of the NV-diamond samples [291].

The technique could be directly applied to characterise the residual stress in various types of diamond nanostructures commonly used for quantum sensing and quantum information science, such as solid-immersion lenses [292], nano-pillars [293, 294], nanobeams [295, 296], and photonic waveguides and cavities [297–300], which could help improve the sensing accuracy or optimise the fabrication processes. Moreover, the technique is compatible with stroboscopic measurements, capable for instance of imaging the time evolution of stress in mechanically driven diamond cantilevers [142, 301, 302], which are a testbed for hybrid spin-mechanical quantum systems. These results establish NV-based wide-field stress mapping as a powerful technique for nanoscale mechanical studies of diamond, which is an intensely interesting material for nanomechanical applications with extreme mechanical properties and sometimes unexpected strain-stress relationships [303]. The technique may also facilitate strain engineering for diamond-based quantum applications [142, 296, 302, 304–307], and find applications in multiplexed nanomechanical sensing for mass spectroscopy and microfluidics [308–311].

Conclusion to Part II

In the second part of this thesis, imaging of different fields with ensemble NV systems was investigated. In Chapter 5, the standard ODMR technique was used to fit the NV Hamiltonian to measure the electric field produced from surface band-bending. This work detected the differences between hydrogen and oxygen terminated diamond surfaces. These results showed a significant electric field for oxygen terminated diamond that is undesirable, however, through measuring the electric field before and after different surface treatments it is possible to optimise this procedure. Improving surface treatment will lead to producing NV^- spins that are populated closer to the surface which is ideal for hyperpolarisation applications. Finally in this chapter we found a non-trivial and unexpected charge injection into the bulk for hydrogen terminated channels. While this effect is undesirable for this 2D hole gas conductor, it was shown that the application of a green laser over a certain intensity can remove the build up of this charge in the bulk by ionising the charges and improving the hydrogen terminated channels conductivity.

In chapter 6 the effect of stress on the NV is exploited in order to measure the full stress tensor. A detailed study of the fitting procedure and the technique limitations is discussed which leads to a greater sensitivity to shear over axial stress (roughly an order of magnitude). To demonstrate the accuracy of the technique, a circle of stress was fabricated through implantation of carbon atoms into the diamond. These results illustrated that the stress can be measured down to 1 MPa (10 MPa) for shear (axial) stress component and determined the expected symmetry from such a stress object. It was also shown that the embedded body force can be extracted from the stress caused by both indents and scratches in the diamond surface. Finally, stress was imaged from different fabrication procedures, indicating a significant stress propagation from metallic contacts, through an

oxide layer and into the diamond. Measurement of the propagated stress fields could be an important technique for developing procedures that minimise unwanted stress in stacked electronics.

7

Conclusion

This thesis developed two distinct types of quantum technologies: hyperpolarisation of nuclear spin through quantum control of diamond spins (Part I) and multi-modal microscopic imaging of magnetic, electric, and stress fields (Part II). In the first part, a detailed understanding of several techniques that allow for polarisation transfer from the central nitrogen vacancy spin to local nuclear spins was developed. One of the technique developed (cross-relaxation induced polarisation) was demonstrated to be capable of meaningfully imparting polarisation onto nuclear spins that are external to the diamond substrate. While this protocol has a particularly exceptional polarisation transfer rate, lacks robustness to experimental errors (e.g. magnetic field misalignment and noise). Therefore, to implement hyperpolarisation on a large scale, a different protocol was developed (PolCPMG) that is more robust to experimental errors than traditional methods, demonstrating remarkable resilience to deliberately introduced detunings. For larger scale applications, it is vital to understand the method of polarisation, the spatial extent, and the lifetime/diffusion. This crucial information can be obtained through spatially measuring the polarisation on a local scale, in which the NV has a distinct advantage over traditional bulk measurements. These results construct a promising route towards the long-standing goal of NV-based hyperpolarisation platform for macroscopic volumes of external sample. Such a system could be used to enable ultra-sensitive NMR spectroscopy, enhance cell biology studies, produce hyperpolarised agents for traditional MRI, or form the basis of a quantum simulator.

In the second part, the category of imaging is developed through the introduction of

an analysis method that is capable of imaging fields that have previously been overlooked, electric fields and stress. First, insidious electric fields that are intrinsic to the diamond surface and are responsible for removing the NV charge state are detected. These measurements facilitate further optimisation of diamond surface treatments that aim to minimise the electric field and thus permit NV spins to exist closer to the surface. Additionally, measuring the electric field gives information about changes in the local charge density, which was used to image parasitic bulk charge injection from the operation of a two dimensional hole gas device. Finally, stress that is embedded in the diamond was measured. To this end, various sources of stress were investigated: indentation, scratches, implantation, evaporation of metals, hybrid diamond contacts, and damage from transistor fabrication and operation. This collection of stress sources in diamond is extremely useful for identifying potential sources of stress, the spatial extent of this stress, and the magnitude of the stress components that are introduced. Through this imaging method, techniques for stress engineering could be optimised, promising to have a host of applications in designer materials.

Appendices

A

Temperature controlled magnet

This appendix contains details about the experimental procedure or analysis protocol that was used in section 3.2. This work was published as a supplementary information for Ref. [184].

A.1 Magnet properties

There are many types of permanent magnet materials which each offer different use cases. This often results in trying to maximise or minimise a certain quality of the magnet. Generally, the magnet quality can be described by 6 factors. Remanence (Br) Is a measure of the volume of magnetisation in the material, coercivity (Hc) is a measure of resistance to demagnetisation by other magets, BH_{max} is the maximum energy product, T_{coef} of Br (α) is a measure of the degree of magnetisation lost for an increase of 1°C, T_{max} is the maximum operating temperature before permanent magnetisation loss occurs, and T_{currie} is the Currie temperature of the material. Neodymium is a great candidate of NV measurements as it offers quite a high magnetic field, however, it comes at the cost of α. As can be see in Table. A.1 there are other materials available that would offer a greater stability than neodymium but would also be difficult to change the magnetisation greatly via temperature.

material	Br (kG)	Hc (kOe)	BH_{max} (MGOe)	T_{coef} of Br (%)	T_{max} (C)	T_{currie} (C)
NdFeB	13	11.5	42	0.11	80-240	310-370
SmCo	10.5	9.2	26	0.04	250	700-800
Alnico	12.5	0.64	5.5	0.02	525-550	860
Ferrite	3.9	3.2	3.5	0.2	250	450
SmEr	10	8	20	0.008	>100	>100

Table A.1: Magnet properties for different materials. SmEr has a full composition of $Sm_{0.8}Er_{0.2}(Co_{0.69}Fe_{0.22}Cu_{0.08}Zr_{0.02})_{7.22}$ [312]

A.2 Magnetic stabilisation

Here we present additional details and measurements to illustrate the stabilisation of the magnet. Without stabilisation of the temperature there can be variations that results in changes in the NV frequency on the order of 2 MHz over the course of 20 hours, shown in Fig. A.1a. These fluctuations in the NV spin transition frequency are directly correlated with the temperature fluctuations of the room shown in the bottom panel. Implementing the PID loop to maintain the magnet temperature reduces the fluctuations to 800 kHz, shown in Fig. A.1b. While the thermistor reading is constant at the magnet surface there is still variation in the magnetisation of the magnet due to room temperature variations.

Comparing Figs. A.1a and A.1b there is a difference in the direction of the change relative to the room temperature change, going from anti-correlated to correlated. When there is no control an increase in room temperature results in a decrease in magnetisation or NV frequency ($\Delta\omega_{NV}$). However, with the PID loop on the changes are reversed, indicating that the change is due to the room temperature affecting the reading by the thermistor rather than changes to the temperature of the magnet. While extensive insulation would mitigate this issue it would also reduce the maximum achievable magnetic field at the NV, by increasing the minimum working distance. A thin layer of insulation was applied to the thermistor but showed no significant increase in stability. Instead we applied a feedback mechanism on the set temperature to compensate for this effect. Assuming that the change in magnetisation of the magnet is given by

$$\Delta M_s = \alpha_M T_M + \alpha_R T_R \tag{A.1}$$

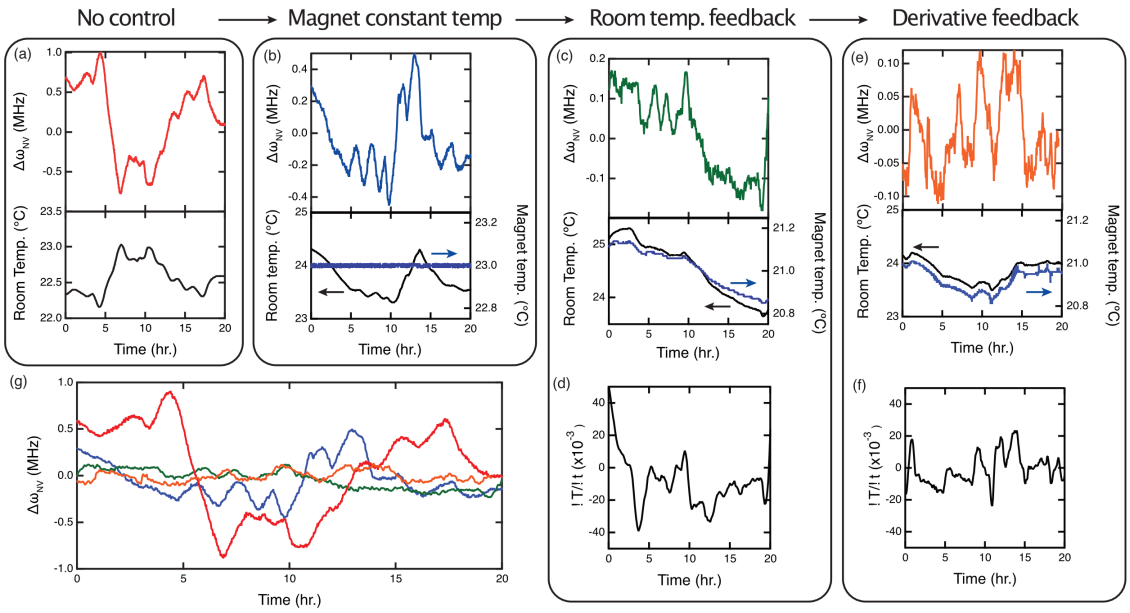

Figure A.1: (a) Changes in the NV frequency over the period of 20 hours (top panel), and the room temperature over this period (bottom panel). The temperature changes result in a variation in NV frequency of roughly 2 MHz peak to peak. (b) Changes in the NV frequency (top panel) while the TEC attempts to maintain a constant temperature of the magnet, reducing the fluctuation to 800 kHz. While the room temperature changed, the reading of the magnet temperature was constant (bottom panel). (c) Modulating the set temperature of the magnet based off the room temperature reduced the fluctuation to 400 kHz. (d) The derivative of the room temperature displayed in (c). (e) Inclusion of the derivative factor, further reducing the fluctuations to 200 kHz. (f) The derivative of the room temperature in (e). (g) Comparison of all the methods, colour matched to the other plots.

where $\alpha_{\mathrm{M}} = 2.7$ (MHz/°C) obtained by measurements, T_{M} and T_{R} are the thermistor temperature reading of the magnet and the room temperature, and α_{R} is a constant that defines the effect of the room temperature on the magnetisation. Minimising the change gives,

$$T_{\mathrm{M}} = -\frac{\alpha_{\mathrm{R}}}{\alpha_{\mathrm{M}}} T_{\mathrm{R}}. \tag{A.2}$$

Including this feedback factor reduces the magnetisation fluctuations from 800 kHz to 400 kHz, shown in Fig. A.1c. To increase the stability further the relative speed of the fluctuation must be coincided. Comparing the derivative of the room temperature (Fig. A.1d) to the changes in magnetisation shows a clear correlation between some of the features. The set temperature can thus be changed to

$$T_{\mathrm{M}} = -\frac{\alpha_{\mathrm{R}}}{\alpha_{\mathrm{M}}} T_{\mathrm{R}} + \frac{\alpha_{\partial}}{\alpha_{\mathrm{M}}} \frac{\partial T_{\mathrm{R}}}{\partial t} \tag{A.3}$$

where α_{∂} is a constant that is modified to decrease the changes from the derivative. Including this feedback reduces the deviation in NV frequency to 200 kHz (Fig. A.1e), which is within the line width of near surface NV centres. The derivative of the room temperature is shown in Fig. A.1f. While some of the changes in $\Delta\omega_{\mathrm{NV}}$ are clearly seen in the derivative they are not completely removed. This is due to noise in the derivative being amplified and creating fast changes in α_{∂}. Therefore, there is a trade off between reducing the changes due to the derivative and introducing noise. While Savitzky-Golay filtering of the data improves this trade off it also introduces a lag time in-between the change in temperature and the reaction of the feedback. A comparison of all four control stages is shown in Fig. A.1g, showing a significant improvement from the feedback system.

A.3 Theory: Bath polarisation measurement

Numerical simulations are performed on a random configuration of $n = 500$-5000 spins at a density of 1.1% ^{13}C. The evolution of the $n+1$ system (where the NV is included) can be obtained using an evolution operator with a scattering matrix argument that is defined

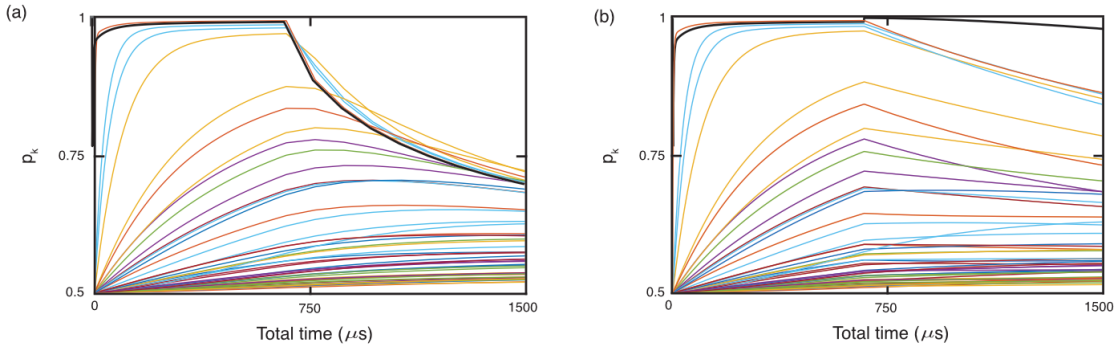

Figure A.2: NV spin population (black) and population of 500 ^{13}C spins for 50 polarisation pulses followed by an evolution time when the NV is left in $|0\rangle$ (a) and for when the NV is put in the non-resonant $|+1\rangle$ state (b).)

by the relevant hyperfine fields, such that

$$S = \text{Diag}\left[\frac{1}{\pi}\frac{\mathbf{A}_{sq}}{\sum_n \mathbf{A}_{sq}} - \sum_n \sqrt{\mathbf{B}_{sq}}\right] + \sqrt{\mathbf{B}_{sq}} - \frac{\mathbf{I}}{T_{1,E}} \tag{A.4}$$

where $\mathbf{A}_{sq} = (\mathbf{A}_{xx} - \mathbf{A}_{yy})^2 + 4\mathbf{A}_{xy}^2$ is the NV-^{13}C hyperfine matrix, $\mathbf{B}_{sq} = (\mathbf{B}_{xx} - \mathbf{B}_{yy})^2 + 4\mathbf{B}_{xy}^2$ is the ^{13}C-^{13}C hyperfine matrix, and $T_{1,E}$ contains both the boundary leakage of polarisation and rethermalisation of the ^{13}C spins. This scattering matrix is effective at simulating both the polarisation build-up and the free evolution time. An example of a 50 polarisation pulses followed by a single evolution time is shown in Fig. A.2 for both the NV in $|0\rangle$ (a) and $|+1\rangle$ (b). When the NV is in the $|0\rangle$ state it decays and reduces the overall polarisation of the bath. However, when the NV is in the $|+1\rangle$ state the polarisation of the bath remains relatively constant over the same time period.

B

Experimental methods for Electric field measurements

This appendix contains details about the experimental procedure or analysis protocol that was used in chapter 5. This work was published as a supplementary information for Ref. [187].

B.1 Diamond samples

The NV-diamond samples used in these experiments were made from 4 mm × 4 mm × 50 μm electronic-grade ([N] < 1 ppb) single-crystal diamond plates with {110} edges and a (001) top facet, purchased from Delaware Diamond Knives, subsequently laser cut into smaller 2 mm × 2 mm × 50 μm plates and acid cleaned (15 minutes in a boiling mixture of sulphuric acid and sodium nitrate). Each plate was then implanted with $^{15}N^{+}$ ions (InnovIon) at a given energy (ranging from 4 to 20 keV), a dose of 10^{13} ions/cm^2, and with a tilt angle of 7°. Following implantation, the diamonds were annealed in a vacuum of $\sim 10^{-5}$ Torr to form the NV centres, using the following sequence [210]: 6h at 400°C, 2h ramp to 800°C, 6h at 800°C, 2h ramp to 1100°C, 2h at 1100°C, 2h ramp to room temperature. To remove the graphitic layer formed during the annealing at the elevated temperatures, the samples were acid cleaned (15 minutes in a boiling mixture of sulphuric acid and sodium nitrate) before any further surface treatment or fabrication step.

B.2 Surface treatments

To form the H-terminated channels measured in chapter 5, the diamond sample was first subject to a soft hydrogen plasma (7 minutes at 400 W, 10 Torr) optimised to make the diamond surface conductive via hydrogenation while preserving the integrity of the NV centres [72]. The channels were then protected by a photoresist mask and the sample subject to a soft oxygen plasma (5 minutes at 50 W, 14 MHz RF with a 0.7 Torr O_2/Ar pressure) optimised to render the surface non-conductive via oxygen termination, while minimising the amount of etching of the diamond. No topography step was observed in atomic force microscopy (AFM) indicating an etching by the oxygen plasma below our AFM resolution (i.e. < 0.5 nm).

The effect of other variants of oxygen termination are investigated. Namely, starting with a diamond (sample #2) oxygen terminated via an oxygen plasma as described previously (labelled as 'Plasma'), we applied the following steps: (i) acid cleaning (15 minutes in a boiling mixture of sulphuric acid and sodium nitrate); (ii) annealing at 500°C in oxygen-rich atmosphere similar to the process used in Ref. [125]; (iii) cleaning in a piranha solution (mixture of 4 ml of sulphuric acid and 2 ml of hydrogen peroxide heated to 90°C) for 10 minutes. The resulting surfaces are labelled as 'Acid', 'O_2 burn' and 'Piranha', respectively.

B.3 Device fabrication

The devices such as the one imaged chapter 5 were fabricated via the following steps. A stack of Ti/Pt/Au (thickness 10/10/70 nm) was evaporated onto the diamond (diamond #2) masked by a photoresist pattern. After lift-off of the photoresist leaving Ti/Pt/Au contacts, the sample was annealed at 600°C for 20 mins in hydrogen gas (10 Torr). At such temperature, Ti atoms are able to diffuse into the diamond, and conversely carbon atoms are able to diffuse into the Ti layer, thus forming a TiC layer extending about 15 nm into the diamond. The thick Au layer serves as the primary contact material for electrical interfacing, while the Pt layer is introduced to act as a barrier preventing diffusion of Au and Ti atoms across the Ti/Au interface. The interest of such a process is to form a clean

quasi-one-dimensional interface with the H-terminated channels subsequently fabricated. Together with the high expected work function of TiC ($\approx$ 5 eV [239]), this results in more consistent formation of Ohmic contacts than with conventional 2D interfaces of H-terminated diamond with Au [237] or Ti [238], for instance. After the TiC/Pt/Au contacts were formed, the H-terminated channels were made via the process outlined above, i.e. hydrogen plasma to H-terminate the bare diamond surface, photo-lithography to protect the channels, and oxygen plasma to O-terminate the unprotected diamond surface. Finally, large Cr/Au (10/70 nm) contact pads partially overlapped with the TiC/Pt/Au contacts were evaporated onto the device for physical wire bonding.

B.4 Imaging set-up

The NV imaging set-up is a custom-built wide-field fluorescence microscope similar to that used in Refs. [21,45], with photographs shown in Fig. B.1. The diamonds were glued on a glass cover slip patterned with a microwave waveguide, connected to a printed circuit board (PCB) with silver epoxy. The diamond devices were electrically connected to the cover slip via wire bonding, and to the PCB board with silver epoxy. The voltage through the device under study was applied using a source-meter unit (Keithley SMU 2450) operated in constant voltage mode. All measurements were performed in an ambient environment at room temperature, under a bias magnetic field $\mathbf{B}_0$ generated using a permanent magnet.

Optical excitation from a 532 nm Verdi laser was gated using an acousto-optic modulator (AA Opto-Electronic MQ180-A0,25-VIS), beam expanded (5x) and focused using a wide-field lens (f = 200 mm) to the back aperture of an oil immersion objective lens (Nikon CFI S Fluor 40x, NA = 1.3). The photoluminescence (PL) from the NV centres is separated from the excitation light with a dichroic mirror and filtered using a bandpass filter before being imaged using a tube lens (f = 300 mm) onto a sCMOS camera (Andor Zyla 5.5-W USB3). Microwave excitation was provided by a signal generator (Rohde & Schwarz SMBV100A) gated using the built-in IQ modulation and amplified (Mini-Circuits ZHL-16W-43+) before being sent to the PCB. A pulse pattern generator (SpinCore PulseBlasterESR-PRO 500 MHz) was used to gate the excitation laser and microwaves and to synchronise the image acquisition. The total CW laser power at the

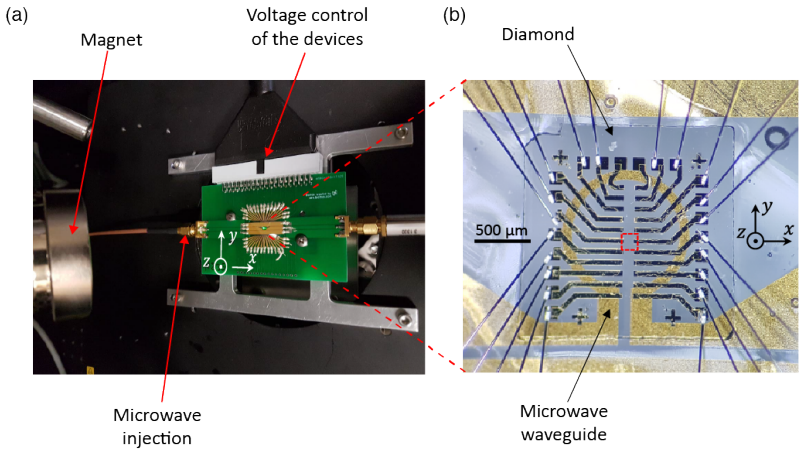

Figure B.1: (a) Photo showing the sample board with microwave and DC inputs, as well as the permanent magnet used to apply the bias magnetic field $\mathbf{B}_0$. (b) Photo of the diamond as mounted. The red box indicates a typical area used for imaging.

Sample	$\varepsilon(D, \mathbf{B})$ (kHz)	$\varepsilon(D, \mathbf{B}, \mathcal{E}_z)$ (kHz)	σ_{f_i} (kHz)
#1	630	45	23
#2	380	60	22
#3	570	63	47
#4	270	90	53
#5	220	61	20

Table B.1: Residual error ε from fitting the measured ODMR frequencies $\{f_i\}_{i=1..8}$ without including the Stark effect (second column) and when including a normal-to-the-surface electric field $\mathcal{E}_z$ (third column). The fourth column indicates the standard error on the $\{f_i\}_{i=1..8}$ from fitting the ODMR spectrum with Lorentzian functions.

sample was 300 mW, which corresponds to a maximum power density of about 5 kW/cm^2 given the $\approx$ 120 μm $1/e^2$ beam diameter. The optically detected magnetic resonance (ODMR) spectra of the NV layer were obtained by sweeping the microwave frequency while repeating the following sequence: 10 μs laser pulse, 1 μs wait time, 300 ns microwave pulse; with total acquisition times of several hours typically.

B.5 Error analysis

We now discuss the sources of error in our reconstruction method. First, it is interesting to examine the residue ε after fitting. This is summarised in Table B.1, which gives the case where the Stark effect is not included in the Hamiltonian, i.e. $\varepsilon(D, \mathbf{B})$, and the case where

the Stark effect is included but the electric field is constrained to be perpendicular to the diamond surface, i.e. $\varepsilon(D, \mathbf{B}, \mathcal{E}_z)$. Also indicated in the uncertainty (standard error) in determining the frequencies $\{f_i\}_{i=1..8}$, denoted as σ_{f_i}, obtained from the Lorentzian fit to the ODMR spectrum and averaged over the eight lines. Clearly, the data is not well fit without including the Stark effect, with $\varepsilon(D, \mathbf{B})$ being 5-30 times larger than the measurement uncertainty σ_{f_i}. Instead, when one includes the Stark effect ($\mathcal{E}_z$ only), one reduces the residue ε by up to an order of magnitude, which is clear evidence that measurable electric fields are present in our sample. The residue is still a factor 2-3 larger than σ_{f_i}, which can be due to one or a combination of the following effects. First, the electric field might be not exactly along the z axis, e.g. due to surface roughness, diamond miscut, or non-uniform density of surface or bulk defects, although fitting $\mathcal{E}_x$ and $\mathcal{E}_y$ as well as $\mathcal{E}_z$ did not significantly reduce the residue ε. Second, other corrections to the Hamiltonian may need to be considered, e.g. the effect of mechanical strain in the diamond (see discussion in Sec. B.6). Third, there may be systematic errors in the $\{f_i\}_{i=1..8}$, for instance due to each ODMR line comprising several sub-lines with uneven amplitudes (they are assumed even in our analysis, see Fig. 5.4 and corresponding discussion) or due to partial overlapping between adjacent lines (leading to systematic errors if the actual line shape is not exactly Lorentzian as it is assumed, which can arise e.g. from the electric field gradient experienced by the NV ensemble). Nevertheless, the fact that simply adding a single parameter to the fit ($\mathcal{E}_z$) reduces the residue by an order of magnitude suggests that this parameter captures very well the physics of the problem.

We listed above the possible causes for systematic errors in the measurements. On top of that, there is a statistical error in the $\{f_i\}_{i=1..8}$ that originates from photon count noise in the ODMR spectrum, which is usually close to the photon shot noise limit in our experiments but can also be affected by readout noise and dark counts of the camera depending on the exact conditions. To characterise this noise, we simply calculate the standard deviation σ_{f_i} from a large ensemble of pixels, which is found to be in the range 20-60 kHz in our experiments (see Table B.1). This uncertainty on the $\{f_i\}_{i=1..8}$ translates into an uncertainty on $\mathcal{E}_z$. Again, we characterise this by taking the standard deviation of the $\mathcal{E}_z$ map. Doing so on a small region gives an uncertainty of the order of 1 kV/cm, i.e. less than 1 % of the mean value, corresponding to the statistical (pixel-to-pixel) noise. By

evaluating the standard deviation over larger areas, one captures statistical noise as well as actual spatial variations of $\mathcal{E}_z$, due e.g. to spatial variations in the density of surface defects.

Finally, we discuss the consequences of the Stark effect from built-in electric fields on the accuracy of magnetometry measurements. In our measurements, because $\mathbf{B}$ is treated as a fit parameter, neglecting the Stark effect leads to a biased estimation of $\mathbf{B}$ in order to minimise $\varepsilon(D, \mathbf{B})$. Taking sample #1 from Table B.1 as an example, we obtain ($D = 2870.2$ MHz, $B_x = 3672$ μT, $B_y = 1027$ μT, $B_z = -4987$ μT, $\mathcal{E}_z = 378.4$ kV/cm) when including $\mathcal{E}_z$, against ($D = 2870.2$ MHz, $B_x = 3699$ μT, $B_y = 1025$ μT, $B_z = -4976$ μT) when neglecting the Stark effect. This shows that neglecting the Stark effect may lead to systematic errors of the order of 30 μT in magnetometry measurements, motivating the need for precise characterisation of built-in electric fields for high-precision magnetometry applications, and minimising the sensitivity to electric fields by careful alignment of an external bias magnetic field.

B.6 On the effect of strain

Mechanical strain acts as an effective electric field in the NV spin Hamiltonian [173], which simply adds to the true electric field and therefore may in principle contribute to the electric fields measured in this work. In this section, we estimate the effect of strain in our samples induced by bulk defects, surface defects as well as dilational dislocations, and conclude that it is negligible compared to the electric field due to surface band bending. This section on strain was developed by Dr. Marcus Doherty.

B.6.1 Strain induced by bulk point defects

In the simplest picture, a point defect is an isotropic point source of expansion or contraction of the lattice [313]. In continuum mechanics, the displacement field $\vec{u}$ of this expansion/contraction is analogous to the electric field of a point charge and takes the form [313]

$$\vec{u} = \frac{A_0}{\left|\vec{r} - \vec{r}_0\right|^3}\left(\vec{r} - \vec{r}_0\right), \tag{B.1}$$

where A_0 is known as the defect strength and $\vec{r}_0$ is the position of the defect. This displacement field is the solution of the elastic equation

$$\vec{\nabla} \cdot \vec{u} = 4\pi A_0 \delta \left(\vec{r} - \vec{r}_0 \right). \tag{B.2}$$

Since the displacement field induced by a point defect is irrotational $\vec{\nabla} \times \vec{u} = \vec{0}$, the displacement field can be expressed in terms of a scalar potential, Φ, via $\vec{u} = -\vec{\nabla}\Phi$. In which case, the elasticity equation becomes (see references [314] for background)

$$-\nabla^2 \Phi = 4\pi A_0 \delta \left(\vec{r} - \vec{r}_0 \right). \tag{B.3}$$

Note the parallel between Φ and the electric potential.

The defect strength is related to the change in volume ΔV_0 induced by the defect [313]

$$A_0 = \frac{\Delta V_0 (\nu + 1)}{12\pi(1 - \nu)} \tag{B.4}$$

where ν is the Poisson ratio of the solid. The change in volume can be obtained from x-ray crystallography that determines the solid's lattice parameter as a function of the defect concentration or by ab initio calculations.

The components of the strain field are defined with respect to the displacement field via

$$\epsilon_{ij} = \frac{1}{2} \left(\frac{\partial u_i}{\partial r_j} + \frac{\partial u_j}{\partial r_i} \right) \tag{B.5}$$

where $i, j = x, y, z, u_i$ denotes the i-vector component of the displacement field and r_i denotes the i-coordinate. The stress is calculated from the strain via

$$\begin{aligned} \sigma_{ii} &= \lambda \mathrm{Tr} \overleftrightarrow{\epsilon} + 2\mu\epsilon_{ii} \\ \sigma_{ij} &= \mu\epsilon_{ii} \quad \text{for } i \neq j \end{aligned} \tag{B.6}$$

where λ and μ are Lame's constant and the shear modulus, respectively.

Assuming that the displacements due to different defects are sufficiently small that they may be added in superposition, the elasticity equation for a continuous number

density ρ of defects is simply

$$-\nabla^2\Phi = 4\pi A_0\rho(\mathbf{r}) \tag{B.7}$$

Consider now a semi-infinite slab in the $x-y$ plane, extending vertically from $z=-h/2$ to $z=h/2$. If the slab has a uniform density ρ of defects, the solutions of the elasticity equation immediately follow as

$$\begin{aligned}
\Phi &= -2\pi A_0\rho z^2 \\
\vec{\mu} &= 4\pi A_0\rho z\hat{z} \\
\epsilon_{zz} &= 4\pi A_0\rho \\
\sigma_{zz} &= 4\pi(\lambda+2\mu)A_0\rho \\
\sigma_{xx} &= \sigma_{yy} = 4\pi\lambda A_0\rho.
\end{aligned} \tag{B.8}$$

All other strain and stress components are zero. Thus, the defects produce uniform stress and strain that is principally in the vertical direction (assuming $\mu \gg \Lambda$) and proportional to the density of defects.

For the N defect in diamond, $A_0\rho = 1.67113\times10^{-8}$ using the x-ray data $\Delta V_0\rho = 0.42\times10^{6}$ ppm^{-1} [315] and the diamond Poisson ratio $\nu = 0.2$. Using $\lambda = 85$ GPa and $\mu = 536$ GPa, the stress components as a function of concentration (units: GPa/ppm) are 242.806×10^{-6} and 17.838×10^{-6} repectively. Since the spin-stress susceptibility parameters are on the order of 1 MHz/GPa, and the N concentrations in our implanted samples are on the order of 10 ppm, we get that the NV frequency shifts induced are ~ 10 kHz, equivalent to ~ 1 kV/cm in terms of effective electric field. This is smaller than our measurement uncertainty and therefore negligible. The strengths of other common defects (N^+, NV^- and NV^0) are smaller than N^0, as predicted by the ab initio calculations in [316]. Thus, even considering multiple defect species, it is unlikely that strain will induce a significant shift in the spin resonances.

B.6.2 Strain induced by surface defects

To model surface defects, reconsider the slab but with a defect density that decays exponentially from the surface

$$\rho(z) = \rho_0 \left(e^{-\left|z-\frac{h}{2}\right|/L} + e^{-\left|\frac{h}{2}+z\right|/L} \right) \tag{B.9}$$

In this case, the elasticity solutions are

$$\begin{aligned}
\Phi &= -4\pi L^2 A_0 \rho_0 \left(e^{-\left|z-\frac{h}{2}\right|/L} + e^{-\left|\frac{h}{2}+z\right|/L} \right) \\
\overrightarrow{\mu} &= 4\pi L A_0 \rho_0 \left(e^{-\left|z-\frac{h}{2}\right|/L} + e^{-\left|\frac{h}{2}+z\right|/L} \right) \hat{z} \\
\epsilon_{zz} &= 4\pi A_0 \rho_0 \left(e^{-\left|z-\frac{h}{2}\right|/L} + e^{-\left|\frac{h}{2}+z\right|/L} \right) \\
\sigma_{zz} &= 4\pi\lambda + 2\mu A_0 \rho_0 \left(e^{-\left|z-\frac{h}{2}\right|/L} + e^{-\left|\frac{h}{2}+z\right|/L} \right) \\
\sigma_{xx} &= \sigma_{yy} = 4\pi\lambda A_0 \rho_0 \left(e^{-\left|z-\frac{h}{2}\right|/L} + e^{-\left|\frac{h}{2}+z\right|/L} \right)
\end{aligned} \tag{B.10}$$

Again, the principal stress in the vertical direction and is proportional to the density of defects. As the density decays exponentially from the surface, defects densities that are highly localised to the surface do not generate stress inside the solid, and their effect on the NV spin resonances can therefore be neglected.

B.6.3 Stress induced by dilational dislocations

A dislocation that induces pure compression/ dilation is equivalent to a line of point defects with uniform density. So, if we say that the dislocations have a uniform density in the transverse plane of a slab, this is equivalent to a uniform plane of point defects. Since we have concluded that the stress/ strain at a given height in the slab depends only on the local density of defects, and we expect dislocations induced by polishing/ surface damage to be localised to the surface, then we can conclude that dislocations do not influence the NVs sufficiently below the surface. Thus, regardless of their strength, dislocations may also be ignored.

C

Modelling of band bending at the diamond surface

In this section, we first present our model of the oxygen- and hydrogen-terminated diamond surfaces, then describe how band bending and electric field are calculated within this model, and finally discuss some results. This model was developed by Dr. Nikolai Dontschuk.

C.1 Models of the diamond surface

Oxygen-terminated diamond

The surface of materials often have electronic energy levels that are distinctly different from the bulk material bands. In semiconductors, these surface states can exist within the band gap of the material, as depicted in Fig. C.1. Any unoccupied (occupied) surface states (with areal density D_{sd}) below (above) the bulk Fermi level will ionise. However, to maintain charge neutrality within the crystal the total charge of the ionised surface states needs to be compensated by an opposite charge from the bulk. In order for charge to build up in the bulk the bands bend towards the surface, which simultaneously reduces the density of the ionised surface states, until charge neutrality is reached. Typically the Fermi level at the surface is pinned close to the surface state energy unless a density of donors that fully compensate the density of surface states can be introduced into the

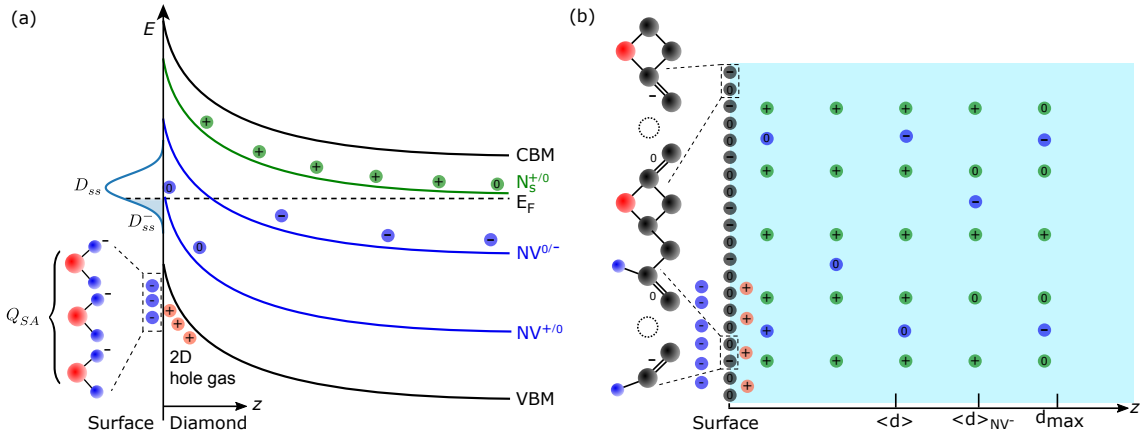

Figure C.1: Band bending of hydrogen terminated diamond. (a) Band diagram of a nitrogen implanted diamond near the surface, showing the conduction band minimum (CBM), valence band maximum (VBM), the $N_S^{+/0}$ charging level, the $NV^{0/-}$ charging level, the $NV^{+/0}$ charging level, and the constant Fermi level E_F. To the left of the vertical axis are: a depiction of the density of states associated with the sp^2 surface defects, which have a total areal density D_{sd}, and an ionised density D_{sd}^-; a depiction of the adsorbed acceptor molecules present close to the VBM for hydrogen-terminated diamond, with an ionised areal density (Q_{sa}), and inducing a 2D hole gas in the diamond. (b) A cartoon depicting the surface and nitrogen induced defects considered in the band modelling (see text).

material. In the case of oxygen-terminated diamond we observed a strong electric field which we ascribe to a upward band bending indicative of a high density of surface states. This is commensurate with published electrical measurements of Fermi level pinning at diamond interfaces [317–319].

Information about the density and energy of any surface states present on oxygen terminated surfaces will then be required to model the expected electric field. The cross section of a (001) diamond surface consists of carbon bonded in a zig-zag pattern between the first and second atomic layer. Each surface carbon atom has two dangling bonds that are satisfied by bonding to an oxygen termination layer. Oxygen can terminate the diamond in a number of ways: an oxygen atom can bond to two surface carbon atoms in an ether like arrangement (depicted in Fig. C.1b), it can double bond to a single surface carbon atom in a ketone like arrangement or a hydroxyl group can terminate a single surface carbon atom. Each of these different arrangements introduce different surface states into the diamond band gap, yet only ether-like terminations are expected to result

in upward band bending in nitrogen doped diamond (where the Fermi level is close to the nitrogen donor level at VBM + 3.75 eV) with an unoccupied state at VBM + 3.4 eV [320]. Such a high unoccupied energy level is unable to explain the large band bending that was measured on all oxygen terminated samples and thus we do not consider the effect of any oxygen induced surface states on the diamond electronic structure. Recently a primal defect, the sp^2 defect, of the diamond surface has been identified to have a much lower acceptor energy around VBM + 1.5 eV [229]. The fundamental structure of this defect is shown in Fig. C.1b, and occurs when a surface carbon atom is removed from the lattice. The dangling bonds that remain then form double bonds with the exposed sub-surface carbon. As the energy of this defect state is well below the nitrogen donor level, and the density is expected to be large, $D_{\mathrm{sd}} > 10^{13}$ cm^{-2}, this defect makes a good candidate to explain the measured electric field under oxygen terminated surfaces. The actual energy of the sp^2 defect surface state is dependent on its local environment, and DFT modelling predict energies within a range from 0.9 eV to 2.2 eV. To capture this range we consider the defect density of states to be Gaussian around 1.5 eV with a full width at half maximum of 0.6 eV, in agreement with the shape of the resonance peak seen in X-ray absorption experiments probing this defect [229].

Bulk defects

The surface charge is compensated by the dielectric response of the diamond, $\epsilon = 5.8$, the ionisation of any defects within the band gap, predominantly nitrogen donors, and any charge carriers (which is practically zero until the Fermi level is within 1 eV of a diamond band). The donors within the diamond are formed by the implantation of nitrogen ions, which has a fixed areal density (fluence) of $D_{\mathrm{areal}} = 10^{13}$ nitrogen cm^{-2} in these experiments. For shallow implants with an implant energy below 30 keV, the depth dependent nitrogen density profile is in general non trivial [175] and is particularly sensitive to the angle of incidence, which here is nominally 7° from the surface normal but is partly randomised by the roughness of the diamond surface. We chose to approximate the nitrogen density profile by a rectangular function bounded by the surface on one end ($d = 0$) and a maximum implant depth parameter, d_{max}, on the other end. Such a simple function is a reasonably good approximation to both theoretically and experimentally determined

profiles in our situation [175,234,321], and avoids the introduction of multiple parameters. The only parameter is $d_{\max}$, which can be related to the implant energy via $d_{\max} = \eta\, E_{\text{imp}}$. To maximise the match between the data and theory, a value of $\eta = 3.5$ was chosen, hence a mean depth $\langle d \rangle = \frac{d_{\max}}{2} = 1.75 E_{\text{imp}}$, also providing an reasonable agreement with previous studies [175, 210, 321]. The volumetric density of nitrogen in the diamond is then calculated as $\frac{D_{\text{areal}}}{d_{\max}}$. The nitrogen implant forms a range of different defects within the diamond: substitutional nitrogen (N_S), nitrogen-vacancy centres (NV) and vacancy defects (which can be single, double or multi-vacancy chains). The majority of the implanted nitrogen ends up as N_S with only $\chi \approx 1\%$ turning into NV for high nitrogen fluences [322], resulting in densities $D_N = (1-\chi)\frac{D_{\text{areal}}}{d_{\max}}$ and $D_{NV} = \chi \frac{D_{\text{areal}}}{d_{\max}}$ for the N_S and NV defects, respectively. The N_S acts as a deep acceptor state, 1.7 eV ($E_{N_S} = 3.75$ eV) away from the conduction band. Whilst the NV defect can become both positively and negatively charged, allowing to act as both a super deep donor ($E_{NV^+} = 0.75 - 1.05$ eV) and mid gap acceptor ($E_{NV^-} = 2.7 - 2.8$ eV) [323]. For simplicity we do not consider other vacancy related defects. Although the expected density of vacancy defects is larger than the density of nitrogen related defects after implantation, multiple annealing steps at 950°C and 1200°C were undertaken to minimise the quantity of vacancy defects and the final density is expected to be low [210, 235, 324].

Hydrogen-terminated diamond

Having presented our model of the oxygen-terminated surface, we now move on to describe the hydrogen-terminated surface. The clean and ordered hydrogen-terminated diamond surface forms a strong dipole field that reduces the diamond's work function, moving the vacuum energy level below the diamond conduction band (observed as a negative electron affinity [325]). An observed result of this low work function is that it is energetically favourable for electrons in the diamond valence band to be excited to adsorbed acceptor molecules in atmospheric conditions. The total negative charge of ionised adsorbed acceptors (Q_{sa}), depicted in Fig. C.1a, needs to be compensated by a positive charge within the diamond, and much like under an oxygen-terminated surface the diamond bands bend upwards towards the surface. As this bending is not pinned to an energy level in the diamond band gap, it often extends all the way into the diamond valence band, forming

a two-dimensional hole gas confined within 5 nm of the surface [237, 326] and resulting in the observed surface conductivity of hydrogen-terminated diamonds [327]. In intrinsic diamond, holes in the valence band are the only positive bulk charge that provides a significant contribution to compensation of the surface charge. In nitrogen doped diamond, however, the ionised nitrogen defects will also partially compensate any surface charge. With a high enough density of nitrogen, the Fermi level at the surface will move far enough from the valence band that no hole layer is formed and the diamond surface ceases to be conductive [328]. In our samples, however, the primal sp^2 defects should still be present because the hydrogenation is unlikely to remove them [229]. As a consequence, the sp^2 defects will once again pin the surface Fermi level position. Like with oxygen termination, the total charge in the acceptor layer is a function of the Fermi level at the diamond surface [329], however to simplify dealing with the effect of both surface acceptors and ionised sp^2 defects, we consider Q_{sa} to be constant. We can relate the measured hydrogen ribbon resistivity (R) to the density of holes at the diamond surface, n_h, using $R = \frac{L}{W\sigma}$, where $L = 100$ μm and $W = 18$ μm are the hydrogen ribbon length and width for our devices. The conductivity of the device is given by $\sigma = e\, n_h\, \mu_h$ where μ_h is the hole mobility in the ribbon. Hole mobilites between $\mu_h = 10 - 100$ cm^{2}V^{-1}s^{-1} are commonly reported [233, 330]. Device resistances of our ribbon ranged from initial values of $R \approx 100$ kΩ to $R > 10$ MΩ after extensive measurement, not taking into account any contact resistance. This provides an estimate for the 2D hole density in the range of $n_h = 3.5 \times 10^{10} - 3.5 \times 10^{12}$ cm^{-2}. Accounting for the 10 keV implant in sample #2 ($d_{\mathrm{max}} = 35$ nm), numerical integration returns that Q_{sa} is within the range 1.08 to 0.98×10^{13} cm^{-2}.

In all cases the upward bending bands will affect the response of the implanted NV defects, de-ionizing the near surface NV where the band bending is strong [331], and creating a space charge layer of ionised N_S (the green circles in Fig. C.1). The space charge layer creates a significant electric field around the NV$^-$ defects, it is this field that can be observed as ODMR shifts [1, 47, 230]. To estimate the amount of NV$^-$ and the size of the electric field that NV$^-$ experiences, the shape of this bending needs to be calculated.

C.2 Calculating band bending

Poisson's equation provides a classical definition of how a charge distribution $\rho(\mathbf{r})$ changes the electric potential $V(\mathbf{r})$ within a dielectric material:

$$\nabla^2 V(\mathbf{r}) = \frac{-\rho(\mathbf{r})}{\epsilon\epsilon_0} \tag{C.1}$$

where ϵ_0 is the vacuum permittivity and ϵ is the relative permittivity of the material. Solving this equation determines how the bands bend given a certain surface potential V_s (or equivalently, a normalised potential ν_s, related to V_s via Eq. C.15), i.e. the boundary condition at the diamond surface. The shape of the bending is only determined by the charges within the diamond, i.e. if you solve for $\nu_s = 5$ and redefine the surface at $\nu = 3$ discarding the higher potentials the solution is the same as solving for $\nu_s = 3$. We take advantage of this and over-solve all our bands with a large ν_s then redefine the surface at the appropriate potential to compensate a given areal density of charge at the diamond surface.

To determine the charge distribution in the diamond we need to consider the densities of electrons, holes and any ionised defect states (negatively charged acceptors and positively charged donors). The density of electrons, holes and ionised defects is determined by the filling of electronic states in the diamond valence and conduction bands and the defect states, respectively. The filling of electronic states is calculated by convolving the energy dependent density of states (DOS) with the probability of a state being occupied by an electron at a given energy. The probability of a state being occupied (unoccupied) is given by the Fermi-Dirac distribution function,

$$f_D(E) = \frac{1}{1 + \exp\left(\frac{E - \mathrm{E_F}}{kT}\right)} \tag{C.2}$$

and its complement,

$$1 - f_D(E) = \frac{1}{1 + \exp\left(\frac{\mathrm{E_F} - E}{kT}\right)} \tag{C.3}$$

where k is the Boltzmann constant, T is the temperature, and the functions are centred

around the Fermi level ($\mathrm{E_F}$) of a material. The Fermi level can be determined by requiring that the material be charge neutral at the Fermi level, giving

$$p + \sum_{\text{Donors}} N_{\mathrm{D}}^{+} = n + \sum_{\text{Acceptors}} N_{\mathrm{A}}^{-} \tag{C.4}$$

where p (n) is the density of holes (electrons), N_{D}^{+} is the density of ionised donors, and N_{A}^{-} is the density of ionised acceptors in the bulk of diamond in thermal equilibrium. We can calculate the electron and hole densities using the effective mass (m^*) approximation for the valence and conduction bands DOS [332]:

$$\begin{aligned} N_{\mathrm{V}}(E) &= \frac{(2m_{\mathrm{V}}^{*})}{2\pi^2 h^3}^{3/2} \sqrt{\mathrm{E_V} - E}, \\ N_{\mathrm{C}}(E) &= \frac{(2m_{\mathrm{C}}^{*})}{2\pi^2 h^3}^{3/2} \sqrt{E - \mathrm{E_C}}, \end{aligned} \tag{C.5}$$

where h is Plank's constant and m_{V}^{*} (m_{C}^{*}) is the effective mass of valance (conduction) band. Typically, the Boltzmann approximation of $f_D(E) \approx e^{(\mathrm{E_F}-E)/kT}$ for $\mathrm{E_F} - E \gg kT$, is used to estimate the electron and hole densities:

$$\begin{aligned} p(z) &= 2\left(\frac{2\pi m_{\mathrm{V}}^{*} kT)}{h^2}\right)^{3/2} e^{\frac{\mathrm{E_V}-\mathrm{E_F}}{kT}} = N_{\mathrm{C}} e^{\frac{\mathrm{E_V}-\mathrm{E_F}}{kT}}, \\ n(z) &= 2\left(\frac{2\pi m_{\mathrm{C}}^{*} kT)}{h^2}\right)^{3/2} e^{\frac{\mathrm{E_F}-\mathrm{E_C}}{kT}} = N_{\mathrm{V}} e^{\frac{\mathrm{E_F}-\mathrm{E_C}}{kT}}, \end{aligned} \tag{C.6}$$

where N_{V} is the effective density of states for holes and N_{C} for electrons. In surface transfer doped hydrogen-terminated diamond, the conduction band at the surface crosses through the Fermi level (hence becomes a degenerate semiconductor) with a relatively small carrier density of 2.5×10^{12} holes cm^{-2}, and the Boltzmann approximation is no longer appropriate. Instead, we have to solve the full convolution:

$$p(z) = N_{\mathrm{V}} \frac{2}{\sqrt{\pi}} \int_0^{\infty} \frac{\sqrt{\epsilon}}{1 + e^{\epsilon - \frac{\mathrm{E_V}-\mathrm{E_F}}{kT}}}\, d\epsilon = N_{\mathrm{V}} \mathcal{F}_{1/2}\left(\frac{\mathrm{E_V} - \mathrm{E_F}}{kT}\right), \tag{C.7}$$

where $\mathcal{F}$ is the set of Fermi Dirac integrals, defined as

$$\mathcal{F}_j(\eta) = \int_0^{\infty} \frac{x^j}{\exp(x - \eta) + 1}\, dx, \qquad \text{for } j > -1. \tag{C.8}$$

These integrals can be accurately and rapidly approximated numerically [333,334]; in this work the open source python package fdint 2.02 [335] was used.

To calculate the density of ionised defects, we approximate the defect DOS as a Dirac delta function $\delta(E - E_0)$ around the defect ionisation energy, $E_0 = \mathrm{E_A}$ for acceptor and $E_0 = \mathrm{E_D}$ for donor transitions, with defect densities of N_A and N_D:

$$\begin{aligned} N_\mathrm{D}^+(z) &= \int_{-\infty}^{\mathrm{E_D}(z)} N_\mathrm{D}(z)\delta(\mathrm{E_D}(z) - E)\,[1 - f_D(E)]\,dE \quad &= N_\mathrm{D}(z)\,[1 - f_D(\mathrm{E_D}(z))]\,, \\ N_\mathrm{A}^-(z) &= \int_{\mathrm{E_A}(z)}^{\infty} N_\mathrm{A}(z)\delta(E - \mathrm{E_A}(z))\,f_D(E)\,dE \quad &= N_\mathrm{A}(z)\,f_D(\mathrm{E_A}(z)). \end{aligned} \tag{C.9}$$

Lateral variations in the surface states and defect densities are ignored and only the charge distribution in z needs to be considered (here z is defined positive going into the diamond). The total charge density within the diamond can then be described by:

$$\rho(\mathbf{r}) = \rho(z) = ep(z) - en(z) + e\sum_{\text{Donors}} N_\mathrm{D}^+(z) - e\sum_{\text{Acceptors}} N_\mathrm{A}^-(z). \tag{C.10}$$

As external potentials affect all the bands equally we re-define the z dependent defect and band energies as a function of a single depth dependent potential. First we define a potential, $\phi(z)$, as the separation between the Fermi level $\mathrm{E_F}$ and the intrinsic energy level E_i (i.e. where the Fermi level would be in an intrinsic diamond),

$$e\phi(z) = \mathrm{E_F} - E_i(z) \tag{C.11}$$

where

$$E_i(z) = \frac{1}{2}\mathrm{E_V}(z) + \frac{1}{2}\mathrm{E_C}(z) - \frac{1}{2}kT\log\frac{N_\mathrm{C}}{N_\mathrm{V}}. \tag{C.12}$$

From Eq. C.11 the potential $V(z)$ can be defined as how far the bands have shifted from their unbent position,

$$V(z) = \phi(z) - \phi_\mathrm{B} \tag{C.13}$$

where

$$\phi_\mathrm{B} \equiv \lim_{z\to\infty}\phi(z). \tag{C.14}$$

In order to solve for the band structure it is also useful to define unitless potentials, such that

$$\begin{aligned} u(z) &= \frac{e\phi(z)}{kT} \\ \nu(z) &= \frac{eV(z)}{kT}. \end{aligned} \tag{C.15}$$

Within the Boltzmann approximation the carrier density can be rewritten in terms of the unitless potential $\nu(z)$:

$$\begin{aligned} p(z) &\approx N_{\mathrm{V}} \exp\left(\frac{-(\mathrm{E_F} - \mathrm{E_V}(z))}{kT}\right) \\ &= N_{\mathrm{V}} \exp\left(\frac{-E_i(z) - e\phi(z) + \mathrm{E_V}(z)}{kT}\right) \\ &= N_{\mathrm{V}} \exp\left(\frac{-\frac{1}{2}\mathrm{E_V}(z) - \frac{1}{2}\mathrm{E_C}(z) + \frac{1}{2}kT\log\frac{N_{\mathrm{C}}}{N_{\mathrm{V}}} - e\phi(z) + \mathrm{E_V}(z)}{kT}\right) \\ &= N_{\mathrm{V}}\sqrt{\frac{N_{\mathrm{C}}}{N_{\mathrm{V}}}} \exp\left(\frac{-e\phi(z)}{kT}\right) \exp\left(\frac{\mathrm{E_V} - \mathrm{E_C}}{2kT}\right) \\ &= \sqrt{(N_{\mathrm{C}}N_{\mathrm{V}})} \exp\left(\frac{\mathrm{E_V} - \mathrm{E_C}}{2kT}\right) \exp\left(-u(z)\right) \\ &= n_i \exp\left(-u(z)\right) \\ &= n_i \exp\left(-u(\infty)\right) \exp\left(-\nu(z)\right) \end{aligned} \tag{C.16}$$

which results in

$$\begin{aligned} p(z) &= p_{\mathrm{B}} e^{-\nu(z)} \\ n(z) &= n_{\mathrm{B}} e^{\nu(z)} \end{aligned} \tag{C.17}$$

where p_{B} and n_{B} are the hole and electron densities at the Fermi level. These carrier densities can also be express in terms of Fermi-Dirac integrals:

$$\begin{aligned} p(z) &= N_{\mathrm{V}} \mathcal{F}_{1/2}\left(\frac{\mathrm{E_V} - \mathrm{E_F}}{kT} - \nu(z)\right), \\ n(z) &= N_{\mathrm{C}} \mathcal{F}_{1/2}\left(\nu(z) + \frac{\mathrm{E_F} - \mathrm{E_C}}{kT}\right), \end{aligned} \tag{C.18}$$

which facilitates the use of the aforementioned numerical approximations.

A donor energy level ($\mathrm{E_D}$) represents the energy required to remove an electron from a crystal defect. The following treatment for including bulk defects is general for all

donors. The ionised donor density can be defined in terms of the donor energy, such that

$$N_{\mathrm{D}}^{+}(z) = N_{\mathrm{D}}(1 - f_D(\mathrm{E_D}(z))) = N_{\mathrm{D}}\frac{1}{1+\exp\left(\frac{\mathrm{E_F}-\mathrm{E_D}(z)}{kT}\right)}. \tag{C.19}$$

Using the unitless potential, this can be rewritten as

$$N_{\mathrm{D}}^{+}(z) = N_{\mathrm{D}}\frac{1}{1+\exp\left(\nu(z)\right)\exp\left(\frac{\mathrm{E_F}-\mathrm{E_D^B}}{kT}\right)} \tag{C.20}$$

where $\mathrm{E_D^B}$ is the energy of the donor in the limit $z \to \infty$. This is similar for an acceptor level,

$$N_{\mathrm{A}}^{-}(z) = N_{\mathrm{A}}\frac{1}{1+\exp\left(-\nu(z)\right)\exp\left(\frac{\mathrm{E_A^B}-\mathrm{E_F}}{kT}\right)}. \tag{C.21}$$

Using the chain rule, we can analytically reduce the second order Poisson's equation to first order by integration of the charge density with respect to ν:

$$\frac{d^2V(z)}{dz^2} = \frac{kT}{e}\frac{d^2\nu(z)}{dz^2} = \frac{-\rho(z)}{\epsilon\epsilon_0} \tag{C.22}$$

$$\Rightarrow \left(\frac{d\nu}{dz}\right)^2 = \frac{e}{\epsilon\epsilon_0 kT}\int -\rho(z)\,d\nu. \tag{C.23}$$

As $\nu(z)$ is unknown, this integral is only solvable if $\rho(z)$ is only a function of ν, and not explicitly a function of z. In that case we get:

$$\int -\rho(z)\,d\nu = \int_0^{\nu(z)} -ep(z) + en(z) - e\sum_{\text{Donors}} N_{\mathrm{D}}^{+}(z) + e\sum_{\text{Acceptors}} N_{\mathrm{A}}^{-}(z)\,d\nu \tag{C.24}$$

By integrating from 0 we ensure that $\frac{d\nu}{dz} = 0$ when $\nu(z) = 0$, i.e. the bands bend until they reach the Fermi level, which occurs when the crystal is charge neutral.

To calculate the Fermi level in the implanted layer, we use the Boltzmann approximation for electron and hole densities and consider the $\mathrm{N_S}$ and NV defects. Eq. C.4

becomes:

$$\begin{aligned} p + \sum_{\text{Donors}} N_{\text{D}}^{+} &= N_{\text{C}} \exp\left(\frac{\text{E}_{\text{V}} - \text{E}_{\text{F}}}{kT}\right) + \frac{D_{\text{N}}}{1 + \exp\left(\frac{\text{E}_{\text{F}} - \text{E}_{\text{N}_{\text{S}}}}{kT}\right)} + \frac{D_{\text{NV}}}{1 + \exp\left(\frac{\text{E}_{\text{F}} - \text{E}_{\text{NV}+}}{kT}\right)} \\ = n + \sum_{\text{Acceptors}} N_{\text{A}}^{-} &= N_{\text{V}} \exp\left(\frac{\text{E}_{\text{F}} - \text{E}_{\text{C}}}{kT}\right) + \frac{D_{\text{NV}}}{1 + \exp\left(\frac{\text{E}_{\text{NV}-} - \text{E}_{\text{F}}}{kT}\right)}. \end{aligned} \tag{C.25}$$

By treating E_{F} as a variable, the roots of Eq. C.25 can be determined numerically.

We then solve for $\nu(z)$ by numerical inversion and integration of $\frac{d\nu}{dz}$, giving

$$z(v) = z_0 + \int_{\nu(z_0)}^{\nu} \frac{dz}{d\nu} d\nu \tag{C.26}$$

where z_0 is the crystal surface and $\nu(z_0) \equiv \nu_s$ is the potential at the surface, which needs to be determined for the different diamond surfaces.

The surface potential is determined by the requirement for total charge at the surface (Q_{sd}) to be equal to the total charge in the bulk Q_{BC}, that is

$$Q_{\text{sd}} = -Q_{\text{BC}}, \tag{C.27}$$

where Q_{sd} can be determined by numerical inversion of $z(\nu)$ and insertion into Eq. C.10. The total surface charge Q_{sd} is determined by the nature of the surface charge. When we consider just the effects of the sp^2 defect (oxygen-terminated diamond), we calculate the density of ionised surface states (D_{sd}^{-}) as a function of the potential:

$$D_{\text{sd}}^{-}(\nu_s) = \int_{-\infty}^{\infty} \frac{\exp\left(-\left(\frac{E - E_s(z)}{2\sigma}\right)^2\right)}{1 + \exp\left(\frac{E - \text{E}_{\text{F}}}{kT}\right)} dE. \tag{C.28}$$

To determine Q_{sd} for an arbitrary ν, this is evaluated such that

$$Q_{\text{sd}} = D_{\text{sd}}^{-}(\nu) = \int_{-\infty}^{\infty} D_{\text{sd}}(E) f_D(E) dE \tag{C.29}$$

$$= \int_{-\infty}^{\infty} \frac{\exp\left(-\left(\frac{\epsilon}{2\sigma}\right)^2\right)}{1 + \exp\left(-\nu\right) \exp\left(\frac{\epsilon - \text{E}_{\text{F}} + E_s}{kT}\right)} d\epsilon \tag{C.30}$$

which requires numerically integration to solve. To determine the bulk charge, we integrate our charge density over z to the maximum implantation depth:

$$Q_{\mathrm{sd}} = en_h + e\sum_{\mathrm{Donors}}\int_0^{d_{\mathrm{max}}} N_{\mathrm{D}}^{+}(z)\,dz - e\sum_{\mathrm{Acceptors}}\int_0^{d_{\mathrm{max}}} N_{\mathrm{A}}^{-}(z)\,dz. \tag{C.31}$$

Integrating to d_{max} ensures that any artificial charge density beyond the max implantation depth (a result of assuming a uniform nitrogen density) has no effect on selecting the correct surface termination. The root of $[Q_{\mathrm{sd}}(\nu) + Q_{\mathrm{BC}}(\nu)]_{\nu_S} = 0$ determines ν_s, i.e. the surface potential which results in the diamond being charge neutral. The same approach is taken for hydrogen-terminated diamond except that:

$$Q_{\mathrm{sd}} = D_{\mathrm{sd}}^{-}(\nu) + Q_{\mathrm{sa}} \tag{C.32}$$

to account for the charge of the ionised adsorbed acceptor layer. Finally the two-dimensional density of the hole layer under a given hydrogen termination can be calculated with

$$n_h = \int_0^{d_{max}} p(z)dz. \tag{C.33}$$

C.3 Results

The first step to calculating the band bending is to determine the Fermi level within the diamond using Eq. C.25. As the nitrogen donor and NV acceptor levels are far from the diamond band edges, the electron and hole densities are practically zero. This means that the Fermi level is only determined by the conversion ratio of $\mathrm{N_S}$ to NV, χ. Fig. C.2a plots the left (blue) and right (orange) hand side of Eq. C.25 as a function of $\mathrm{E_F}$ for $\chi = 1\%$ and 20% with $D_{\mathrm{N}} = 10^{18}$ cm^{-3} (larger values of D_{N} do not change the point of intersection). The solutions, where the blue and orange intersect, are plotted in Fig. C.2b showing the expected bulk Fermi level for a range of NV conversion ratios. For all modelling in this work, one has $\mathrm{E_F} \approx 3.85$ eV.

Fig. C.3a shows an example of the calculated band bending for two shallow N implants, $D_{\mathrm{areal}} = 10^{13}$ N cm^{-2} with $d_{\mathrm{max}} = 14$ nm (~ 4 keV implant) and 70 nm (~ 20 keV), at both oxygen and hydrogen surfaces. For oxygen-terminated surfaces, the integrated

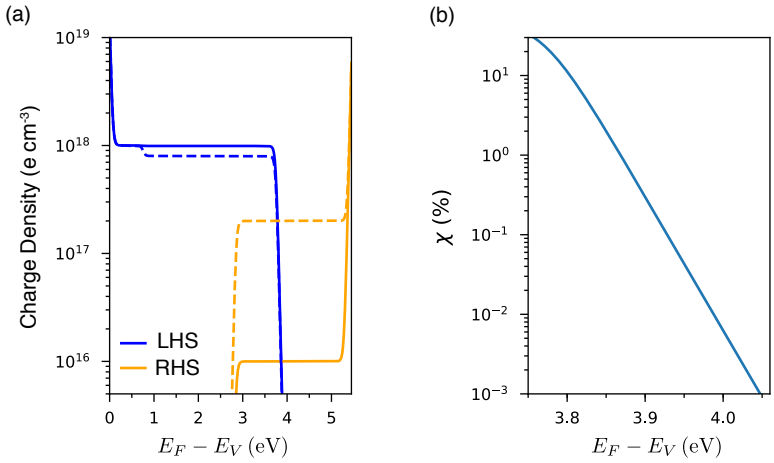

Figure C.2: The Fermi level in nitrogen implanted diamond. (a) Visualisation of the neutrality condition (Eq. C.25) showing the left-hand side in blue (LHS, positive charge) and the right-hand side in orange (RHS, negative charge) as a function of the Fermi level. The N_S to NV conversion efficiency is set to $\chi = 1\%$ (solid lines) and $\chi = 20\%$ (dashed lines). (b) Calculated Fermi level as a function of χ.

DOS, or total number of defect states, is $D_{sd} = 5 \times 10^{13}$ cm^{-2} or $\approx 2\%$ of the surface [229]. A total density of ionised surface acceptors $Q_{sa} = 0.98 \times 10^{13}$ cm^{-2} is used to determine the bending under the hydrogen surface. For each case, a Gaussian DOS is plotted at the surface to depict the surface states, and shading indicates the states that are filled. In the case of the hydrogen surface with $d_{max} = 70$ nm, the valence band bends up to the Fermi level generating the conductive 2DHG as expected. However, for the hydrogen surface with $d_{max} = 14$ nm where the density of donors is much closer to the surface, the density of surface adsorbed acceptors (Q_{sa}) is not large enough to fully compensate the bulk charge and the valence band at the surface no longer bends enough to reach the Fermi level. The edge of the surface acceptor level then pins the Fermi level, as with oxygen-terminated diamond. In this case the hydrogen termination is not expected to be conductive, as it is not energetically favourable for a hole layer to form. It is this transition that is partially responsible for the non-monotonic behaviour of the models, calculated using the best fit value $Q_{sa} = 7 \times 10^{12}$ cm^{-2}. The model then suggests that the some of the samples used ($d_{max} = 35$ nm) were close to the conducting/insulating transition. This explains the observed rapid laser induced degradation of the devices, as only small changes to the total acceptor density are required for complete loss of the 2D

hole layer near the transition. Namely, once the surface acceptor density drops below the density of positive charge from the implanted nitrogen density ($Q_{\mathrm{sa}} < 0.98 \times 10^{13}$ cm^{-2} for $D_{\mathrm{areal}} = 10^{13}$ cm^{-2}), the 2D hole density decreases rapidly, e.g. $Q_{\mathrm{sa}} = 0.97 \times 10^{13}$ cm^{-2} corresponds to a 2D hole density of $n_h \approx 100$ cm^{-2}.

Fig. C.3b depicts the electric field associated with this bending, and the filled regions show the density of NV^- as determined by d_{max} and the ionization state in thermal equilibrium (i.e. where the NV^- band crosses the Fermi level (E_F) in figure C.3a). As the neutral NV^0 defect does not contribute to the ODMR signal, the measured electric field, denoted as $\langle \varepsilon_z \rangle$, is the average of the field weighted by the density of NV^-.

We now discuss some of the other predictions afforded by our model. In particular, the de-ionisation of the near surface NV^- due to band bending provides an explanation for the difficulties encountered in creating NV^- very close to the surface (e.g. $\langle d_{\mathrm{NV^-}} \rangle <$ 5 nm). Figure C.4a shows the expected average depth of NV^-, $\langle d_{\mathrm{NV^-}} \rangle$ for a $D_{\mathrm{areal}} = 10^{13}$ cm^{-2} nitrogen implant compared to the expected average implant depth, $\langle d_{\mathrm{N}} \rangle$, which is determined by the implant energy via $\langle d_{\mathrm{N}} \rangle = \eta E_{\mathrm{imp}}/2$. When the surface defect density is equal to or larger than the nitrogen implant density, $D_{\mathrm{sd}} \geqslant D_{\mathrm{areal}}$, $\langle d_{\mathrm{NV^-}} \rangle \approx 5$ nm even for $E_{\mathrm{imp}} = 1$ keV implants expected to produced NVs mainly in the top 2 nm. One approach to overcome this issue to produce the nearest surface NV^- possible is to increase the implant density. Fig C.4c shows the total NV ionisation ratio as a function of D_{areal} with a relatively low surface defect density of $D_{\mathrm{sd}} = 10^{13}$ cm^{-2}. Even for the $E_{\mathrm{imp}} = 3$ keV implant, $D_{\mathrm{areal}} > D_{\mathrm{sd}}$ is required to achieve complete NV^- ionisation and produce near-surface NV^-. This problem is compounded by the expected high density of surface defects [229], highlighting the importance of controlling the formation of this defect for near-surface sensing.

Figure C.4c shows the relative population of substitutional nitrogen in its neutral state (N_S^0), known as the P1 centre in electron spin resonance measurements, as a function of implantation energy for a D_{areal} in a diamond with a surface defect density $D_{\mathrm{sd}} = 10^{13}$ cm^{-2}. The concentration of P1 is a function of both the implant energy and the density of surface states. No P1 centres are expected to exist in low energy implants, the energy of which is D_{sd} dependent potentially providing an independent way to verify the density of surface defects in a sample.

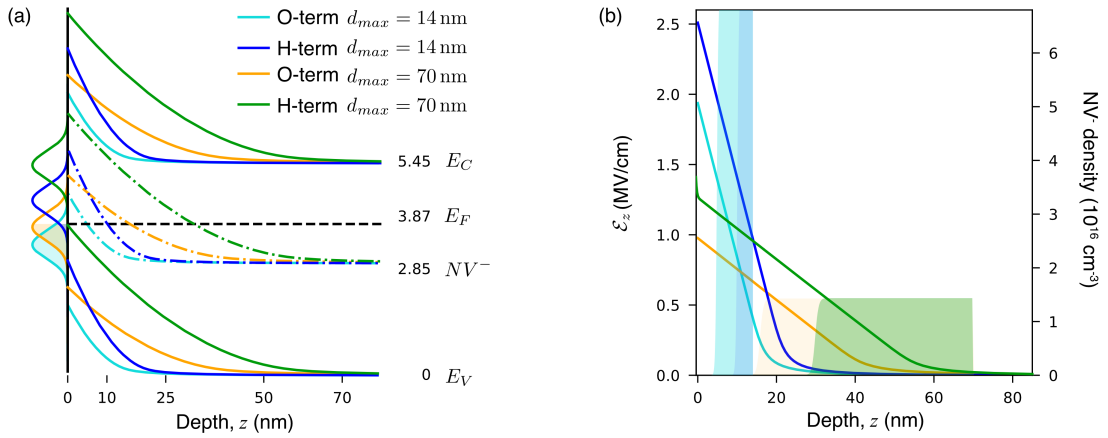

Figure C.3: Electronic bands near the surface of a nitrogen implanted diamond. (a) Band position as a function of depth from the surface for both hydrogen and oxygen terminated diamond with different nitrogen implants. (b) Calculated electric field (ε_z) as a function of depth (lines, left axis) and calculated density of NV^- at thermal equilibrium (shaded area, right axis).

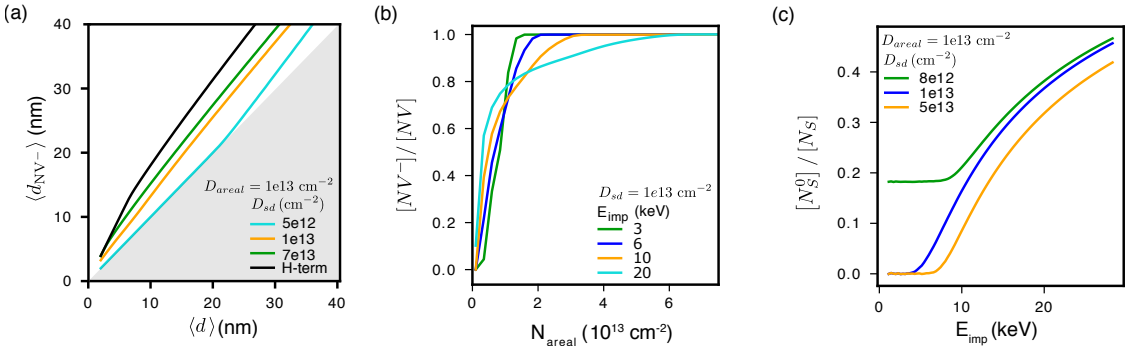

Figure C.4: Model sensitivity to density of states. (a) The average NV^- depth versus the average nitrogen depth from implantation for a range of different D_{sd} densities, and for a hydrogen-terminated diamond (black line), with a fixed implant density of $D_{\mathrm{areal}} = 10^{13}$ cm^{-2}. (b) The ratio of NV^- to total NV as a function of implantation density for common implantation energies. (c) The ratio of unionised N_S, also known as P1 centres, as a function of implantation energy for an implant density of $D_{\mathrm{areal}} = 10^{13}$ cm^{-2}.

D

Experimental methods and additional data for stress measurements

D.1 Diamond samples

The relevant parameters for the six diamonds used in this work, labelled #1 to #6, are listed in Table D.1, indicating the type of surface (polished or as-grown) as well as the parameters of the nitrogen implant used to create the NV defects.

Diamond	Surface	Energy (keV)	Fluence (ions/cm^2)
#1	A	6	10^{13}
#2	A	4	10^{13}
#3	A	4	10^{13}
#4	P	4	10^{13}
#5	P	30	3×10^{12}
#6	A	4	10^{13}

Table D.1: List of diamonds used in this work, indicating the type of surface (polished 'P', or as-grown 'A'), the implantation energy and fluence of the nitrogen implant used to create the NV defects. Samples #2 and #6 were also patterned and implanted with 5 keV C to a fluence of 10^{15} and 10^{16} carbon cm^{-2}, respectively.

D.2 Stress from different carbon implant shapes

Various structures were fabricated with the C_3 implant in diamond #2, imaged in Figure D.1 showing the PL image, a stress map (σ_{xy}, which has the largest signal-to-noise ratio) and a line cut for different shapes. The square ring (Figure D.1a,b) has a very similar stress pattern to the circular ring and has a maximum shear stress magnitude of $|\sigma_{xy}| \approx 15$ MPa localised at the edges of the damaged region. Figure D.1c,d show the case of closed squares of different sizes, indicating that the maxima coincide with the edges of the carbon implant with a small increase of the magnitude of shear stress with increasing size. The smallest squares (1×1 μm) are still resolvable on the right of the image. Lines of different widths are imaged in Figure D.1e,f, showing more clearly the size dependence. A 1 μm-wide line following a zigzag pattern is imaged in Figure D.1g,h, clearly showing that lines separated by less than 1 μm can be resolved, allowing us to conclude that the spatial resolution of the technique is at least better than 1 μm.

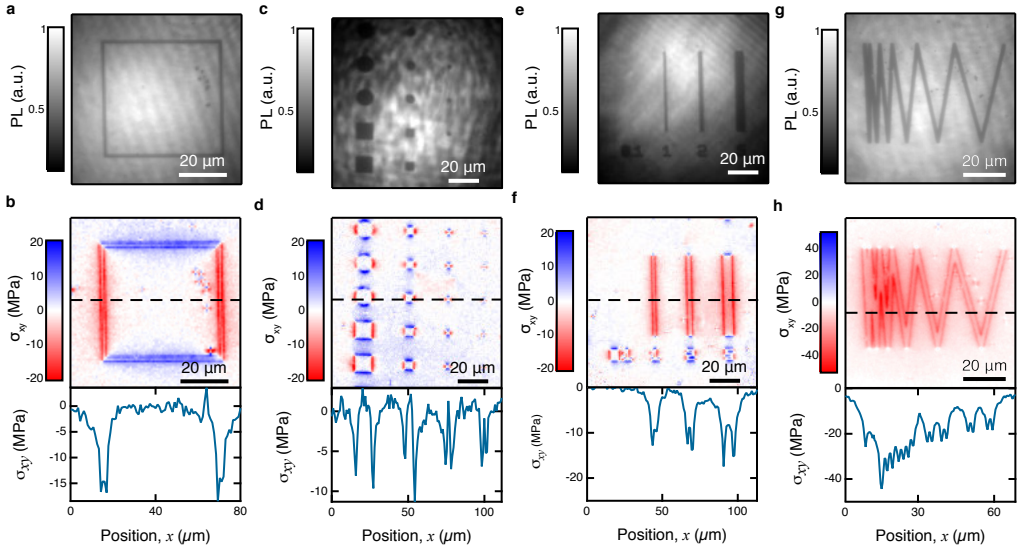

Figure D.1: Stress induced from different shapes of carbon implant in diamond #2. (a) NV PL of a square ring, with a wall width of 1 μm. (b) Measured stress component, σ_{xy}, from the square ring shown in (a) with a line cut along the dashed line. (c) NV PL of a series of solid squares and circles varying in width/radius from 10 μm (left) to 1 μm (right). (d) σ_{xy} stress from (c) with a line cut along the dashed line. (e) NV PL of a series of solid lines varying in width from 0.1 μm (left) to 5 μm (right). (f) σ_{xy} stress from (e) with a line cut along the dashed line. (g) NV PL of a solid lines with a width of 1 μm in a zigzag pattern. (h) σ_{xy} stress from (g) with a line cut along the dashed line.

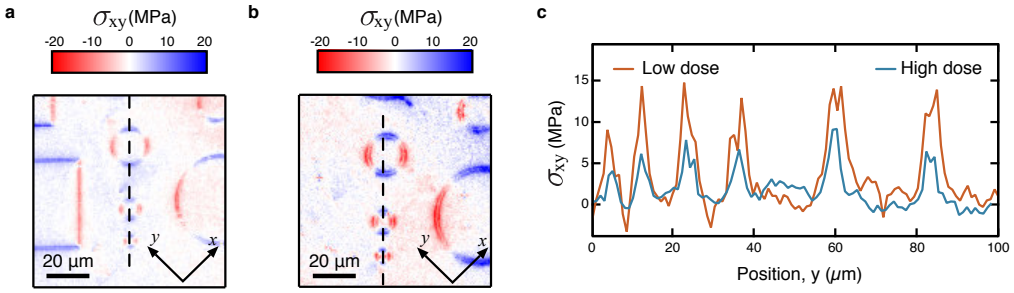

Figure D.2: Effect of carbon implant fluence. (a,b) σ_{xy} map of diamond #6 (a) and diamond #2 (b), which were implanted with C_3 to a fluence of 3.4×10^{15} and 3.4×10^{14} molecules cm^{-2}, respectively. (c) Line cuts along the dashed lines in (a,b).

D.3 Effect of carbon implant fluence and post-annealing

We fabricated similar structures in a separate diamond (diamond #6) nominally identical to the previous one (in particular same parameters for the nitrogen implant used to create the NVs), but increasing the fluence of the C_3 implant to 3.4×10^{15} molecules/cm^2. Despite this fluence being ten times as large as previously, we found the measured stress to be actually smaller than in the low fluence sample, by roughly a factor of 2, as shown in Figure D.2. This can be explained by a difference in stress relief via the free surface, which was confirmed by AFM (Figure D.3a) where the bulge of the diamond surface in diamond #6 was 10 nm high (Figure D.3b) against 2 nm in diamond #2.

The stress introduced by the C implant was gauged by recording changes in the lineshape of the first order Raman peak at 1332 cm^{-1} [267, 280, 316]. The volume of the lattice probed by Raman is defined by the 100x objective (NA = 0.95) point spread function rather than, as in the case of NV sensing, the position of the quantum probes and their own range of view. This volume thus encompasses the region of the implant as well as the underlying substrate where a range of strains may exist that act to broaden the Raman signal and further limiting its sensitivity. Since Raman is not sensitive to the full strain tensor, if we assume a hydrostatic stress, $\sigma_{\text{hydro}} = \sigma_{xx} = \sigma_{yy} = \sigma_{zz}$, we have $\sigma_{\text{hydro}} = \Delta\omega/\alpha_h$, where $\Delta\omega$ is the change in the Raman shift position and $\alpha_h = 3$ cm^{-1} GPa^{-1} is the average hydrostatic stress gauge factor. The Raman measurement was performed with a Renishaw InVia Raman system equipped with a 2400 l/mm grating and a 532 nm wavelength laser which was scanned across the surface of the diamond to

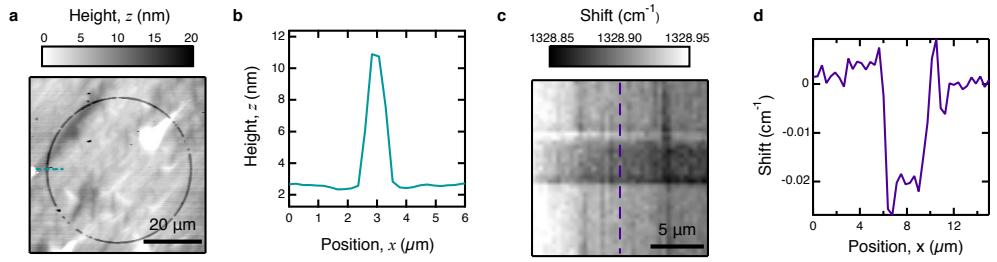

Figure D.3: AFM imaging and Raman spectroscopy in diamond #6. (a) Atomic force microscopy (AFM) image of a ring implant in diamond #6. The discontinuities in the ring are due to imperfections in the implantation mask. (b) Line cut of the AFM image along the dashed line in (a). (c) Map of the diamond Raman line in a 5-μm-wide implanted strip (horizontal). (d) Line cut of the relative shift in the diamond Raman line along the dashed line in (c).

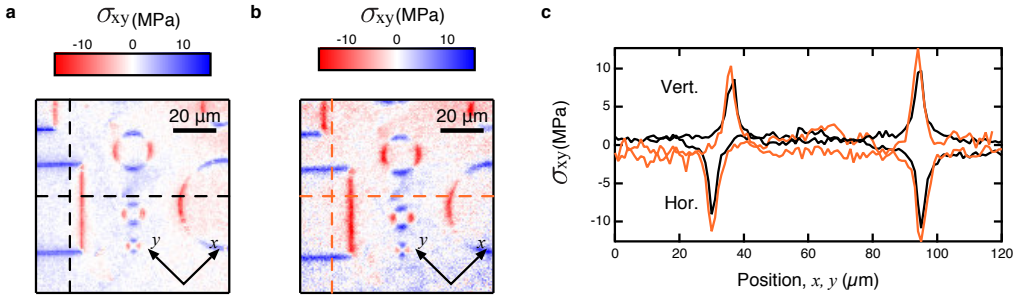

Figure D.4: Effect of annealing in diamond #6. (a) σ_{xy} map of an implanted region in diamond #6, before annealing. (b) σ_{xy} map of the same region after annealing at 800°C for 1 hour. (c) Line cuts along the colour coded dashed lines in (a) and (b).

generate an image. A spatial map of the diamond line shift across a 5-μm-wide implanted strip in diamond #6 is shown in Figure D.3c. A line cut across the strip indicates a shift of 0.02±0.02 cm^{-1} (Figure D.3d), which is near the sensitivity limit of the Raman measurement (0.025 cm^{-1}). This leads to a stress of $\sigma_{\text{hydro}} = 20 \pm 20$ MPa.

We also looked at the effect of annealing the sample, which is expected to convert the amorphous carbon region generated through the implant into graphite. As the graphite has a longer bond length than both the diamond and the amorphous carbon, this procedure will enhance the stress that is embedded. The stress maps (σ_{xy}) of the same region before and after annealing the sample at 800°C for 1 hour are shown in Figure D.4a and D.4b, respectively. The comparison (Figure D.4c) indicates that there is a small increase in the stress upon annealing of the order of 20%, similar to previous results [280].

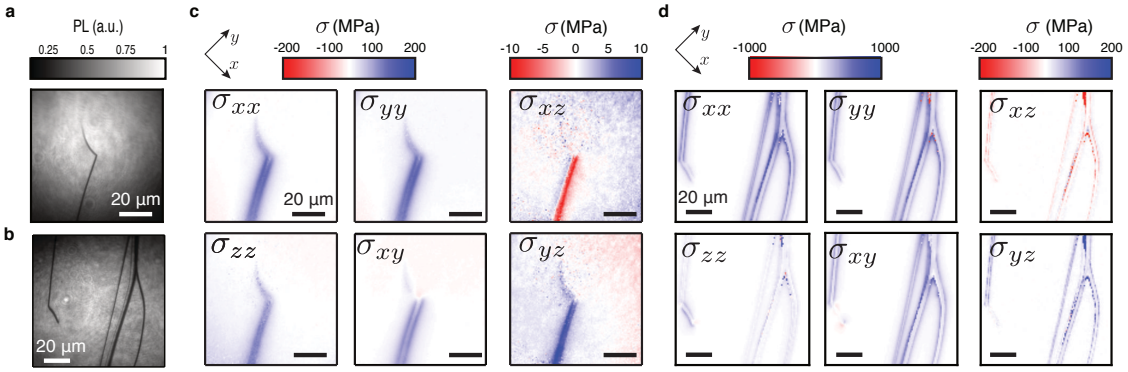

Figure D.5: Stress maps of scratches in diamond #1. (a,b) PL images of a region comprising a shallow scratch (a, 5 nm deep) and deep scratches (b, 20 nm deep). (c) Maps of the six stress components corresponding to (a). (d) Maps of the six stress components corresponding to (b).

D.4 Additional data: Scratches

In Fig. 6.5, we showed the body force of a shallow scratch (5 nm deep recess at most) derived from the stress tensor. The full stress maps are shown in Fig. D.5c, with the PL image recalled in Figure D.5a. Furthermore, we showed ODMR spectra of selected pixels near deeper scratches (up to 20 nm deep recesses). The PL image of the corresponding region is shown in Fig. D.5b, with the stress maps shown in Fig. D.5d. Here, the stress can be in excess of 1 GPa, which causes some artefacts in the images (and apparent noise in these regions) because the ODMR lines may overlap [210].

List of Figures

List of Tables

Bibliography

[1] M. W. Doherty, N. B. Manson, P. Delaney, F. Jelezko, J. Wrachtrup, and L. C. L. Hollenberg, "The nitrogen-vacancy colour centre in diamond," *Phys. Rep.*, vol. 528, pp. 1–45, jun 2013.

[2] T. H. Taminiau, J. Cramer, T. van der Sar, V. V. Dobrovitski, R. Hanson, and T. V. D. Sar, "Universal control and error correction in multi-qubit spin registers in diamond," *Nat. Nanotechnol.*, vol. 9, no. 3, pp. 171–176, 2014.

[3] J. Cramer, N. Kalb, M. A. Rol, B. Hensen, M. S. Blok, M. Markham, D. J. Twitchen, R. Hanson, and T. H. Taminiau, "Repeated quantum error correction on a continuously encoded qubit by real-time feedback," *Nat. Commun.*, vol. 7, 2016.

[4] S. B. van Dam, P. C. Humphreys, F. Rozpedek, S. Wehner, and R. Hanson, "Multiplexed entanglement generation over quantum networks using multi-qubit nodes," *Quantum Sci. Technol.*, vol. 2, no. 3, p. 34002, 2017.

[5] N. Kalb, A. A. Reiserer, P. C. Humphreys, J. J. W. Bakermans, S. J. Kamerling, N. H. Nickerson, S. C. Benjamin, D. J. Twitchen, M. Markham, and R. Hanson, "Entanglement distillation between solid-state quantum network nodes," *Science (80-.).*, vol. 356, no. 6341, pp. 928–932, 2017.

[6] R. Hanson, V. V. Dobrovitski, A. E. Feiguin, O. Gywat, and D. D. Awschalom, "Coherent dynamics of a single spin interacting with an adjustable spin bath," *Science (80-.).*, vol. 320, pp. 352–355, apr 2008.

[7] L. Jiang, J. S. Hodges, J. R. Maze, P. Maurer, J. M. Taylor, D. G. Cory, P. R. Hemmer, R. L. Walsworth, A. Yacoby, A. S. Zibrov, and M. D. Lukin, "Repetitive Readout of a Single Electronic Spin via Quantum Logic with Nuclear Spin Ancillae," *Science (80-.).*, vol. 326, no. 5950, pp. 267–272, 2009.

[8] P. Neumann, J. Beck, M. Steiner, F. Rempp, H. Fedder, P. R. Hemmer, J. Wrachtrup, and F. Jelezko, "Single-Shot Readout of a Single Nuclear Spin," *Science (80-.).*, vol. 329, pp. 542–544, jul 2010.

[9] P. C. Maurer, G. Kucsko, C. Latta, L. Jiang, N. Y. Yao, S. D. Bennett, F. Pastawski, D. Hunger, N. Chisholm, M. Markham, D. J. Twitchen, J. I. Cirac, and M. D. Lukin, "Room-Temperature Quantum Bit Memory Exceeding One Second," *Science (80-.).*, vol. 336, no. 6086, pp. 1283–1286, 2012.

[10] M. Pfender, N. Aslam, P. Simon, D. Antonov, G. Thiering, S. Burk, F. Fávaro De Oliveira, A. Denisenko, H. Fedder, J. Meijer, J. A. Garrido, A. Gali, T. Teraji, J. Isoya, M. W. Doherty, A. Alkauskas, A. Gallo, A. Grüneis, P. Neumann, and J. Wrachtrup, "Protecting a Diamond Quantum Memory by Charge State Control," *Nano Lett.*, vol. 17, no. 10, pp. 5931–5937, 2017.

[11] M. Pfender, N. Aslam, H. Sumiya, S. Onoda, P. Neumann, J. Isoya, C. A. Meriles, and J. Wrachtrup, "Nonvolatile nuclear spin memory enables sensor-unlimited nanoscale spectroscopy of small spin clusters," *Nat. Commun.*, vol. 8, p. 834, dec 2017.

[12] G. D. Fuchs, G. Burkard, P. V. Klimov, and D. D. Awschalom, "A quantum memory intrinsic to single nitrogen-vacancy centres in diamond," *Nat. Phys.*, vol. 7, pp. 789–793, oct 2011.

[13] G. Waldherr, Y. Wang, S. Zaiser, M. Jamali, T. Schulte-Herbrüggen, H. Abe, T. Ohshima, J. Isoya, J. F. Du, P. Neumann, and J. Wrachtrup, "Quantum error correction in a solid-state hybrid spin register.," *Nature*, vol. 506, no. 7487, pp. 204–7, 2014.

[14] F. Casola, T. Van Der Sar, and A. Yacoby, "Probing condensed matter physics with magnetometry based on nitrogen-vacancy centres in diamond," *Nat. Rev. Mater.*, vol. 3, p. 17088, jan 2018.

[15] L. Rondin, J.-P. P. Tetienne, T. Hingant, J.-F. F. Roch, P. Maletinsky, and V. Jacques, "Magnetometry with nitrogen-vacancy defects in diamond," *Reports Prog. Phys.*, vol. 77, p. 56503, may 2014.

[16] L. Childress, M. V. Gurudev Dutt, J. M. Taylor, A. S. Zibrov, F. Jelezko, J. Wrachtrup, P. R. Hemmer, and M. D. Lukin, "Coherent dynamics of coupled

electron and nuclear spin qubits in diamond.," *Science*, vol. 314, pp. 281–5, oct 2006.

[17] R. Schirhagl, K. Chang, M. Loretz, and C. L. Degen, "Nitrogen-Vacancy Centers in Diamond: Nanoscale Sensors for Physics and Biology," *Annu. Rev. Phys. Chem.*, vol. 65, pp. 83–105, apr 2014.

[18] D. Lee, K. W. Lee, J. V. Cady, C. Jin-ming, C. Xiang-dong, F. Le-le, I. Aharonovich, S. Castelletto, D. A. Simpson, S. Pezzagna, D. Rogalla, D. Wildanger, H. Yamano, S. Kawai, K. Kato, T. Kageura, M. Inaba, and T. Okada, "Charge state stabilization of shallow nitrogen vacancy centers in diamond by oxygen surface modification remarks Charge state stabilization of shallow nitrogen vacancy centers in diamond by oxygen surface modi fi cation," *Jpn. J. Appl. Phys.*, vol. 56, p. 04CK08, 2017.

[19] C. L. Degen, F. Reinhard, and P. Cappellaro, "Quantum sensing," *Rev. Mod. Phys.*, vol. 89, no. 3, 2017.

[20] F. Jelezko and J. Wrachtrup, "Single defect centres in diamond: A review," *Phys. Status Solidi Appl. Mater. Sci.*, vol. 203, no. 13, pp. 3207–3225, 2006.

[21] J.-P. Tetienne, N. Dontschuk, D. A. Broadway, A. Stacey, D. A. Simpson, and L. C. L. Hollenberg, "Quantum imaging of current flow in graphene," *Sci. Adv.*, vol. 3, p. e1602429, sep 2017.

[22] J. P. Tetienne, T. Hingant, J. V. Kim, L. Herrera Diez, J. P. Adam, K. Garcia, J. F. Roch, S. Rohart, A. Thiaville, D. Ravelosona, and V. Jacques, "Nanoscale imaging and control of domain-wall hopping with a nitrogen-vacancy center microscope," *Science (80-.).*, vol. 344, no. 6190, pp. 1366–1369, 2014.

[23] Y. Dovzhenko, F. Casola, S. Schlotter, T. X. Zhou, F. Büttner, R. L. Walsworth, G. S. D. Beach, and A. Yacoby, "Magnetostatic twists in room-temperature skyrmions explored by nitrogen-vacancy center spin texture reconstruction," *Nat. Commun.*, vol. 9, no. 1, p. 2712, 2018.

[24] T. Van Der Sar, F. Casola, R. Walsworth, and A. Yacoby, "Nanometre-scale probing of spin waves using single-electron spins," *Nat. Commun.*, vol. 6, pp. 1–8, 2015.

[25] P. Andrich, C. F. de las Casas, X. Liu, H. L. Bretscher, J. R. Berman, F. J. Heremans, P. F. Nealey, and D. D. Awschalom, "Long-range spin wave mediated control of defect qubits in nanodiamonds," *npj Quantum Inf.*, vol. 3, no. 1, p. 28, 2017.

[26] D. Le Sage, K. Arai, D. R. Glenn, S. J. DeVience, L. M. Pham, L. Rahn-Lee, M. D. Lukin, A. Yacoby, A. Komeili, and R. L. Walsworth, "Optical magnetic imaging of living cells," *Nature*, vol. 496, pp. 486–489, apr 2013.

[27] D. R. Glenn, K. Lee, H. Park, R. Weissleder, A. Yacoby, M. D. Lukin, H. Lee, R. L. Walsworth, and C. B. Connolly, "Single-cell magnetic imaging using a quantum diamond microscope," *Nat. Methods*, vol. 12, no. 8, pp. 736–738, 2015.

[28] Q. Chen, I. Schwarz, F. Jelezko, A. Retzker, and M. B. Plenio, "Resonance-inclined optical nuclear spin polarization of liquids in diamond structures," *Phys. Rev. B - Condens. Matter Mater. Phys.*, vol. 93, p. 060408, feb 2016.

[29] P. London, J. Scheuer, J.-M. Cai, I. Schwarz, A. Retzker, M. B. Plenio, M. Katagiri, T. Teraji, S. Koizumi, J. Isoya, R. Fischer, L. P. McGuinness, B. Naydenov, and F. Jelezko, "Detecting and Polarizing Nuclear Spins with Double Resonance on a Single Electron Spin," *Phys. Rev. Lett.*, vol. 111, p. 067601, aug 2013.

[30] P. Wang, B. Liu, and W. Yang, "Strongly polarizing weakly coupled 13C nuclear spins with optically pumped nitrogen-vacancy center," *Sci. Rep.*, vol. 5, p. 15847, nov 2015.

[31] R. Fischer, C. O. Bretschneider, P. London, D. Budker, D. Gershoni, and L. Frydman, "Bulk Nuclear Polarization Enhanced at Room Temperature by Optical Pumping," *Phys. Rev. Lett.*, vol. 111, p. 057601, jul 2013.

[32] D. Abrams, M. E. Trusheim, D. Englund, M. D. Shattuck, and C. A. Meriles, "Dynamic Nuclear Spin Polarization of Liquids and Gases in Contact with Nanostructured Diamond Dynamic Nuclear Spin Polarization of Liquids and Gases in Contact with Nanostructured Diamond," *Nano Lett.*, vol. 14, no. 5, pp. 2471–2478, 2014.

[33] D. A. Broadway, J.-P. Tetienne, A. Stacey, J. D. A. Wood, D. A. Simpson, L. T. Hall, and L. C. L. Hollenberg, "Quantum probe hyperpolarisation of molecular nuclear spins," *Nat. Commun.*, vol. 9, p. 1246, dec 2018.

[34] J. Scheuer, I. Schwartz, Q. Chen, D. Schulze-Sünninghausen, P. Carl, P. Höfer, A. Retzker, H. Sumiya, J. Isoya, B. Luy, M. B. Plenio, B. Naydenov, and F. Jelezko, "Optically induced dynamic nuclear spin polarisation in diamond," *New J. Phys.*, vol. 18, p. 013040, jan 2016.

[35] A. B. Schmidt, S. Berner, W. Schimpf, C. Müller, T. Lickert, N. Schwaderlapp, S. Knecht, J. G. Skinner, A. Dost, P. Rovedo, J. Hennig, D. Von Elverfeldt, and J. B. Hövener, "Liquid-state carbon-13 hyperpolarization generated in an MRI system for fast imaging," *Nat. Commun.*, vol. 8, p. 14535, mar 2017.

[36] P. Fernández-Acebal and M. B. Plenio, "Sensing phases of water via nitrogen-vacancy centres in diamond," *Sci. Rep.*, vol. 8, no. 1, pp. 1–8, 2018.

[37] G. A. Álvarez, C. O. Bretschneider, R. Fischer, P. London, H. Kanda, S. Onoda, J. Isoya, D. Gershoni, and L. Frydman, "Local and bulk 13C hyperpolarization in nitrogen-vacancy-centred diamonds at variable fields and orientations," *Nat. Commun.*, vol. 6, p. 8456, sep 2015.

[38] J. P. King, K. Jeong, C. C. Vassiliou, C. S. Shin, R. H. Page, C. E. Avalos, H.-J. Wang, and A. Pines, "Room-temperature in situ nuclear spin hyperpolarization from optically pumped nitrogen vacancy centres in diamond," *Nat. Commun.*, vol. 6, p. 8965, dec 2015.

[39] H.-J. J. Wang, C. S. Shin, C. E. Avalos, S. J. Seltzer, D. Budker, A. Pines, and V. S. Bajaj, "Sensitive magnetic control of ensemble nuclear spin hyperpolarization in diamond," *Nat. Commun.*, vol. 4, p. 1940, jun 2013.

[40] M. Loretz, H. Takahashi, T. F. Segawa, J. M. Boss, and C. L. Degen, "Optical hyperpolarization of nitrogen donor spins in bulk diamond," *Phys. Rev. B*, vol. 95, p. 064413, feb 2017.

[41] Q. Chen, I. Schwarz, F. Jelezko, A. Retzker, and M. B. Plenio, "Optical hyperpolarization of C 13 nuclear spins in nanodiamond ensembles," *Phys. Rev. B - Condens. Matter Mater. Phys.*, vol. 92, no. 18, p. 184420, 2015.

[42] E. Rej, T. Gaebel, T. Boele, D. E. J. Waddington, and D. J. Reilly, "Hyperpolarized nanodiamond with long spin-relaxation times," *Nat. Commun.*, vol. 6, p. 8459, oct 2015.

[43] A. Gruber, A. Dräbenstedt, C. Tietz, L. Fleury, J. Wrachtrup, C. von Borczyskowski, and C. von Borczyskowski, "Scanning Confocal Optical Microscopy and Magnetic Resonance on Single Defect Centers," *Science (80-.).*, vol. 276, pp. 2012–2014, jun 1997.

[44] G. Balasubramanian, I. Y. Chan, R. Kolesov, M. Al-Hmoud, J. Tisler, C. Shin, C. Kim, A. Wojcik, P. R. Hemmer, A. Krueger, T. Hanke, A. Leitenstorfer, R. Bratschitsch, F. Jelezko, and J. Wrachtrup, "Nanoscale imaging magnetometry with diamond spins under ambient conditions," *Nature*, vol. 455, pp. 648–651, oct 2008.

[45] D. A. Simpson, J. P. Tetienne, J. M. McCoey, K. Ganesan, L. T. Hall, S. Petrou, R. E. Scholten, and L. C. Hollenberg, "Magneto-optical imaging of thin magnetic films using spins in diamond," *Sci. Rep.*, vol. 6, no. October 2015, p. 22797, 2016.

[46] M. W. Doherty, J. Michl, F. Dolde, I. Jakobi, P. Neumann, N. B. Manson, and J. Wrachtrup, "Measuring the defect structure orientation of a single NV- centre in diamond," *New J. Phys.*, vol. 16, pp. 0–20, 2014.

[47] F. Dolde, H. Fedder, M. W. Doherty, T. Nöbauer, F. Rempp, G. Balasubramanian, T. Wolf, F. Reinhard, L. C. L. Hollenberg, F. Jelezko, and J. Wrachtrup, "Electric-field sensing using single diamond spins," *Nat. Phys.*, vol. 7, pp. 459–463, jun 2011.

[48] M. E. Trusheim and D. Englund, "Wide-field strain imaging with preferentially aligned nitrogen-vacancy centers in polycrystalline diamond," *New J. Phys.*, vol. 18, no. 12, 2016.

[49] S. Rajendran, N. Zobrist, A. O. Sushkov, R. L. Walsworth, and M. Lukin, "A method for directional detection of dark matter using spectroscopy of crystal defects," *Phys. Rev. D*, vol. 96, p. 35009, aug 2017.

[50] J. M. Taylor, P. Cappellaro, L. Childress, L. Jiang, D. Budker, P. R. Hemmer, A. Yacoby, R. L. Walsworth, and M. D. Lukin, "High-sensitivity diamond magnetometer with nanoscale resolution," *Nat. Phys.*, vol. 4, pp. 810–816, oct 2008.

[51] J. R. Maze, P. L. Stanwix, J. S. Hodges, S. Hong, J. M. Taylor, P. Cappellaro, L. Jiang, M. V. G. Dutt, E. Togan, A. S. Zibrov, A. Yacoby, R. L. Walsworth, and M. D. Lukin, "Nanoscale magnetic sensing with an individual electronic spin in diamond," *Nature*, vol. 455, pp. 644–647, oct 2008.

[52] N. Bar-Gill, L. M. Pham, A. Jarmola, D. Budker, and R. L. Walsworth, "Solid-state electronic spin coherence time approaching one second," *Nat. Commun.*, vol. 4, p. 1743, apr 2013.

[53] G. Balasubramanian, P. Neumann, D. Twitchen, M. Markham, R. Kolesov, N. Mizuochi, J. Isoya, J. Achard, J. Beck, J. Tissler, V. Jacques, P. R. Hemmer,

F. Jelezko, and J. Wrachtrup, "Ultralong spin coherence time in isotopically engineered diamond," *Nat. Mater.*, vol. 8, pp. 383–387, may 2009.

[54] J. H. Cole and L. C. L. Hollenberg, "Scanning quantum decoherence microscopy," *Nanotechnology*, vol. 20, no. 49, p. 495401, 2009.

[55] P. Neumann, I. Jakobi, F. Dolde, C. Burk, R. Reuter, G. Waldherr, J. Honert, T. Wolf, A. Brunner, J. H. Shim, D. Suter, H. Sumiya, J. Isoya, and J. Wrachtrup, "High-Precision Nanoscale Temperature Sensing Using Single Defects in Diamond," *Nano Lett.*, vol. 13, pp. 2738–2742, jun 2013.

[56] G. Kucsko, P. C. Maurer, N. Y. Yao, M. Kubo, H. J. Noh, P. K. Lo, H. Park, and M. D. Lukin, "Nanometre-scale thermometry in a living cell," *Nature*, vol. 500, pp. 54–58, aug 2013.

[57] H. Clevenson, M. E. Trusheim, C. Teale, T. Schröder, D. Braje, and D. Englund, "Broadband magnetometry and temperature sensing with a light-trapping diamond waveguide," *Nat. Phys.*, vol. 11, pp. 393–397, may 2015.

[58] D. M. Toyli, C. F. de las Casas, D. J. Christle, V. V. Dobrovitski, and D. D. Awschalom, "Fluorescence thermometry enhanced by the quantum coherence of single spins in diamond.," *Proc. Natl. Acad. Sci. U. S. A.*, vol. 110, no. 21, pp. 8417–21, 2013.

[59] T. Plakhotnik, M. W. Doherty, J. H. Cole, R. Chapman, and N. B. Manson, "All-Optical Thermometry and Thermal Properties of the Optically Detected Spin Resonances of the NVâĂŞ Center in Nanodiamond," *Nano Lett.*, vol. 14, pp. 4989–4996, sep 2014.

[60] I. Lovchinsky, J. D. Sanchez-Yamagishi, E. K. Urbach, S. Choi, S. Fang, T. I. Andersen, K. Watanabe, T. Taniguchi, A. Bylinskii, E. Kaxiras, P. Kim, H. Park, and M. D. Lukin, "Magnetic resonance spectroscopy of an atomically thin material using a single-spin qubit," *Science (80-.).*, vol. 355, no. 6324, pp. 503–507, 2017.

[61] D. R. Glenn, D. B. Bucher, J. Lee, M. D. Lukin, H. Park, and R. L. Walsworth, "High-resolution magnetic resonance spectroscopy using a Solid-State spin sensor," *Nature*, vol. 555, pp. 351–354, may 2018.

[62] N. Aslam, M. Pfender, P. Neumann, R. Reuter, A. Zappe, F. D. Oliveira, A. Denisenko, H. Sumiya, S. Onoda, and J. Isoya, "Supplementary Material for

Nanoscale nuclear magnetic resonance with chemical resolution," *Science (80-.).*, 2017.

[63] S. Schmitt, T. Gefen, F. M. Stürner, T. Unden, G. Wolff, C. Müller, J. Scheuer, B. Naydenov, M. Markham, S. Pezzagna, J. Meijer, I. Schwarz, M. Plenio, A. Retzker, L. P. McGuinness, and F. Jelezko, "Submillihertz magnetic spectroscopy performed with a nanoscale quantum sensor," *Science (80-.).*, vol. 356, no. 6340, 2017.

[64] J. M. Boss, K. S. Cujia, J. Zopes, and C. L. Degen, "Quantum sensing with arbitrary frequency resolution," *Science (80-.).*, vol. 356, no. 6340, 2017.

[65] T. Rosskopf, J. Zopes, J. M. Boss, and C. L. Degen, "A quantum spectrum analyzer enhanced by a nuclear spin memory," *npj Quantum Inf.*, vol. 3, no. 1, p. 33, 2017.

[66] S. Kaufmann, D. A. Simpson, L. T. Hall, V. Perunicic, P. Senn, S. Steinert, L. P. McGuinness, B. C. Johnson, T. Ohshima, F. Caruso, J. Wrachtrup, R. E. Scholten, P. Mulvaney, and L. Hollenberg, "Detection of atomic spin labels in a lipid bilayer using a single-spin nanodiamond probe," *Proc. Natl. Acad. Sci.*, vol. 110, pp. 10894–10898, jul 2013.

[67] Q. Y. Cao, Z. J. Shu, P. C. Yang, M. Yu, M. S. Gong, J. Y. He, R. F. Hu, A. Retzker, M. B. Plenio, C. Müller, N. Tomek, B. Naydenov, L. P. McGuinness, F. Jelezko, and J. M. Cai, "Protecting quantum spin coherence of nanodiamonds in living cells," *Preprint*, oct 2017.

[68] L. P. McGuinness, Y. Yan, A. Stacey, D. A. Simpson, L. T. Hall, D. Maclaurin, S. Prawer, P. Mulvaney, J. Wrachtrup, F. Caruso, R. E. Scholten, and L. C. L. Hollenberg, "Quantum measurement and orientation tracking of fluorescent nanodiamonds inside living cells," *Nat. Nanotechnol.*, vol. 6, pp. 358–363, jun 2011.

[69] S. Steinert, F. Ziem, L. T. Hall, A. Zappe, M. Schweikert, N. Götz, A. Aird, G. Balasubramanian, L. Hollenberg, and J. Wrachtrup, "Magnetic spin imaging under ambient conditions with sub-cellular resolution," *Nat. Commun.*, vol. 4, p. 1607, mar 2013.

[70] J. F. Barry, M. J. Turner, J. M. Schloss, D. R. Glenn, Y. Song, M. D. Lukin, H. Park, and R. L. Walsworth, "Optical magnetic detection of single-neuron action potentials using quantum defects in diamond," *Proc. Natl. Acad. Sci.*, vol. 113, pp. 14133–14138, dec 2016.

[71] J. H. N. Loubser and J. A. van Wyk, "Electron spin resonance in the study of diamond," *Reports Prog. Phys.*, vol. 41, pp. 1201–1248, aug 1978.

[72] M. V. Hauf, B. Grotz, B. Naydenov, M. Dankerl, S. Pezzagna, J. Meijer, F. Jelezko, J. Wrachtrup, M. Stutzmann, F. Reinhard, and J. A. Garrido, "Chemical control of the charge state of nitrogen-vacancy centers in diamond," *Phys. Rev. B - Condens. Matter Mater. Phys.*, vol. 83, no. 8, pp. 1–4, 2011.

[73] C. Schreyvogel, V. Polyakov, R. Wunderlich, J. Meijer, and C. E. Nebel, "Active charge state control of single NV centres in diamond by in-plane Al-Schottky junctions," *Sci. Rep.*, vol. 5, p. 12160, dec 2015.

[74] N. B. Manson and J. P. Harrison, "Photo-ionization of the nitrogen-vacancy center in diamond," *Diam. Relat. Mater.*, vol. 14, no. 10, pp. 1705–1710, 2005.

[75] M. W. Doherty, N. B. Manson, P. Delaney, and L. C. L. Hollenberg, "The negatively charged nitrogen-vacancy centre in diamond: the electronic solution," *New J. Phys.*, vol. 13, no. 2, p. 25019, 2011.

[76] M. Steiner, P. Neumann, J. Beck, F. Jelezko, and J. Wrachtrup, "Universal enhancement of the optical readout fidelity of single electron spins at nitrogen-vacancy centers in diamond," *Phys. Rev. B - Condens. Matter Mater. Phys.*, vol. 81, no. 3, pp. 1–6, 2010.

[77] E. van Oort, N. B. Manson, and M. Glasbeek, "Optically detected spin coherence of the diamond N-V centre in its triplet ground state," *J. Phys. C Solid State Phys.*, vol. 21, no. 23, p. 4385, 1988.

[78] J.-P. Tetienne, L. Rondin, P. Spinicelli, M. Chipaux, T. Debuisschert, J.-F. Roch, and V. Jacques, "Magnetic-field-dependent photodynamics of single NV defects in diamond: an application to qualitative all-optical magnetic imaging," *New J. Phys.*, vol. 14, p. 103033, oct 2012.

[79] M. L. Goldman, A. Sipahigil, M. W. Doherty, N. Y. Yao, S. D. Bennett, M. Markham, D. J. Twitchen, N. B. Manson, A. Kubanek, and M. D. Lukin, "Phonon-Induced Population Dynamics and Intersystem Crossing in Nitrogen-Vacancy Centers," *Phys. Rev. Lett.*, vol. 114, p. 145502, apr 2015.

[80] M. L. Goldman, M. W. Doherty, A. Sipahigil, N. Y. Yao, S. D. Bennett, N. B. Manson, A. Kubanek, and M. D. Lukin, "State-selective intersystem crossing in

nitrogen-vacancy centers," *Phys. Rev. B*, vol. 91, p. 165201, apr 2015.

[81] J. P. D. Martin, N. B. Manson, D. C. Doetschman, M. J. Sellars, R. Neuhaus, and E. A. Wilson, "Spectral hole burning and Raman heterodyne signals associated with an avoided crossing in the NV centre in diamond," *J. Lumin.*, vol. 86, no. 3, pp. 355–362, 2000.

[82] N. B. Manson, J. P. Harrison, and M. J. Sellars, "Nitrogen-vacancy center in diamond: Model of the electronic structure and associated dynamics," *Phys. Rev. B*, vol. 74, p. 104303, sep 2006.

[83] J. Harrison, M. J. Sellars, and N. B. Manson, "Optical spin polarisation of the N-V centre in diamond," *J. Lumin.*, vol. 107, no. 1, pp. 245–248, 2004.

[84] N. B. Manson, X.-F. He, and P. T. H. Fisk, "Raman heterodyne detected electron-nuclear-double-resonance measurements of the nitrogen-vacancy center in diamond," *Opt. Lett.*, vol. 15, pp. 1094–1096, oct 1990.

[85] X. He, P. T. H. Fisk, and N. B. Manson, "AutlerâĂŞTownes effect of the photoexcited diamond nitrogenâĂŘvacancy center in its triplet ground state," *J. Appl. Phys.*, vol. 72, no. 1, pp. 211–217, 1992.

[86] N. B. Manson, X.-F. He, and P. T. H. Fisk, "Raman heterodyne studies of the nitrogen-vacancy centre in diamond," *J. Lumin.*, vol. 53, no. 1, pp. 49–54, 1992.

[87] X.-F. He, N. B. Manson, and P. T. H. Fisk, "Paramagnetic resonance of photoexcited N- V defects in diamond. I. Level anticrossing in the ^{3} A ground state," *Phys. Rev. B*, vol. 47, pp. 8809–8815, apr 1993.

[88] S. Felton, A. M. Edmonds, M. E. Newton, P. M. Martineau, D. Fisher, D. J. Twitchen, and J. M. Baker, "Hyperfine interaction in the ground state of the negatively charged nitrogen vacancy center in diamond," *Phys. Rev. B*, vol. 79, p. 75203, feb 2009.

[89] B. Smeltzer, J. McIntyre, and L. Childress, "Robust control of individual nuclear spins in diamond," *Phys. Rev. A*, vol. 80, p. 50302, nov 2009.

[90] A. Gali, M. Fyta, and E. Kaxiras, "Ab initio supercell calculations on nitrogen-vacancy center in diamond: Electronic structure and hyperfine tensors," *Phys. Rev. B*, vol. 77, p. 155206, apr 2008.

[91] A. Gali, "Identification of individual C 13 isotopes of nitrogen-vacancy center in diamond by combining the polarization studies of nuclear spins and first-principles calculations," *Phys. Rev. B - Condens. Matter Mater. Phys.*, vol. 80, no. 24, pp. 1–4, 2009.

[92] J. R. Rabeau, P. Reichart, G. Tamanyan, D. N. Jamieson, S. Prawer, F. Jelezko, T. Gaebel, I. Popa, M. Domhan, and J. Wrachtrup, "Implantation of labelled single nitrogen vacancy centers in diamond using15N," *Appl. Phys. Lett.*, vol. 88, pp. 1–3, jan 2006.

[93] G. D. Fuchs, V. V. Dobrovitski, R. Hanson, A. Batra, C. D. Weis, T. Schenkel, and D. D. Awschalom, "Excited-state spectroscopy using single Spin manipulation in diamond," *Phys. Rev. Lett.*, vol. 101, p. 117601, sep 2008.

[94] S. Felton, A. M. Edmonds, M. E. Newton, P. M. Martineau, D. Fisher, and D. J. Twitchen, "Electron paramagnetic resonance studies of the neutral nitrogen vacancy in diamond," *Phys. Rev. B*, vol. 77, p. 81201, feb 2008.

[95] A. Dréau, M. Lesik, L. Rondin, P. Spinicelli, O. Arcizet, J. F. Roch, and V. Jacques, "Avoiding power broadening in optically detected magnetic resonance of single NV defects for enhanced dc magnetic field sensitivity," *Phys. Rev. B - Condens. Matter Mater. Phys.*, vol. 84, no. 19, pp. 1–8, 2011.

[96] L. T. Hall, J. H. Cole, and L. C. L. Hollenberg, "Analytic solutions to the central-spin problem for nitrogen-vacancy centers in diamond," *Phys. Rev. B*, vol. 90, p. 75201, aug 2014.

[97] E. L. Hahn, "Spin Echoes," *Phys. Rev.*, vol. 80, pp. 580–594, nov 1950.

[98] H. Y. Carr and E. M. Purcell, "Effects of Diffusion on Free Precession in Nuclear Magnetic Resonance Experiments," *Phys. Rev.*, vol. 94, pp. 630–638, may 1954.

[99] S. R. Hartmann and E. L. Hahn, "Nuclear Double Resonance in the Rotating Frame," *Phys. Rev.*, vol. 128, pp. 2042–2053, dec 1962.

[100] L. M. Pham, D. L. Sage, P. L. Stanwix, T. K. Yeung, D. Glenn, A. Trifonov, P. Cappellaro, P. R. Hemmer, M. D. Lukin, H. Park, A. Yacoby, and R. L. Walsworth, "Magnetic field imaging with nitrogen-vacancy ensembles," *New J. Phys.*, vol. 13, p. 045021, apr 2011.

[101] K. Chang, A. Eichler, J. Rhensius, L. Lorenzelli, and C. L. Degen, "Nanoscale Imaging of Current Density with a Single-Spin Magnetometer," *Nano Lett.*, vol. 17, no. 4, pp. 2367–2373, 2017.

[102] F. Jelezko, T. Gaebel, I. Popa, M. Domhan, A. Gruber, and J. Wrachtrup, "Observation of Coherent Oscillation of a Single Nuclear Spin and Realization of a Two-Qubit Conditional Quantum Gate," *Phys. Rev. Lett.*, vol. 93, p. 130501, sep 2004.

[103] S. E. Lillie, D. A. Broadway, J. D. A. Wood, D. A. Simpson, A. Stacey, J.-P. Tetienne, and L. C. L. Hollenberg, "Environmentally Mediated Coherent Control of a Spin Qubit in Diamond," *Phys. Rev. Lett.*, vol. 118, p. 167204, apr 2017.

[104] C. Belthangady, N. Bar-Gill, L. M. Pham, K. Arai, D. Le Sage, P. Cappellaro, and R. L. Walsworth, "Dressed-State Resonant Coupling between Bright and Dark Spins in Diamond," *Phys. Rev. Lett.*, vol. 110, p. 157601, apr 2013.

[105] N. Timoney, I. Baumgart, M. Johanning, A. F. Varón, M. B. Plenio, A. Retzker, and C. Wunderlich, "Quantum gates and memory using microwave-dressed states.," *Nature*, vol. 476, pp. 185–188, aug 2011.

[106] J. Scheuer, I. Schwartz, S. Müller, Q. Chen, I. Dhand, M. B. Plenio, B. Naydenov, and F. Jelezko, "Robust techniques for polarization and detection of nuclear spin ensembles," *Phys. Rev. B*, vol. 96, p. 174436, nov 2017.

[107] G.-Q. Liu, Q.-Q. Jiang, Y.-C. Chang, D.-Q. Liu, W.-X. Li, C.-Z. Gu, H. C. Po, W.-X. Zhang, N. Zhao, and X.-Y. Pan, "Protection of centre spin coherence by dynamic nuclear spin polarization in diamond.," *Nanoscale*, vol. 6, pp. 10134–9, sep 2014.

[108] F. Shagieva, S. Zaiser, P. Neumann, D. B. Dasari, R. Stöhr, A. Denisenko, R. Reuter, C. A. Meriles, and J. Wrachtrup, "Microwave-Assisted Cross-Polarization of Nuclear Spin Ensembles from Optically Pumped Nitrogen-Vacancy Centers in Diamond," *Nano Lett.*, vol. 18, pp. 3731–3737, may 2018.

[109] A. Jarmola, V. M. Acosta, K. Jensen, S. Chemerisov, and D. Budker, "Temperature- and Magnetic-Field-Dependent Longitudinal Spin Relaxation in Nitrogen-Vacancy Ensembles in Diamond," *Phys. Rev. Lett.*, vol. 108, p. 197601, may 2012.

[110] J. D. A. Wood, D. A. Broadway, L. T. Hall, A. Stacey, D. A. Simpson, J.-P. Tetienne, and L. C. L. Hollenberg, "Wide-band, nanoscale magnetic resonance spectroscopy

using quantum relaxation of a single spin in diamond," *Phys. Rev. B - Condens. Matter Mater. Phys.*, vol. 94, pp. 1–16, oct 2016.

[111] J. D. A. Wood, J.-P. Tetienne, D. A. Broadway, L. T. Hall, D. A. Simpson, A. Stacey, and L. C. L. Hollenberg, "Microwave-free nuclear magnetic resonance at molecular scales," *Nat. Commun.*, vol. 8, p. 15950, jul 2017.

[112] B. A. Myers, a. Das, M. C. Dartiailh, K. Ohno, D. D. Awschalom, and a. C. Bleszynski Jayich, "Probing surface noise with depth-calibrated spins in diamond," *Phys. Rev. Lett.*, vol. 113, p. 27602, jul 2014.

[113] L. T. Hall, P. Kehayias, D. A. Simpson, A. Jarmola, A. Stacey, D. Budker, and L. C. L. Hollenberg, "Detection of nanoscale electron spin resonance spectra demonstrated using nitrogen-vacancy centre probes in diamond," *Nat. Commun.*, vol. 7, p. 10211, jan 2016.

[114] A. Laraoui and C. A. Meriles, "Approach to dark spin cooling in a diamond nanocrystal," *ACS Nano*, vol. 7, no. 4, pp. 3403–3410, 2013.

[115] H. J. Mamin, M. Kim, M. H. Sherwood, C. T. Rettner, K. Ohno, D. D. Awschalom, and D. Rugar, "Nanoscale Nuclear Magnetic Resonance with a Nitrogen-Vacancy Spin Sensor," *Science (80-.).*, vol. 339, pp. 557–560, feb 2013.

[116] T. Staudacher, F. Shi, S. Pezzagna, J. Meijer, J. Du, C. A. Meriles, F. Reinhard, and J. Wrachtrup, "Nuclear magnetic resonance spectroscopy on a (5-nanometer)3 sample volume.," *Science*, vol. 339, pp. 561–3, feb 2013.

[117] A. Bienfait, J. J. Pla, Y. Kubo, M. Stern, X. Zhou, C. C. Lo, C. D. Weis, T. Schenkel, M. L. W. Thewalt, D. Vion, D. Esteve, B. Julsgaard, K. Mølmer, J. J. L. Morton, and P. Bertet, "Reaching the quantum limit of sensitivity in electron spin resonance," *Nat. Nanotechnol.*, vol. 11, pp. 253–257, dec 2015.

[118] M. Loretz, J. M. Boss, T. Rosskopf, H. J. Mamin, D. Rugar, and C. L. Degen, "Spurious Harmonic Response of Multipulse Quantum Sensing Sequences," *Phys. Rev. X*, vol. 5, p. 021009, apr 2015.

[119] M. S. Grinolds, M. Warner, K. De Greve, Y. Dovzhenko, L. Thiel, R. L. Walsworth, S. Hong, P. Maletinsky, and A. Yacoby, "Subnanometre resolution in three-dimensional magnetic resonance imaging of individual dark spins," *Nat. Nanotechnol.*, vol. 9, no. 4, 2014.

[120] H. J. Mamin, M. H. Sherwood, and D. Rugar, "Detecting external electron spins using nitrogen-vacancy centers," *Phys. Rev. B*, vol. 86, p. 195422, nov 2012.

[121] F. Shi, Q. Zhang, P. Wang, H. Sun, J. J. Wang, X. Rong, M. Chen, C. Ju, F. Reinhard, H. Chen, J. Wrachtrup, J. J. Wang, and J. Du, "Single-protein spin resonance spectroscopy under ambient conditions," *Science (80-.).*, vol. 347, pp. 1135–1138, mar 2015.

[122] M. S. Grinolds, S. Hong, P. Maletinsky, L. Luan, M. D. Lukin, R. L. Walsworth, and A. Yacoby, "Nanoscale magnetic imaging of a single electron spin under ambient conditions," *Nat. Phys.*, vol. 9, p. 215, feb 2013.

[123] D. A. Simpson, E. Morrisroe, J. M. McCoey, A. H. Lombard, D. C. Mendis, F. Treussart, L. T. Hall, S. Petrou, and L. C. Hollenberg, "Non-Neurotoxic Nanodiamond Probes for Intraneuronal Temperature Mapping," *ACS Nano*, vol. 11, pp. 12077–12086, dec 2017.

[124] C. Foy, L. Zhang, M. E. Trusheim, R. Kevin, M. Walsh, E. N. Wang, and D. R. Englund, "Wide-field Magnetic Field and Temperature Imaging using Nanoscale Quantum Sensors," pp. 1–19, 2019.

[125] I. Lovchinsky, A. O. Sushkov, E. Urbach, N. P. de Leon, S. Choi, K. De Greve, R. Evans, R. Gertner, E. Bersin, C. Müller, L. McGuinness, F. Jelezko, R. L. Walsworth, H. Park, M. D. Lukin, N. P. de Leon, S. Choi, K. D. Greve, R. Evans, R. Gertner, E. Bersin, C. Müller, L. McGuinness, F. Jelezko, R. L. Walsworth, H. Park, and M. D. Lukin, "Nuclear magnetic resonance detection and spectroscopy of single proteins using quantum logic," *Science (80-.).*, vol. 351, p. aad8022, feb 2016.

[126] S. Kolkowitz, A. Safira, A. A. High, R. C. Devlin, S. Choi, Q. P. Unterreithmeier, D. Patterson, A. S. Zibrov, V. E. Manucharyan, H. Park, and M. D. Lukin, "Probing Johnson noise and ballistic transport in normal metals with a single-spin qubit," *Science (80-.).*, vol. 347, p. 1129, mar 2015.

[127] C. Du, T. van der Sar, T. X. Zhou, P. Upadhyaya, F. Casola, H. Zhang, M. C. Onbasli, C. A. Ross, R. L. Walsworth, Y. Tserkovnyak, and A. Yacoby, "Control and local measurement of the spin chemical potential in a magnetic insulator," *Science (80-.).*, vol. 357, pp. 195–198, jul 2017.

[128] T. Staudacher, N. Raatz, S. Pezzagna, J. Meijer, F. Reinhard, C. A. Meriles, and J. Wrachtrup, "Probing molecular dynamics at the nanoscale via an individual paramagnetic centre," *Nat Commun*, vol. 6, p. 8527, 2015.

[129] C. Müller, X. Kong, J.-M. Cai, K. Melentijević, A. Stacey, M. Markham, D. Twitchen, J. Isoya, S. Pezzagna, J. Meijer, J. F. Du, M. B. Plenio, B. Naydenov, L. P. McGuinness, and F. Jelezko, "Nuclear magnetic resonance spectroscopy with single spin sensitivity.," *Nat. Commun.*, vol. 5, p. 4703, 2014.

[130] P. Kehayias, A. Jarmola, N. Mosavian, I. Fescenko, F. M. Benito, A. Laraoui, J. Smits, L. Bougas, D. Budker, A. Neumann, S. R. J. Brueck, and V. M. Acosta, "Solution nuclear magnetic resonance spectroscopy on a nanostructured diamond chip," *Nat. Commun.*, vol. 8, p. 188, jan 2017.

[131] S. J. DeVience, L. M. Pham, I. Lovchinsky, A. O. Sushkov, N. Bar-Gill, C. Belthangady, F. Casola, M. Corbett, H. Zhang, M. D. Lukin, H. Park, A. Yacoby, and R. L. Walsworth, "Nanoscale NMR spectroscopy and imaging of multiple nuclear species," *Nat. Nanotechnol.*, vol. 10, pp. 129–134, feb 2015.

[132] L. M. Pham, S. J. DeVience, F. Casola, I. Lovchinsky, A. O. Sushkov, E. Bersin, J. Lee, E. Urbach, P. Cappellaro, H. Park, A. Yacoby, M. D. Lukin, and R. L. Walsworth, "NMR Technique for Determining the Depth of Shallow Nitrogen-Vacancy Centers in Diamond," *Phys. Rev. B*, vol. 045425, pp. 1–14, 2016.

[133] V. S. Perunicic, L. T. Hall, D. A. Simpson, C. D. Hill, and L. C. L. Hollenberg, "Towards single-molecule NMR detection and spectroscopy using single spins in diamond," *Phys. Rev. B - Condens. Matter Mater. Phys.*, vol. 89, p. 054432, feb 2014.

[134] V. S. Perunicic, C. D. Hill, L. T. Hall, and L. C. Hollenberg, "A quantum spin-probe molecular microscope," *Nat. Commun.*, vol. 7, pp. 1–10, 2016.

[135] A. Laraoui, D. Pagliero, and C. A. Meriles, "Imaging nuclear spins weakly coupled to a probe paramagnetic center," *Phys. Rev. B - Condens. Matter Mater. Phys.*, vol. 91, no. 20, pp. 1–7, 2015.

[136] A. Ajoy, U. Bissbort, M. D. Lukin, R. L. Walsworth, and P. Cappellaro, "Atomic-scale nuclear spin imaging using quantum-assisted sensors in diamond," *Phys. Rev. X*, vol. 5, no. 1, pp. 1–11, 2015.

[137] M. Kost, J. Cai, and M. B. Plenio, "Resolving single molecule structures with Nitrogen-vacancy centers in diamond," *Sci. Rep.*, vol. 5, pp. 1–10, 2015.

[138] J. Zopes, K. S. Cujia, K. Sasaki, J. M. Boss, K. M. Itoh, and C. L. Degen, "Three-dimensional localization spectroscopy of individual nuclear spins with sub-Angstrom resolution," *Nat. Commun.*, vol. 9, jun 2018.

[139] A. Ajoy, K. Liu, R. Nazaryan, X. Lv, P. R. Zangara, B. Safvati, G. Wang, D. Arnold, G. Li, A. Lin, P. Raghavan, E. Druga, S. Dhomkar, D. Pagliero, J. A. Reimer, D. Suter, C. A. Meriles, and A. Pines, "Orientation-independent room temperature optical 13 C hyperpolarization in powdered diamond," *Sci. Adv.*, vol. 4, no. 5, p. eaar5492, 2018.

[140] L. Robledo, H. Bernien, T. van der Sar, R. Hanson, T. van der Sar, and R. Hanson, "Spin dynamics in the optical cycle of single nitrogen-vacancy centres in diamond," *New J. Phys.*, vol. 13, p. 25013, feb 2011.

[141] P. Maletinsky, S. Hong, M. S. Grinolds, B. Hausmann, M. D. Lukin, R. L. Walsworth, M. Loncar, and A. Yacoby, "A robust scanning diamond sensor for nanoscale imaging with single nitrogen-vacancy centres," *Nat. Nanotechnol.*, vol. 7, p. 320, apr 2012.

[142] A. Barfuss, J. Teissier, E. Neu, A. Nunnenkamp, and P. Maletinsky, "Strong mechanical driving of a single electron spin," *Nat. Phys.*, vol. 11, no. October, p. 820, 2015.

[143] M. S. J. Barson, P. Peddibhotla, P. Ovartchaiyapong, K. Ganesan, R. L. Taylor, M. Gebert, Z. Mielens, B. Koslowski, D. A. Simpson, L. P. Mcguinness, S. Prawer, S. Onoda, T. Ohshima, A. C. B. Jayich, F. Jelezko, N. B. Manson, M. W. Doherty, J. McCallum, S. Prawer, S. Onoda, T. Ohshima, A. C. Bleszynski Jayich, F. Jelezko, N. B. Manson, and M. W. Doherty, "Nanomechanical Sensing Using Spins in Diamond," *Nano Lett.*, vol. 17, no. 3, pp. 1496–1503, 2017.

[144] J. P. Tetienne, A. Lombard, D. A. Simpson, C. Ritchie, J. Lu, P. Mulvaney, and L. C. Hollenberg, "Scanning Nanospin Ensemble Microscope for Nanoscale Magnetic and Thermal Imaging," *Nano Lett.*, vol. 16, no. 1, pp. 326–333, 2016.

[145] S. Bodenstedt, I. Jakobi, J. Michl, I. Gerhardt, P. Neumann, and J. Wrachtrup, "Nanoscale Spin Manipulation with Pulsed Magnetic Gradient Fields from a Hard Disc Drive Writer," *Nano Lett.*, vol. 18, pp. 5389–5395, sep 2018.

[146] J. P. Tetienne, T. Hingant, L. J. Martínez, S. Rohart, A. Thiaville, L. H. Diez, K. Garcia, J. P. Adam, J. V. Kim, J. F. Roch, I. M. Miron, G. Gaudin, L. Vila, B. Ocker, D. Ravelosona, and V. Jacques, "The nature of domain walls in ultrathin ferromagnets revealed by scanning nanomagnetometry," *Nat. Commun.*, vol. 6, pp. 1–6, 2015.

[147] D. Schmid-Lorch, T. Haberle, F. Reinhard, A. Zappe, M. Slota, L. Bogani, A. Finkler, and J. Wrachtrup, "Relaxometry and Dephasing Imaging of Superparamagnetic Magnetite Nanoparticles Using a Single Qubit," *Nano Lett.*, vol. 15, no. 8, pp. 4942–4947, 2015.

[148] A. Ariyaratne, D. Bluvstein, B. A. Myers, and A. C. B. Jayich, "Nanoscale electrical conductivity imaging using a nitrogen-vacancy center in diamond," *arXiv*, 2017.

[149] D. A. Simpson, R. G. Ryan, L. T. Hall, E. Panchenko, S. C. Drew, S. Petrou, P. S. Donnelly, P. Mulvaney, and L. C. L. Hollenberg, "Electron paramagnetic resonance microscopy using spins in diamond under ambient conditions," *Nat. Commun.*, vol. 8, p. 458, dec 2017.

[150] R. R. Fu, B. P. Weiss, E. A. Lima, R. J. Harrison, X. N. Bai, S. J. Desch, D. S. Ebel, C. Suavet, H. Wang, D. Glenn, D. Le Sage, T. Kasama, R. L. Walsworth, and A. T. Kuan, "Solar nebula magnetic fields recorded in the Semarkona meteorite," *Science (80-.).*, vol. 346, no. 6213, pp. 1089–1092, 2014.

[151] S. Steinert, F. Dolde, P. Neumann, A. Aird, B. Naydenov, G. Balasubramanian, F. Jelezko, and J. Wrachtrup, "High sensitivity magnetic imaging using an array of spins in diamond," *Rev. Sci. Instrum.*, vol. 81, p. 43705, apr 2010.

[152] F. Ziem, M. Garsi, H. Fedder, and J. Wrachtrup, "Quantitative nanoscale MRI with a wide field of view," jul 2018.

[153] J. E. Lang, T. Madhavan, J.-P. Tetienne, D. A. Broadway, L. T. Hall, T. Teraji, T. S. Monteiro, A. Stacey, and L. C. L. Hollenberg, "Nonvanishing effect of detuning errors in dynamical-decoupling-based quantum sensing experiments," *Phys. Rev. A*, vol. 99, p. 12110, jan 2019.

[154] J.-P. Tetienne, T. Hingant, L. Rondin, A. Cavaillès, L. Mayer, G. Dantelle, T. Gacoin, J. Wrachtrup, J.-F. Roch, and V. Jacques, "Spin relaxometry of sin-

gle nitrogen-vacancy defects in diamond nanocrystals for magnetic noise sensing," *Phys. Rev. B*, vol. 87, p. 235436, jun 2013.

[155] A. O. Sushkov, N. Chisholm, I. Lovchinsky, M. Kubo, P. K. Lo, S. D. Bennett, D. Hunger, A. Akimov, R. L. Walsworth, H. Park, and M. D. Lukin, "All-Optical Sensing of a Single-Molecule Electron Spin," *Nano Lett.*, vol. 14, pp. 6443–6448, nov 2014.

[156] M. Pelliccione, B. A. Myers, L. M. Pascal, A. Das, and A. C. Bleszynski Jayich, "Two-dimensional nanoscale imaging of gadolinium spins via scanning probe relaxometry with a single spin in diamond," *Phys. Rev. Appl.*, vol. 2, no. 5, pp. 1–7, 2014.

[157] P. London, R. Fischer, I. Alvizu, J. R. Maze, and D. Gershoni, "Local probing of nuclear bath polarization with a single electronic spin," *Phys. Rev. B*, vol. 92, p. 241117, dec 2015.

[158] M. Loretz, S. Pezzagna, J. Meijer, and C. L. Degen, "Nanoscale nuclear magnetic resonance with a 1.9-nm-deep nitrogen-vacancy sensor," *Appl. Phys. Lett.*, vol. 104, p. 33102, jan 2014.

[159] W. V. Smith, P. P. Sorokin, I. L. Gelles, and G. J. Lasher, "Electron-Spin Resonance of Nitrogen Donors in Diamond," *Phys. Rev.*, vol. 115, pp. 1546–1552, sep 1959.

[160] R. J. Cook and D. H. Whiffen, "Electron Nuclear Double Resonance Study of a Nitrogen Centre in Diamond," *Proc. R. Soc. A Math. Phys. Eng. Sci.*, vol. 295, pp. 99–106, nov 1966.

[161] D. A. Broadway, J. D. A. Wood, L. T. Hall, A. Stacey, M. Markham, D. A. Simpson, J.-P. Tetienne, and L. C. L. Hollenberg, "Anticrossing Spin Dynamics of Diamond Nitrogen-Vacancy Centers and All-Optical Low-Frequency Magnetometry," *Phys. Rev. Appl.*, vol. 6, p. 064001, dec 2016.

[162] R. J. Epstein, F. M. Mendoza, Y. K. Kato, and D. D. Awschalom, "Anisotropic interactions of a single spin and dark-spin spectroscopy in diamond," *Nat. Phys.*, vol. 1, pp. 94–98, nov 2005.

[163] A. Laraoui, J. S. Hodges, and C. A. Meriles, "Nitrogen-Vacancy-Assisted Magnetometry of Paramagnetic Centers in an Individual Diamond Nanocrystal," *Nano Lett.*, vol. 12, pp. 3477–3482, jul 2012.

[164] G. de Lange, T. van der Sar, M. Blok, Z.-H. Wang, V. Dobrovitski, and R. Hanson, "Controlling the quantum dynamics of a mesoscopic spin bath in diamond," *Sci. Rep.*, vol. 2, p. 382, dec 2012.

[165] H. S. Knowles, D. M. Kara, and M. Atatüre, "Observing bulk diamond spin coherence in high-purity nanodiamonds," *Nat. Mater.*, vol. 13, pp. 21–25, jan 2014.

[166] K. Holliday, N. B. Manson, M. Glasbeek, E. van Oort, and E. van Oort, "Optical hole-bleaching by level anti-crossing and cross relaxation in the N-V centre in diamond," *J. Phys. Condens. Matter*, vol. 1, p. 7093, oct 1989.

[167] C. Wei and N. B. Manson, "Observation of the dynamic Stark effect on electromagnetically induced transparency," *Phys. Rev. A*, vol. 60, pp. 2540–2546, sep 1999.

[168] E. A. Wilson, N. B. Manson, and C. Wei, "Perturbing an electromagnetic induced transparency within an inhomogeneously broadened transition," *Phys. Rev. A*, vol. 67, p. 23812, feb 2003.

[169] A. Wickenbrock, H. Zheng, L. Bougas, N. Leefer, S. Afach, A. Jarmola, V. M. Acosta, and D. Budker, "Microwave-free magnetometry with nitrogen-vacancy centers in diamond," *Appl. Phys. Lett.*, vol. 109, p. 53505, jun 2016.

[170] H. Wieder and T. G. Eck, ""Anticrossing" Signals in Resonance Fluorescence," *Phys. Rev.*, vol. 153, pp. 103–112, jan 1967.

[171] V. Jacques, P. Neumann, J. Beck, M. Markham, D. Twitchen, J. Meijer, F. Kaiser, G. Balasubramanian, F. Jelezko, and J. Wrachtrup, "Dynamic Polarization of Single Nuclear Spins by Optical Pumping of Nitrogen-Vacancy Color Centers in Diamond at Room Temperature," *Phys. Rev. Lett.*, vol. 102, p. 057403, feb 2009.

[172] V. Ivády, K. Szász, A. L. Falk, P. V. Klimov, D. J. Christle, E. Janzén, I. A. Abrikosov, D. D. Awschalom, and A. Gali, "Theoretical model of dynamic spin polarization of nuclei coupled to paramagnetic point defects in diamond and silicon carbide," *Phys. Rev. B*, vol. 92, p. 115206, sep 2015.

[173] M. W. Doherty, F. Dolde, H. Fedder, F. Jelezko, J. Wrachtrup, N. B. Manson, and L. C. L. Hollenberg, "Theory of the ground-state spin of the NV^- center in diamond," *Phys. Rev. B*, vol. 85, p. 205203, may 2012.

[174] J. R. Maze, A. Dréau, V. Waselowski, H. Duarte, J.-F. J.-F. Roch, V. Jacques, A. Dreau, V. Waselowski, H. Duarte, J.-F. J.-F. Roch, and V. Jacques, "Free in-

duction decay of single spins in diamond," *New J. Phys.*, vol. 14, p. 103041, oct 2012.

[175] O. Lehtinen, B. Naydenov, P. Börner, K. Melentjevic, C. Müller, L. P. McGuinness, S. Pezzagna, J. Meijer, U. Kaiser, and F. Jelezko, "Molecular dynamics simulations of shallow nitrogen and silicon implantation into diamond," *Phys. Rev. B*, vol. 93, p. 35202, jan 2016.

[176] R. Christopher deCharms, "Applications of real-time fMRI," *Nat. Rev. Neurosci.*, vol. 9, pp. 720–729, sep 2008.

[177] A. J. Rossini, A. Zagdoun, M. Lelli, A. Lesage, C. Copéret, and L. Emsley, "Dynamic nuclear polarization surface enhanced NMR spectroscopy," *Acc. Chem. Res.*, vol. 46, pp. 1942–1951, sep 2013.

[178] P. Nikolaou, B. M. Goodson, and E. Y. Chekmenev, "NMR hyperpolarization techniques for biomedicine," *Chemistry*, vol. 21, pp. 3156–3166, feb 2015.

[179] V. Bajaj, C. Farrar, M. Hornstein, I. Mastovsky, J. Vieregg, J. Bryant, B. Eléna, K. Kreischer, R. Temkin, and R. Griffin, "Dynamic nuclear polarization at 9T using a novel 250GHz gyrotron microwave source," *J. Magn. Reson.*, vol. 160, pp. 85–90, feb 2003.

[180] M. Viteau, A. Chotia, M. Allegrini, N. Bouloufa, O. Dulieu, D. Comparat, and P. Pillet, "Optical pumping and vibrational cooling of molecules," *Science (80-.).*, vol. 321, no. 5886, pp. 232–234, 2008.

[181] A. Morello, J. J. Pla, F. A. Zwanenburg, K. W. Chan, K. Y. Tan, H. Huebl, M. Möttönen, C. D. Nugroho, C. Yang, J. A. Van Donkelaar, A. D. Alves, D. N. Jamieson, C. C. Escott, L. C. Hollenberg, R. G. Clark, and A. S. Dzurak, "Single-shot readout of an electron spin in silicon," *Nature*, vol. 467, pp. 687–691, oct 2010.

[182] F. A. Zwanenburg, A. S. Dzurak, A. Morello, M. Y. Simmons, L. C. Hollenberg, G. Klimeck, S. Rogge, S. N. Coppersmith, and M. A. Eriksson, "Silicon quantum electronics," *Rev. Mod. Phys.*, vol. 85, pp. 961–1019, jul 2013.

[183] H. S. Knowles, D. M. Kara, and M. Atatüre, "Demonstration of a Coherent Electronic Spin Cluster in Diamond," *Phys. Rev. Lett.*, vol. 117, no. 10, p. 100802, 2016.

[184] D. A. Broadway, S. E. Lillie, N. Dontschuk, A. Stacey, L. T. Hall, J.-P. Tetienne, and L. C. L. Hollenberg, "High precision single qubit tuning via thermo-magnetic field control," *Appl. Phys. Lett.*, vol. 112, p. 103103, mar 2018.

[185] K. Hatada, H. Ishikawa, T. Kitayama, and H. Yuki, "Mechanism of proton spinâĂŘlattice relaxation in poly(methyl methacrylate)," *Die Makromol. Chemie*, vol. 178, no. 9, pp. 2753–2758, 1977.

[186] K. Golman, R. in 't Zandt, and M. Thaning, "Real-time metabolic imaging.," *Proc. Natl. Acad. Sci. U. S. A.*, vol. 103, pp. 11270–5, jul 2006.

[187] D. A. Broadway, N. Dontschuk, A. Tsai, S. E. Lillie, C. T.-K. Lew, J. C. McCallum, B. C. Johnson, M. W. Doherty, A. Stacey, L. C. L. Hollenberg, and J.-P. Tetienne, "Spatial mapping of band bending in semiconductor devices using in situ quantum sensors," *Nat. Electron.*, vol. 1, pp. 502–507, sep 2018.

[188] H. J. Mamin, "Nitrogen-Vacancy Spin Sensors for Nanoscale Nuclear Magnetic Resonance," tech. rep., IBM, Phoenix, Arizona, 2017.

[189] T. Häberle, T. Oeckinghaus, D. Schmid-Lorch, M. Pfender, F. F. De Oliveira, S. A. Momenzadeh, A. Finkler, and J. Wrachtrup, "Nuclear quantum-assisted magnetometer," *Rev. Sci. Instrum.*, vol. 88, oct 2017.

[190] B. C. Stipe, H. J. Mamin, C. S. Yannoni, T. D. Stowe, T. W. Kenny, and D. Rugar, "Electron Spin Relaxation Near a Micron-Size Ferromagnet," *Phys. Rev. Lett.*, vol. 87, p. 277602, dec 2001.

[191] A. Ajoy, X. Lv, E. Druga, K. Liu, B. Safvati, A. Morabe, M. Fenton, R. Nazaryan, S. Patel, T. F. Sjolander, J. A. Reimer, D. Sakellariou, C. A. Meriles, and A. Pines, "Wide dynamic range magnetic field cycler: Harnessing quantum control at low and high fields," aug 2018.

[192] A. Ajoy, R. Nazaryan, E. Druga, K. Liu, A. Aguilar, B. Han, M. Gierth, J. T. Oon, B. Safvati, R. Tsang, J. H. Walton, D. Suter, C. A. Meriles, J. A. Reimer, and A. Pines, "Room temperature "Optical Nanodiamond Hyperpolarizer": physics, design and operation," pp. 1–15, nov 2018.

[193] A. Ajoy, B. Safvati, R. Nazaryan, J. T. Oon, B. Han, P. Raghavan, R. Nirodi, A. Aguilar, K. Liu, X. Cai, X. Lv, E. Druga, C. Ramanathan, J. A. Reimer, C. A.

Meriles, D. Suter, and A. Pines, "Hyperpolarized relaxometry based nuclear T1 noise spectroscopy in hybrid diamond quantum registers," pp. 1–16, feb 2019.

[194] P. Fernández-Acebal, O. Rosolio, J. Scheuer, C. Müller, S. Müller, S. Schmitt, L. P. McGuinness, I. Schwarz, Q. Chen, A. Retzker, B. Naydenov, F. Jelezko, and M. B. Plenio, "Toward Hyperpolarization of Oil Molecules via Single Nitrogen Vacancy Centers in Diamond," *Nano Lett.*, vol. 18, no. 3, pp. 1882–1887, 2018.

[195] P. R. Zangara, S. Dhomkar, A. Ajoy, K. Liu, R. Nazaryan, D. Pagliero, D. Suter, J. A. Reimer, A. Pines, and C. A. Meriles, "Dynamics of frequency-swept nuclear spin optical pumping in powdered diamond at low magnetic fields," *Proc. Natl. Acad. Sci.*, p. 201811994, jan 2019.

[196] I. Schwartz, J. Scheuer, B. Tratzmiller, S. Müller, Q. Chen, I. Dhand, Z.-Y. Wang, C. Müller, B. Naydenov, F. Jelezko, and M. B. Plenio, "Robust optical polarisation of nuclear spin baths using Hamiltonian engineering of NV centre quantum dynamics," *Sci. Adv.*, vol. 4, p. eaat8978, aug 2018.

[197] V. S. Bajaj, M. L. Mak-Jurkauskas, M. Belenky, J. Herzfeld, and R. G. Griffin, "Functional and shunt states of bacteriorhodopsin resolved by 250 GHz dynamic nuclear polarization–enhanced solid-state NMR," *Proc. Natl. Acad. Sci.*, vol. 106, no. 23, pp. 9244–9249, 2009.

[198] M. J. Bayro, G. T. Debelouchina, M. T. Eddy, N. R. Birkett, C. E. MacPhee, M. Rosay, W. E. Maas, C. M. Dobson, and R. G. Griffin, "Intermolecular Structure Determination of Amyloid Fibrils with Magic-Angle Spinning and Dynamic Nuclear Polarization NMR," *J. Am. Chem. Soc.*, vol. 133, no. 35, pp. 13967–13974, 2011.

[199] J. Cai, a. Retzker, F. Jelezko, and M. B. Plenio, "A large-scale quantum simulator on a diamond surface at room temperature," *Nat. Phys.*, vol. 9, no. 1, pp. 1–6, 2013.

[200] J.-P. P. Tetienne, R. W. De Gille, D. A. Broadway, T. Teraji, S. E. Lillie, J. M. McCoey, N. Dontschuk, L. T. Hall, A. Stacey, D. A. Simpson, and L. C. L. Hollenberg, "Spin properties of dense near-surface ensembles of nitrogen-vacancy centers in diamond," *Phys. Rev. B*, vol. 97, p. 85402, feb 2018.

[201] J. E. Lang, R. B. Liu, and T. S. Monteiro, "Dynamical-decoupling-based quantum sensing: Floquet spectroscopy," *Phys. Rev. X*, vol. 5, pp. 1–12, oct 2015.

[202] D. B. Bucher, D. R. Glenn, H. Park, M. D. Lukin, and R. L. Walsworth, "Hyperpolarization-enhanced NMR spectroscopy with femtomole sensitivity using quantum defects in diamond," oct 2018.

[203] J. Smits, J. T. Damron, P. Kehayias, A. F. McDowell, N. Mosavian, I. Fescenko, N. Ristoff, A. Laraoui, A. Jarmola, and V. M. Acosta, "Two-dimensional nuclear magnetic resonance spectroscopy with a microfluidic diamond quantum sensor," *Sci. Adv.*, vol. 5, p. eaaw7895, jul 2019.

[204] S. E. Lillie, N. Dontschuk, D. A. Broadway, D. L. Creedon, L. C. Hollenberg, and J.-P. Tetienne, "Imaging Graphene Field-Effect Transistors on Diamond Using Nitrogen-Vacancy Microscopy," *Phys. Rev. Appl.*, vol. 12, p. 024018, aug 2019.

[205] M. J. H. Ku, T. X. Zhou, Q. Li, Y. J. Shin, J. K. Shi, C. Burch, H. Zhang, F. Casola, T. Taniguchi, K. Watanabe, P. Kim, A. Yacoby, and R. L. Walsworth, "Imaging Viscous Flow of the Dirac Fluid in Graphene Using a Quantum Spin Magnetometer," may 2019.

[206] H. Zheng, Z. Sun, G. Chatzidrosos, C. Zhang, K. Nakamura, H. Sumiya, T. Ohshima, J. Isoya, J. Wrachtrup, A. Wickenbrock, and D. Budker, "Microwave-free vector magnetometry with nitrogen-vacancy centers along a single axis in diamond," 2019.

[207] P. Wang, Z. Yuan, P. Huang, X. Rong, M. Wang, X. Xu, C. Duan, C. Ju, F. Shi, and J. Du, "High-resolution vector microwave magnetometry based on solid-state spins in diamond," *Nat. Commun.*, vol. 6, mar 2015.

[208] K. Yahata, Y. Matsuzaki, S. Saito, H. Watanabe, and J. Ishi-Hayase, "Demonstration of vector magnetic field sensing by simultaneous control of nitrogen-vacancy centers in diamond using multi-frequency microwave pulses," *Appl. Phys. Lett.*, vol. 114, nov 2019.

[209] S. Hsieh, P. Bhattacharyya, C. Zu, T. Mittiga, T. J. Smart, F. Machado, B. Kobrin, T. O. Höhn, N. Z. Rui, M. Kamrani, S. Chatterjee, S. Choi, M. Zaletel, V. V. Struzhkin, J. E. Moore, V. I. Levitas, R. Jeanloz, and N. Y. Yao, "Imaging stress and magnetism at high pressures using a nanoscale quantum sensor," dec 2018.

[210] J.-P. Tetienne, D. Broadway, S. Lillie, N. Dontschuk, T. Teraji, L. Hall, A. Stacey, D. Simpson, and L. Hollenberg, "Proximity-Induced Artefacts in Magnetic Imaging with Nitrogen-Vacancy Ensembles in Diamond," *Sensors*, vol. 18, p. 1290, apr 2018.

[211] J. M. Schloss, J. F. Barry, M. J. Turner, and R. L. Walsworth, "Simultaneous Broadband Vector Magnetometry Using Solid-State Spins," *Phys. Rev. Appl.*, vol. 10, no. 3, 2018.

[212] A. Nowodzinski, M. Chipaux, L. Toraille, V. Jacques, J.-F. Roch, and T. Debuisschert, "Nitrogen-Vacancy centers in diamond for current imaging at the redistributive layer level of Integrated Circuits," *Microelectron. Reliab.*, vol. 55, pp. 1549–1553, aug 2015.

[213] M. Lesik, T. Plisson, L. Toraille, J. Renaud, F. Occelli, M. Schmidt, O. Salord, A. Delobbe, T. Debuisschert, L. Rondin, P. Loubeyre, and J.-F. Roch, "Magnetic measurements on micron-size samples under high pressure using designed NV centers," dec 2018.

[214] J. Michl, T. Teraji, S. Zaiser, I. Jakobi, G. Waldherr, F. Dolde, P. Neumann, M. W. Doherty, N. B. Manson, J. Isoya, and J. Wrachtrup, "Perfect alignment and preferential orientation of nitrogen-vacancy centers during chemical vapor deposition diamond growth on (111) surfaces," *Appl. Phys. Lett.*, vol. 104, no. 10, 2014.

[215] M. Lesik, J. P. Tetienne, A. Tallaire, J. Achard, V. Mille, A. Gicquel, J. F. Roch, and V. Jacques, "Perfect preferential orientation of nitrogen-vacancy defects in a synthetic diamond sample," *Appl. Phys. Lett.*, vol. 104, p. 113107, 2014.

[216] J. H. Stathis and S. Zafar, "The negative bias temperature instability in MOS devices: A review," *Microelectron. Reliab.*, vol. 46, no. 2, pp. 270–286, 2006.

[217] P. Zhang, E. Tevaarwerk, B. N. Park, D. E. Savage, G. K. Celler, I. Knezevic, P. G. Evans, M. A. Eriksson, and M. G. Lagally, "Electronic transport in nanometre-scale silicon-on-insulator membranes," *Nature*, vol. 439, no. 7077, pp. 703–706, 2006.

[218] B. Kaczer, J. Franco, P. Weckx, P. Roussel, V. Putcha, E. Bury, M. Simicic, A. Chasin, D. Linten, B. Parvais, F. Catthoor, G. Rzepa, M. Waltl, and T. Grasser, "A brief overview of gate oxide defect properties and their relation to MOSFET instabilities and device and circuit time-dependent variability," *Microelectron. Reliab.*, vol. 81, pp. 186–194, 2018.

[219] J. R. Weber, W. F. Koehl, J. B. Varley, a. Janotti, B. B. Buckley, C. G. Van de Walle, and D. D. Awschalom, "Quantum computing with defects.," *Proc. Natl. Acad. Sci. U. S. A.*, vol. 107, no. 19, pp. 8513–8518, 2010.

[220] M. Kaviani, P. Deák, B. Aradi, T. Frauenheim, J.-P. Chou, and A. Gali, "Proper Surface Termination for Luminescent Near-Surface NV Centers in Diamond," *Nano Lett.*, vol. 14, pp. 4772–4777, aug 2014.

[221] M. Usman, J. Bocquel, J. Salfi, B. Voisin, A. Tankasala, R. Rahman, M. Y. Simmons, S. Rogge, and L. L. C. Hollenberg, "Spatial metrology of dopants in silicon with exact lattice site precision," *Nat. Nanotechnol.*, vol. 11, p. 763, 2016.

[222] F. Dolde, M. W. Doherty, J. Michl, I. Jakobi, B. Naydenov, S. Pezzagna, J. Meijer, P. Neumann, F. Jelezko, N. B. Manson, and J. Wrachtrup, "Nanoscale detection of a single fundamental charge in ambient conditions using the NV - Center in diamond," *Phys. Rev. Lett.*, vol. 112, no. 9, p. 97603, 2014.

[223] S. Pezzagna, D. Rogalla, H. Becker, I. Jakobi, F. Dolde, B. Naydenov, J. Wrachtrup, F. Jelezko, C. Trautmann, and J. Meijer, "Creation of colour centres in diamond by collimated ionâĂŘimplantation through nanoâĂŘchannels in mica," *Phys. status solidi*, vol. 208, no. 9, pp. 2017–2022, 2011.

[224] K. Ohno, F. Joseph Heremans, L. C. Bassett, B. A. Myers, D. M. Toyli, A. C. Bleszynski Jayich, C. J. Palmstrøm, and D. D. Awschalom, "Engineering shallow spins in diamond with nitrogen delta-doping," *Appl. Phys. Lett.*, vol. 101, p. 82413, aug 2012.

[225] M. Lesik, N. Raatz, A. Tallaire, P. Spinicelli, R. John, J. Achard, A. Gicquel, V. Jacques, J. Roch, J. Meijer, and S. Pezzagna, "Production of bulk NV centre arrays by shallow implantation and diamond CVD overgrowth," *Phys. status solidi*, vol. 213, pp. 2594–2600, 2016.

[226] L. Zhang, J. Chen, L. Fan, O. Diéguez, J. Cao, Z. Pan, Y. Wang, J. Wang, M. Kim, S. Deng, J. Wang, H. Wang, J. Deng, R. Yu, J. F. Scott, and X. Xing, "Giant polarization in super-tetragonal thin films through interphase strain," *Science (80-.).*, vol. 497, no. August, pp. 494–497, 2018.

[227] A. L. Falk, P. V. Klimov, B. B. Buckley, V. Ivády, I. a. Abrikosov, G. Calusine, W. F. Koehl, Á. Gali, and D. D. Awschalom, "Electrically and mechanically tunable electron spins in silicon carbide color centers," *Phys. Rev. Lett.*, vol. 112, no. 18, p. 187601, 2014.

[228] G. Wolfowicz, S. Whiteley, and D. Awschalom, "Electrometry by optical charge conversion of deep defects in 4H-SiC," *Preprint*, p. arXiv:1803.05956, mar 2018.

[229] A. Stacey, N. Dontschuk, J.-P. Chou, D. A. Broadway, A. K. Schenk, M. J. Sear, J.-P. Tetienne, A. Hoffman, S. Prawer, C. I. Pakes, A. Tadich, N. P. de Leon, A. Gali, and L. C. L. Hollenberg, "Evidence for Primal sp 2 Defects at the Diamond Surface: Candidates for Electron Trapping and Noise Sources," *Adv. Mater. Interfaces*, vol. 6, p. 1801449, feb 2019.

[230] T. Iwasaki, W. Naruki, K. Tahara, T. Makino, H. Kato, M. Ogura, D. Takeuchi, S. Yamasaki, and M. Hatano, "Direct Nanoscale Sensing of the Internal Electric Field in Operating Semiconductor Devices Using Single Electron Spins," *ACS Nano*, vol. 11, no. 2, pp. 1238–1245, 2017.

[231] P. Strobel, M. Riedel, J. Ristein, and L. Ley, "Surface transfer doping of diamond," *Nature*, vol. 430, no. 6998, p. 439, 2004.

[232] F. Maier, M. Riedel, B. Mantel, J. Ristein, and L. Ley, "Origin of Surface Conductivity in Diamond," *Phys. Rev. Lett.*, vol. 85, pp. 3472–3475, oct 2000.

[233] C. I. Pakes, J. a. Garrido, and H. Kawarada, "Diamond surface conductivity: Properties, devices, and sensors," *MRS Bull.*, vol. 39, no. 06, pp. 542–548, 2014.

[234] F. Fávaro de Oliveira, S. A. Momenzadeh, D. Antonov, J. Scharpf, C. Osterkamp, B. Naydenov, F. Jelezko, A. Denisenko, and J. Wrachtrup, "Toward Optimized Surface δ-Profiles of Nitrogen-Vacancy Centers Activated by Helium Irradiation in Diamond," *Nano Lett.*, vol. 16, pp. 2228–2233, apr 2016.

[235] F. F. de Oliveira, D. Antonov, Y. Wang, P. Neumann, S. A. Momenzadeh, T. Häußermann, A. Pasquarelli, A. Denisenko, and J. Wrachtrup, "Tailoring spin defects in diamond," *Nat. Commun.*, vol. 8, p. 15409, jan 2017.

[236] A. Stacey, T. J. Karle, L. P. McGuinness, B. C. Gibson, K. Ganesan, S. Tomljenovic-Hanic, A. D. Greentree, A. Hoffman, R. G. Beausoleil, and S. Prawer, "Depletion of nitrogen-vacancy color centers in diamond via hydrogen passivation," *Appl. Phys. Lett.*, vol. 100, no. 7, pp. 6–10, 2012.

[237] M. V. Hauf, P. Simon, M. Seifert, A. W. Holleitner, M. Stutzmann, and J. A. Garrido, "Low dimensionality of the surface conductivity of diamond," *Phys. Rev. B - Condens. Matter Mater. Phys.*, vol. 89, no. 11, pp. 1–5, 2014.

[238] G. Akhgar, O. Klochan, L. H. Willems van Beveren, M. T. Edmonds, F. Maier, B. J. Spencer, J. C. McCallum, L. Ley, A. R. Hamilton, and C. I. Pakes, "Strong and tunable spin-orbit coupling in a two-dimensional hole gas in ionic-liquid gated diamond devices," *Nano Lett.*, vol. 16, no. 6, pp. 3768–3773, 2016.

[239] C. K. Kim, H. J. Ahn, J. M. Moon, S. S. H. Lee, D. I. Moon, J. S. Park, B. J. Cho, Y. K. Choi, and S. S. H. Lee, "Temperature control for the gate workfunction engineering of TiC film by atomic layer deposition," *Solid. State. Electron.*, vol. 114, pp. 90–93, dec 2015.

[240] S. Dhomkar, H. Jayakumar, P. R. Zangara, and C. A. Meriles, "Charge Dynamics in near-Surface, Variable-Density Ensembles of Nitrogen-Vacancy Centers in Diamond," *Nano Lett.*, vol. 18, pp. 4046–4052, may 2018.

[241] M. Nesládek, L. M. Stals, A. Stesmans, K. Iakoubovskij, G. J. Adriaenssens, J. Rosa, and M. Vaněček, "Dominant defect levels in diamond thin films: A photocurrent and electron paramagnetic resonance study," *Appl. Phys. Lett.*, vol. 72, no. 25, pp. 3306–3308, 1998.

[242] M. Ershov, H. C. Liu, L. Li, M. Buchanan, Z. R. Wasilewski, and A. K. Jonscher, "Negative capacitance effect in semiconductor devices," *IEEE Trans. Electron Devices*, vol. 45, no. 10, pp. 2196–2206, 1998.

[243] A. K. Jonscher, "The physical origin of negative capacitance," *J. Chem. Soc. Faraday Trans. 2*, vol. 82, no. 1, p. 75, 1986.

[244] F. Lemmi and N. M. Johnson, "Negative capacitance in forward biased hydrogenated amorphous silicon p+-i-n+ diodes," *Appl. Phys. Lett.*, vol. 74, no. 2, pp. 251–253, 1999.

[245] W. P. Leroy, C. Detavernier, R. L. Van Meirhaeghe, A. J. Kellock, and C. Lavoie, "Solid-state formation of titanium carbide and molybdenum carbide as contacts for carbon-containing semiconductors," *J. Appl. Phys.*, vol. 99, no. 6, 2006.

[246] G. Chicot, T. N. Tran Thi, A. Fiori, F. Jomard, E. Gheeraert, E. Bustarret, and J. Pernot, "Hole transport in boron delta-doped diamond structures," *Appl. Phys. Lett.*, vol. 101, no. 16, p. 162101, 2012.

[247] J. Scharpf, A. Denisenko, C. I. Pakes, S. Rubanov, A. Bergmaier, G. Dollinger, C. Pietzka, and E. Kohn, "Transport behaviour of boron delta-doped diamond,"

Phys. status solidi, vol. 210, no. 10, pp. 2028–2034, 2013.

[248] H. Kawarada, "High-Current Metal Oxide Semiconductor Field-Effect Transistors on H-Terminated Diamond Surfaces and Their High-Frequency Operation," *Jpn. J. Appl. Phys.*, vol. 51, no. 9R, p. 90111, 2012.

[249] M. Kasu, "Diamond field-effect transistors for RF power electronics: Novel NO_2 hole doping and low-temperature deposited Al_2O_3 passivation," *Jpn. J. Appl. Phys.*, vol. 56, no. 1S, p. 01AA01, 2017.

[250] M. T. Edmonds, L. H. W. V. Beveren, O. Klochan, J. Cervenka, K. Ganesan, S. Prawer, L. Ley, A. R. Hamilton, and C. I. Pakes, "Spin âĹŠ Orbit Interaction in a Two-Dimensional Hole Gas at the Surface of Hydrogenated Diamond," *Nano Lett.*, vol. 15, pp. 16–20, 2014.

[251] G. Akhgar, D. L. Creedon, L. H. W. V. Beveren, A. Stacey, D. I. Hoxley, C. Mccallum, L. Ley, A. R. Hamilton, C. I. Pakes, G. Akhgar, D. L. Creedon, L. H. W. V. Beveren, L. H. Willems van Beveren, A. Stacey, D. I. Hoxley, J. C. McCallum, L. Ley, A. R. Hamilton, and C. I. Pakes, "G-factor and well width variations for the two-dimensional hole gas in surface conducting diamond," *Appl. Phys. Lett.*, vol. 112, p. 42102, jan 2018.

[252] P. Kehayias, M. J. Turner, R. Trubko, J. M. Schloss, C. A. Hart, M. Wesson, D. R. Glenn, and R. L. Walsworth, "Imaging crystal stress in diamond using ensembles of nitrogen-vacancy centers," 2019.

[253] J. Li, Z. Shan, and E. Ma, "Elastic strain engineering for unprecedented materials properties," *MRS Bull.*, vol. 39, no. 2, pp. 108–114, 2014.

[254] M. Chu, Y. Sun, U. Aghoram, and S. E. Thompson, "Strain: A Solution for Higher Carrier Mobility in Nanoscale MOSFETs," *Annu. Rev. Mater. Res.*, vol. 39, pp. 203–229, jul 2009.

[255] B. G. Shin, G. H. Han, S. J. Yun, H. M. Oh, J. J. Bae, Y. J. Song, C.-Y. Park, and Y. H. Lee, "Indirect Bandgap Puddles in Monolayer MoS2 by Substrate-Induced Local Strain," *Adv. Mater.*, vol. 28, pp. 9378–9384, 2016.

[256] A. R. Adams, "Strained-Layer Quantum-Well Lasers," *IEEE J. Sel. Top. Quantum Electron.*, vol. 17, pp. 1364–1373, sep 2011.

[257] A. M. Smith, A. M. Mohs, and S. Nie, "Tuning the optical and electronic properties of colloidal nanocrystals by lattice strain," *Nat. Nanotechnol.*, vol. 4, p. 56, dec 2008.

[258] G.-X. Ni, H.-Z. Yang, W. Ji, S.-J. Baeck, C.-T. Toh, J.-H. Ahn, V. M. Pereira, and B. Özyilmaz, "Tuning Optical Conductivity of Large-Scale CVD Graphene by Strain Engineering," *Adv. Mater.*, vol. 26, pp. 1081–1086, 2013.

[259] R. S. Jacobsen, K. N. Andersen, P. I. Borel, J. Fage-Pedersen, L. H. Frandsen, O. Hansen, M. Kristensen, A. V. Lavrinenko, G. Moulin, H. Ou, C. Peucheret, B. Zsigri, and A. Bjarklev, "Strained silicon as a new electro-optic material," *Nature*, vol. 441, p. 199, may 2006.

[260] Y. L. Tang, Y. L. Zhu, E. A. Eliseev, W. Y. Wang, Y. J. Wang, Y. B. Xu, Z. D. Zhang, and S. J. Pennycook, "Observation of a periodic array of flux- closure quadrants in strained ferroelectric PbTiO3 films," *Science*, vol. 348, no. April, pp. 1–10, 2015.

[261] J.-P. Locquet, J. Perret, J. Fompeyrine, E. Mächler, J. W. Seo, and G. Van Tendeloo, "Doubling the critical temperature of La 1.9 Sr 0.1 CuO 4 using epitaxial strain," *Nature*, vol. 394, no. 6692, p. 453, 1998.

[262] J. Vanhellemont, I. D. Wolf, K. G. F. Janssens, S. Frabboni, R. Balboni, and A. Armigliato, "On the assessment of local stress distributions in integrated circuits," *Appl. Surf. Sci.*, vol. 63, no. 1, pp. 119–125, 1993.

[263] S. C. Jain, H. E. Maes, K. Pinardi, and I. De Wolf, "Stresses and strains in laticeâĂŘmismatched stripes, quantum wires, quantum dots, and substrates in Si technology," *J. Appl. Phys.*, vol. 79, no. 11, pp. 8145–8165, 1996.

[264] A. S. Voloshin and C. P. Burger, "Half-fringe photoelasticity: A new approach to whole-field stress analysis," *Exp. Mech.*, vol. 23, pp. 304–313, sep 1983.

[265] Y. Tang, D. H. Rich, E. H. Lingunis, and N. M. Haegel, "PolarizedâĂŘcathodoluminescence study of stress for GaAs grown selectively on patterned Si(100)," *J. Appl. Phys.*, vol. 76, no. 5, pp. 3032–3040, 1994.

[266] S. I. Wright, M. M. Nowell, and D. P. Field, "A Review of Strain Analysis Using Electron Backscatter Diffraction," *Microsc. Microanal.*, vol. 17, no. 3, pp. 316–329, 2011.

[267] Y. Kato, H. Umezawa, S.-i. Shikata, and T. Teraji, "Local stress distribution of dislocations in homoepitaxial chemical vapor deposite single-crystal diamond," *Diam. Relat. Mater.*, vol. 23, pp. 109–111, 2012.

[268] M. Holt, R. Harder, R. Winarski, and V. Rose, "Nanoscale Hard X-Ray Microscopy Methods for Materials Studies," *Annu. Rev. Mater. Res.*, vol. 43, no. 1, pp. 183–211, 2013.

[269] M. J. Hÿtch and A. M. Minor, "Observing and measuring strain in nanostructures and devices with transmission electron microscopy," *MRS Bull.*, vol. 39, no. 2, pp. 138–146, 2014.

[270] S. Whiteley, F. Heremans, G. Wolfowicz, D. Awschalom, and M. Holt, "Imaging dynamically-driven strain at the nanometer-scale using stroboscopic Scanning X-ray Diffraction Microscopy," *ArXiv e-prints*, aug 2018.

[271] M. Hÿtch, F. Houdellier, F. Hüe, and E. Snoeck, "Nanoscale holographic interferometry for strain measurements in electronic devices," *Nature*, vol. 453, p. 1086, jun 2008.

[272] G. H. Loechelt, N. G. Cave, and J. Menéndez, "Polarized off-axis Raman spectroscopy: A technique for measuring stress tensors in semiconductors," *J. Appl. Phys.*, vol. 86, no. 11, pp. 6164–6180, 1999.

[273] F. Grazioso, B. R. Patton, P. Delaney, M. L. Markham, D. J. Twitchen, and J. M. Smith, "Measurement of the full stress tensor in a crystal using photoluminescence from point defects: The example of nitrogen vacancy centers in diamond," *Appl. Phys. Lett.*, vol. 103, no. 10, p. 101905, 2013.

[274] M. W. Doherty, V. V. Struzhkin, D. a. Simpson, L. P. McGuinness, Y. Meng, A. Stacey, T. J. Karle, R. J. Hemley, N. B. Manson, L. C. L. Hollenberg, and S. Prawer, "Electronic properties and metrology applications of the diamond NV - Center under pressure," *Phys. Rev. Lett.*, vol. 112, no. 4, p. 47601, 2014.

[275] E. Bauch, C. A. Hart, J. M. Schloss, M. J. Turner, J. F. Barry, P. Kehayias, S. Singh, and R. L. Walsworth, "Ultralong Dephasing Times in Solid-State Spin Ensembles via Quantum Control," *Phys. Rev. X*, vol. 8, p. 31025, jul 2018.

[276] S. Ali Momenzadeh, F. F. de Oliveira, P. Neumann, D. D. Bhaktavatsala Rao, A. Denisenko, M. Amjadi, Z. Chu, S. Yang, N. B. Manson, M. W. Doherty,

and J. Wrachtrup, "Thin Circular Diamond Membrane with Embedded Nitrogen-Vacancy Centers for Hybrid Spin-Mechanical Quantum Systems," *Phys. Rev. Appl.*, vol. 6, no. 2, p. 24026, 2016.

[277] S. E. Lillie, D. A. Broadway, N. Dontschuk, A. Zavabeti, D. A. Simpson, T. Teraji, T. Daeneke, L. C. L. Hollenberg, and J.-p. Tetienne, "Magnetic noise from ultrathin abrasively deposited materials on diamond," *Phys. Rev. Mater.*, vol. 2, p. 116002, nov 2018.

[278] N. Tsubouchi, M. Ogura, Y. Horino, and H. Okushi, "Low-resistance p+ layer formation into diamond using heavily B ion implantation," *Appl. Phys. Lett.*, vol. 89, no. 1, p. 12101, 2006.

[279] J. Forneris, P. Traina, D. G. Monticone, G. Amato, L. Boarino, G. Brida, I. P. Degiovanni, E. Enrico, E. Moreva, V. Grilj, and Others, "Electrical stimulation of non-classical photon emission from diamond color centers by means of sub-superficial graphitic electrodes," *Sci. Rep.*, vol. 5, p. 15901, 2015.

[280] P. Olivero, F. Bosia, B. A. Fairchild, B. C. Gibson, A. D. Greentree, P. Spizzirri, and S. Prawer, "Splitting of photoluminescent emission from nitrogen-vacancy centers in diamond induced by ion-damage-induced stress," *New J. Phys.*, vol. 15, pp. 0–22, 2013.

[281] C. A. Brookes, "Plastic deformation and anisotropy in the hardness of diamond," *Nature*, vol. 228, no. 5272, p. 660, 1970.

[282] Y. G. Gogotsi, A. Kailer, and K. G. Nickel, "Pressure-induced phase transformations in diamond," *J. Appl. Phys.*, vol. 84, no. 3, pp. 1299–1304, 1998.

[283] S. Dub, P. Lytvyn, V. Strelchuk, A. Nikolenko, Y. Stubrov, I. Petrusha, T. Taniguchi, and S. Ivakhnenko, "Vickers Hardness of Diamond and cBN Single Crystals: AFM Approach," *Crystals*, vol. 7, no. 12, p. 369, 2017.

[284] C. J. H. Wort and R. S. Balmer, "Diamond as an electronic material," *Mater. Today*, vol. 11, no. 1-2, pp. 22–28, 2008.

[285] J.-P. Tetienne, N. Dontschuk, D. A. Broadway, S. E. Lillie, T. Teraji, D. A. Simpson, A. Stacey, and L. C. L. Hollenberg, "Apparent delocalization of the current density in metallic wires observed with diamond nitrogen-vacancy magnetometry," *Phys. Rev. B*, vol. 99, no. 1, p. 014436, 2019.

[286] Y. Jingu, K. Hirama, and H. Kawarada, "Ultrashallow TiC Source/Drain Contacts in Diamond MOSFETs Formed by Hydrogenation-Last Approach," *IEEE Trans. Electron Devices*, vol. 57, pp. 966–972, may 2010.

[287] Y. Hoshino, H. Kato, T. Makino, M. Ogura, T. Iwasaki, M. Hatano, and S. Yamasaki, "Electrical properties of lateral pâĂŞn junction diodes fabricated by selective growth of n+ diamond," *Phys. status solidi*, vol. 209, pp. 1761–1764, 2012.

[288] K. Hirama, H. Takayanagi, S. Yamauchi, Y. Jingu, H. Umezawa, and H. Kawarada, "High-performance p-channel diamond MOSFETs with alumina gate insulator," in *2007 IEEE Int. Electron Devices Meet.*, pp. 873–876, dec 2007.

[289] D. Wildanger, J. R. Maze, and S. W. Hell, "Diffraction unlimited all-optical recording of electron spin resonances," *Phys. Rev. Lett.*, vol. 107, p. 17601, 2011.

[290] X.-D. Chen, S. Li, A. Shen, Y. Dong, C.-H. Dong, G.-C. Guo, and F.-W. Sun, "Near-Infrared-Enhanced Charge-State Conversion for Low-Power Optical Nanoscopy with Nitrogen-Vacancy Centers in Diamond," *Phys. Rev. Appl.*, vol. 7, p. 14008, jan 2017.

[291] E. E. Kleinsasser, M. M. Stanfield, J. K. Q. Banks, Z. Zhu, W.-D. Li, V. M. Acosta, H. Watanabe, K. M. Itoh, and K.-M. C. Fu, "High density NV sensing surface created via He^+ ion implantation of ^{12}C diamond," *Appl. Phys. Lett.*, vol. 108, p. 202401, 2016.

[292] M. Jamali, I. Gerhardt, M. Rezai, K. Frenner, H. Fedder, and J. Wrachtrup, "Microscopic diamond solid-immersion-lenses fabricated around single defect centers by focused ion beam milling," *Rev. Sci. Instrum.*, vol. 85, p. 123703, 2014.

[293] T. M. Babinec, B. J. M. Hausmann, M. Khan, Y. Zhang, J. R. Maze, P. R. Hemmer, and M. Loncar, "A diamond nanowire single-photon source.," *Nat. Nanotechnol.*, vol. 5, no. 3, pp. 195–199, 2010.

[294] P. Appel, E. Neu, M. Ganzhorn, A. Barfuss, M. Batzer, M. Gratz, A. Tschöpe, and P. Maletinsky, "Fabrication of all diamond scanning probes for nanoscale magnetometry," *Rev. Sci. Instrum.*, vol. 87, no. April, p. 63703, 2016.

[295] B. Khanaliloo, H. Jayakumar, A. C. Hryciw, D. P. Lake, H. Kaviani, and P. E. Barclay, "Single-Crystal Diamond Nanobeam Waveguide Optomechanics," *Phys. Rev. X*, vol. 5, no. 4, p. 41051, 2015.

[296] Y. I. Sohn, S. Meesala, B. Pingault, H. A. Atikian, J. Holzgrafe, M. GündoÇğan, C. Stavrakas, M. J. Stanley, A. Sipahigil, J. Choi, M. Zhang, J. L. Pacheco, J. Abraham, E. Bielejec, M. D. Lukin, M. Atatüre, and M. Lončar, "Controlling the coherence of a diamond spin qubit through its strain environment," *Nat. Commun.*, vol. 9, p. 2012, dec 2018.

[297] J. Riedrich-Möller, L. Kipfstuhl, C. Hepp, E. Neu, C. Pauly, F. Mücklich, A. Baur, M. Wandt, S. Wolff, M. Fischer, S. Gsell, M. Schreck, and C. Becher, "One- and two-dimensional photonic crystal microcavities in single crystal diamond," *Nat. Nanotechnol.*, vol. 7, no. 1, pp. 69–74, 2011.

[298] M. J. Burek, N. P. De Leon, B. J. Shields, B. J. M. Hausmann, Y. Chu, Q. Quan, A. S. Zibrov, H. Park, M. D. Lukin, and M. Lončar, "Free-standing mechanical and photonic nanostructures in single-crystal diamond," *Nano Lett.*, vol. 12, no. 12, pp. 6084–6089, 2012.

[299] A. Faraon, C. Santori, Z. Huang, V. M. Acosta, and R. G. Beausoleil, "Coupling of nitrogen-vacancy centers to photonic crystal cavities in monocrystalline diamond," *Phys. Rev. Lett.*, vol. 109, no. 3, p. 33604, 2012.

[300] B. J. M. Hausmann, I. B. Bulu, P. B. Deotare, M. McCutcheon, V. Venkataraman, M. L. Markham, D. J. Twitchen, and M. Loncar, "Integrated High Quality Factor Optical Resonators in Diamond.," *Nano Lett.*, vol. 12, pp. 1578âĹŠ–1582, 2013.

[301] Y. Tao, J. M. Boss, B. A. Moores b, and C. L. Degen, "Single-crystal diamond nanomechanical resonators with quality factors exceeding one million," *Nat. Commun.*, vol. 5, p. 3638, 2014.

[302] P. Ovartchaiyapong, K. W. Lee, B. A. Myers, and A. C. B. Jayich, "Dynamic strain-mediated coupling of a single diamond spin to a mechanical resonator," *Nat. Commun.*, vol. 5, p. 4429, dec 2014.

[303] A. Banerjee, D. Bernoulli, H. Zhang, M.-F. Yuen, J. Liu, J. Dong, F. Ding, J. Lu, M. Dao, W. Zhang, Y. Lu, and S. Suresh, "Ultralarge elastic deformation of nanoscale diamond," *Science (80-.).*, vol. 360, no. 6386, pp. 300–302, 2018.

[304] E. R. Macquarrie, T. A. Gosavi, N. R. Jungwirth, S. A. Bhave, and G. D. Fuchs, "Mechanical spin control of nitrogen-vacancy centers in diamond," *Phys. Rev. Lett.*, vol. 111, no. 22, p. 227602, 2013.

[305] J. Teissier, A. Barfuss, P. Appel, E. Neu, and P. Maletinsky, "Strain coupling of a nitrogen-vacancy center spin to a diamond mechanical oscillator," *Phys. Rev. Lett.*, vol. 113, no. 2, pp. 1–5, 2014.

[306] H. Y. Chen, E. R. MacQuarrie, and G. D. Fuchs, "Orbital State Manipulation of a Diamond Nitrogen-Vacancy Center Using a Mechanical Resonator," *Phys. Rev. Lett.*, vol. 120, no. 16, p. 167401, 2018.

[307] E. R. Macquarrie, T. A. Gosavi, S. A. Bhave, and G. D. Fuchs, "Continuous dynamical decoupling of a single diamond nitrogen-vacancy center spin with a mechanical resonator," *Phys. Rev. B*, vol. 92, no. 22, p. 224419, 2015.

[308] E. Gil-Santos, D. Ramos, J. Martínez, M. Fernández-Regúlez, R. García, Á. San Paulo, M. Calleja, and J. Tamayo, "Nanomechanical mass sensing and stiffness spectrometry based on two-dimensional vibrations of resonant nanowires," *Nat. Nanotechnol.*, vol. 5, no. 9, pp. 641–645, 2010.

[309] J. L. Arlett, E. B. Myers, and M. L. Roukes, "Comparative advantages of mechanical biosensors," *Nat. Nanotechnol.*, vol. 6, no. 4, pp. 203–215, 2011.

[310] M. Calleja, P. M. Kosaka, Á. San Paulo, and J. Tamayo, "Challenges for nanomechanical sensors in biological detection," *Nanoscale*, vol. 4, no. 16, pp. 4925–4938, 2012.

[311] M. S. Hanay, S. I. Kelber, C. D. O'Connell, P. Mulvaney, J. E. Sader, and M. L. Roukes, "Inertial imaging with nanomechanical systems," *Nat. Nanotechnol.*, vol. 10, no. 4, pp. 339–344, 2015.

[312] H. F. Mildrum, J. B. Krupar, and A. E. Ray, "High coercive force 2-17type Sm1-xErx(Co0.69Fe0.22Cu0.08Zr0.02)7.22magnets with a low temperature coefficient," *J. Less-Common Met.*, vol. 93, pp. 261–267, sep 1983.

[313] A. M. Stoneham, "The shapes of inhomogeneously broadened resonance lines II. Second-order effects," *J. Phys. C Solid State Phys.*, vol. 1, p. 302, jun 1968.

[314] A. E. H. Love, *A treatise on the mathematical theory of elasticity.* New york: Dover publications, 2011.

[315] A. R. Lang, M. Moore, A. P. W. Makepeace, W. Wierzchowski, and C. M. Welbourn, "On the Dilatation of Synthetic Type Ib Diamond by Substitutional Nitrogen Im-

purity," *Philos. Trans. R. Soc. A Math. Phys. Eng. Sci.*, vol. 337, pp. 497–520, dec 1991.

[316] T. B. Biktagirov, A. N. Smirnov, V. Y. Davydov, M. W. Doherty, A. Alkauskas, B. C. Gibson, and V. A. Soltamov, "Strain broadening of the 1042-nm zero phonon line of the NV- center in diamond: A promising spectroscopic tool for defect tomography," *Phys. Rev. B*, vol. 96, no. 7, pp. 1–7, 2017.

[317] J. C. Zheng, X. N. Xie, A. T. S. Wee, and K. P. Loh, "Oxygen-induced surface state on diamond (100)," *Diam. Relat. Mater.*, vol. 10, no. 3-7, pp. 500–505, 2001.

[318] Y. Garino, T. Teraji, S. Koizumi, Y. Koide, and T. Ito, "P-type diamond Schottky diodes fabricated by vacuum ultraviolet light/ozone surface oxidation: Comparison with diodes based on wet-chemical oxidation," *Phys. Status Solidi Appl. Mater. Sci.*, vol. 206, no. 9, pp. 2082–2085, 2009.

[319] Y. Mori, H. Kawarada, and A. Hiraki, "Properties of metal/diamond interfaces and effects of oxygen adsorbed onto diamond surface," *Appl. Phys. Lett.*, vol. 58, no. 9, pp. 940–941, 1991.

[320] S. J. Sque, R. Jones, and P. R. Briddon, "Structure, electronics, and interaction of hydrogen and oxygen on diamond surfaces," *Phys. Rev. B - Condens. Matter Mater. Phys.*, vol. 73, no. 8, 2006.

[321] D. M. Toyli, C. D. Weis, G. D. Fuchs, T. Schenkel, and D. D. Awschalom, "Chip-scale nanofabrication of single spins and spin arrays in diamond," *Nano Lett.*, vol. 10, no. 8, pp. 3168–3172, 2010.

[322] S. Pezzagna, B. Naydenov, F. Jelezko, J. Wrachtrup, and J. Meijer, "Creation efficiency of nitrogen-vacancy centres in diamond," *New J. Phys.*, vol. 12, p. 65017, jun 2010.

[323] P. Deák, B. Aradi, M. Kaviani, T. Frauenheim, and A. Gali, "Formation of NV centers in diamond: A theoretical study based on calculated transitions and migration of nitrogen and vacancy related defects," *Phys. Rev. B - Condens. Matter Mater. Phys.*, vol. 89, no. 7, pp. 1–12, 2014.

[324] J. P. Goss, P. R. Briddon, M. J. Rayson, S. J. Sque, and R. Jones, "Vacancy-impurity complexes and limitations for implantation doping of diamond," *Phys. Rev. B - Condens. Matter Mater. Phys.*, vol. 72, no. 3, 2005.

[325] D. Takeuchi, H. Kato, G. S. Ri, T. Yamada, P. R. Vinod, D. Hwang, C. E. Nebel, H. Okushi, and S. Yamasaki, "Direct observation of negative electron affinity in hydrogen-terminated diamond surfaces," *Appl. Phys. Lett.*, vol. 86, p. 152103, apr 2005.

[326] J. Ristein, "Surface science of diamond: Familiar and amazing," *Surf. Sci.*, vol. 600, no. 18, pp. 3677–3689, 2006.

[327] B. Koslowski, S. Strobel, and P. Ziemann, "Comment on âĂIJorigin of surface conductivity in diamondâĂİ," *Phys. Rev. Lett.*, vol. 87, no. 20, pp. 209701–209705, 2001.

[328] B. Grotz, M. V. Hauf, M. Dankerl, B. Naydenov, S. Pezzagna, J. Meijer, F. Jelezko, J. Wrachtrup, M. Stutzmann, F. Reinhard, and J. a. Garrido, "Charge state manipulation of qubits in diamond," *Nat. Commun.*, vol. 3, p. 729, 2012.

[329] A. N. Newell, D. A. Dowdell, and D. H. Santamore, "Surface effects on nitrogen vacancy centers neutralization in diamond," *J. Appl. Phys.*, vol. 120, no. 18, 2016.

[330] H. Sato and M. Kasu, "Maximum hole concentration for Hydrogen-terminated diamond surfaces with various surface orientations obtained by exposure to highly concentrated NO2," *Diam. Relat. Mater.*, vol. 31, pp. 47–49, jan 2013.

[331] C. Schreyvogel, V. Polyakov, S. Burk, H. Fedder, A. Denisenko, F. Fávaro de Oliveira, R. Wunderlich, J. Meijer, V. Zuerbig, J. Wrachtrup, and C. E. Nebel, "Active and fast charge-state switching of single NV centres in diamond by in-plane Al-Schottky junctions," *Beilstein J. Nanotechnol.*, vol. 7, pp. 1727–1735, 2016.

[332] B. G. Streetman and S. Banerjee, *Solid state electronic devices*. Upper Saddle River, N.J. : Prentice Hall, 5th ed ed., 2000.

[333] T. Fukushima, "Precise and fast computation of generalized Fermi-Dirac integral by parameter polynomial approximation," *Appl. Math. Comput.*, vol. 270, pp. 802–807, 2015.

[334] T. Fukushima, "Precise and fast computation of Fermi-Dirac integral of integer and half integer order by piecewise minimax rational approximation," *Appl. Math. Comput.*, vol. 259, pp. 708–729, 2015.

[335] S. J. Maddox, "fdint 2.02," 2017.